

University of Windsor

Scholarship at UWindor

Electronic Theses and Dissertations

Theses, Dissertations, and Major Papers

1995

Wear regimes and transitions in ceramic particulate-reinforced aluminum alloys.

Jie. Zhang
University of Windsor

Follow this and additional works at: <https://scholar.uwindsor.ca/etd>

Recommended Citation

Zhang, Jie., "Wear regimes and transitions in ceramic particulate-reinforced aluminum alloys." (1995). *Electronic Theses and Dissertations*. 4555.
<https://scholar.uwindsor.ca/etd/4555>

This online database contains the full-text of PhD dissertations and Masters' theses of University of Windsor students from 1954 forward. These documents are made available for personal study and research purposes only, in accordance with the Canadian Copyright Act and the Creative Commons license—CC BY-NC-ND (Attribution, Non-Commercial, No Derivative Works). Under this license, works must always be attributed to the copyright holder (original author), cannot be used for any commercial purposes, and may not be altered. Any other use would require the permission of the copyright holder. Students may inquire about withdrawing their dissertation and/or thesis from this database. For additional inquiries, please contact the repository administrator via email (scholarship@uwindsor.ca) or by telephone at 519-253-3000ext. 3208.



National Library
of Canada

Bibliothèque nationale
du Canada

Acquisitions and
Bibliographic Services Branch

Direction des acquisitions et
des services bibliographiques

395 Wellington Street
Ottawa, Ontario
K1A 0N4

395, rue Wellington
Ottawa (Ontario)
K1A 0N4

Your No. Votre référence

Our No. Notre référence

NOTICE

The quality of this microform is heavily dependent upon the quality of the original thesis submitted for microfilming. Every effort has been made to ensure the highest quality of reproduction possible.

If pages are missing, contact the university which granted the degree.

Some pages may have indistinct print especially if the original pages were typed with a poor typewriter ribbon or if the university sent us an inferior photocopy.

Reproduction in full or in part of this microform is governed by the Canadian Copyright Act, R.S.C. 1970, c. C-30, and subsequent amendments.

AVIS

La qualité de cette microforme dépend grandement de la qualité de la thèse soumise au microfilmage. Nous avons tout fait pour assurer une qualité supérieure de reproduction.

S'il manque des pages, veuillez communiquer avec l'université qui a conféré le grade.

La qualité d'impression de certaines pages peut laisser à désirer, surtout si les pages originales ont été dactylographiées à l'aide d'un ruban usé ou si l'université nous a fait parvenir une photocopie de qualité inférieure.

La reproduction, même partielle, de cette microforme est soumise à la Loi canadienne sur le droit d'auteur, SRC 1970, c. C-30, et ses amendements subséquents.

**WEAR REGIMES AND TRANSITIONS IN CERAMIC
PARTICULATE-REINFORCED ALUMINUM ALLOYS**

by

Jie Zhang

A Dissertation

**Submitted to the Faculty of Graduate Studies and Research
Through the Engineering Materials Program in the
Department of Mechanical and Materials Engineering
in Partial Fulfilment of the Requirements for
the Degree of Doctor of Philosophy at the
University of Windsor**

Windsor, Ontario, Canada

© Jie Zhang, 1995



National Library
of Canada

Acquisitions and
Bibliographic Services Branch

395 Wellington Street
Ottawa, Ontario
K1A 0N4

Bibliothèque nationale
du Canada

Direction des acquisitions et
des services bibliographiques

395, rue Wellington
Ottawa (Ontario)
K1A 0N4

Your title Votre référence

Your title Votre référence

The author has granted an irrevocable non-exclusive licence allowing the National Library of Canada to reproduce, loan, distribute or sell copies of his/her thesis by any means and in any form or format, making this thesis available to interested persons.

L'auteur a accordé une licence irrévocable et non exclusive permettant à la Bibliothèque nationale du Canada de reproduire, prêter, distribuer ou vendre des copies de sa thèse de quelque manière et sous quelque forme que ce soit pour mettre des exemplaires de cette thèse à la disposition des personnes intéressées.

The author retains ownership of the copyright in his/her thesis. Neither the thesis nor substantial extracts from it may be printed or otherwise reproduced without his/her permission.

L'auteur conserve la propriété du droit d'auteur qui protège sa thèse. Ni la thèse ni des extraits substantiels de celle-ci ne doivent être imprimés ou autrement reproduits sans son autorisation.

ISBN 0-612-10971-2

Canada

Name Jie Zhang

Dissertation Abstracts International is arranged by broad, general subject categories. Please select the one subject which most nearly describes the content of your dissertation. Enter the corresponding four-digit code in the spaces provided.

Metallurgy

SUBJECT TERM

0743

U·M·I

SUBJECT CODE

Subject Categories

THE HUMANITIES AND SOCIAL SCIENCES

COMMUNICATIONS AND THE ARTS

Architecture 0729
 Art History 0377
 Cinema 0900
 Dance 0378
 Fine Arts 0357
 Information Science 0723
 Journalism 0391
 Library Science 0399
 Mass Communications 0708
 Music 0413
 Speech Communication 0459
 Theater 0465

EDUCATION

General 0515
 Administration 0514
 Adult and Continuing 0516
 Agricultural 0517
 Art 0273
 Bilingual and Multicultural 0282
 Business 0688
 Community College 0275
 Curriculum and Instruction 0727
 Early Childhood 0518
 Elementary 0524
 Finance 0277
 Guidance and Counseling 0519
 Health 0680
 Higher 0745
 History of 0520
 Home Economics 0278
 Industrial 0521
 Language and Literature 0279
 Mathematics 0280
 Music 0522
 Philosophy of 0998
 Physical 0523

Psychology 0525
 Reading 0535
 Religious 0527
 Sciences 0714
 Secondary 0533
 Social Sciences 0534
 Sociology of 0340
 Special 0529
 Teacher Training 0530
 Technology 0710
 Tests and Measurements 0288
 Vocational 0747

LANGUAGE, LITERATURE AND LINGUISTICS

Language
 General 0679
 Ancient 0289
 Linguistics 0290
 Modern 0291
 Literature
 General 0401
 Classical 0294
 Comparative 0295
 Medieval 0297
 Modern 0298
 African 0316
 American 0591
 Asian 0305
 Canadian (English) 0352
 Canadian (French) 0355
 English 0593
 Germanic 0311
 Latin American 0312
 Middle Eastern 0315
 Romance 0313
 Slavic and East European 0314

PHILOSOPHY, RELIGION AND THEOLOGY

Philosophy 0422
 Religion
 General 0318
 Biblical Studies 0321
 Clergy 0319
 History of 0320
 Philosophy of 0322
 Theology 0469

SOCIAL SCIENCES

American Studies 0323
 Anthropology
 Archaeology 0324
 Cultural 0326
 Physical 0327
 Business Administration
 General 0310
 Accounting 0272
 Banking 0770
 Management 0454
 Marketing 0338
 Canadian Studies 0385
 Economics
 General 0501
 Agricultural 0503
 Commerce-Business 0505
 Finance 0508
 History 0509
 Labor 0510
 Theory 0511
 Folklore 0358
 Geography 0366
 Gerontology 0351
 History
 General 0578

Ancient 0579
 Medieval 0581
 Modern 0582
 Black 0328
 African 0331
 Asia, Australia and Oceania 0332
 Canadian 0334
 European 0335
 Latin American 0336
 Middle Eastern 0333
 United States 0337
 History of Science 0585
 Law 0398
 Political Science
 General 0615
 International Law and Relations 0616
 Public Administration 0617
 Recreation 0814
 Social Work 0452
 Sociology
 General 0626
 Criminology and Penology 0627
 Demography 0938
 Ethnic and Racial Studies 0631
 Individual and Family Studies 0628
 Industrial and Labor Relations 0629
 Public and Social Welfare 0630
 Social Structure and Development 0700
 Theory and Methods 0344
 Transportation 0709
 Urban and Regional Planning 0999
 Women's Studies 0453

THE SCIENCES AND ENGINEERING

BIOLOGICAL SCIENCES

Agriculture
 General 0473
 Agronomy 0285
 Animal Culture and Nutrition 0475
 Animal Pathology 0476
 Food Science and Technology 0359
 Forestry and Wildlife 0478
 Plant Culture 0479
 Plant Pathology 0480
 Plant Physiology 0817
 Range Management 0777
 Wood Technology 0746
 Biology
 General 0306
 Anatomy 0287
 Biostatistics 0308
 Botany 0309
 Cell 0379
 Ecology 0329
 Entomology 0353
 Genetics 0369
 Limnology 0793
 Microbiology 0410
 Molecular 0307
 Neuroscience 0317
 Oceanography 0416
 Physiology 0433
 Radiation 0821
 Veterinary Science 0778
 Zoology 0472
 Biophysics
 General 0786
 Medical 0760
 EARTH SCIENCES
 Biogeochemistry 0425
 Geochemistry 0996

Geodesy 0370
 Geology 0372
 Geophysics 0373
 Hydrology 0388
 Mineralogy 0411
 Paleobotany 0345
 Paleocology 0426
 Paleontology 0418
 Paleozoology 0985
 Palynology 0427
 Physical Geography 0368
 Physical Oceanography 0415

HEALTH AND ENVIRONMENTAL SCIENCES

Environmental Sciences 0768
 Health Sciences
 General 0566
 Audiology 0300
 Chemotherapy 0992
 Dentistry 0567
 Education 0350
 Hospital Management 0769
 Human Development 0758
 Immunology 0982
 Medicine and Surgery 0564
 Mental Health 0347
 Nursing 0569
 Nutrition 0570
 Obstetrics and Gynecology 0380
 Occupational Health and Therapy 0354
 Ophthalmology 0381
 Pathology 0571
 Pharmacology 0419
 Pharmacy 0572
 Physical Therapy 0382
 Public Health 0573
 Radiology 0574
 Recreation 0575

Speech Pathology 0460
 Toxicology 0383
 Home Economics 0386

PHYSICAL SCIENCES

Pure Sciences
 Chemistry
 General 0485
 Agricultural 0749
 Analytical 0486
 Biochemistry 0487
 Inorganic 0488
 Nuclear 0738
 Organic 0490
 Pharmaceutical 0491
 Physical 0494
 Polymer 0495
 Radiation 0754
 Mathematics 0405
 Physics
 General 0605
 Acoustics 0986
 Astronomy and Astrophysics 0606
 Atmospheric Science 0608
 Atomic 0748
 Electronics and Electricity 0607
 Elementary Particles and High Energy 0798
 Fluid and Plasma 0759
 Molecular 0609
 Nuclear 0610
 Optics 0752
 Radiation 0756
 Solid State 0611
 Statistics 0463
 Applied Sciences
 Applied Mechanics 0346
 Computer Science 0984

Engineering
 General 0537
 Aerospace 0538
 Agricultural 0539
 Automotive 0540
 Biomedical 0541
 Chemical 0542
 Civil 0543
 Electronics and Electrical 0544
 Heat and Thermodynamics 0348
 Hydraulic 0545
 Industrial 0546
 Marine 0547
 Materials Science 0794
 Mechanical 0548
 Metallurgy 0743
 Mining 0551
 Nuclear 0552
 Packaging 0549
 Petroleum 0765
 Sanitary and Municipal 0554
 System Science 0790
 Geotechnology 0428
 Operations Research 0796
 Plastics Technology 0795
 Textile Technology 0994

PSYCHOLOGY

General 0621
 Behavioral 0384
 Fluid 0622
 Clinical 0622
 Developmental 0620
 Experimental 0623
 Industrial 0624
 Personality 0625
 Physiological 0989
 Psychobiology 0349
 Psychometrics 0632
 Social 0451



To My Dear Wife

Xiaobo Luo

ABSTRACT

The purpose of this work was to study the dry sliding wear properties of aluminum matrix composites A356Al-SiC, 6061Al-Al₂O₃, 2014Al-SiC, with 0-20 pct. volume fraction reinforcement. Experiments were performed within a load range of 1 to 450 N and a sliding velocity range of 0.1 to 5.0 m/s. Two types of counterface materials namely SAE52100 bearing steel and mullite, were used. Three different wear rate regimes were observed in the composites. These were: (i) regime I (ultra mild wear regime), which occurred at low loads and low sliding velocities, where ceramic particles acted as load bearing elements. In this region increasing the particle size and volume fraction of particles improved the wear resistance of the composites. (ii) In regime II (mild wear regime) that covered mid-range loads, there was no significant difference between the wear rates of the unreinforced and the reinforced alloys. In this regime, particles at the contact surfaces fractured and shear forces were transmitted to the aluminum matrix. Wear proceeded by a subsurface delamination process. In addition to promoting subsurface cracking, particles also caused the abrasion of the aluminum matrix. (iii) The transition from regime II (mild wear) to regime III (severe wear) occurred at higher loads and/or higher sliding velocities when the contact surface temperature exceeded a critical value. The transition loads and temperatures were higher in the composites compared to the unreinforced Al alloys. Increasing particle size improves the wear resistance in regime I and delays transition to regime II. However there is no obvious difference in the wear resistances of the composites reinforced with different particle sizes in regime II and

regime III. Increasing the volume percent of particles delays the transitions between regime I and regime II as well as between regime II and regime III. Subjecting the materials to wear against a mullite counterface, which has a smaller thermal conductivity than a counterface made of steel, led to the occurrence of severe wear at lower loads. Different types of wear maps, including wear regime maps, wear rate maps, wear temperature maps and wear mechanism maps, have been constructed by considering the applied mechanical parameters such as the load and the sliding velocity. These maps provide a convenient way to summarize wear rate controlling mechanisms in metal matrix composites.

To study the plastic deformation and damage accumulation below the contact surfaces, new metallographic techniques have been developed and used to determine the magnitude of the shear strains and the microhardness gradients in near surface regions. Under dry sliding wear conditions, both the magnitude of plastic strains and the depth of heavily deformed zones increased with sliding distance and applied load. The flow stress and the plastic strains in the deformed zones are shown to obey a Voce type work hardening law. A model based on the hypothesis that delamination cracks leading to the generation of wear debris are formed by the coalescence of voids at a critical depth below the worn surfaces has been proposed. It is shown that the critical depth for maximum rate of damage accumulation is determined by a competition between the plastic strain which enhances void growth and the hydrostatic pressure which suppresses it.

ACKNOWLEDGEMENTS

The author wishes to express his sincere gratitude to Dr. A.T. Alpas for his academically inspiring guidance, supervision, suggestions, encouragement, as well as his friendship during his graduate study at University of Windsor.

The valuable suggestions and discussions with Dr. Y.Q. Ding and Dr. D.F. Watt are deeply appreciated. Sincere gratitude is also extended to Dr. J.D. Embury for his helpful discussions and comments.

The author would also like to thank Mr. John Robinson for his assistance with some experimental work and Mrs. Barbara Denomey for her help during his graduate study.

Particular appreciation is expressed to the NSERC and an industrial consortium of Alcan, INCO, Ontario Hydro, Pratt and Whitney, and Sherritt and Gordon for providing financial support for the research.

TABLE OF CONTENTS

ABSTRACT	(i)
ACKNOWLEDGEMENTS	(iii)
LIST OF FIGURES	(vii)
LIST OF TABLES	(xiv)
LIST OF SYMBOLS	(xv)
Chapter 1 Introduction	1
Chapter 2 Literature Review	5
2.1 General Classification of Wear Types	5
2.1.1 Abrasive Wear	6
2.1.2 Sliding Wear	6
2.1.3 Rolling Contact Wear	7
2.1.4 Fretting Wear	8
2.1.5 Erosive Wear	8
2.1.6 Corrosive Wear	8
2.2 Sliding Wear	9
2.2.1 Archard Wear equation	9
2.2.2 Transitions in Sliding Wear	11
2.2.3 Subsurface Zones in Sliding Wear	15
2.2.4 Transfer and Mechanical Mixing	18
2.3 Stress, Strain States and Contact Temperatures	18
2.3.1 Elastic Stresses in Surface Contact	18
2.3.1.1. Point Force Loading	19
2.3.1.2. Hertzian Contacts	21
2.3.1.3. Stress Field Under Normal and Tangential Force	23
2.3.2 Plastic Deformation of The Surface Layer	24
2.3.3 Surface Temperatures and Wear Mechanism Maps	26
2.4 Wear of Metal Matrix Composites	29
2.4.1 Introduction	29
2.4.2 Abrasive Wear of MMCs	31
2.4.3 Erosive Wear of MMCs	36
2.4.4 Sliding Wear of MMCs	40
2.4.4.1. Hard Particle/Fiber Reinforcement	40
2.4.4.2. Soft Particle Reinforcement	45
Chapter 3 Experimental Details	49
3.1 Materials	49

3.1.1	Al-Si-Mg Aluminum Alloy (A356) Reinforced with sic Particles	49
3.1.2	Al-Mg-Si Aluminium Alloy (6061) Reinforced with Al ₂ O ₃ Particles	53
3.1.3	Al-Cu-Mg Aluminium Alloys (2014Al, 2124Al) Reinforced with SiC Particles	57
3.2	Wear Tests: Measurement of Wear Rates	57
3.3	Subsurface Displacement and Microhardness Measurements	61
3.4	Contact Surface Temperature Measurements	66
3.5	Metallography of Cross-sections below the Worn Surfaces	66
Chapter 4. Experimental Results		70
4.1	Experimental Results on Al-Si-Mg (A356) Aluminum Alloy Reinforced with SiC Particles	70
4.1.1	Volumetric Wear-Sliding Distance Diagrams	70
4.1.2	Wear Rate Regimes and Transitions	72
4.1.3	Wear Debris	83
4.1.4	Bulk Temperature-Sliding Distance Diagrams	86
4.2	Experimental Results on Al-Mg-Si (6061) Aluminum Alloy Reinforced with Al₂O₃ Particles	89
4.2.1	Volumetric Wear-Sliding Distance Diagrams	89
4.2.2	Wear Rate Regimes and Transitions	93
4.2.3	Comparison of the \dot{W} of 6061Al-20%Al ₂ O ₃ With the Unreinforced 6061Al	95
4.2.4	Wear of Steel Counterface Against 6061Al-20%Al ₂ O ₃	97
4.2.5	Metallography of Worn Surfaces and Wear Debris	97
4.2.6	Effect of Sliding Velocity on the Wear Rates	105
4.2.7	Bulk Temperature Diagrams	110
4.2.8	Effect of Counterface Materials	116
4.3	Effect of microstructural factors on the wear rates of MMCs	120
4.3.1	Effect of Volume Fraction of particles on the Wear Rates	120
4.3.2	Effect of Particle Size on the Wear Rates	122
4.4	Subsurface Strains and Stresses	125
4.4.1	Strain Accumulation below the worn surfaces	125
4.4.2	Flow Stress of the Subsurfaces	131
Chapter 5 Discussion		135
5.1	Wear Mechanisms in Particle Reinforced Al Alloys	135
5.1.1	Wear Mechanisms in Regime I (Ultra Mild Wear)	135
5.1.2	Wear Mechanisms in Regime II (Mild Wear)	138
5.1.3	Wear Mechanisms in Regime III (Severe Wear)	148
5.2	Factors Influencing the Wear Transitions	156

5.2.1	Effect of Sliding Velocity	156
5.2.2	Effect of Temperature	158
5.3	Effect of Microstructure on Wear Rates	165
5.3.1	Effect of Particulate Size	165
5.3.2	Effect of Volume Fraction	167
5.4	Effect of Counterface Material	169
5.5	Wear Mechanism Maps	170
5.6	Modelling of Wear Mechanisms: a Model for Delamination Wear (Regime II)	177
5.6.1	Subsurface Stress-Strain Behavior	183
5.6.2	Delamination Wear in Ductile Materials Containing Second Phase Particles	184
Chapter 6	CONCLUSIONS AND RECOMMENDATIONS.	196
6.1	New Information Revealed by This Work	196
6.2	General Summary and Conclusions	198
6.2.1	Wear Regime and Mechanisms	198
6.2.2	Factors Influencing Wear Rates and Wear Transitions	199
6.2.3	Wear Mechanism Maps	200
6.2.4	Modelling of Delamination Wear	201
6.3	Recommendations for Future Work	202
	APPENDIX	203
	REFERENCES	205
	LIST OF PUBLICATIONS/PRESENTATIONS.	217
	VITA AUCTORIS	219

LIST OF FIGURES

Fig. 1. Different types of wear rate vs sliding distance curves	10
Fig. 2. Wear of aluminum-8% silicon alloy	13
Fig. 3. Transitional wear behavior for a carbon steel	16
Fig. 4. Schematic description of subsurface zones in sliding wear	17
Fig. 5. Coordinate system for axially symmetric point loading P	20
Fig. 6. Two spherical bodies in contact	22
Fig. 7. Steady-state plastic deformation regions in an elastic-perfectly plastic material under a sliding contact, for a maximum applied normal stress $p_0=4k$ and different friction coefficients	25
Fig. 8. Heat transfer in pin-on-disk configuration	27
Fig. 9. Wear map for carbon steel	30
Fig. 10. Relative wear resistance (RWR) for Al-11.8%Si-4.0%Mn matrix MMCs containing various volume fractions of 100 μm zircon particles, tested under low stress and high stress (pin on abrasive-covered drum) conditions	34
Fig. 11. Relative wear resistance for an Al6061/SiC _p MMC containing 20vol.% reinforcement, in tests sliding against continuous belts of abrasive paper carrying alumina particles of different sizes	35
Fig. 12. Erosion against impact angle for Al6061 MMCs containing various volume fractions of Saffil RF alumina fibre, eroded by 100 μm silicon carbide and silica particles at 65 m/s	38
Fig. 13. Wear resistance for the slurry erosion of an Al5083 MMC containing alumina-silica fibres at various volume fractions, for impact angles of 15° and 90°	39
Fig. 14. Weight-loss vs sliding distance plot for aluminum-matrix alloys 2014 and 2024 and composites of 2024 containing different weight percentages of four different-sized Al ₂ O ₃ particles	42

Fig. 15. Steady state wear rate vs. sliding velocity for (a) unreinforced 7091 alloy, and (b) reinforced composites of 7091 with SiC _p , perpendicularly oriented SiC _w and parallel-oriented SiC _w	44
Fig. 16. Optical micrographs of peak-aged microstructures of A356Al-20%SiC. Si particles are light grey phase.	50
Fig. 17. Histograms of the size distribution of SiC particles in A356Al-20%SiC	52
Fig. 18. Microstructure of 6061Al-20%Al ₂ O ₃	55
Fig. 19. Histograms of the size distribution of Al ₂ O ₃ particles in 6061Al-20%Al ₂ O ₃	56
Fig. 20. Block-on-ring wear apparatus	58
Fig. 21. Wear sample geometry manufactured to conform with the steel counterbody	62
Fig. 22. A typical volume (weight) loss vs. sliding distance for the A356Al alloy.	63
Fig. 23. (a) Schematic representation of a taper section taken from the worn specimen; (b) An enlarged taper section to illustrate the calculation of the depth corresponding to microindentation impressions	65
Fig. 24. Schematic illustration of the temperature measurement set-up with the block-on-ring apparatus	67
Fig. 25. Volume loss vs. sliding distance curves for A356Al alloy	71
Fig. 26. Wear rate vs. applied load diagram for A356Al and A356Al-20%SiC	74
Fig. 27. EDS data showing the variation of the ratio of iron to aluminum and silicon with the applied load for A356Al and A356Al-20%SiC	75
Fig. 28. Scanning electron micrographs showing (a) the overall view of the wear scar and (b) details of an iron-rich transfer layer deposited onto the surface of A356Al-20%SiC in regime I	76
Fig. 29. X-ray diffraction analysis of the loose debris of A356Al-20%SiC worn against SAE52100 bearing steel in regime I	77
Fig. 30. Deformation microstructure of A356Al below the worn surface; load=20 N; sliding distance 1000 m. Note the grains elongated in the sliding direction	78

Fig. 31. Void and crack nucleation around the silicon particles under the contact surface of A356Al	79
Fig. 32. Subsurface crack propagation of A356Al, load = 17 N	81
Fig. 33. Worn surface morphology of A356Al-20%SiC tested at 27 N. This is a typical morphology for the composites and the unreinforced alloys in regime II	82
Fig. 34. Worn surface morphology of unreinforced A356Al tested at 147 N. (regime III)	84
Fig. 35. X-ray diffraction analysis of the loose debris of A356Al worn against SAE52100 bearing steel in regime II	87
Fig. 36. X-ray diffraction analysis of the loose debris of A356Al-20%SiC worn against SAE52100 bearing steel in regime II	88
Fig. 37. The temperature distribution at the contact surface of (a) A356Al and (b) A356Al-20%SiC as a function of sliding distance	90
Fig. 38. Volume loss vs. sliding distance curves for 6061Al and 6061Al-20%Al ₂ O ₃ at different load levels	92
Fig. 39. Wear rate vs. applied load diagram for 6061Al and 6061Al-20%Al ₂ O ₃	94
Fig. 40. Wear-sliding distance curve of 6061Al-20%Al ₂ O ₃ at 150 N which shows sliding distance dependent transition from mild wear to severe wear	96
Fig. 41. Wear rate vs. applied load diagram for the SAE52100 bearing steel counterface rubbed against 6061Al and 6061Al-20%Al ₂ O ₃	98
Fig. 42. Surface morphologies of 6061Al-20%Al ₂ O ₃ specimens worn at different rates representing: Regime I, Regime II and Regime III	99
Fig. 43. EDS analysis of the 6061Al-20%Al ₂ O ₃ worn surface revealing that the transfer layers on the contact surface are iron-rich. (Counterbody: SAE52100 steel)	101
Fig. 44. Scanning electron micrograph of the contact surface of the composite (load = 3 N). The contact surface is covered by iron-rich transfer layers. The Al ₂ O ₃ particles ahead of the wear front form protrusions on the unworn surface (regime I)	102
Fig. 45. X-ray diffraction analysis of the loose debris of 6061Al-20%Al ₂ O ₃ worn against SAE52100 bearing steel in regime I	103

Fig. 46. Debris of 6061Al-20%Al ₂ O ₃ (regime II); (a) platelike debris particles; (b) equiaxed particles	104
Fig. 47. X-ray diffraction analysis of the loose debris of 6061Al-20%Al ₂ O ₃ worn against SAE52100 bearing steel in regime II	106
Fig. 48. X-ray diffraction analysis of the loose debris of 6061Al worn against SAE52100 bearing steel in regime II	107
Fig. 49. X-ray diffraction analysis of the loose debris of 6061Al worn against SAE52100 bearing steel in regime III	108
Fig. 50. Wear rate vs. sliding velocity for 6061Al and 6061Al-20%Al ₂ O ₃	109
Fig. 51. Wear rate vs. applied load diagram for 6061Al with different sliding velocities	112
Fig. 52. Wear rate vs. applied load diagram for 6061Al-20%Al ₂ O ₃ with different sliding velocities	113
Fig. 53. Temperature distribution at the contact surface of 6061Al and 6061Al-20%Al ₂ O ₃ as a function of sliding distance	115
Fig. 54. Temperature distribution at the contact surface of 6061Al as a function of sliding time and sliding velocity (4.9 N)	117
Fig. 55. Temperature distribution at the contact surface of 6061Al as a function of sliding time and sliding velocity (49 N)	118
Fig. 56. Wear rate vs. applied load diagrams for 6061Al and 6061Al-20%Al ₂ O ₃ worn on SAE52100	119
Fig. 57. Wear rate vs. applied load diagrams for 6061Al, 6061Al-10%Al ₂ O ₃ and 6061Al-20%Al ₂ O ₃	121
Fig. 58. Wear rate vs. applied load diagrams for 2014Al, 2124Al-20%SiC and 2014Al-20%SiC	124
Fig. 59. (a) Polished cross-section of an unworn specimen showing the interface between the marker and the specimen. (b) Displacement of the interface in a specimen worn at load=45 N, sliding distance=100 m	126
Fig. 60. Subsurface displacement gradient as a function of sliding distance	128

Fig. 61. Equivalent plastic strain gradient as a function of sliding distance	129
Fig. 62. Plastic strain vs. depth below the worn surfaces at different loads	130
Fig. 63. Vickers hardness (and flow strength) vs. depth below the worn surfaces	134
Fig. 64. Morphology of SiC particles (15.8 μm) on the polished surface of 2014Al- 20%SiC before the wear test	137
Fig. 65. Schematic description of sliding wear mechanisms in particulate composites at low loads	139
Fig. 66. (a) Examples of broken Al_2O_3 particles on the worn surface of the composite; (b) cross-section through the worn surface revealing the cleavage fracture of a particle; (c) particle loss from the surface by a pull-out process; the arrow shows a particle which is about to detach; (d) a cavity left behind possibly by a decohered particle (regime II)	140
Fig. 67. EDS analysis of the worn surface of A356Al-20%SiC in region II	142
Fig. 68. Loose debris particles generated from the 6061Al-20% Al_2O_3 at 40 N; (a) overall view of the plate-like debris; (b) top view of a debris particle (regime II)	143
Fig. 69. Subsurface crack in 6061Al-10% Al_2O_3	145
Fig. 70. X-ray diffraction analysis of the black debris of 6061Al worn against 6061Al in regime II (after filtering)	146
Fig. 71. The temperature distribution at the contact surface of 6061Al as functions of sliding time and sliding velocity	147
Fig. 72. Schematic representation of the wear mechanisms in regime II	149
Fig. 73. Cross-section of 6061Al-20% Al_2O_3 showing (a) the layers consisting of broken Al_2O_3 particles on the test piece and (b) same layers transferred on to the SAE52100 counterface (regime III)	152
Fig. 74. Debris particles produced from the surface of 6061Al-20% Al_2O_3 at 300 N; (a) overall view of debris particles; (b) high magnification cross-sectional view of a debris particle showing its lamellar structure (regime III)	154
Fig. 75. Worn surface morphology in regime III (6061Al-20% Al_2O_3 , 230 N); tensile dimples formed during fracturing of the "shear wedges"	155

Fig. 76. Material squeezed out of the front edge of the worn surface (prow). Large debris particles are formed as a result of tearing away from the prow. (6061Al-20%Al ₂ O ₃ , 270 N, regime III)	157
Fig. 77. Temperature of the worn surfaces after sliding to 1000 m vs. applied load for 6061Al and 6061Al-20%Al ₂ O ₃	160
Fig. 78. Temperature of the worn surfaces after sliding to 1000 m vs. applied load for A356Al and A356Al-20%SiC	161
Fig. 79. Temperature of the worn surfaces after sliding to 1000 m vs. sliding velocity on 6061Al at 4.9 N and 49 N	162
Fig. 80. Effect of heat dissipation rate of the test system	164
Fig. 81. Schematic illustration of the effect of the particle size on the wear of the matrix in regime I	166
Fig. 82. Temperature vs. sliding distance diagram for 6061Al against SAE52100 steel slider and mullite slider	171
Fig. 83. Wear regime map of 6061Al alloy	172
Fig. 84. Wear regime map of 6061Al-20%Al ₂ O ₃	173
Fig. 85. Wear rate map of 6061Al alloy	175
Fig. 86. Wear rate map of 6061Al-20%Al ₂ O ₃	176
Fig. 87. Wear temperature map of 6061Al alloy	178
Fig. 88. Wear mechanism map of 6061Al-20%Al ₂ O ₃	179
Fig. 89. Wear regime map of 6061Al alloy reinforced with 0%, 10% and 20%Al ₂ O ₃ particles	180
Fig. 90. Cumulative flow stress vs. plastic strain curve for the material below the contact surfaces	185
Fig. 91. Variation of the work hardening rate with flow stress	186
Fig. 92. Hydrostatic pressure gradients at different C levels compared with flow stress gradient	190

Fig. 93. Change in the damage rate with the depth below the contact surfaces
.....192

Fig. 94. Variation of the critical depth at which the subsurface damage rate is maximum
with the sliding distance193

Fig. 95. Normalized C vs. Z_c at two applied load levels 10 N and 45 N195

LIST OF TABLES

Table I	Composition of matrix materials	51
Table II	Average particle size, bulk hardness, and density of the materials tested	54
Table III	Coefficients for wear equations $\dot{W} = k \cdot P^n$	85
Table IV	Variation of transition load P_t of 6061Al-20%Al ₂ O ₃ between regime I and II as a function of velocity.	111
Table V	Variation of transition load P_t between regime II and III as a function of velocity.	114
Table VI	Effect of particle volume fraction of Al ₂ O ₃ on transition load . . .	123
Table VII	Coefficients A and B in eqn. (4.2): $\epsilon = A \cdot \exp(-BZ)$	132
Table VIII	The transition load and transition temperature for unreinforced and reinforced materials ($V = 0.8$ m/s)	151
Table IX	Summary of wear characteristics for 6061Al and 6061Al-20%Al ₂ O ₃ sliding on SAE52100 steel	181

LIST OF SYMBOLS

A	the extrapolated strain at the surface;
B	a wear constant;
C	a constant factor;
D	distance between microindentation impression and the boundary of tapered surface and worn surface;
G	a constant;
H	hardness;
K	a wear constant;
L_{avg}	the average size of reinforced particle size;
L_{max}	the largest diagonals of reinforced particle size;
L_{min}	the smallest diagonals of reinforced particle size;
n	the wear exponent;
P	applied load;
P_t	transition load;
R	the radius of void;
\dot{R}	void growth rate;
S	sliding distance
T	temperature;
T_0	the reference temperature;
T_b	average contact surface temperature;
T_m	melting temperature of materials;
T_t	transition temperature;
V	sliding velocity;
V_f	volume fraction of reinforced particle;
W	wear of volume loss or weight loss;
\dot{W}	wear rate;
Z	subsurface depth;
Z_c	the critical depth;
γ	an amplification factor (of 1-2);
ϵ	equivalent plastic strain;
ϵ_c	a constant;
$\dot{\epsilon}$	the strain rate;
θ	angle between the actual surface and tapered section;
σ_0	the bulk flow strength;
σ_f	the flow strength;
σ_F	the fracture strength;
σ_H	the hydrostatic stress;
σ_s	the saturation stress;
ϕ	shear angle of the interface;

CHAPTER I INTRODUCTION

Metal matrix composites (MMCs) combine a number of attractive mechanical and physical properties and are rapidly becoming viable alternatives to conventional structural materials. These materials have a metallic matrix, usually an aluminium or magnesium alloy, in which strengthening phases in the form of fibers, particles, or whiskers are dispersed. The attractive physical and mechanical properties that can be obtained with metal matrix composites, such as high specific modulus, strength, and thermal stability have been documented extensively ^[1-4]. MMCs combine high strength and high modulus, with acceptable levels of ductility and toughness. It has been estimated that, in aerospace applications, for example, weight savings of greater than 40% are possible through the use of MMCs in lieu of high-strength aluminum or titanium alloys ^[2]. The weight savings are due to not only a reduction in the density of the alloys but also an increase in their elastic modulus. For example, a 50% increase in modulus, is achieved by substituting an unreinforced wrought Al alloy with 20% silicon carbide particulate ^[5], which resulted in a 10% weight reduction. In the automotive industry, the unique properties of MMCs have led automotive engineers to identify a number of applications for these materials, such as drive shafts and connecting rods where elastic modulus and tensile strength are important, or brake rotors, cam shafts, valve trains, cylinder liners and piston rings where good friction and wear performances are required ^[3, 6]. Other potential applications are also under consideration. These include brake calipers, pump housings, gears, valves, brackets, pulleys, electronic packaging applications, turbocharger and supercharger compressors, and

suspension components ^[3].

Another perceived attractive feature of MMCs, as compared to the unreinforced monolithic alloys, is their better wear resistance and this has drawn widespread attention recently. However, the study of friction and wear phenomena between two sliding solids is very complicated. This is because friction and wear characteristics are not intrinsic material properties (unlike tensile strength or Young's modulus) but they are the result of the interactions of complex surface effects, environment and applied mechanical factors. Coefficients of friction and wear resistance are also known to vary with the geometric configuration of the tribological system. Any change in load, speed, or environmental conditions may cause catastrophic changes in the wear rate of one or both of the surfaces in contact ^[7, 8]. Furthermore, in a single wear test several wear mechanisms can operate in concert and the stress-strain fields under the contact surface may be very complex. All these factors have not only made rationalization of the process of debris formation and modelling of wear performance of MMCs extremely challenging but also the comparison of experimental results obtained by different investigators very difficult.

The objective of the study is to develop new methods to investigate the dry sliding wear behavior of aluminium alloys reinforced by SiC and Al₂O₃ particles and to understand the sliding wear mechanisms in these materials. This is achieved by studying the effects of applied mechanical factors such as the load, sliding velocity, temperature,

and counterface materials. The effect of microstructural factors *e.g.* particulate size and volume fraction were also systematically studied. The stress and strain gradients generated during sliding wear were measured using metallographic techniques specially developed for this purpose. Material characterization techniques such as scanning electron microscopy and x-ray diffractometry have been extensively used to delineate the wear mechanisms operating under various conditions. Results were organized in the form of wear mechanism maps and certain important types of wear, in particular delamination wear, were modelled by considering the damage accumulation processes beneath the contact surface.

Three types of particulate reinforced aluminum alloy matrix composites were studied in this work as model materials. These were: (I) a cast A356 (Al-7%Si) alloy reinforced with 0, 10, 15 and 20 vol% SiC particles. The main reason for choosing A356 aluminum alloy based composites was because of their widespread use in internal combustion engine applications since these alloys have excellent castability; (ii) a wrought 6061 (Al-Mg-Si) alloy reinforced with 0, 10 and 20 vol% Al₂O₃ particles; (iii) a wrought 2124 (Al-Cu-Mg) alloy reinforced with (0 and 20 vol%) SiC particles.

This thesis is divided into 6 chapters. In Chapter II, basic aspects of wear phenomena in metallic systems are given and previous work done on the dry sliding wear of metal matrix composites is reviewed. Chapter III describes the details of the experimental methods used. The results are presented in Chapter IV. Chapter V contains

the discussions. In this chapter the classification of the wear behaviour of MMCs of three wear regimes is introduced for the first time. The main factors which influence the wear transitions, such as sliding velocity, surface temperature, reinforcement particulate size, volume fraction, counterface materials and testing history are discussed. Wear mechanism maps are also presented as a useful method to present wear resistance data. A new approach to modelling of the delamination wear is developed by considering the plastic deformation and damage accumulation processes below the worn surfaces. Finally, Chapter VI gives the conclusions of the work.

CHAPTER II LITERATURE REVIEW

The objective of this chapter is to provide a critical review of the results obtained from prior investigations of wear. The chapter starts with a general description of the wear mechanisms and wear types, and then focusses on the wear behaviour of materials in dry sliding condition. Current knowledge on the stress-strain states beneath the contact surfaces are also reviewed. Finally, studies performed on the wear of Metal Matrix Composites are summarized.

2.1. GENERAL CLASSIFICATION OF WEAR TYPES

Wear can be defined as the progressive loss of material from the surfaces in contact as a result of relative motion at the surfaces ^[9]. Wear usually proceeds by disintegration of the material in the immediate vicinity of the surface. In an attempt to classify various forms of wear, a large number of terms related to describing the features of worn surfaces and wear modes have been proposed ^[10-21]. The wear types observed in industrial practice can be broadly classified as follows

1. Abrasive Wear
2. Sliding Wear
3. Rolling Contact Wear
4. Fretting Wear
5. Erosive Wear
6. Corrosive Wear

2.1.1. Abrasive Wear

Abrasive wear occurs when a sharp particle or asperity penetrates a softer surface and ploughs that surface or cuts a chip. The term abrasive wear covers two types of situations, known respectively, i) as two-body abrasion and ii) three-body abrasion. In two-body abrasion a rough hard surface slides against a relatively soft opposing surface, whereas in three-body abrasion rough hard particles trapped between the two sliding surfaces cause one or both of them to be abraded ^[22]. Literature on abrasive wear is exhaustive. A detailed quantitative description of abrasive wear was first developed by Rabinowicz ^[23] and materials aspects of abrasive wear are recently reviewed by Zum Gahr ^[21].

2.1.2. Sliding Wear

Sliding wear is defined as a motion of two relatively moving bodies, in which their surface velocities (magnitude and/or direction) in the common contact area are different ^[9]. Accordingly, sliding wear refers to a type of wear generated by pure sliding without rolling or spinning. It can be further divided into two types ^[18, 24-26]: (a). Mild Wear: which usually occurs at low loads and sliding velocities and (b). Severe Wear: which is promoted by high contact temperatures, loads and velocities. Sliding wear is usually thought to involve debris formation mechanisms such as adhesion, delamination, fatigue and oxidation ^[16, 25, 27, 28]. According to the earlier theories of adhesion ^[29], when asperities come into contact, they adhere strongly to each other and form asperity junctions. Subsequent separation of the surfaces occurs in the bulk of the softer asperities,

which adhere to the harder surface ^[23]. Whenever material is removed from the original surface in this way, an adhesive wear fragment is created. Adhesion is favoured by clean surfaces, non-oxidising conditions, and by chemical and structural similarities between the sliding couple ^[30]. However it is difficult to prove asperity fracture phenomena by metallographic and other surface characterization techniques. It is increasingly becoming clear that adhesion may not be a mechanism itself but a result of severe localized surface deformation. The intensity of deformation and the nature of stress-strain distribution near the contact surfaces may determine the debris formation mechanisms. These may include (i) brittle fracture by inter- or intra-grain crack propagation in ceramics ^[31, 32], (ii) delamination in ductile materials for which a subsurface crack growth as a result of a void nucleation and propagation (*e.g.* around second phase particles and precipitates) may lead to the formation of plate-like flaky debris particles ^[33], (iii) fatigue where local cyclic plastic deformation at the crack tip (possibly mode II, shear type) may lead to crack growth again resulting in flaky debris particles ^[34-36].

2.1.3. Rolling Contact Wear

Rolling Contact Wear is also referred to as Surface Fatigue Wear ^[21]. During the contact, the surface is deformed elastically but a local plastic deformation zone surrounded by elastic material could be formed near the surface. Microcracks may form, grow, and coalesce forming wear particles by cyclic loading and unloading. This type of wear is encountered commonly in railway tracks and is usually modelled by finite element analyses ^[37].

2.1.4. Fretting Wear

Fretting wear occurs when contacting surfaces undergo oscillatory tangential displacement of small amplitude. This type of wear occurs as a result of interaction of several operating processes. These processes include the removal of metal particles from the surface in a finely divided form by a mechanical grinding action, or as a result of disruption of oxide films on the surface, and the abrasive action of oxide debris ^[12].

2.1.5. Erosive Wear

Erosive wear by solid particle impingement arises from the impact of hard abrasive particles on a target surface. Erosion is a complex phenomenon that is affected by many variables including the size, shape, hardness, flow rate, velocity and impingement angle of the erosive particles, and is believed to occur by a combination of cutting (or abrasion) and deformation ^[17].

2.1.6. Corrosive Wear

During corrosive wear (oxidation wear ^[27, 28]) films formed by reaction with the environment or the lubricant are removed by sliding. When rubbing takes place in a corrosive environment, then surface reactions can take place and reaction products can be formed on one or both surfaces. These reaction products can be removed by rubbing, and the cycle of reaction and removal can be repeated alternately. Theories of corrosive wear can be quite complex. The most common corrosive medium is the oxygen content of air. The effects of oxidation depend not only on the oxidation rate, but also on the

mechanical properties of both the oxide and the substrate, and the adhesion of the oxide to the substrate [27, 28].

2.2. SLIDING WEAR

2.2.1. ARCHARD WEAR EQUATION

In dry sliding wear, it is often found that the wear rate changes with sliding distance during the early stages of sliding due to the changes in the condition and structure of the surface layers. However, after an initial period of running, three basic types of wear have been observed. (figure 1 [12, 13, 24, 38-41]). Type A curve: In this type of wear, the wear rate depends linearly on the sliding distance. This could be mild or severe wear. Type B curve: Initially the wear rate is high so that the surfaces and debris appear to be metallic. The curve shows a transitional behavior and the wear rate reduces to a lower steady value for the remainder of the test. Type C curve also shows a transitional behavior but in this case severe wear follows mild wear.

Archard [42] first derived a theoretical expression (Linear Wear Law or Archard Equation) which predicts the rate of sliding wear \dot{W} ($=V/S$)

$$\frac{V}{S} = k \frac{P}{H} \quad (2.1)$$

Where V is the wear volume, S is the sliding distance, P is the applied normal load, H is the bulk hardness of the material subjected to wear in sliding contact, and k is a constant which is called the wear coefficient. The value of k strongly depends on the sliding environment (for example, changes in the humidity of air can change the wear

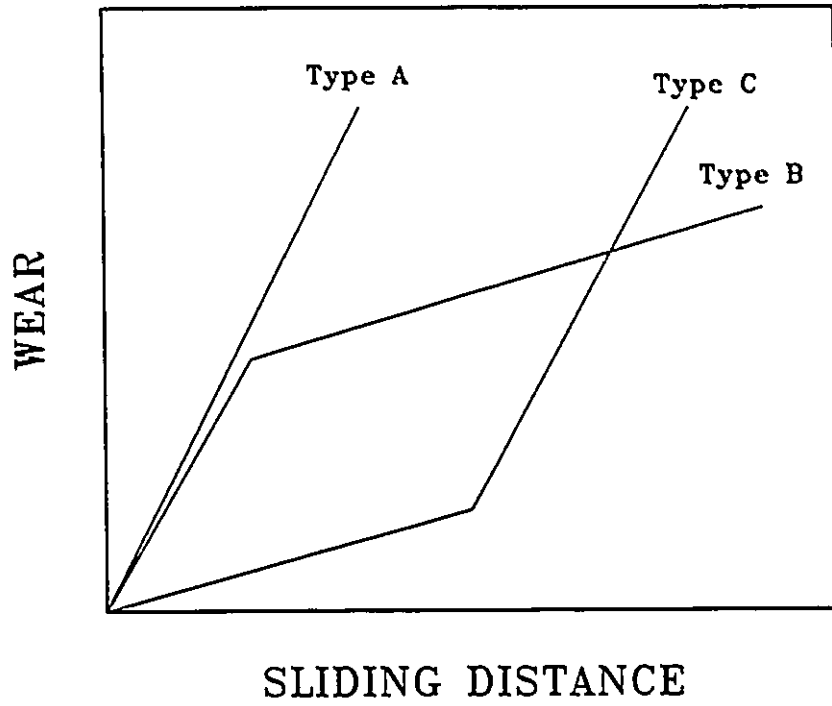


Figure 1. Different types of wear rate vs sliding distance curves (after Eyre [12], Archard and Hirst [24])

coefficient of brass by a factor of 100 ^[25]).

Although it is widely known, the Archard equation should be used with caution, because the Archard equation is valid only for low loads up to some point at which the rate of wear changes catastrophically. When the applied loads are above that point, (in Type C curve) the wear coefficient is no longer a constant, and it may rise rapidly for small increases in load. This limitation basically arises from the fact that the law assumes that the wear is controlled only by the bulk hardness of the material (measured at room temperature) ^[43]. In fact, the existence of abrupt transitions makes it risky to use the Archard wear equation for design purposes over a wide range of load conditions ^[44, 45]. However the Archard equation is considered a good description of equilibrium wear rates (Type A).

2.2.2. TRANSITIONS IN SLIDING WEAR

An increase in sliding velocity, applied load or temperature during wear can lead to a transition in the wear mode from mild to severe wear ^[38]. For steels, the terms mild wear and oxidative wear are often used interchangeably. This is because mild wear involves reactions between the iron atom at the surface and any ambient oxygen. Mild wear is also regarded as a variation of adhesive wear ^[25]. In steels, mild wear occurs when the sliding contact of surfaces become covered by oxide layers (*e.g.* α -Fe₂O₃, Fe₃O₄ or FeO ^[21]) or surface layers produced by certain tribochemical reactions. It is thought that the surface oxide layers generated by the rubbing process separate the sliding surfaces and give protection to them ^[27, 28, 46]. The debris in mild wear is mainly very fine oxides, and

the particles may range in diameter down to 100 Å^[25]. The influence of oxides on wear has been reviewed in detail by Quinn^[27, 28], and Scott and Wood^[47].

Three possible mechanisms for the removal of materials in mild wear have been proposed. These are: (i) breaking and removal of the protective oxide films which are formed at the real areas of contact when the oxide reaches a critical thickness^[27, 28], (ii) removal of metal which is in the form of finely divided particles as a result of subsurface fracture. Archard^[13] suggested that the progression of wear in the mild regime would involve gradual transfer of debris removed from the test specimen to form a film on the counter surface. This may be followed by oxidation of the film with subsequent loss of the oxidized particles from the system as wear debris^[13]. (iii) removal of oxidised material may give rise to an abrasive powder that may contribute to the wear process. This mechanism has often been cited as important when the metal oxides have a hard abrasive structure (*e.g.* Al₂O₃)^[13].

In aluminium-silicon alloys worn against steel, Shivanath *et al*^[48] observed mild and severe types of wear (Figure 2). According to the authors, mild wear occurred when the surface of Al-Si alloy is covered with an oxide or oxide/metal surface layer. They suggested that the oxide layer (of unknown composition) separated the aluminium silicon and the steel surfaces. Wear of the Al-Si alloy occurred by a process of spalling of the layer which occurs fairly irregularly over the surface and at any one time only part of the surface was in contact with the steel counterface. Wear rates were low (10⁻³ to 10⁻² mm³/m) because the amount of metal removed was confined to the thickness of the oxide layer.

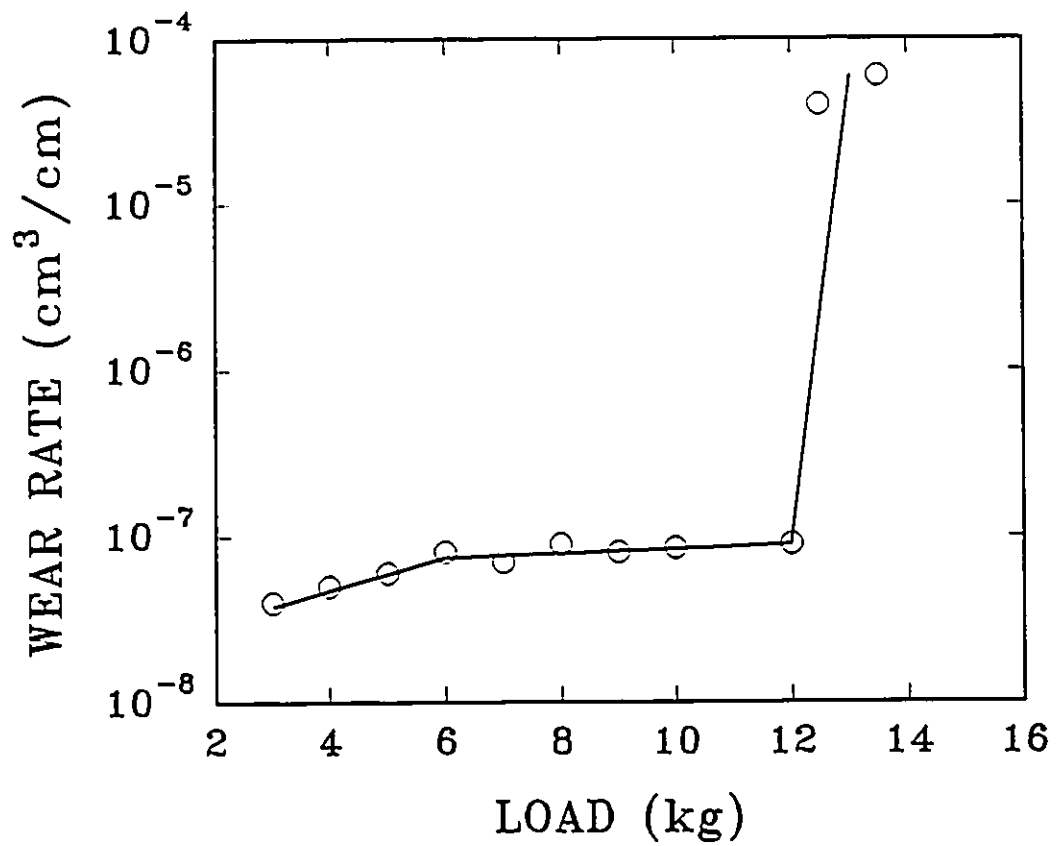


Figure 2. Wear of aluminum-8% silicon alloy.
(after Shivanath etc. [48])

Severe wear (which is also referred as scuffing^[49] or galling^[50]) occurs when direct metallic contact exists between the surfaces of the sliding pair (e.g. if unprotected by oxides or lubricants) and when high loads and/or high sliding velocities are applied. Severe wear is often recognized with the unaided eye by the large amount of material transfer from the sample surface to the harder counterface; and, with microscopy, in the form of rough, torn surfaces and massive plastic deformation at the contact surfaces. This has led some observers to suggest that wear occurs by "adhesion". However adhesion is not a mechanism in itself but rather a consequence of severe plastic deformation and damage, as will be discussed later in this thesis. The debris is usually in the form of large metallic fragments^[19]. This form of wear involves the departure of discrete fragments from a surface which need not be the one from which the metal originates. According to Finkin [25], a multi-step process often occurs in which small fragments transfer from one surface to the other and become detached from the second surface in the form of particles very much larger than the original fragments. The difference in wear rates for the mild and severe types may be a factor of 10^4 [25].

Shivanath *et al* [48] observed that in an Al-Si alloy, wear occurred with the separation of large fragments of metal, some of which adhered to the steel counterface. Mild and severe wear regimes in this alloy can be recognized by their distinctive wear rates. *i.e.*

Mild wear rate: 10^{-3} to 10^{-2} mm³/m

Severe wear rate: 1 to 10 mm³/m

In a tribological system which consisted of a 0.52% carbon steel pin sliding against

a ring of the same material, Welsh ^[38] observed that transitions can change from a low wear rate to a high wear rate and then again to a lower wear rate when the load and speed were varied over a sufficiently wide range. The pattern of wear for the carbon steel is given in Figure 3. The concept of wear transitions has been developed by Lim and Ashby in a form which is potentially useful for industrial design. This will be reviewed in section 2.3.3.

2.2.3. SUBSURFACE ZONES IN SLIDING WEAR

It is well established that sliding friction produces large amounts of near-surface plastic deformation ^[51-60]. Rice and his co-workers ^[60] suggested that the material under the worn surfaces consists of three distinct zones. According to Rice's ^[60] description Zone 1 (Fig.4) represents the original undeformed material. Zone 2 contains plastically deformed material, where plastic shear strains increase towards the contact surface. Depending upon the material, environment and contact geometry, Zone 2 may become harder or softer than the bulk material. In ductile materials, voids may develop within this zone or cracks may nucleate in more brittle materials. Zone 3 is a tribolayer which forms on the surface and consists of a mixture of original specimen material and chemical species from the counterface and from the test environment. Frequently, Zone 3 appears homogeneous and as having a fine microstructure ^[44]. However, not all three zones are found under all test conditions.

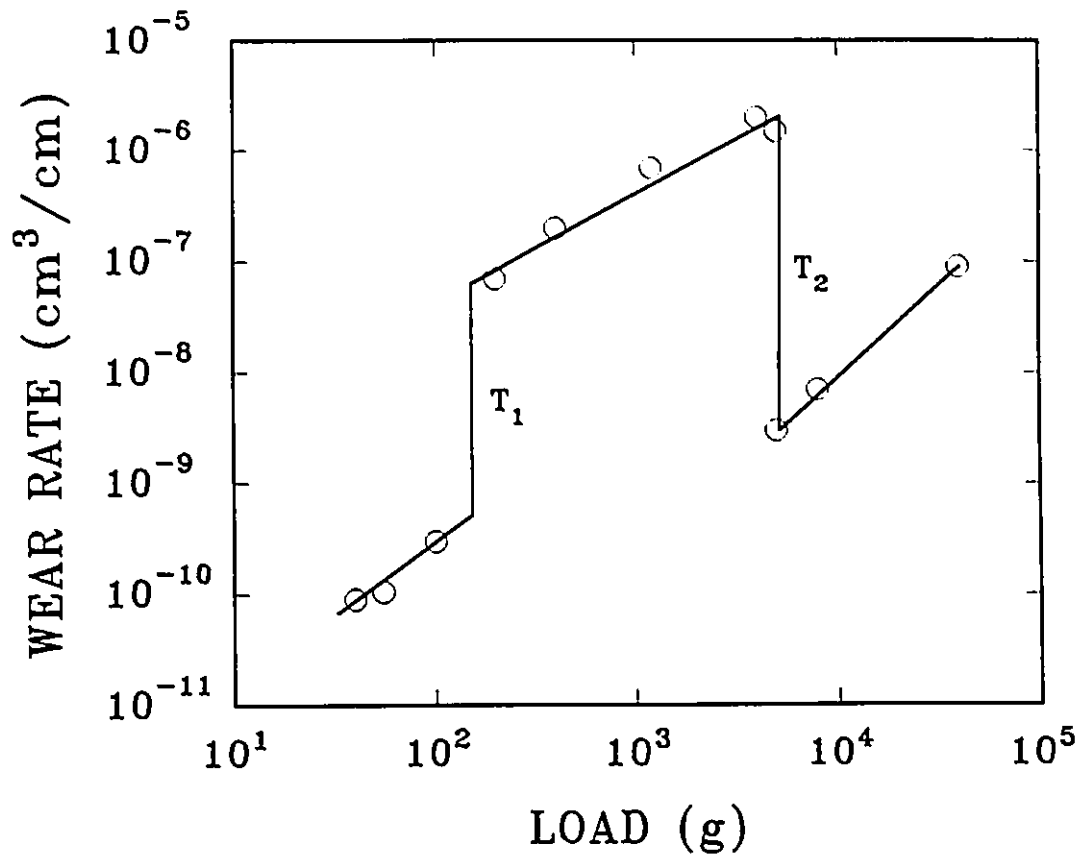


Figure 3. Transitional wear behavior for a carbon steel. (after Welsh [38])

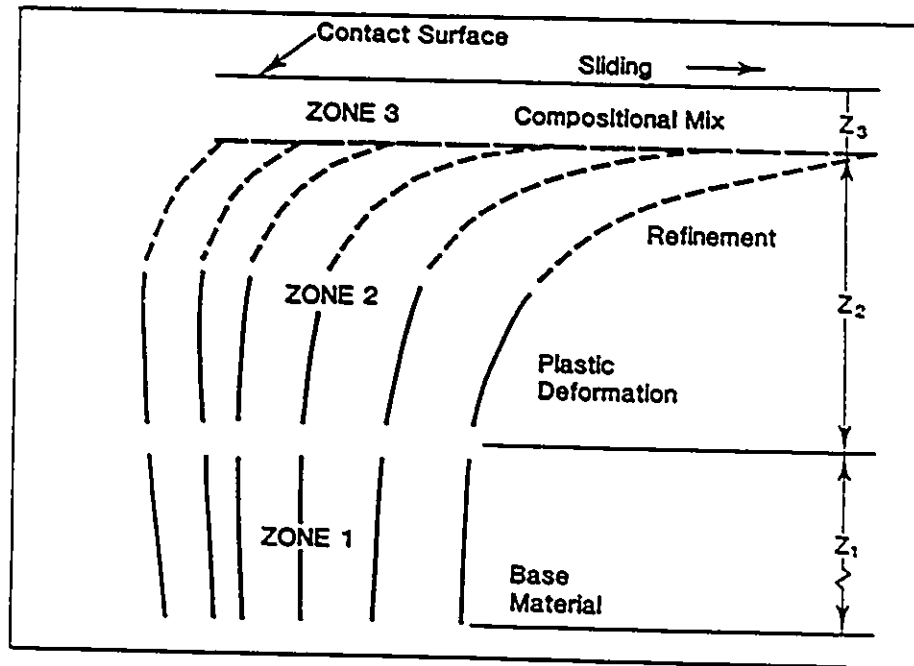


Figure 4. Schematic description of subsurface zones in sliding wear. (after Rice etc. [60])

2.2.4. TRANSFER AND MECHANICAL MIXING

It is widely recognized that transfer of material from one sliding component to another can occur in dry sliding systems. This phenomenon has led to the idea that sliding wear involves adhesion, and that suitable surface layers or coatings may reduce wear by reducing adhesion ^[44]. There is experimental evidence that in some systems the tribolayers are composed of ultrafine grained crystalline material ^[62], ranging from about 3 nanometers to several tens of nanometers ^[63].

Rigney and his co-workers ^[62, 64] observed that with Cu, Cu-Ni, Cu-Al, Ni and Mo sliding against steel, wear debris generated from surface material contained components from both mating materials. The wear debris and the surface layers had similar (ultrafine) grain structure, and the same average composition. It has been shown that during sliding, back transfer of the material to the counterface is very common ^[25]. Cocks ^[65] and Antler ^[66] have suggested that the preferential material transfer direction may depend not only on the material combination in the tribosystem but also on the geometry of the system. For similar metals, the rate of material transfer may be as high as 50-100 times that of dissimilar metal systems ^[25].

2.3. STRESS, STRAIN STATES AND CONTACT TEMPERATURES

2.3.1 ELASTIC STRESSES IN SURFACE CONTACT

To understand how loose wear debris particles form, it is necessary to consider the nature of the stress-strain fields which exist beneath the contact surface. If the contact surface of a solid body is subjected to an increasing load it deforms first elastically and

then the stress below the contact surface reaches the yield stress σ_y , from which point onwards it continues to deform plastically. In certain contact situations some asperities are deformed elastically, while others are deformed plastically.

2.3.1.1. POINT FORCE LOADING

Considering the stress situation in an elastic half-space subjected to a normal point load P (Figure 5), the stress components in a polar coordinate system can be given as below (Boussinesq solution) ^[67]:

$$\begin{aligned}
 \sigma_r &= \frac{P}{\pi R^2} \left[\left(\frac{1-2\nu}{4} \right) \sec^2 \frac{\phi}{2} - \frac{3}{2} \cos \phi \sin^2 \phi \right] \\
 \sigma_{\theta\theta} &= \frac{P}{\pi R^2} \left[\left(\frac{1-2\nu}{2} \right) \left(\cos \phi - \frac{1}{2} \sec^2 \frac{\phi}{2} \right) \right] \\
 \sigma_z &= \frac{P}{\pi R^2} \left[-\frac{3}{2} \cos^3 \phi \right] \\
 \sigma_r &= \frac{P}{\pi R^2} \left[-\frac{3}{2} \cos^2 \phi \sin \phi \right] \\
 \sigma_{r\theta} &= \sigma_{\theta z} = 0
 \end{aligned} \tag{2.2}$$

The principal normal stresses can be determined as follows:

$$\begin{aligned}
 \sigma_{11} &= \sigma_{rr} \sin^2 \alpha + \sigma_{zz} \cos^2 \alpha - 2\sigma_{rz} \sin \alpha \cos \alpha \\
 \sigma_{22} &= \sigma_{\theta\theta} \\
 \sigma_{33} &= \sigma_{rr} \cos^2 \alpha + \sigma_{zz} \sin^2 \alpha + 2\sigma_{rz} \sin \alpha \cos \alpha
 \end{aligned} \tag{2.3}$$

where

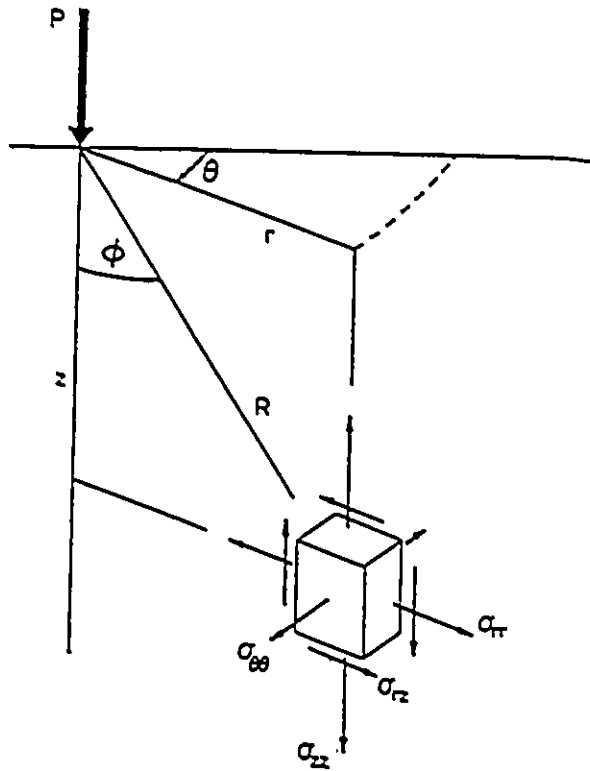


Figure 5. Coordinate system for axially symmetric point loading P .
(after Lawn and Swain [67])

$$\alpha = \frac{1}{2} \arctan \frac{2\sigma_r}{\sigma_z - \sigma_\theta} \quad (2.4)$$

the magnitude of the component of hydrostatic compression is

$$\sigma_H = -\frac{1}{3} (\sigma_{11} + \sigma_{22} + \sigma_{33}) \quad (2.5)$$

Equation (2.2) indicates that the stresses approach infinity at the origin. Obviously, this singularity is a result of the assumption that the cross-sectional area of the point force indenter is equal to zero. In real situations, no physical indenter has a nonzero area of contact. Furthermore, the stress cannot increase indefinitely since the material will either yield or fracture when the stresses exceed the inherent strength of the material, relieving the stress concentration at the point of loading.

2.3.1.2 HERTZIAN CONTACTS

Consider the case of two spheres in contact (Figure 6). When the contact area is free of friction, the interfacial stress consists of only the normal pressure acting between the two spheres. The pressure distribution is hemispheric, which may be expressed as ^[33]

$$(\sigma_{zz})_{z=0} = -p = -p_0 \frac{(a^2 - r^2)^{\frac{1}{2}}}{a} \quad (2.6)$$

where a is the radius of the contact area and p_0 is the maximum pressure acting at $r=0$ and $z=0$ (i.e., the center of the contact area). The radius a and the peak pressure p_0 are

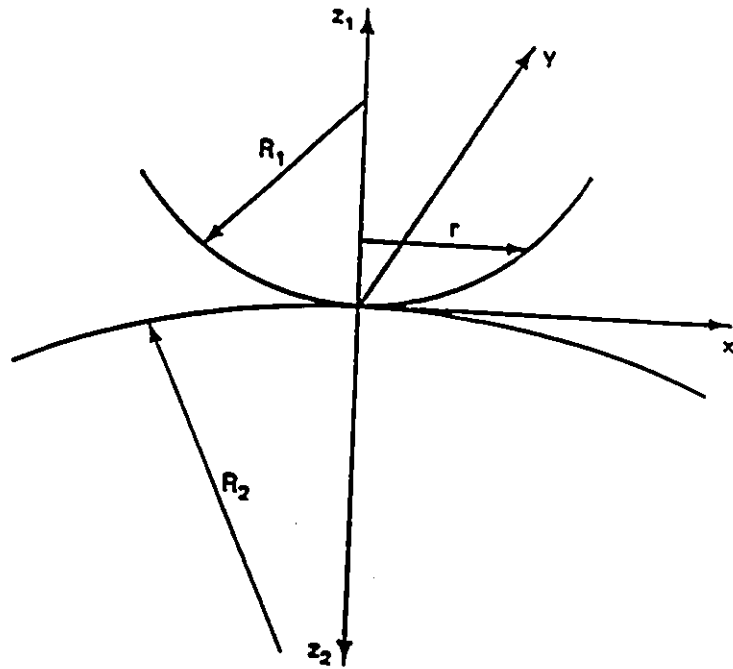


Figure 6. Two spherical bodies in contact. (after Suh [33])

$$a = \left[\frac{3p}{16} \frac{k_1 + k_2}{\rho_1 + \rho_2} \right]^{\frac{1}{3}} = \left[\frac{3p}{4} \frac{(k_1 + k_2) R_1 R_2}{R_1 + R_2} \right]^{\frac{1}{3}} \quad (2.7)$$

$$p_0 = \frac{3p}{2\pi a^2}$$

where

$$k_i = \frac{1 - \nu_i^2}{E_i} \quad i = 1, 2 \quad (2.8)$$

$$\rho_i = \frac{1}{R_i} = \text{curvature of the sphere } i$$

The magnitude of p_0 indicates that the maximum pressure at the center of the contact zone is 1.5 times the average pressure between the spherical contacts. The magnitudes of the other principal stresses, σ_{rr} and $\sigma_{\theta\theta}$, are equal to $(1/2 + \nu)\sigma_{zz}$. The maximum shear stress τ_1 is equal to $0.31p_0$ at a depth of $0.48a$ ($\nu=0.3$)^[68].

2.3.1.3. STRESS DISTRIBUTION DUE TO NORMAL LOAD AND ITS TANGENTIAL COMPONENTS

The original Hertzian theory of static elastic contact predicts that the maximum unidirectional shear stress is some distance below the contact surface while the maximum compressive stress occurs at the surface^[69]. By considering the stress field under a model asperity sliding on an homogeneous medium, Suh^[33] predicted the presence of tensile stresses roughly parallel to the sliding direction behind the slider. A similar result was also given by Rohatgi *et al*^[70]. They suggested that a tensile principal stress should exist

parallel to the friction force at the surface at the trailing end of the contact area. This tensile stress can contribute to initiating a surface crack and provide the driving force to propagate it. When the stress distribution over the entire contact surface is calculated, the magnitudes of the stresses change in a cyclical pattern with position corresponding to the number of asperities on the surface ^[70]. This cyclic variation of stress parallel to the contact surface suggests that the surface maybe subjected to a fatigue damage.

2.3.2. PLASTIC DEFORMATION OF THE SURFACE LAYER

As indicated before, in most tribological systems the surface layer undergoes plastic deformation. When these materials are subjected to continuous monotonous or cyclic loading during sliding, plastic strains accumulate with sliding and may lead to subsurface crack nucleation. Microscopic observations of wear samples and debris show that subsurface plastic deformation is a very important component of sliding wear ^[44].

Jahanmir and Suh ^[71] used the Merwin-Johnson ^[72] method to determine the size of the plastically deforming zone, and the stress-strain distributions during steady-state sliding in semi-infinite elastoplastic solids. They considered an applied normal stress, $p_0=4k$, (where k is the yield strength in shear), and different tangential stresses ranging from $q_0=0$ to $4k$ as shown in Figure 7. Figure 7 indicates that the size of the plastic region increases with increasing coefficient of friction. For a coefficient of friction smaller than a critical value (0.25 in this case), the plastic region is located below the surface, whereas at larger coefficients of friction the plastic region extends to the surface. They noted that σ_{xx} is always compressive, whereas σ_{zz} becomes tensile behind the contact (although it is

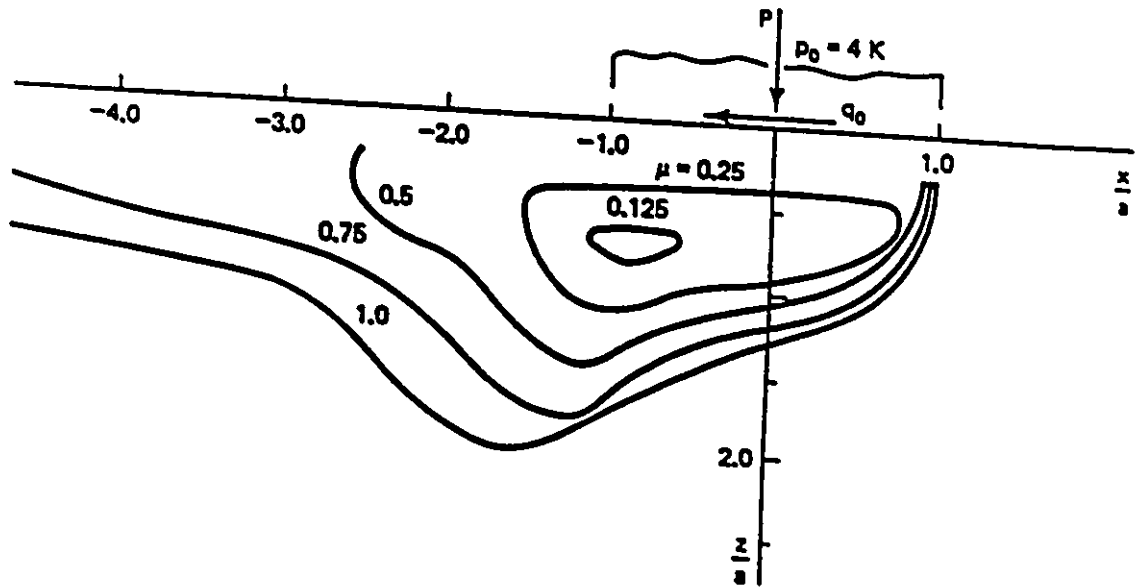


Figure 7. Steady-state plastic deformation regions in an elastic-perfectly plastic material under a sliding contact, for a maximum applied normal stress $p_0=4k$ and different friction coefficients μ which given on the contour (tangential stress $q_0=P_0 \times \mu$). (after Jahanmir and Suh [71]).

very small, $\sigma_{xz}/P_0 < 0.02$) and close to the surface. The only non zero plastic strain found in this modelling is the shear strain, which accumulates after each passage of the slider. A similar solution has also been found by Sin and Suh using a finite element method [73].

2.3.3. SURFACE TEMPERATURES AND WEAR MECHANISM MAPS

When two surfaces are put in relative motion, most of the work done against friction is turned into heat. The resulting rise in temperature may modify the mechanical and metallurgical properties of the sliding surfaces, and may cause oxidation or even melting. The frictional heat is most rigorously generated at asperities which make up the true area of contact at the sliding interface. The instantaneous temperature of these contact points (named the flash temperature) is higher than the average (or bulk) temperature of the surface, especially at low loads and sliding velocities.

Many attempts have been made to measure or predict contact surface temperatures [8, 23, 29, 54, 74-94]. Temperatures generated by sliding processes were first calculated by Jaeger [76] using a so called moving heat source analysis, in which the energy input is modelled as a plane heat source moving along the surface. In only a few analyses was the energy input due to the plastic deformation of subsurface regions taken into account [54, 82, 86].

Recently Ashby presented temperature maps for frictional heating in dry sliding processes [8, 92, 93]. Ashby's model relates to a pin-on-disk configuration, as shown in Figure 8. The heat q , which is generated at the contact surface, per unit of nominal contact area A_n per second is:

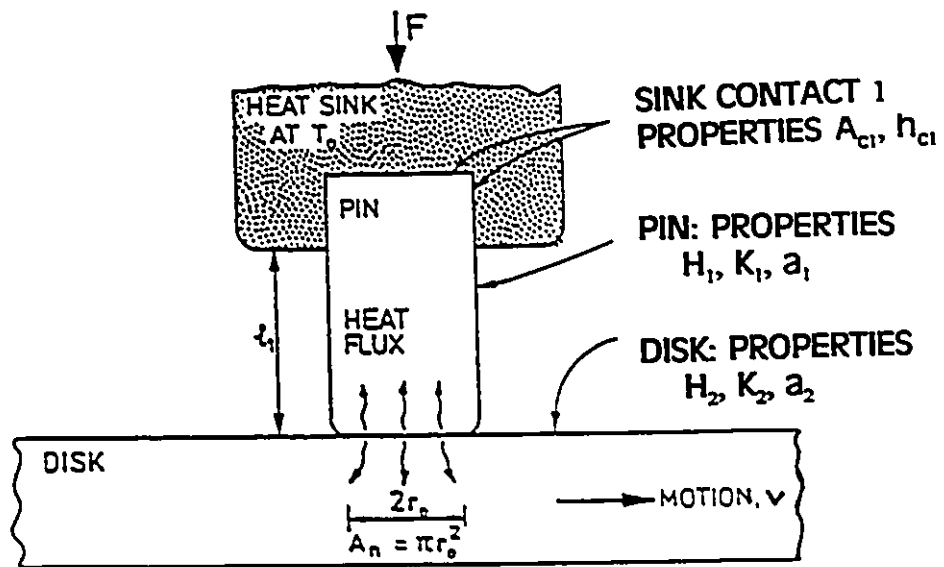


Figure 8. Heat transfer in pin-on-disk configuration. (after Kong and Ashby [92])

$$q = \frac{\mu F v}{A_n} \quad (2.9)$$

where μ =friction coefficient, F =normal force and v =sliding velocity. The heat flows into the two solids, partitioned between them in a way which depends on their geometry and thermal properties.

Two temperatures are of interest as mentioned before. The first is the bulk (or mean) temperature, T_b , which is given by:

$$T_b - T_o = \frac{\mu F v}{A_n} \left[\frac{1}{\frac{k_1}{l_{1b}} + \frac{k_2}{l_{2b}}} \right] \quad (2.10)$$

where T_o is the temperature of the remote sink to which the heat flows, k_1 , and k_2 are the thermal conductivities of each of the two surfaces in contact, and l_{1b} and l_{2b} are two diffusion distances from T to T_o .

The second temperature of interest is the flash temperature, T_f . The average flash temperature, T_p , is expressed in a form which closely parallels that for the bulk temperature T_b :

$$T_f - T_b' = \frac{\mu F v}{A_r} \left[\frac{1}{\frac{k_1}{l_{1f}} + \frac{k_2}{l_{2f}}} \right] \quad (2.11)$$

where the sink temperature T_o , is replaced by the effective sink temperature T_b' , the nominal contact area A_n by real total asperity contact area, and l_{1b} and l_{2b} by two further effective heat-diffusion distances l_{1f} and l_{2f} . These depend on the size of the asperities and

on whether heat flow is transient or steady.

Lim and Ashby suggested that the various regimes of mechanical and corrosive wear for any particular pair of rubbing materials could be shown on a single wear map plotted on axes of normalised pressure p/H (p -pressure, H -hardness) and sliding velocity. As an example of this technique, a wear map for soft carbon steels sliding in air at room temperature is shown in Figure 9. In principle, the map can be divided into areas corresponding to different wear regimes, with boundaries of sliding speed and contact pressure.

2.4. WEAR OF METAL MATRIX COMPOSITES

2.4.1. INTRODUCTION

Metal matrix composites (MMCs), which are made of high-strength, high ductility metallic alloys reinforced with ceramic particulates, whiskers or fibres, can be regarded as advanced materials. These materials have emerged from the need for lighter-weight, higher-performance components in the aerospace and the automotive industries [3, 6, 95]. MMCs possess a combination of superior physical and mechanical properties, such as high specific modulus, strength, thermal stability, and low density [1-4] which are not achievable with monolithic alloys. These distinctive properties have promoted an increasing number of applications for these materials, especially in automotive industries (for example drive shafts, brake rotors, engine blocks, cam shafts, valve trains, cylinder liners, connecting rod, piston, brake calipers, pump housings, gears, valves, brackets, pulleys, suspension components, *etc.*) [3, 6, 96]. Some of these applications involve

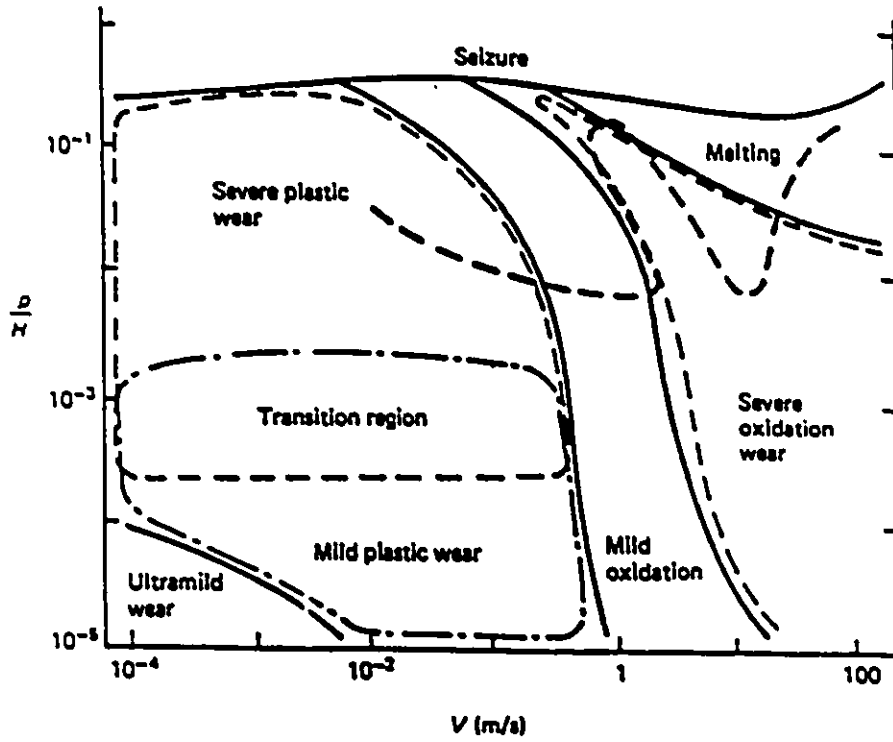


Figure 9. Wear mechanism map for carbon steel. P=pressure; H=hardness. (after Lim and Ashby [8]).

components in sliding contact with each other; hence they require enhanced friction and wear performance.

The mechanical properties of a material are important in determining its tribological behaviour. In metal-matrix composites, the mechanical properties depend on the amount, size, shape, and distribution of the dispersed phases as well as on the mechanical properties of the matrix material and the nature of the interface^[97]. In the case of continuous fiber composites, the strength increases with the volume fraction of the fibers^[98]. In the case of composites reinforced with hard particles, the strength increases with volume percentage of particles and reduction in particle size^[2, 99]. However the fracture toughness of particulate composites is lower than that of the matrix alloy, and decreases with increasing volume fraction of a dispersed phase^[4].

During the last two decades the wear performance of metal matrix composites has been widely studied in Al, Mg, Cu, Sn, Ag-Cu, Cu-Zr, Al-Mg and Al-Cu based systems incorporating different reinforcing phases such as carbides (SiC, B₄C), nitrides (Si₃N₄, AlN), oxides (Al₂O₃, SiO₂) and carbon^[97, 100-108]. The main results are reviewed in this section.

2.4.2. ABRASIVE WEAR OF MMCs

Abrasive wear usually can be classified on the basis of the nature of interactions between the abrasive particles and the contact surfaces, such as two body (the abrasive particles were fixed firmly to the counterface) or three body (the particles were entrapped between two surfaces but free to move at some extent). In three-body abrasive wear,

abrasive particles such as silica sand tend to break down and bury themselves in alloys with relatively soft matrices ^[97]. Hard particles in composites resist scratching because of their high hardness under low loads and may crack into small pieces under heavy loads ^[97]. The broken particles remain embedded in the matrix during wear. In this case, composite strength and fracture toughness both play important roles. Some investigators reported that micro-machining is the dominant mechanism of material removal during abrasion wear in composites as in the unreinforced matrices. But removed chips in the debris of composites are approximately the same size as the hard particles ^[97].

The abrasion resistance of a material is generally determined by two different types of tests ^[109]: (1) low-stress abrasion tests, such as rubber wheel abrasion tests, in which silica sand particles are fed into the region of contact between the rim of a rotating rubber-rimmed wheel and a stationary plane specimen pressed against the wheel under a fixed normal load. (2) high-stress abrasion tests, such as pin-on-disk and pin-on-drum types of tests. In low-stress tests, the abrading particles do not break; in high-stress tests, the abrading particles do break. In the context of the wear of MMCs, the terms low-stress and high-stress have also been used to denote the extent of fracture in individual regions of the reinforcing phase. The abrasive particles are generally rounded sand (SiO_2), crushed quartz, or silicon carbide particles of different grit sizes and shapes. The size and shape of abrading particles, as well as their relative hardness with respect to the composite being tested, are important parameters in determining the extent of wear ^[97].

Under conditions of "low stress" abrasion, MMCs are usually found to provide appreciably better wear resistance than the unreinforced matrix alloy. According to Prasad

and Das ^[95], this is due to the protrusion of the reinforcement offering protection to the softer matrix. Bhansali and Mehrabian ^[110], for example, have reported the relative wear resistance (RWR) values (the wear rate of the unreinforced matrix divided by that of the MMCs under the same conditions) as high as 11 for the 2024Al/Al₂O₃ containing 20wt% particles 142 μm in size, using a dry sand/rubber wheel abrasion tester under a normal load of 134 N. In general, the abrasive wear resistance increases with reinforcing particle size and volume fraction ^[101, 110, 111]. Rohatgi ^[97] and coworkers pointed out that for a given volume fraction of particles, composites that contain harder particles should exhibit a lower wear rate. But other results show that fracture of the reinforcement, or failure of the interface between the reinforcement and the matrix, may result in lower values of RWR than might otherwise be expected. For example, silicon carbide itself is appreciably harder than alumina, but Al alloy/SiC_p MMCs tested by Bhansali and Mehrabian ^[110] using the rubber wheel method have shown similar wear resistance to MMCs reinforced with the same proportion of alumina particles of the same size. Here the weakness of the interface with the matrix is thought to have played a major role, and prevented the reinforcement from achieving its full potential.

In high stress abrasion, the particle interaction can be very severe, leading to widespread fracture of the hard but brittle particles. And the RWR of MMCs is found generally to be lower than in the low stress case. Figure 10 illustrates typical results for an Al-11.8Si-4.0Mg matrix MMC containing 100 μm zircon particles, under conditions of both high and low stress abrasion ^[112]. Under conditions of high stress abrasion, the benefits of reinforcement with hard particles were much less.

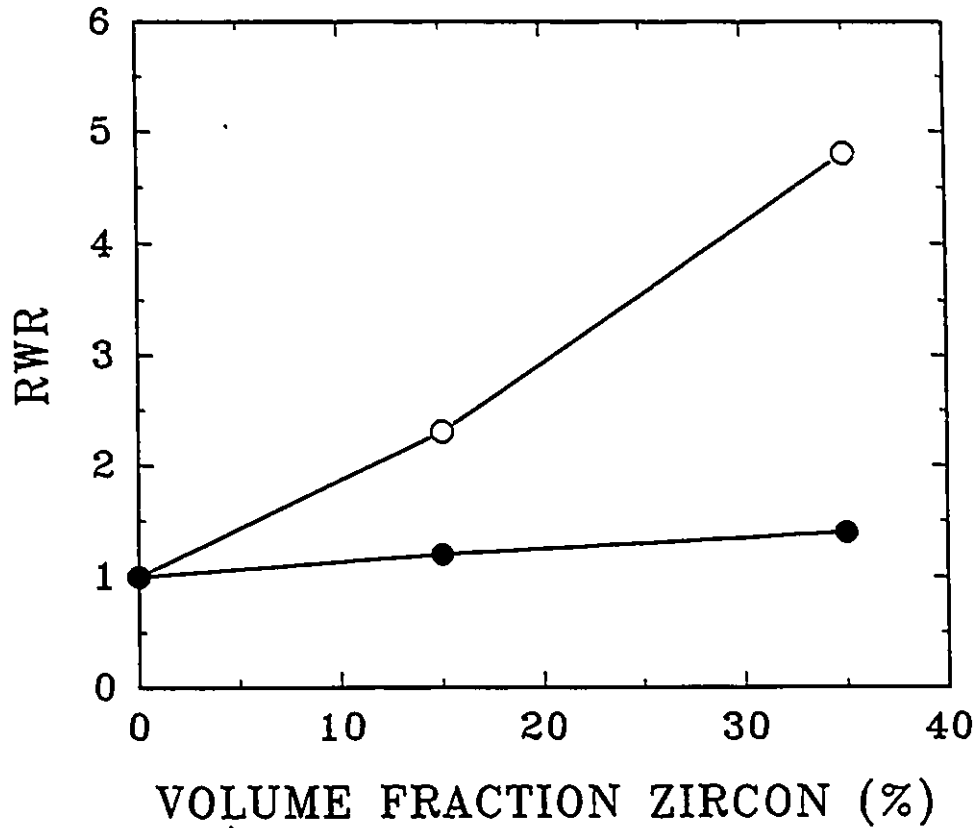


Figure 10. Relative wear resistance (RWR) for Al-11.8%Si-4.0%Mn matrix MMCs containing various volume fractions of 100 μm zircon particles, tested under low stress and high stress (pin on abrasive-covered drum) conditions. (after Prasad et al [112])

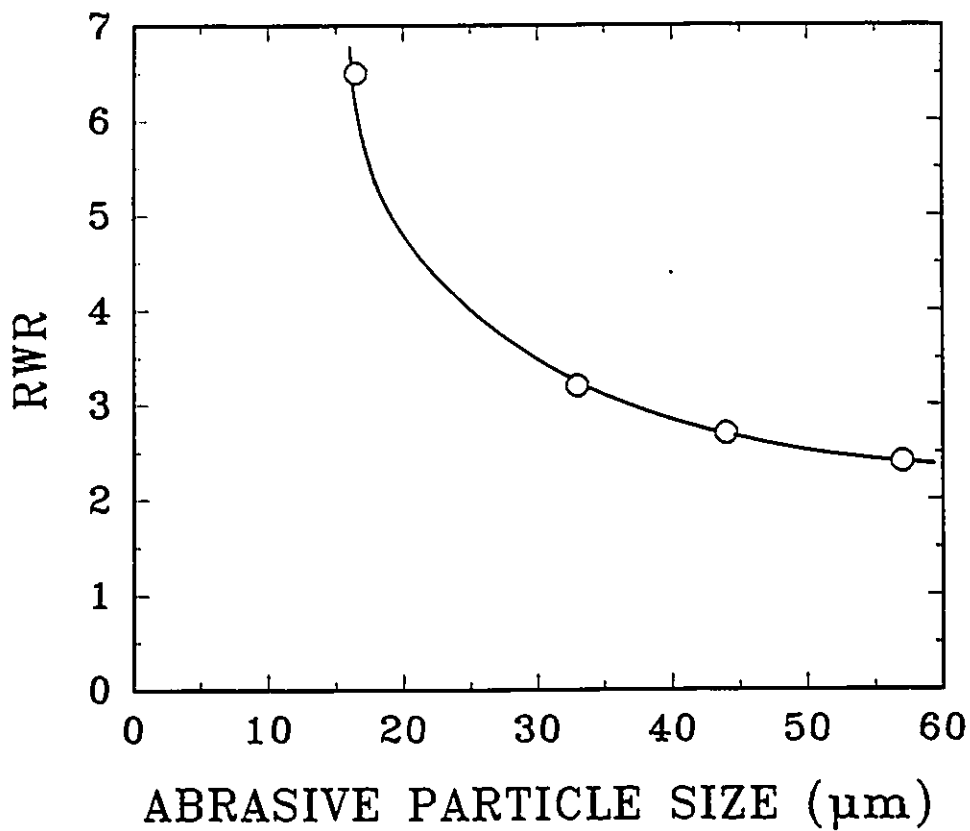


Figure 11. Relative wear resistance for an Al6061/SiC_p MMC containing 20vol.% reinforcement, in tests sliding against continuous belts of abrasive paper carrying alumina particles of different sizes. (after Wilson and Ball [113])

The load carried on each abrasive particle and the nature of the particles themselves are the important factors determining the severity of contact; in addition the size of the particles is also important. It is generally found that for small abrasive particles the benefits of reinforcement are greater than for the larger. This is illustrated in Figure 11 for a 6061Al/SiC_p MMC containing 20 vol% reinforcement. In tests on continuous belts of abrasive paper carrying alumina particles of different sizes, the value of RWR increased with decreasing abrasive particle size, to a peak value of 6.4 for the smallest abrasive particles ^[113]. In a more detailed study of the effect of abrasive particle size on the abrasion of 6061Al/Al₂O₃ short fiber-reinforced MMCs, Wang and Hutchings ^[114] showed that the RWR varied with both the fiber volume fraction and the SiC abrasive particle size. For small abrasive particles, the highest volume fraction of reinforcement gave the highest wear resistance, and the mechanism of wear involved plastic grooving of the alumina fibres. With larger abrasive particles, fracture of the fibres occurred and the benefits of reinforcement were limited; for volume fractions greater than about 20% further reinforcement actually led to a reduction in RWR. A similar increase in RWR with decreasing abrasive particle size has also been noted for alumina and SiC reinforced particulate Al matrix MMCs ^[115].

2.4.3. EROSIIVE WEAR OF MMCs

In most cases, the abrasive wear resistance of composites increases with increasing particle volume fraction of hard particles, as discussed above. However, in the case of erosive wear, opposite results have been reported. For example, the erosive wear rate in

iron- and cobalt-base composites increases with carbide particle content when tested with quartz erodent ^[97].

Goretta *et al* ^[116] tested 2014Al together with particulate MMCs based on this alloy containing 20 vol% of either alumina or silicon carbide and found the wear rates of MMC materials were greater than that of the matrix alloy under all conditions. They also found that erosive wear rates reach a maximum when the impact angle of the erodent Al₂O₃ was 15° to 30°. Similar results have also been reported by Wilson and Ball ^[113], for a 6061Al/SiC particulate MMC eroded by silicon carbide particles.

Since the erosion rates of metallic alloys are not likely to be reduced by additions of hard particles, and erosive particles in practical applications are rarely so hard as silicon carbide or alumina, some attention is given to examine the erosion behaviour of MMCs impacted by silica particles. For example, Wang and Hutchings ^[117] measured the erosion by silica particles at 65 m/s of 6061Al MMCs containing various volume fractions of short alumina fibres. They found that although under most conditions the MMCs showed higher wear rates than the matrix alloy, Figure 12, at the lowest impact angle (20°) the pattern was reversed, and a measurable decrease in erosion rate was associated with increasing fibre reinforcement.

Another case showing that reinforcement may reduce the erosion wear rate is when rather lower impact velocities or/and angle are involved. Figure 13 ^[100], for example, shows that for an aluminium-magnesium alloy MMC containing short alumina-silica fibres, there is a marked increase in erosion resistance with fibre content when the impact angle is low (15°), although very little benefit is seen from reinforcement at normal

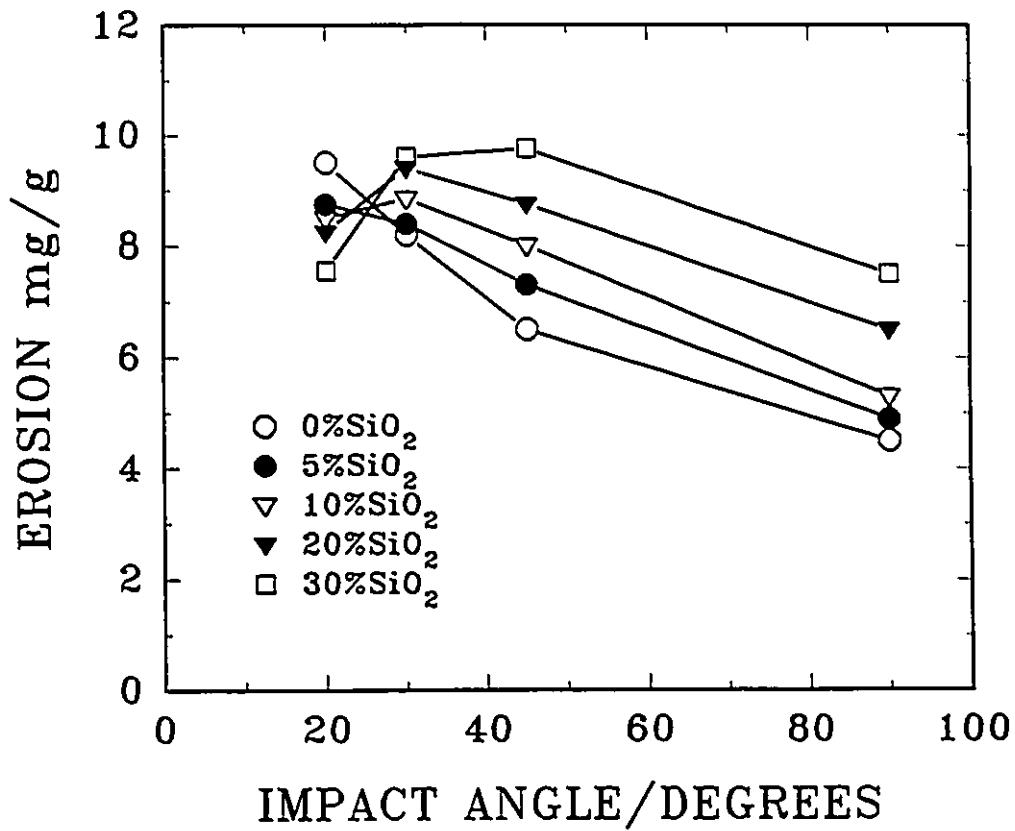


Figure 12. Erosion (expressed as mass loss per unit mass of erodent particles) plotted against impact angle for Al6061 MMCs containing various volume fractions of Saffil RF alumina fibre, eroded by 100 μ m silicon carbide and silica particles at 65 m/s. (after Wang and Hutchings [117])

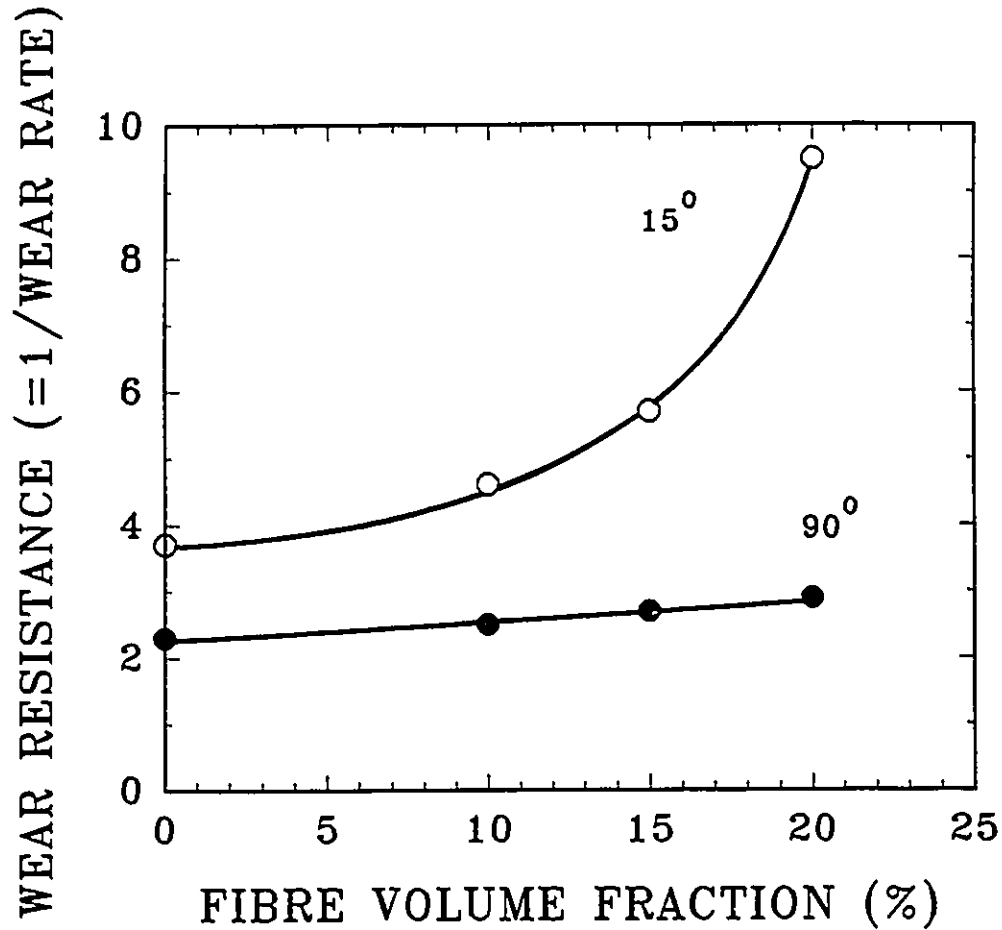


Figure 13. Wear resistance (defined as the reciprocal of erosion rate, in arbitrary units) for the slurry erosion of an Al5083 MMC containing alumina-silica fibres at various volume fractions, for impact angles of 15° and 90° . The erodent particles were silica, $200\text{--}300\ \mu\text{m}$ in size, at an impact velocity of $17\ \text{m/s}$. (after Turenne etc. [118])

impact. These data were obtained at an impact velocity of 17 m/s, with silica sand particles. Turenne et al. ^[118] have studied the slurry erosion of a particulate MMC with a rather higher volume fraction of reinforcement (35 vol% alumina in 5083Al). In this material, eroded by silica sand slurry at 15 m/s, they found that the benefits of reinforcement depended on both the erodent particle size and the angle of impingement. For small erodent particles (106 μm) at all angles, the MMC showed much lower wear rates (by a factor of up to 7) than the matrix alloy. However, for large particles (600 μm) the wear rate of the composite was less than the matrix alloy only at impact angles below about 60°; at normal incidence the MMCs wore at a higher rate than the unreinforced matrix.

2.4.4. SLIDING WEAR OF MMCs

In many tribological applications, there are two ways to improve the wear resistance of materials: soft matrix reinforced by hard phase (such as ceramic particles) and relatively hard matrix reinforced with soft phase (such as graphite). For example, incorporation of both hard ceramic particles (e.g. alumina ^[119], silicon carbide ^[119], silica ^[120], bauxite ^[101], or zircon ^[121]) and a soft solid lubricant (e.g. graphite ^[122, 123], or mica ^[124, 125]) into an aluminum alloy have been reported to increase the wear resistance under some test conditions.

2.4.4.1. HARD PARTICLE/FIBER REINFORCEMENT

Under dry sliding situations, the sliding wear resistance of composites with hard

particle/fiber reinforcement is very complex, and contradictory results have been often reported by different researchers. For example, Saka and Karalekas^[108] observed a decrease in the sliding wear resistance with increasing particle concentration in a Cu-Al₂O₃ composite against a WC-Co-coated steel in a block-on-ring configuration. Different from them, Surappa *et al*^[19] found that the addition of 5% Al₂O₃ particles to hypereutectic Al-Si alloys does not significantly contribute to the wear resistance. A similar observation has been reported by Prasad and Mecklenburg^[26]. They found no significant differences in the friction behaviour of the MMCs and the unreinforced alloy, using kaowool (Al₂O₃-SiO₂) and saffil (Al₂O₃) fiber-reinforced aluminum metal-matrix composites on 440 steel with ball-on-disc configuration, when metallographically polished samples were used as test specimens. But when the surface of the MMCs was etched, the friction coefficient of MMCs dropped to a low value of 0.18. The results of this study indicate that smearing of aluminum on wear surfaces plays a crucial role in governing the frictional performance of an aluminum alloy matrix composite.

Hosking *et al.*^[19] studied the wear behaviour of an Al-(Al₂O₃)_p composite and an Al-SiC_p composite in a wide range of reinforced particle sizes (from 1 to 142) and weight percentages (from 2% to 30%) tested against an AISI 52100 ball-bearing on a pin-on-disc machine. They found aluminium matrices containing hard non-metals exhibit excellent friction and wear properties especially with high weight percent of reinforcement, Figure 14. For example, composites of alloy 2024 plus 20 wt% of 142 μm sized Al₂O₃ particles showed a weight loss of about 2 orders of magnitude less than that of the matrix alloy under 50 g applied normal load. And they also found an increase in the dry sliding wear

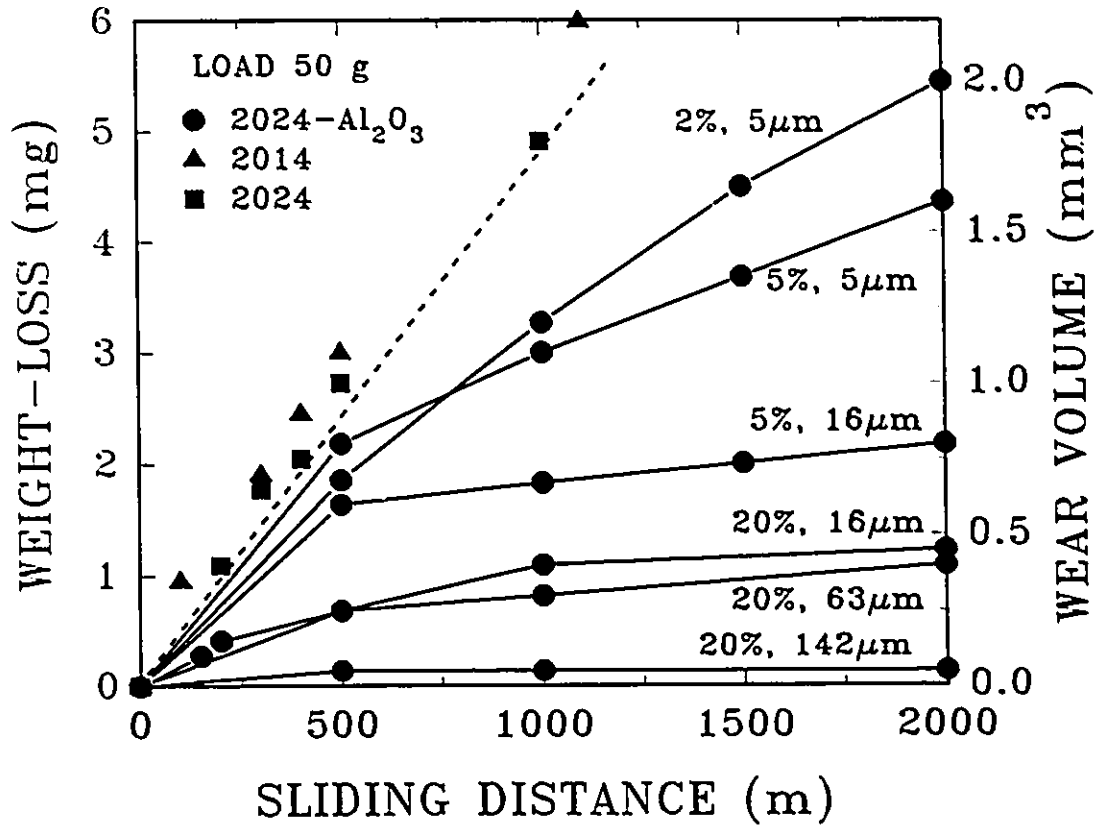


Figure 14. Weight-loss vs sliding distance of plot for aluminum-matrix alloys 2014 and 2024 and composites of 2024 containing different weight percentages of four different-sized Al₂O₃ particles. (after Hosking [119])

resistance with increasing weight percent and size of non-metallic particles for both composites.

Wang and Rack ^[104], utilizing a pin-on-disc configuration, studied the wear resistance of SiC-particulate- and SiC-whisker- reinforced 7091 Al metal matrix composites on a stainless steel as a function of sliding distance and sliding velocity under a constant pressure. They observed that at sliding velocities below 1.2 m/s, SiC reinforcement does not affect wear resistance, but at sliding velocities greater than 1.2 m/s, the wear rates of the reinforced materials were lower than for the unreinforced matrix, Figure 15. A temperature increase with sliding velocity for both the reinforced and the unreinforced alloys has been reported. The rate of temperature increase is higher for the unreinforced alloy than for the reinforced composite. Wang and Rack also studied the effect of applied load and reported that under limited loading conditions the steady state wear resistance of SiC-whisker-reinforced aluminum composites was more than an order of magnitude greater than that of the unreinforced matrix alloys.

As it is shown above, wear behaviour can be markedly changed by embedding a second phase in a single-phase matrix. Second phases can affect sliding wear by the following mechanisms ^[21, 104, 127-129]: (1) carrying the applied load imposed by the counterbody and protecting the ductile matrix from damage. (2) reducing the real area of contact between a solid body and a counterbody, for example, composites reinforced by ceramic particles with a low tendency to adhere to the counterbody can increase adhesive wear resistance by lowering the real area of contact. (3) increasing high-temperature deformation resistance. (4) hardening the matrix and reducing the ductility. (5) the hard

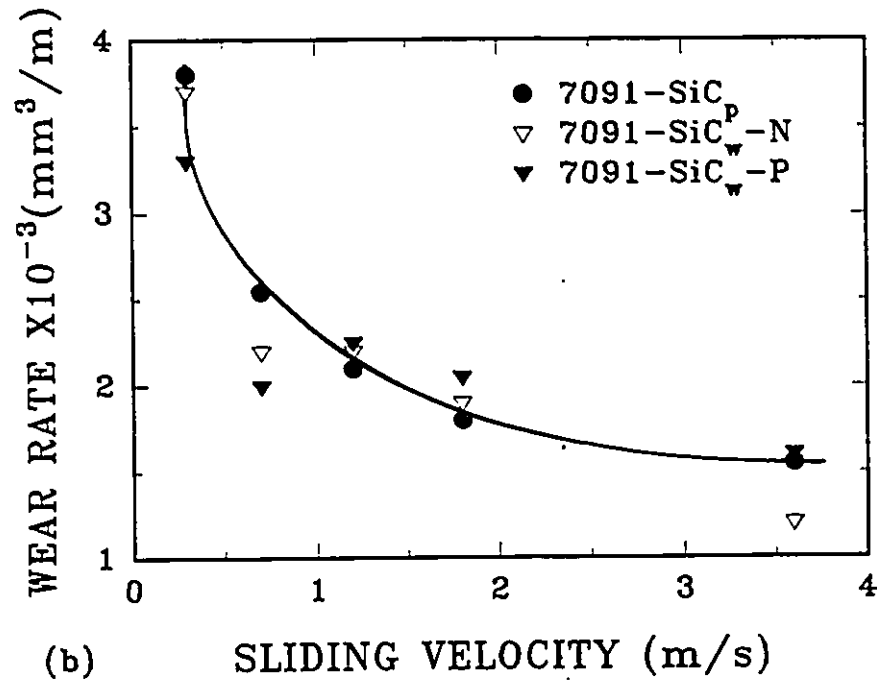
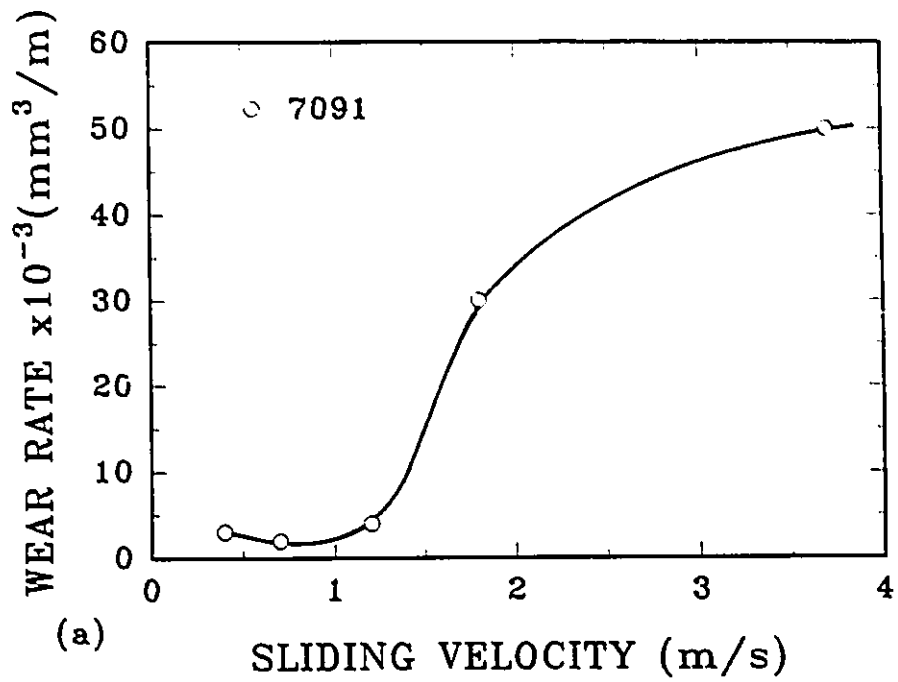


Figure 15. Steady state wear rate vs. sliding velocity for (a) unreinforced 7091 alloy, and (b) reinforced composites of 7091 with SiC_P, perpendicularly oriented SiC_w and parallel-oriented SiC_w. (after Wang and Rack [104])

particles are fractured and the wear behaviour is dependent on this mixed surface layer of fractured hard particles and matrix material. (6) the reinforcement phase is pulled out of the matrix, as a consequence of debonding, causing contact and sliding of the matrix material. (7) delamination occurs whereby fatigue causes fracture along particle-matrix interfaces. (8) particle abrasion.

So the size, shape, volume fraction, interfacial bonding condition and distribution of reinforcement are very important to the wear resistance of composite materials. And the poor wear resistance of composite materials in some test conditions has usually been attributed to the poor particle-matrix interfacial bonding and as well to the associated reduction of the ductility. It has also been pointed out that the wear properties of MMCs depend very much on the tribosystem and the type of MMCs.

2.4.4.2. SOFT PARTICLE/FIBER REINFORCEMENT

When lamellar solids such as graphite are applied to sliding surfaces, friction and wear are observed to decrease. The crystal structure of a lamellar solid has sheets or layers weakly bonded with each other but the bonding within the sheet is quite strong. These solids are thus strong in compression but weak in shear, and act as solid lubricants. In metal matrix-graphite composites, graphite particles are embedded in the matrix, and the formation of a graphite film which prevents direct contact between the mating surfaces will take place by transfer of the graphite from the particles embedded in the matrix on to the tribosurfaces. One of the main difficulties in using graphite as a solid lubricant lies in maintaining a continuous supply of graphite which acts as a solid lubricant between

two sliding surfaces. Similar systems include composites containing dispersoids such as MoS₂ and PTFE.

The particulate composites of graphite and a matrix alloy are characterised by (a) the composition and microstructure of the matrix alloy, (b) the size, volume fraction, and distribution of particles, and (c) the nature of the interface between the matrix and the dispersed graphite.

Most metal matrix-graphite particle composites exhibit low friction, low wear rates, and excellent anti-seizing properties ^[123, 130, 131]. For example, the friction coefficients for different matrix composites decrease with graphite content before a critical volume level of about 20 vol% and reach a lowest value around 0.2, which is close to the friction coefficient of pure graphite, when above 20 vol% of graphite. This is because when the graphite content is below the critical level, the extent of coverage of the tribosurface by a solid lubricating film increases with the graphite content of the matrix. For composites containing graphite in excess of the critical amount, above which the friction coefficient approaches a constant value regardless of the matrix, the sliding surface is completely covered with a graphite solid lubricating film ^[123].

Similar to the friction coefficient, the wear rates of graphite reinforced composites decrease with increasing graphite content and do not significantly change with graphite content once the film of graphite completely covers the sliding surface. It is likely that the wear rate may increase when the graphite content in the matrix reaches very high values, because of the decrease in strength of the matrix at very high graphite levels and the formation of a thick graphite film of thickness exceeding the critical value, which can

itself wear by delamination within the film in a manner similar to that of bulk graphite. Rohatgi *et al* point out that the larger graphite particle size results in lower wear ^[123].

However, there have been some conflicting reports on the dry sliding wear behaviour of aluminium alloy-graphite composites. Jha *et al* ^[132] reported that the dry sliding wear rates of 6061 aluminium alloy composites containing up to 14 vol% graphite particles were found to increase as the graphite volume fraction increases. Except at the lowest pressure (0.04 MPa), the wear rate of the composites was found to be higher than that of the matrix alloy. Similar findings were reported by Biswas *et al* ^[133] in Al-Si alloy composites containing 2.7 and 5.7 wt% graphite particles and Gibson *et al* ^[130] for composites with a higher (greater than 8 wt%) graphite content. The lower wear resistance in these cases is attributed to the porosity levels in the composites. In another paper ^[134] Jha *et al* etched the composite prior to the wear test. They found a substantial improvement in wear rate over that of the base alloy. The worn surfaces in this case showed patches of graphite layers sticking to them and the debris were small and equiaxed. That is because graphite particles, in the case of etched composites, come directly in contact with the steel disc at the start of the experiment. The sliding action would then smear the graphite layers, giving rise to a graphite layer on the surface of the matrix alloy.

The seizure resistance can also be improved significantly by dispersing graphite particles in the metal matrix ^[135]. Rohatgi *et al* ^[123] suggest that the improvement in galling resistance is primarily due to the formation of a graphite film and that there is an observed minimum graphite content of about 2 wt% required to prevent galling in Al-Si-

Ni alloy. Das and Prasad ^[131] found that 3 wt% of graphite in an Al-Si-Cu alloys (LM30) increases the seizure pressure by 2 MPa over that for the base alloy.

As is shown above in the literature survey, although a qualitative picture of the friction and wear behaviour of metal matrix composites is emerging, a quantitative understanding of their tribological behaviour is far from satisfactory. A theoretical basis to predict the tribological behaviour of metal matrix composites does not exist. Even the experimental literature suffers from lack of standardization; test conditions used by different investigators are not clearly indicated and are quite different. Consequently conflicting results are often reported, and only a correlation of results in terms of broad trends is possible. Therefore the wear behaviour of metal matrix composites (such as microstructure, counterface, temperature *etc.*) should be investigated in more detail.

CHAPTER III EXPERIMENTAL DETAILS

3.1. MATERIALS

3.1.1. Al-Si-Mg ALUMINUM ALLOY (A356) REINFORCED WITH SiC PARTICLES

Both the unreinforced A356Al alloy and the A356Al-SiC composites containing 10, 13, 16 and 20 vol% SiC particles (Duralcan F3A) were produced by Alcan International, Kingston, ON, Canada, and supplied in the form of extruded rods of 25 mm diameter. The chemical composition of the A356 alloy is given in Table I. The wear samples (5mm × 10mm × 10mm rectangular blocks) were cut from these rods and solution treated at 540 °C for 4 hours, quenched into warm water (40 °C), and artificially aged at 155 °C for 9 hours *i.e.* T6 condition.

The optical micrographs in Figure 16 illustrate typical microstructures of the A356Al-20%SiC. This micrograph is taken from the surface perpendicular to the extrusion direction and represents the microstructure of the surfaces which was prepared for subsequent sliding wear tests. The size distribution of the SiC particles were determined by quantitative metallography using a digital image analyzer. Both the largest (L_{max}) and smallest (L_{min}) diagonals of SiC particles were measured. As an example, the particle size distribution histograms of A356Al-20%SiC are shown in Figure 17. The figure also shows the size distribution of silicon in the matrix. In the peak-aged condition the average silicon particle size in the composites was similar to that in the matrix

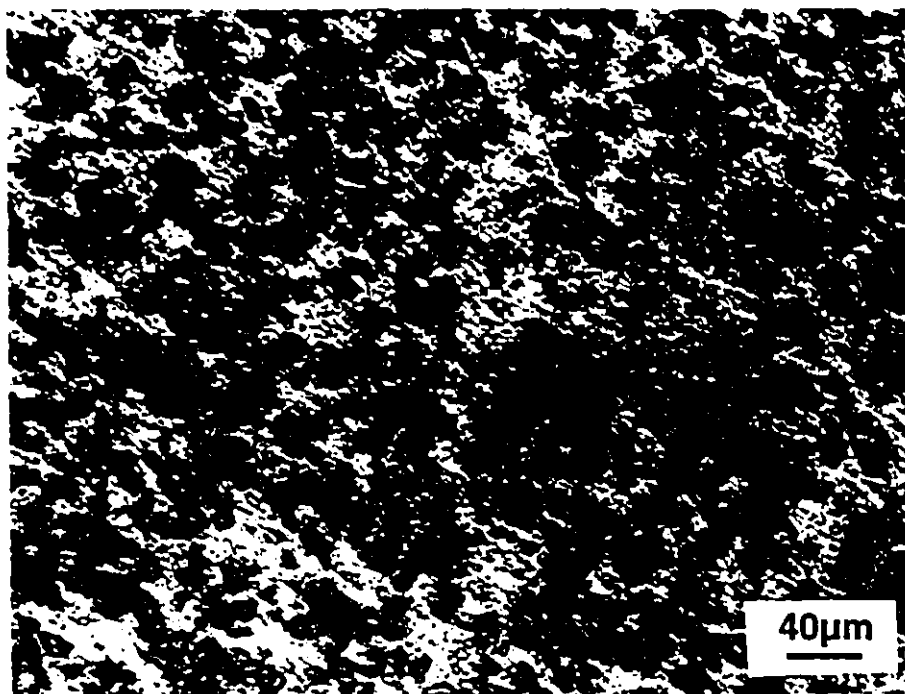
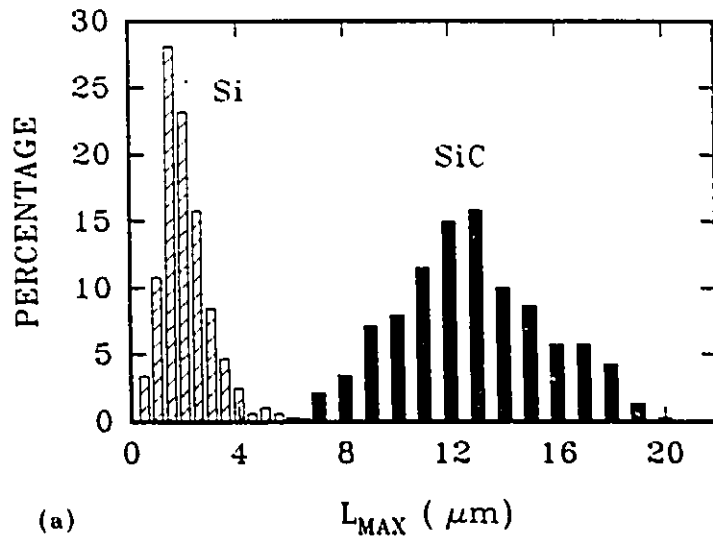


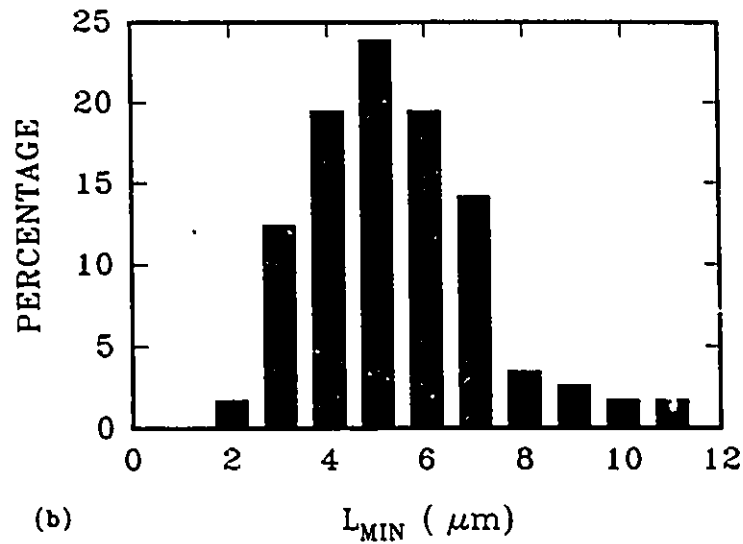
Figure 16. Optical micrograph of peak-aged microstructure of A356Al-20%SiC. Si particles are light grey phase.

Table I. Composition (Weight Percent) of Matrix Materials

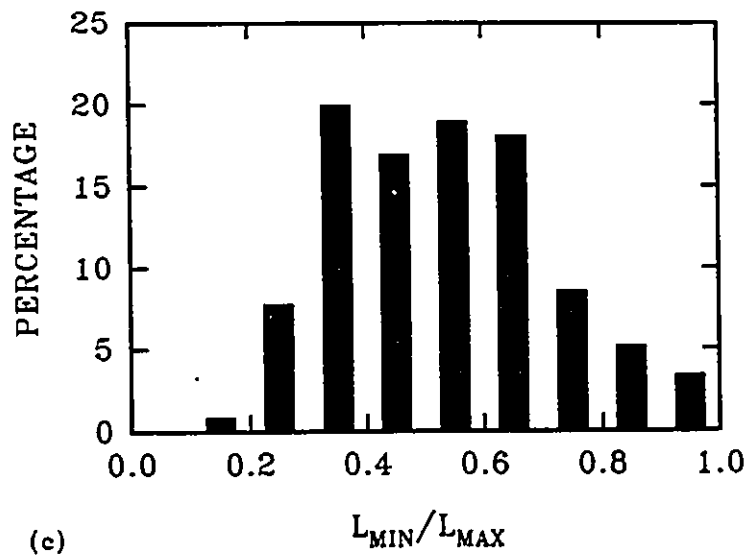
	Mg	Si	Cu	Zn	Cr	Fe	Mn	Ti	Al
A356	0.4	7.0	0.1	0.1	---	0.11	0.05	0.2	balance
6061	1.0	0.6	0.3	0.3	0.2	0.7	0.1	0.1	balance
2014	0.5	0.9	4.4	0.3	0.1	0.7	0.8	0.1	balance
2124	1.2	0.2	4.4	0.3	0.1	0.3	0.6	0.1	balance



(a)



(b)



(c)

Figure 17. Histograms of the size distribution of SiC particles in A356Al-20%SiC; (a) maximum size, L_{max} (largest diameter) distribution; (b) minimum size, L_{min} , (smallest diameter) distribution; (c) distribution of the aspect ratio (L_{min}/L_{max}).

material ($1.8 \mu\text{m} \pm 0.9 \mu\text{m}$). The average maximum and minimum sizes of the SiC particles determined according to this method are summarized in Table II.

Table II also shows the Vickers hardnesses of the materials in the T6 condition. The measurements were made by applying a load of 1 kg, and the values shown are the averages of at least 10 measurements. The density measurements were performed according to the ASTM Standard C127-88.

3.1.2. Al-Mg-Si ALUMINIUM ALLOY (6061Al) REINFORCED WITH Al_2O_3 PARTICLES

Wrought unreinforced 6061 Al alloy and 6061Al- Al_2O_3 composites containing (10 and 20 vol% Al_2O_3 particles, Duralcan W6A) were produced by Alcan International, Kingston, ON, Canada by a Duralcan process. The wear samples (5mm \times 10mm \times 10mm rectangular blocks) were prepared from the billets fabricated by casting and hot extrusion. The chemical composition of the matrix alloy is given in Table I. The wear samples (both unreinforced and composites) were solution treated at 530 °C for 1 hour, water quenched, naturally aged at 25 °C for 2 days, and then subjected to an artificial aging at 175 °C for 16 hours in order to achieve the T6 condition.

Figure 18 illustrates the typical microstructure of the 6061Al-20% Al_2O_3 specimen surface perpendicular to the extrusion direction (test surface). The size distributions of the Al_2O_3 particles are shown in Figure 19. The distribution of the largest (L_{max}), smallest (L_{min}) and average sizes of Al_2O_3 particles are summarized in Table II.

Table II. Average Particle Size, Bulk Hardness,
and Density of the Materials Tested

Material	L_{min} (μm)	L_{max} (μm)	L_{avg} (μm)	Hardness (VHN) (1 kg)	Density (Mg/m^3)
A356	---	---	---	60.3±0.7	2.669
A356-10%SiC	6.5±1.5	12.1±2.9	9.3±2.8	81.7±3.7	2.731
A356-10%SiC	12.9±4.7	22.6±5.7	17.8±5.2	80.1±8.9	2.728
A356-13%SiC	6.9±2.6	11.8±3.8	9.4±3.3	105.4±3.9	2.759
A356-16%SiC	10.3±3.1	18.1±5.4	14.2±4.1	118.2±8.3	2.778
A356-20%SiC	6.8±2.0	12.7±3.8	9.6±3.2	115.8±2.8	2.778
6061	---	---	---	120.2±1.9	2.712
6061-10%Al ₂ O ₃	8.1±3.3	20.1±4.9	14.1±4.6	133.5±1.7	2.804
6061-20%Al ₂ O ₃	12.8±4.8	25.4±5.3	19.1±5.2	170.1±7.0	2.957
2014	---	---	---	157.9±3.2	2.566
2014-20%SiC	10.3±4.4	21.3±6.1	15.8±5.0	189.8±7.8	2.736
2124-20%SiC	2.1±1.1	2.7±1.9	2.4±1.7	178.1±3.5	2.795

- * average smallest particle size
- ** average largest particle size
- *** average particle size

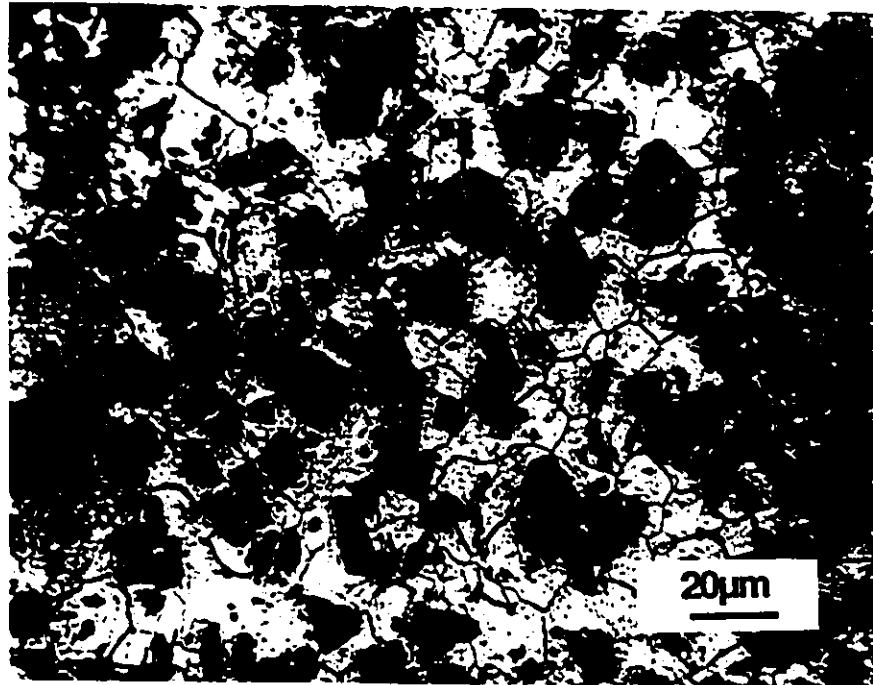


Figure 18. Microstructure of 6061Al-20%Al₂O₃.

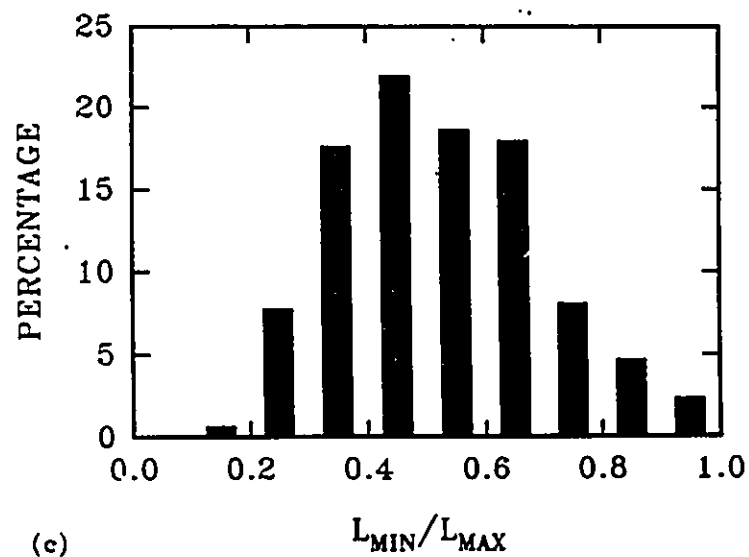
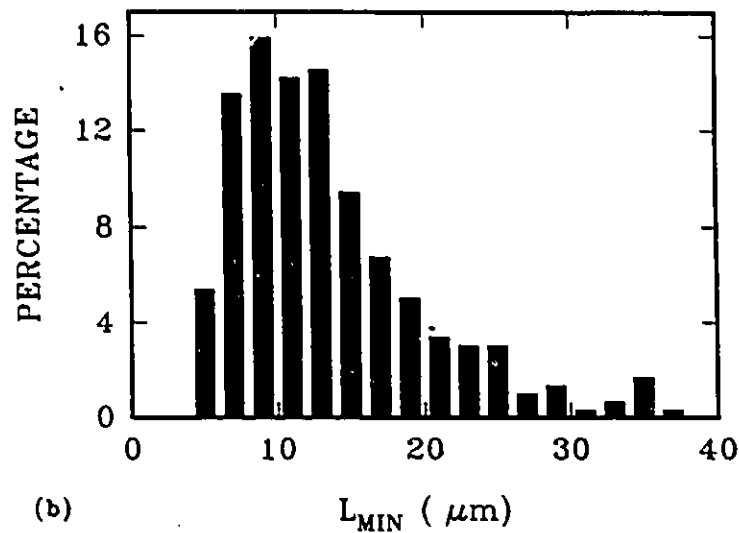
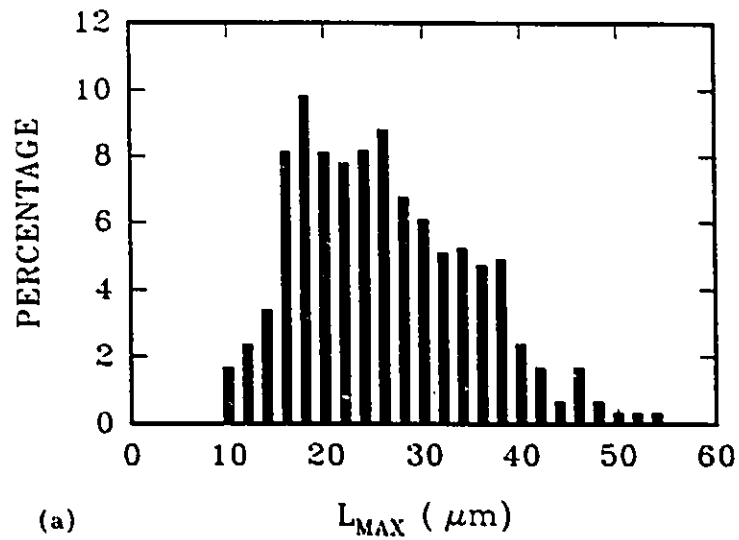


Figure 19. Histograms of the size distribution of Al_2O_3 particles in 6061Al-20% Al_2O_3 : (a) maximum size, L_{max} (largest diameter) distribution; (b) minimum size, L_{min} , (smallest diameter) distribution; (c) distribution of the aspect ratio (L_{min}/L_{max}).

3.1.3. Al-Cu-Mg ALUMINIUM ALLOYS (2014Al, 2124Al) REINFORCED WITH SiC PARTICLES

These composites were selected to study the effect of particle size on the wear rates. 2014Al-SiC (20Vol%SiC) was produced by a molten metal mixing technique followed by casting and co-extrusion operations (Alcan International). The average particle size of this material was $15.8 \pm 5.0 \mu\text{m}$. The 2124Al-SiC (20Vol%SiC) had a finer average particle size of $2.4 \pm 1.7 \mu\text{m}$ (Table II). This material was manufactured by British Petroleum Composites Ltd., U. K., by using a powder metallurgy route and supplied in the form of hot-rolled sheets (2 mm in thickness). The matrix compositions of the two composites were comparable (Table I). The wear samples of 2014Al-20%SiC were in the form of $5\text{mm} \times 10\text{mm} \times 10\text{mm}$ rectangular prisms like the previously described composites but the wear specimen made from 2124Al-20%SiC were thinner $2\text{mm} \times 5\text{mm} \times 10\text{mm}$ and were held in the wear machine using a specially made clamp. Both composites and the control alloy 2014Al were solution treated at $505 \text{ }^\circ\text{C}$ for 1 hour, water quenched, and immediately subjected to aging at $190 \text{ }^\circ\text{C}$ for 8 hours.

3.2. WEAR TESTS: MEASUREMENT OF WEAR RATES

Dry sliding wear tests were performed using a block-on-ring type wear apparatus designed and built at the University of Windsor. A schematic of the wear apparatus is given in Figure 20. The set-up consisted of a wear testing machine and a temperature measurement setup. The ring counterface was rotated by a 1 HP D.C. electric motor. The specimens in the form of blocks were kept stationary. During the wear test, the

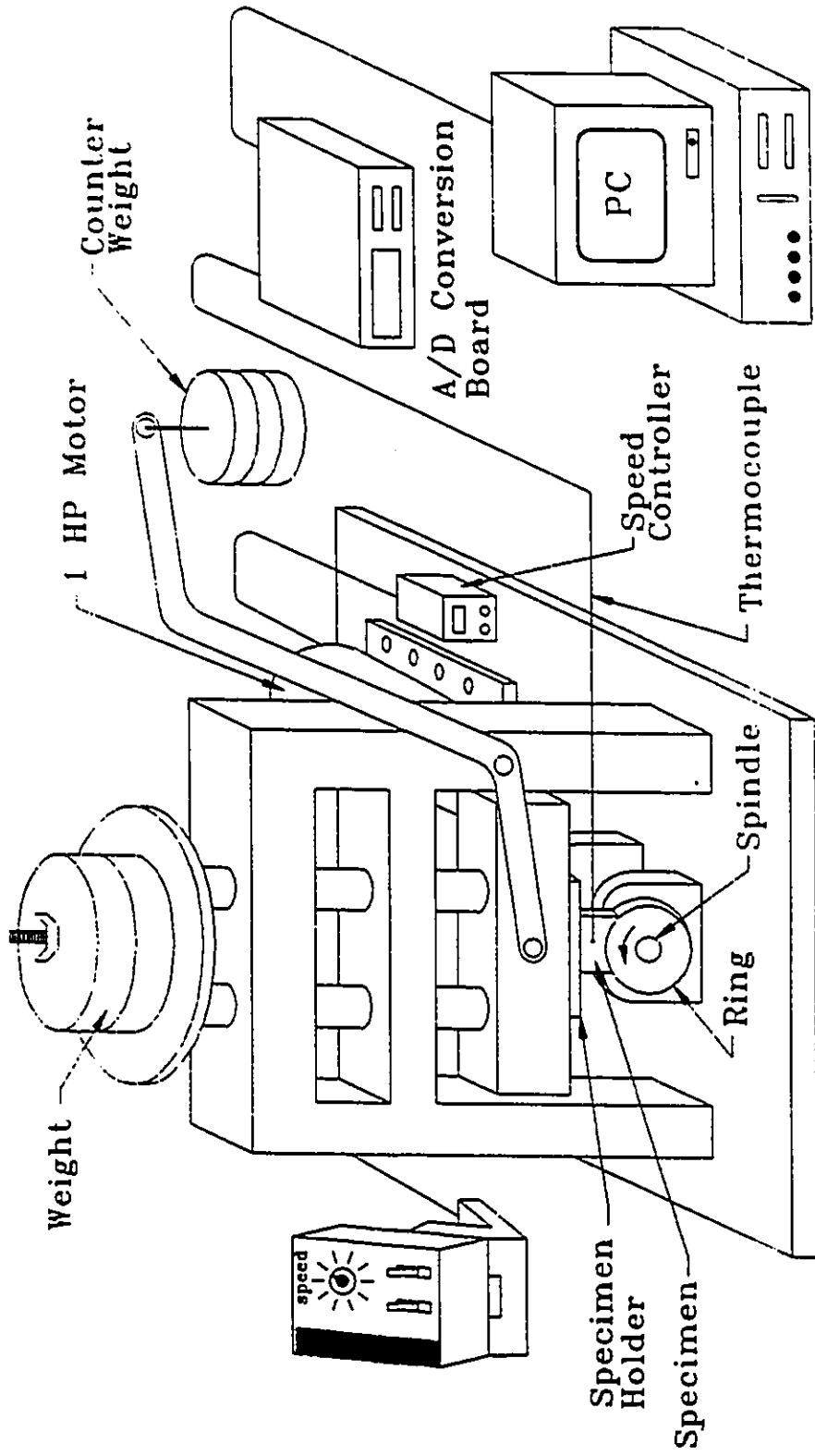


Figure 20. Block-on-Ring Wear Apparatus

temperature of the contact surfaces was continuously measured by a thermocouple and recorded by a data acquisition system that consisted of a multifunction analog-to-digital conversion board connected to a micro-computer.

Two types of counterface materials were used as slider rings: These were (AISI) SAE 52100 bearing steel (0.98 to 1.1 wt%C, 0.25 to 0.45 wt%Mn, 0.15 to 0.30 wt%Si, 1.30 to 1.60 wt%Cr, balance Fe) and mullite ($3\text{Al}_2\text{O}_3 \cdot 2\text{SiO}_2$, supplied by Coors Ceramics, CO). The widths of both slider rings were 12 mm. The outer diameter of the slider ring made of SAE 52100 steel and mullite were 38 mm and 46 mm respectively. The narrow rectangular faces of the specimens (5mm \times 10mm) were put in contact with the slider rings. The properties of the counterface materials relevant to the wear tests were their hardnesses and thermal conductivities. The Vickers hardness of the mullite was 1700 kg/mm² and its thermal conductivity (at 25°C) was specified as 4.1 W/mk by the manufacturer. The surface hardness of the SAE 52100 steel was measured to be 950 kg/mm² and its thermal conductivity (at 25 °C) was 45 W/mk ^[172].

Conventional aluminum alloy polishing techniques were used to prepare the contact surfaces of the monolithic and composite aluminum specimens for the wear tests. The procedure consisted of grinding surfaces manually by 240, 320, 400, and 600-grit SiC papers respectively and then polishing them with 5, 1, and 0.05- μm alumina powder slurry using a low-speed polishing machine. The polished surfaces were cleaned ultrasonically in acetone and methanol solutions. The counterface materials were also polished and cleaned before each wear test. Steel sliders were polished using the same procedure described above. For mullite sliders, the final polishing was performed using

a 5- μm and then a 1- μm diamond paste. Counterface materials were also cleaned ultrasonically in acetone and methanol before use.

The tests were carried out with a sliding velocity range of 0.1 to 4.0 m/s and a load range of 1 to 450 N. At each load level weight losses from the surfaces of specimens were determined as a function of sliding distance. The weight losses were calculated from the differences in weight of specimens measured before and after the sliding tests to the nearest 0.1 mg using an analytical balance. The weight of the worn specimens was measured after removing the loose debris from the worn surface using acetone, and methanol in an ultrasonic cleaner. A separate specimen was used to measure the weight loss for each sliding distance. Results from the specimens with wear track geometries that were not compatible with the specifications of ASTM standard G77-83 were discarded.

At a given load level (except the loads near the transitions) the weight loss from the worn surfaces were found to increase linearly with the sliding distance following a transient period at the beginning of the test. The wear rates were calculated from the slopes of the weight loss vs sliding distance curves determined at several applied load levels within the 1 to 450 N load range. The wear rates measured in weight units were then converted to volumetric wear rates using the densities of the materials listed in Table II, and these were plotted against the applied load on a double logarithmic scale. When the applied load during the test was found to be near the transition load, an increase in the wear rate with sliding distance (time) was observed. In this case the wear rate was calculated by the gradient of

the wear curve at a sliding distance of 10^3 m. All tests were performed at room temperature (20-24 °C) and relative humidity around 55%.

In “regular” wear tests the initial contact geometry (formed by a cylindrical ring in contact with a flat surface) was linear. This was modified to a concave surface as the material was removed from the surface. However, in order to maintain a uniform contact geometry during the tests which required an “equilibrium surface geometry” such as those for the displacement gradient, microhardness gradient measurements and surface temperature measurements, the test surfaces of the samples were machined to a radius of 19 mm to conform them with the curvature of the convex surfaces of the steel slider ring. The specimen geometry used in these tests is shown in Figure 21. In this way, the initial linear contact and the high nominal stresses generated at the beginning of block-on-ring tests were minimized.

3.3 SUBSURFACE DISPLACEMENT AND MICROHARDNESS MEASUREMENTS

These tests were performed to study the changes in the mechanical properties of the material adjacent to the contact surfaces. In order to measure the sliding displacements below the worn surfaces a reference marker was introduced in a slit (400 μm wide) cut perpendicular to the contact surface (Figure 21). A rectangular platelet which was machined from the same material used to fabricate the test pieces, was used as a marker. Both surfaces of the platelet were polished to gradually reduce its thickness until it snugly fitted in the slit. An example of wear tests performed with and without the

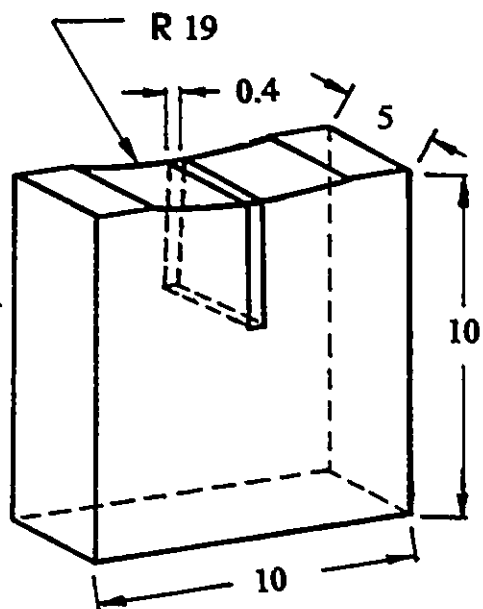


Figure 21. Wear sample geometry manufactured to conform with the steel counterbody. The radius of curvature on the contact surface conforms with the radius of the slider (all dimensions in mm). For measuring the sliding displacements below the worn surfaces, a platelet reference marker made of the same Al alloy was inserted in the slit cut normal to the contact surface.

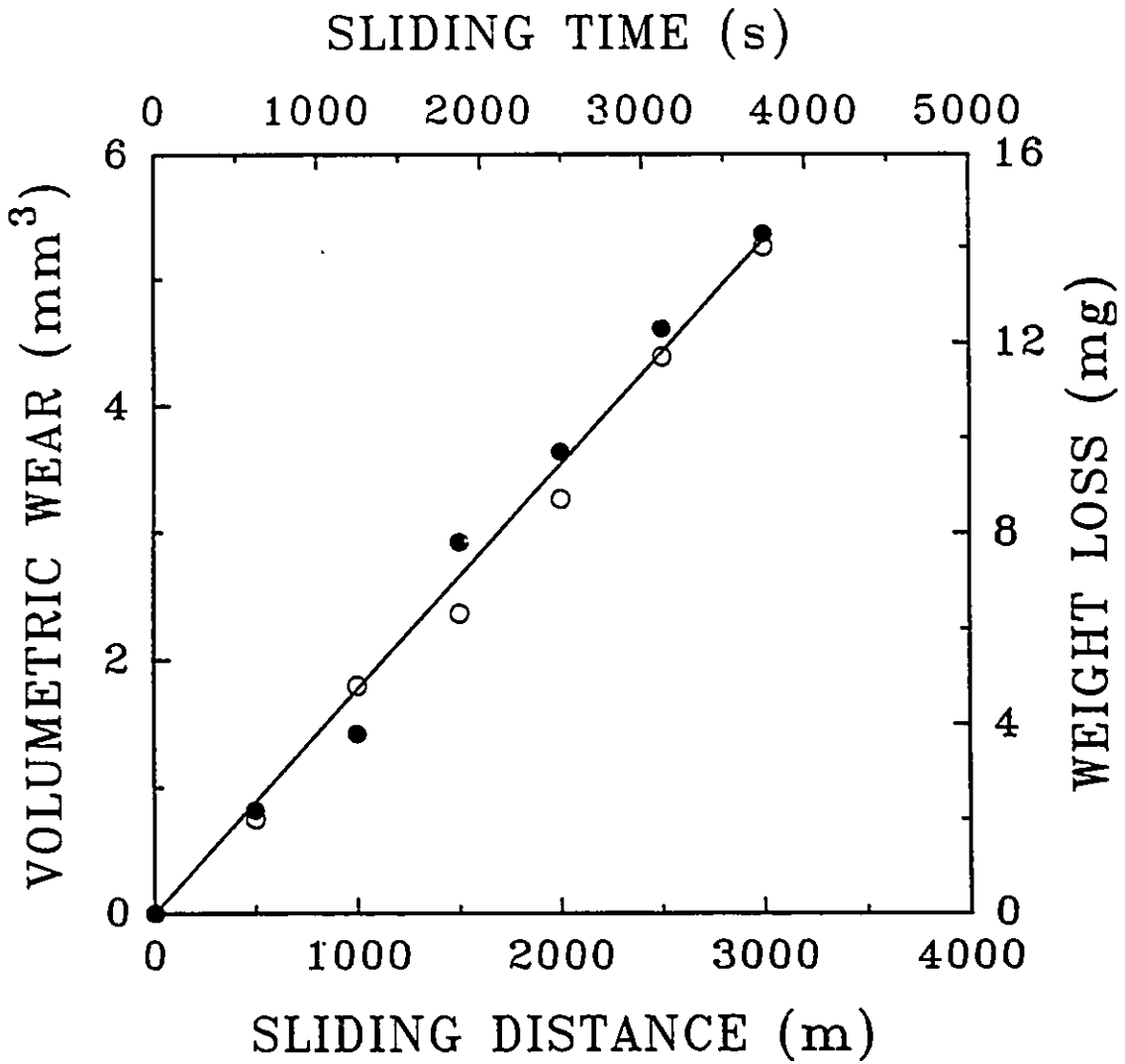


Figure 22. A typical volume (weight) loss vs. sliding distance plot (O) with, (●) without the marker platelet. Load: 17 N; Sample: A356Al.

marker platelet is given in Figure 22. No obvious difference in the wear behavior between these two kinds of specimens has been found. After the wear test, the forward displacements at the interfaces between the plate and the rest of the specimen were measured by sectioning the specimen through the centre in a plane normal to the worn surface but parallel to the sliding direction (transverse section). The displacement gradients were analyzed to estimate the shear strain gradients (section 4.4) established during the test. It was important to use the same material as the bulk for the platelet because hardness differences between the layers in the laminated materials are known to influence the wear resistance [56, 173].

The hardness distributions in the material near the worn surfaces were measured using a Vickers microhardness tester (Micromet II Microhardness Tester), under a load of 25 gf. Microindentations were made on taper sections which were cut at an angle about 5° to the worn surfaces by a low speed diamond saw (Figure 23(a)) and polished first by 240, 320, 400, and 600-grit SiC papers, then with 5, 1, and 0.05 μm aluminum oxide powder. The value of the angle between the actual surface and tapered section, θ, (Figure 23) was calculated using the following equation:

$$\theta = \frac{\sum_1^n \arctan \left(\frac{z_i}{d_i} \right)}{n} \quad (3.1)$$

where the number of measurements $n \geq 3$. The values z_i and d_i were measured on carefully polished cross-sections as shown in Figure 23(b) by a graduated eyepiece of an optical microscope (within an accuracy of 0.1 μm). Then, the depth corresponding to the

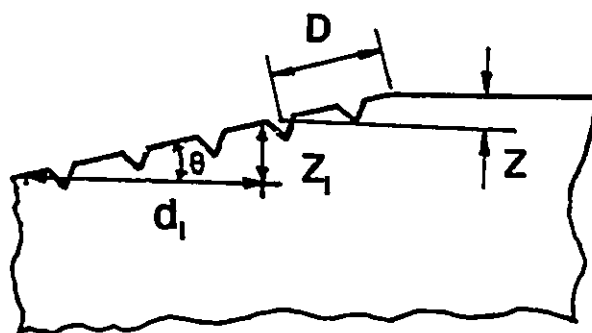
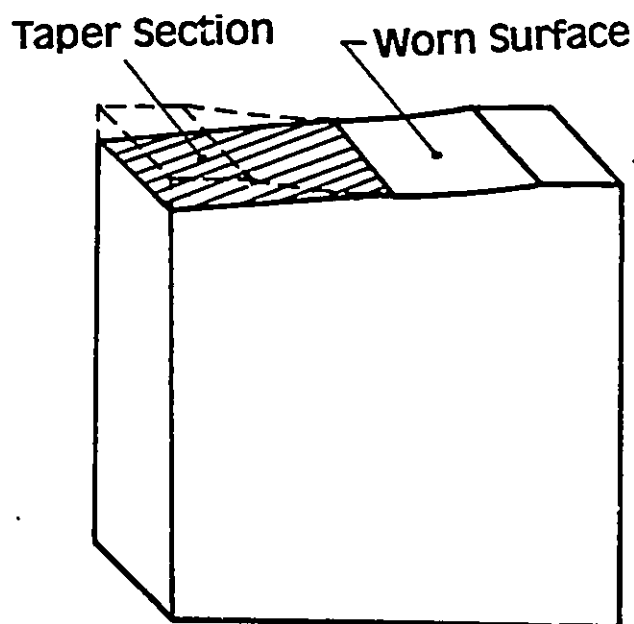


Figure 23. (a) Schematic representation of a taper section taken from the worn specimen; (b) An enlarged taper section to illustrate the calculation of the depth corresponding to microindentation impressions. (The actual depth of indentations was smaller than shown here).

microindentation impression was calculated by

$$Z = D \sin \theta \quad (3.2)$$

where D is the distance between microindentation impression and the boundary of tapered surface and worn surface (Figure 23(b)). Using this metallographic procedure the depth of the subsurface region affected by the wear process could be enlarged by about 10 times. The microhardness values (see section 4.4) were averages of three readings at a given distance below the worn surfaces.

3.4. CONTACT SURFACE TEMPERATURE MEASUREMENTS

Two different types of temperatures were simultaneously measured during the sliding test. One was the average contact surface temperature of the sample and the other was the reference temperature (about a distance of 7.5 mm away from the contact surfaces). As shown in Figure 24, a thin (diameter: 0.3 mm) chromel-alumel type thermocouple was inserted in the specimen through a hole drilled slightly larger than the diameter of the thermocouple. For the measurements of surface temperature, prior to the tests the end of the thermocouple was put in contact with the slider ring. During the actual test, after a certain sliding distance usually the tip of the thermocouple became in contact with the debris that covered the entrance of the hole. The temperature rises were measured as a function of sliding distances at various loads and recorded *via* a digital data acquisition system installed in a personal computer.

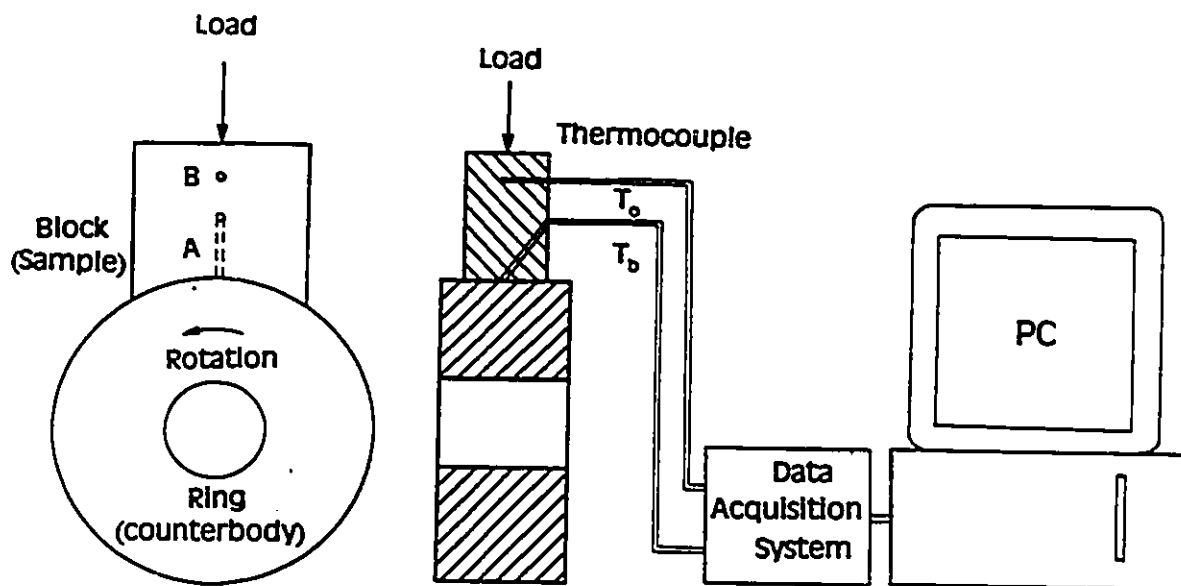


Figure 24. Schematic illustration of the temperature measurement set-up with the block-on-ring apparatus.

3.5. METALLOGRAPHY OF CROSS-SECTIONS BELOW THE WORN SURFACES

A comprehensive understanding of wear processes requires a thorough knowledge of the nature and changes experienced by the contacting bodies. This includes the microstructure of the test materials, the examination of worn surfaces (topography, microstructure, composition, reaction films, transfer layers) and wear debris (size, shape, composition, microstructure).

The metallographic cross-sections (transverse, longitudinal) from the worn samples of unreinforced Al alloy were prepared using standard metallographic procedures. For the MMC samples, after wet grinding on 200, 320, 400 and 600-grit SiC papers, the polishing procedure was followed with 6 μm and then 1 μm diamond paste on fine polishing cloth. In this way, the reinforced ceramic particles appear flat on the polished surfaces.

Materials were etched with Keller's reagent (2 ml HF, 3 ml HCl, 5 ml HNO₃ and 190 ml H₂O). To examine cross-sections perpendicular to the worn surface, the worn surfaces were covered with acetone soluble lacquer to protect them from the chemical attack. After etching, the lacquer coating was removed by dissolving it in acetone in an ultrasonic cleaner.

Microstructural investigations and semi-quantitative chemical analyses on the worn surfaces, the cross-sections (both longitudinal and transverse section) as well as on the loose debris generated during wear were performed by an optical (Leitz Laborlux 12 ME) metallographic microscope and a scanning electron microscope, SEM, (SEMCO Nanolab7). The latter was equipped with an energy dispersive spectroscopy (EDS)

system. The debris particles formed during mild wear tests were coated by a thin layer of gold prior to the SEM examination since these particles were often oxidized or mixed with oxides during the tests. A Rigaku X ray diffraction XRD system with Cu-K α radiation was used for the X-ray diffraction analyses of the debris.

CHAPTER IV EXPERIMENTAL RESULTS

4.1. EXPERIMENTAL RESULTS ON Al-Si-Mg (A356) ALUMINUM ALLOY REINFORCED WITH SiC PARTICLES

4.1.1. VOLUMETRIC WEAR-SLIDING DISTANCE DIAGRAMS

To determine the wear rates (\dot{W}) of the composites and the unreinforced alloy, the weight losses from the surfaces of the specimens were measured as a function of sliding distance at several load levels within the 1-350 N load range. The sliding velocity was kept constant at $V=0.8$ m/s. A linear relation was observed between the weight loss and the sliding distance. The measured weight losses were then converted to volumes using the densities of the materials. Typical volumetric wear vs. sliding distance curves for the unreinforced A356Al and the A356Al-SiC composites are shown in Figures 25(a)-(c). Each point on these volumetric wear-sliding distance plots represents data from a different sample worn for a given sliding distance. The wear rates at each applied load can be calculated from the slope of volume loss vs. sliding distance curves using a linear regression method. The results reveal that the effect of SiC reinforcement on the wear rate varies with the applied load. The main features of the results presented in Figure 25 are as follows.

At the lowest load (1 N, Figure 25(a)), SiC reinforcement has a beneficial effect on the wear resistance. At this load the wear rates of composites are more than one order of magnitude lower than those of the unreinforced A356Al. Similarly, towards the other end of the applied load spectrum (98 N, Figure 25(c)) there exists about two

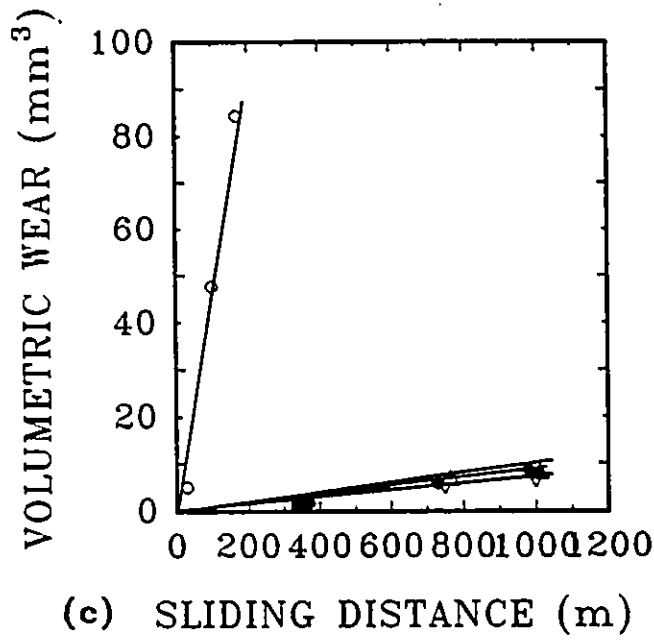
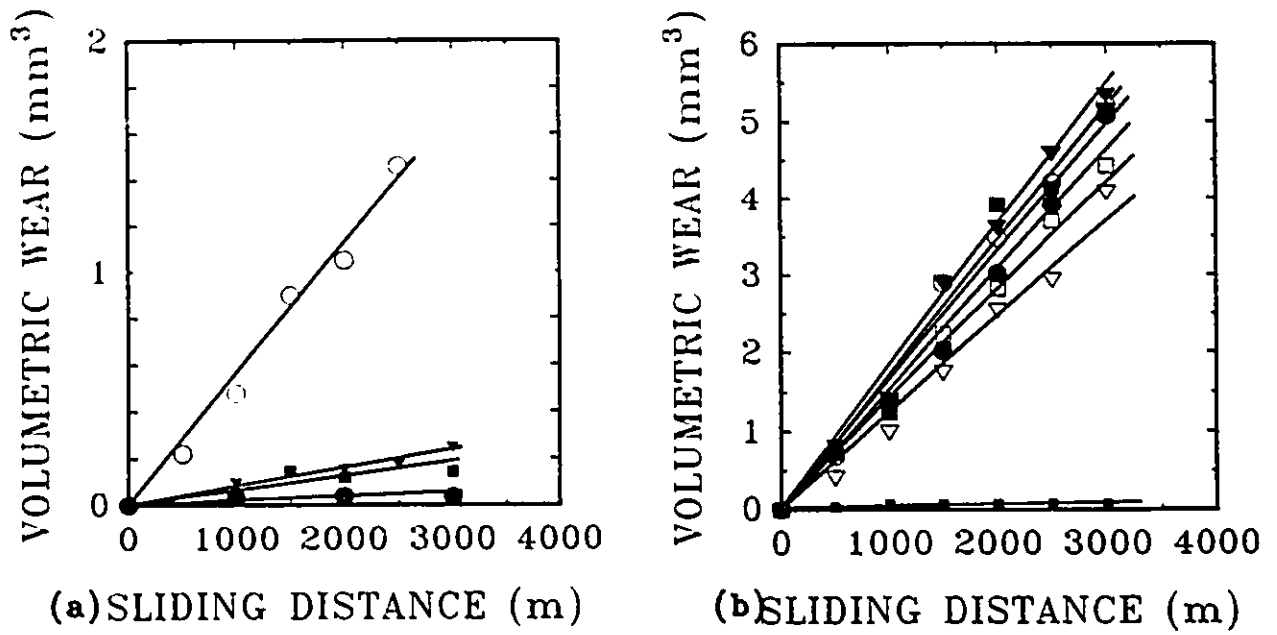


Figure 25. Volume loss vs. sliding distance curves at (a) 1 N; (b) 17 N and (c) 98 N for (\circ) A356Al; (\bullet) A356Al-10%SiC (9.3 μm); (∇) A356Al-10%SiC (17.8 μm); (\blacktriangledown) A356Al-13%SiC (9.4 μm); (\square) A356Al-16%SiC (14.2 μm) and (\blacksquare) A356Al-20%SiC (9.6 μm). Note the wear rates for A356Al-20%SiC at 17 N are represented by two different curves.

orders of magnitude difference between the wear rates of the unreinforced A356Al and those of the composites. From Figure 25(c), the wear rates of the composites with 10 and 20% SiC can be calculated as 3.26×10^{-3} and 2.66×10^{-3} mm^3m^{-1} respectively, compared with 2.21×10^{-1} mm^3m^{-1} for that of the unreinforced alloy. At intermediate load levels, such as 17 N, both the unreinforced alloy and the alloys incorporating SiC particles exhibit similar wear behaviour (Figure 25(b)). The wear rates for all the specimens tested (0%-20% SiC) fall within a narrow range of 1.2×10^{-3} to 2.1×10^{-3} mm^3m^{-1} . It is seen that at this load there is no significant difference between the wear rates of the alloys regardless of the volume fraction and the size of SiC particles. It should be noted that at 17 N, the wear rates of the composite containing 20%SiC are represented by two different curves. About 50% of A356Al-20%SiC samples show a wear rate around 10^{-3} mm^3m^{-1} which is comparable to that of the unreinforced alloy. However, the rest show a wear rate around 10^{-4} mm^3m^{-1} as in the tests at 1 N. This dual wear behaviour for A356Al-20%SiC indicates that 17 N is within the wear transition range for 20%SiC reinforced composite. The wear transitions will be discussed in detail in section 5.1.

In summary the volumetric wear-distance curves reveal that the load dependence of the wear resistances of the unreinforced A356Al and its SiC-reinforced composites show a complex behaviour. To obtain a more complete picture of the dependence of the wear resistance to the test load, wear rate vs applied load diagrams have been constructed as described in section 4.1.2.

4.1.2. WEAR RATE REGIMES AND TRANSITIONS

The wear rates determined from the volumetric wear-distance plots such as the ones in Figure 25 can be plotted against the applied load, both on a logarithmic scale. Figure 26 shows the log wear rate vs. log load data for the A356Al-20%SiC and for the unreinforced A356Al alloy. The figure indicates that the effect of SiC particles on the wear rates varies with the applied load. With respect to the differences in the wear rates of the composite and the unreinforced alloy three different wear rate regimes can be identified. These regions marked as I, II and III on the diagram are the low, mild and severe wear regimes respectively.

(1) At low loads below 10 N (regime I), the wear rates of the SiC reinforced composite are an order of magnitude lower than those of the unreinforced alloys. EDS analysis (Figure 27) indicated that the contact surfaces of the composite specimens that exhibited low rates ($<7 \times 10^{-4} \text{ mm}^3\text{m}^{-1}$) were characterized by the formation of iron-rich layers ($[\text{Fe}/(\text{Al}+\text{Si})]>3$). The morphology of the layers deposited on the surface of composites is shown in Figure 28. The X-ray diffraction plot shown in Figure 29 reveals that the iron detached from the surface of the SAE 52100 steel slider was oxidized mainly to $\alpha\text{-Fe}_2\text{O}_3$ during the transfer process.

(2) At the 'intermediate' load levels *i.e.* 20 to 90 N (regime II) both the unreinforced and SiC reinforced alloys exhibit similar wear rates. In this regime the worn surfaces of the materials were characterized by plastic deformation (Figure 30) and damage in the form of void formation (Figure 31). The amount of iron deposited

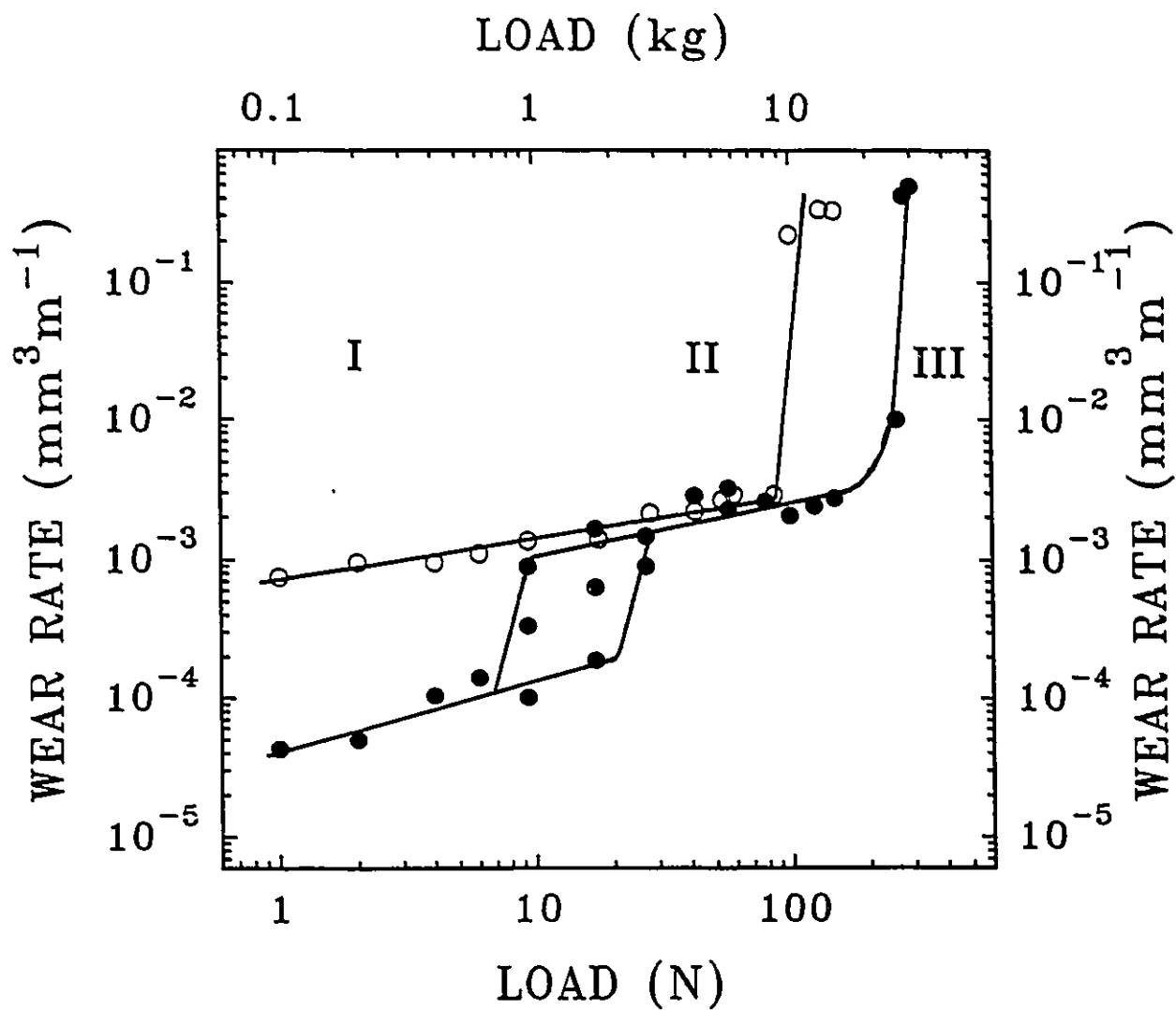


Figure 26. Wear rate vs. applied load diagram for (○) A356Al (●) A356Al-20%SiC. Counterface: SAE52100, Speed: 0.8 m/s.

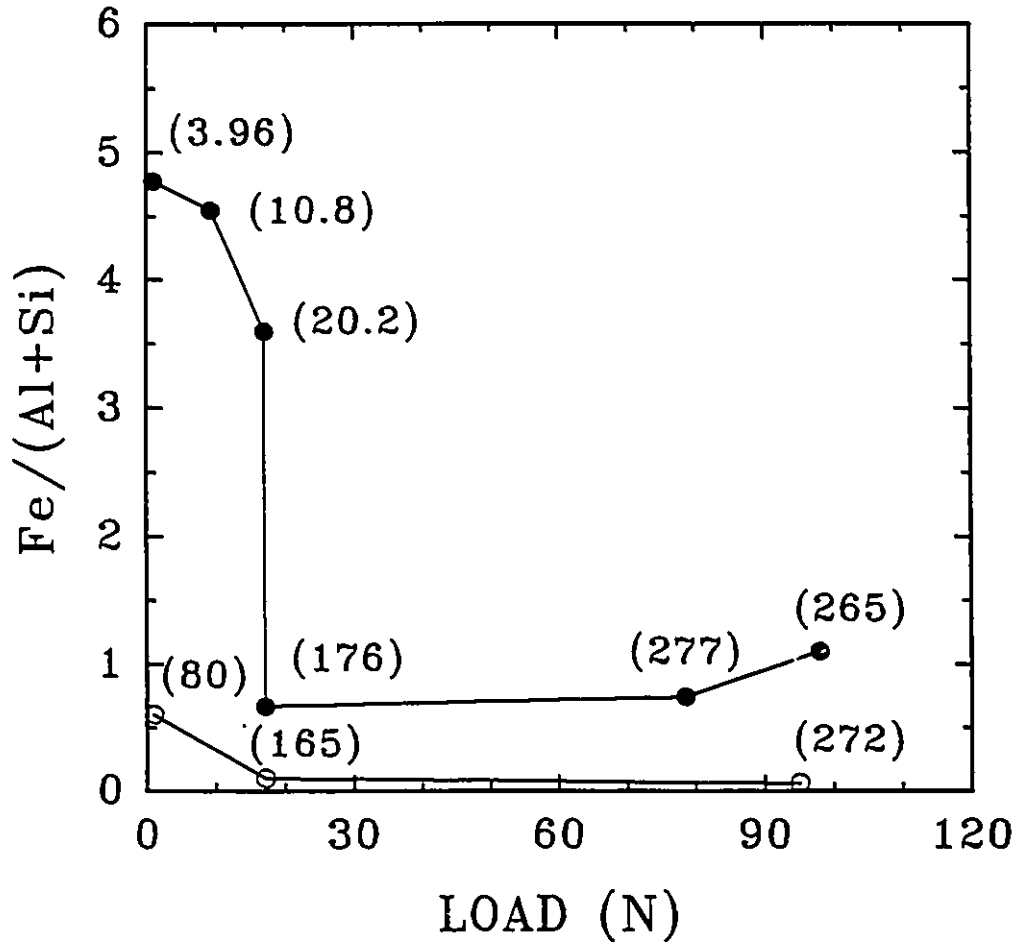


Figure 27. EDS data showing the variation of the ratio of iron to aluminium and silicon with the applied load. Each data point in this figure is the average of 2 measurements on 8-10 randomly selected areas (0.2 mm^2 each) on the worn surfaces. Numbers in parentheses indicate the wear rates ($\times 10^{-5} \text{ mm}^3 \text{ m}^{-1}$). (O) A356Al; (●) A356Al-20%SiC.

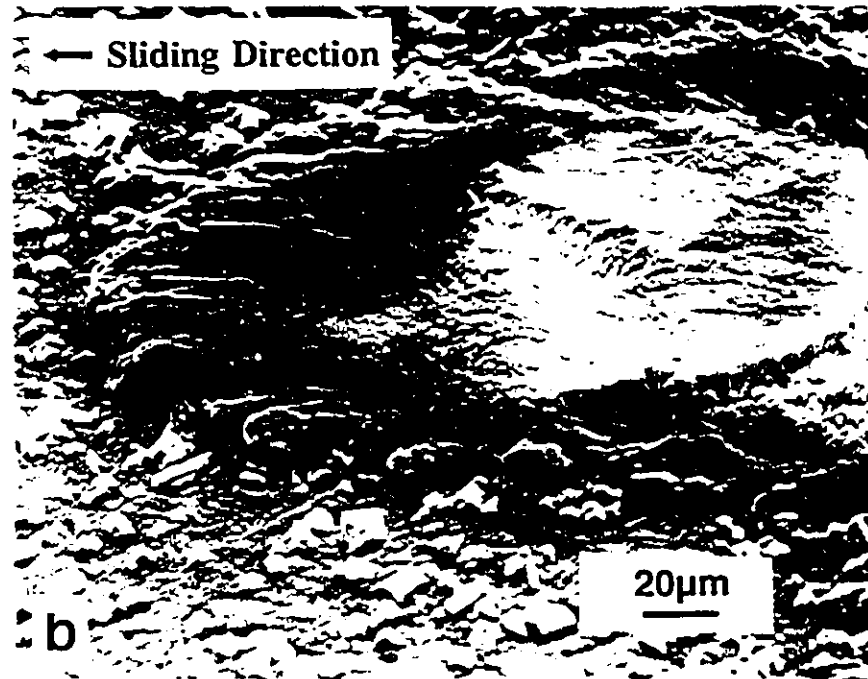
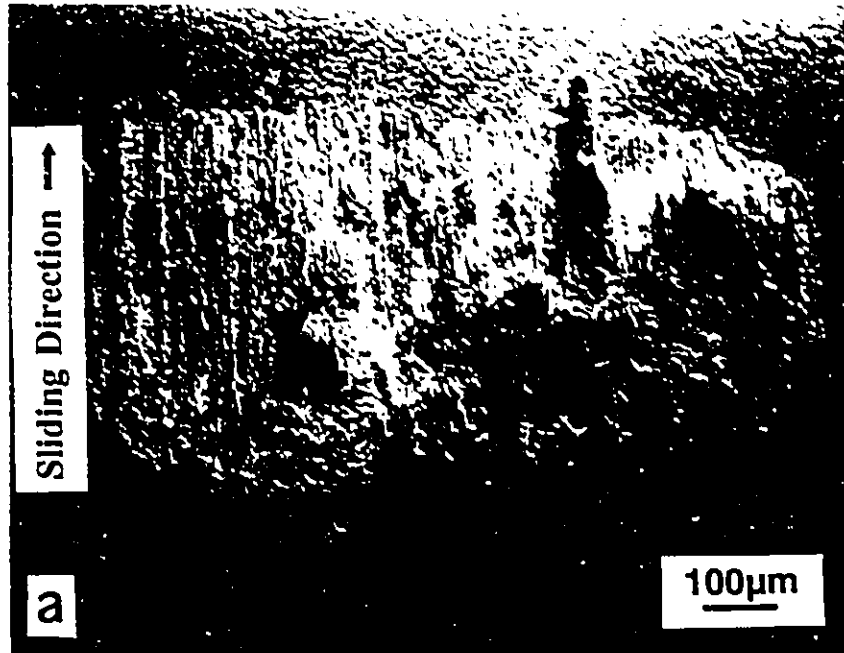


Figure 28. Scanning electron micrograph showing (a) the overall view of the wear scar and (b) details of an iron-rich transfer layer deposited onto the surface of A356Al-20%SiC in regime I.

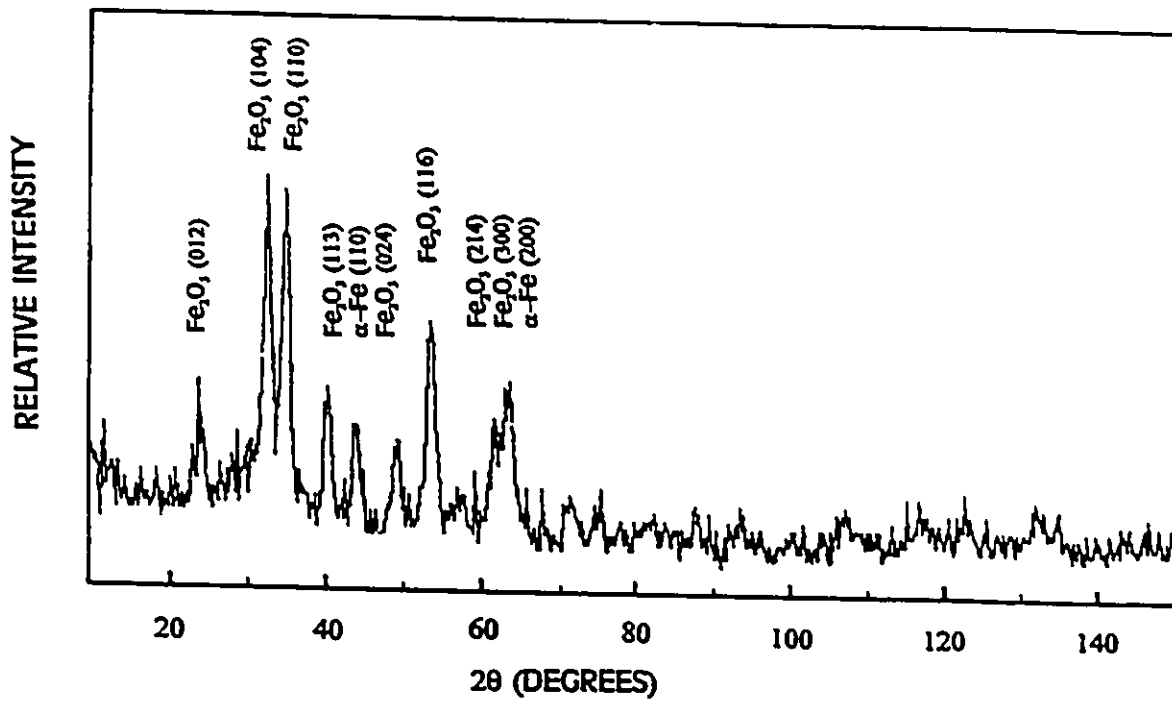


Figure 29. X-ray diffraction analysis of the loose debris of A356Al-20%SiC worn against SAE 52100 bearing steel in regime I. (Using Cu-K α).

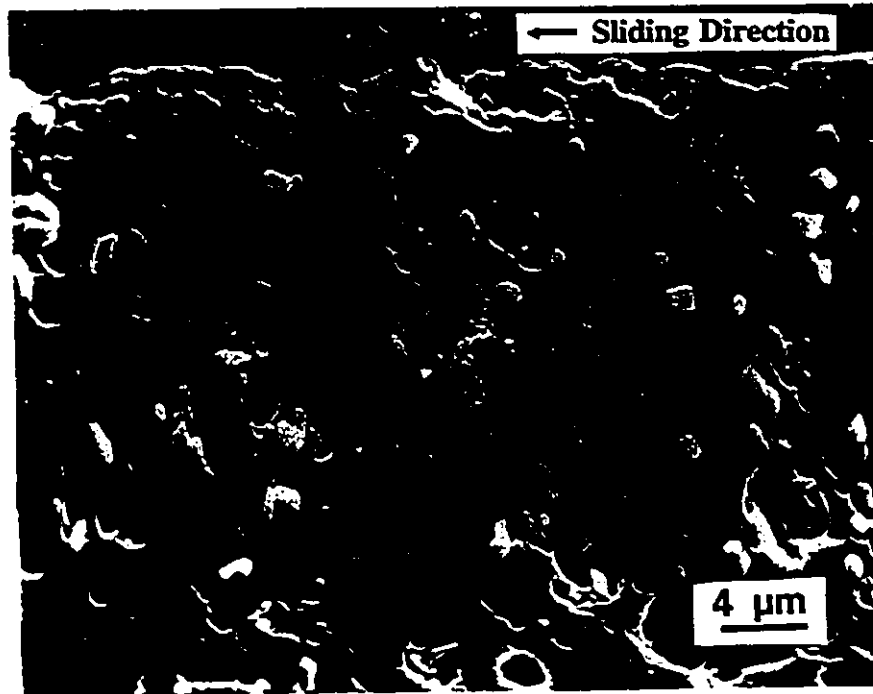


Figure 30. Deformation microstructure of unreinforced A356Al below the worn surface; load=20 N; sliding distance 1000 m. Note the grains elongated in the sliding direction and the particles are Si particles with average size of 1.8 μm. (etched with Keller's reagent).

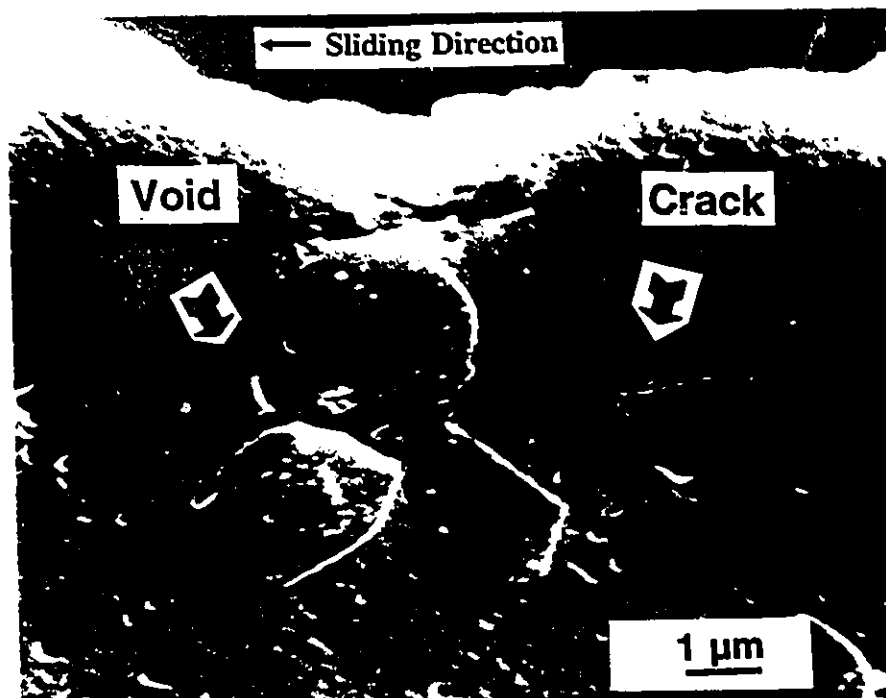


Figure 31. Void and crack nucleation around the silicon particles under the contact surface of A356Al.

on the surface was very small (Figure 27). It was observed that SiC particles on the surfaces were fractured during the wear. Observations made on the longitudinal cross-sections perpendicular to worn surfaces indicated the existence of subsurface cracks that appeared to have propagated along the SiC/aluminum matrix interfaces. On the other hand, in the unreinforced alloys subsurface crack nucleation was found to be associated with silicon particles. A subsurface crack propagating parallel to the contact surface in an A356Al alloy is shown in Figure 32. The surface morphologies of A356Al and A356Al-20%SiC were similar (Figure 33) indicating that possibly a common wear mechanism *i.e.* subsurface delamination prevailed in both unreinforced and reinforced alloys in this wear regime.

A dual wear behaviour has been observed in the load range of 10-30 N, which is between regime I and II, for A356Al-20%SiC (also for other A356Al-SiC composites). When the applied load falls within this region, some composite samples showed wear rates around $10^{-3} \text{ mm}^3\text{m}^{-1}$ and others around $10^{-4} \text{ mm}^3\text{m}^{-1}$ (and some ranging between these two extremes). In contrast to this behaviour in the composites, none of the unreinforced A356Al specimens exhibited wear rates lower than $10^{-3} \text{ mm}^3\text{m}^{-1}$ although they were tested under identical conditions. Thus the dual wear behaviour in the transition region is associated with the presence of SiC particles, and could be due to the non-uniform distribution of the particles on the contact surfaces (*i.e.* a sample with higher local SiC concentration on the surface would be more abrasive to the steel counterface and once the iron oxide layers were established on the contact surfaces it would continue to show very low wear rates). However if the local area fraction of SiC

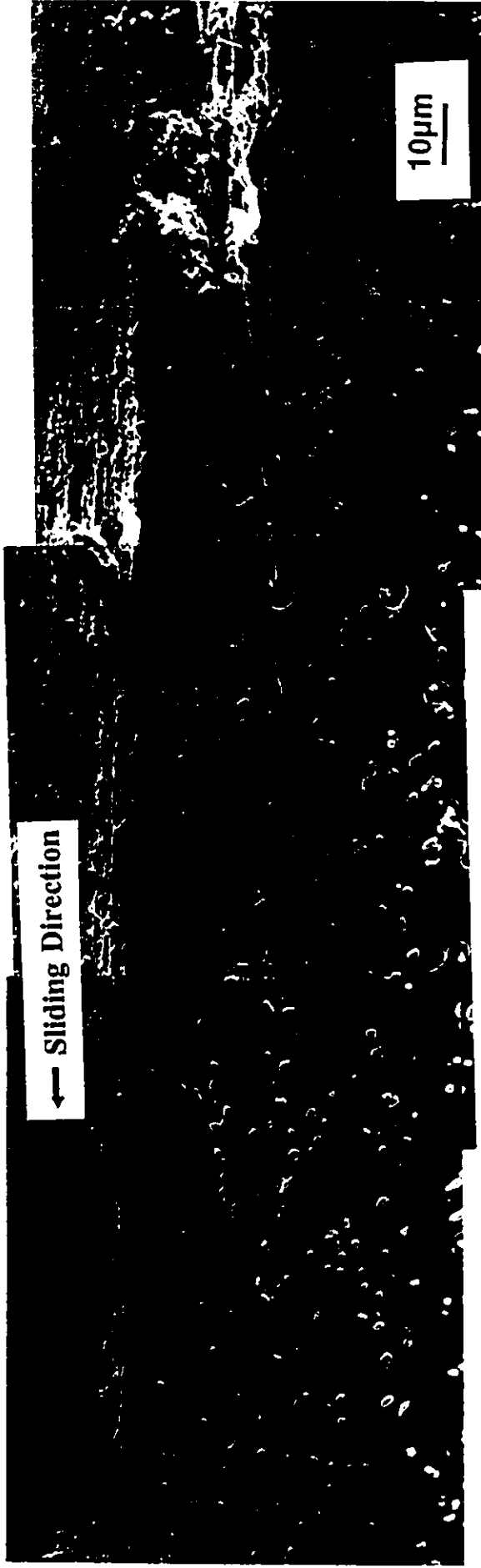


Figure 32. Subsurface crack propagation of unreinforced A356Al, load=17 N, (etched with Keller's reagent). Note the particles are Si particles with average size of 1.8 μm .

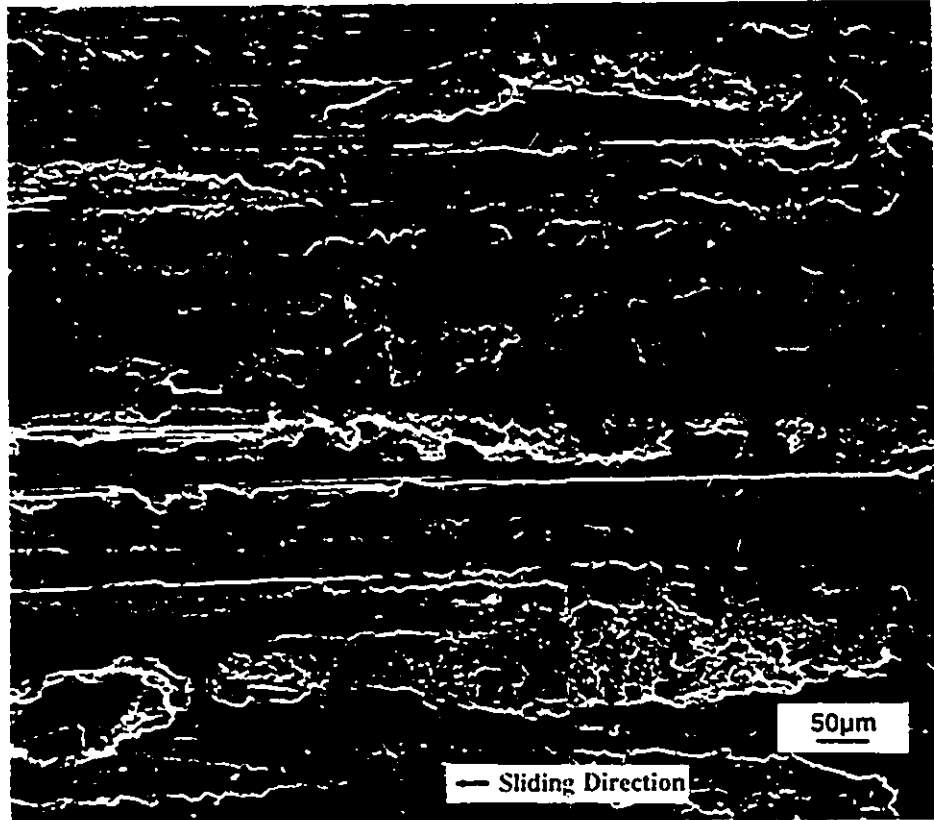


Figure 33. Worn surface morphology of A356Al-20%SiC tested at 27 N. This is a typical morphology for the composites and the unreinforced alloys in regime II.

is low, the particles on the contact surface would be more likely to fracture. Strains transmitted to the matrix would activate subsurface damage accumulation events leading to higher wear rates. Because of this statistical nature of the wear process the transition does not occur at a single load. But there exists a range of loads, where composite materials show characteristics of either regime I or regime II.

(3) The transition to severe wear takes place at 95 N where the wear rates increase abruptly from $3.2 \times 10^{-3} \text{ mm}^3\text{m}^{-1}$ to $2 \times 10^{-1} \text{ mm}^3\text{m}^{-1}$. This transition marks the onset of the severe wear regime for the matrix alloy (regime III in Figure 26). Typical features of the worn surfaces of unreinforced A356Al are shown in Figure 34. The transition to severe wear is delayed to a higher load of 250 N in the A356Al-20% SiC.

In order to give a more quantitative description of the wear resistance, regression analyses were performed. In each of the regimes identified in Figure 26 it is found that the wear rates \dot{W} obey a power law expression of the form:

$$\dot{W} = K (P)^n \quad (4.1)$$

where P is the applied load, K is the wear constant and n is defined as the wear exponent. The application of this equation in regime III requires some caution because in this regime wear rates are affected by the friction-induced temperature increase. The numerical values of the constants K and n in the above equation are given in Table III. Note that this empirical expression is in accord with the basic form of Archard's Law ^[24, 42] except that in the original Archard's equation, the exponent n is given as unity.

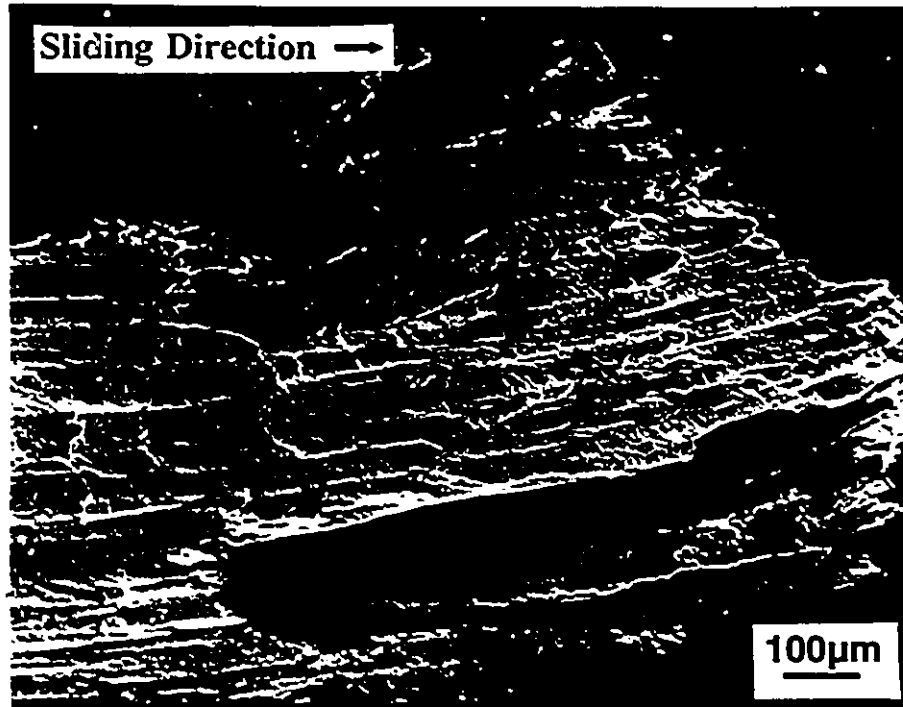


Figure 34. Worn surface morphology of unreinforced A356Al tested at 147 N. (regime III).

Table III. Coefficients for Wear Equations $\dot{W}=k \cdot P^n$

Material	Regime I	Regime II	Regime III
Counterface 52100 steel			
6061Al	---	$6.7 \times 10^{-4} P^{0.5}$	$2.8 \times 10^{-10} P^{4.2}$
6061Al-10%Al ₂ O ₃	$5.4 \times 10^{-6} P^{0.8}$	$3.7 \times 10^{-4} P^{0.5}$	$3.8 \times 10^{-15} P^{6.0}$
6061Al-20%Al ₂ O ₃	$6.2 \times 10^{-6} P^{0.6}$	$1.1 \times 10^{-4} P^{0.5}$	$2.3 \times 10^{-9} P^{3.1}$
2014	---	$2.3 \times 10^{-4} P^{0.4}$	$1.3 \times 10^{-15} P^{6.2}$
2124Al-20%SiC (2.4 μm)	$7.9 \times 10^{-5} P^{0.8}$	$1.2 \times 10^{-4} P^{0.6}$	$7.9 \times 10^{-27} P^{10.7}$
2024Al-20%SiC (15.8 μm)	$6.5 \times 10^{-6} P^{0.9}$	$2.1 \times 10^{-4} P^{0.4}$	$2.0 \times 10^{-26} P^{10.2}$
A356Al	---	$7.1 \times 10^{-4} P^{0.5}$	$4.3 \times 10^{-18} P^{6.8}$
A356Al-20%SiC	$3.6 \times 10^{-5} P^{0.6}$	$4.4 \times 10^{-4} P^{0.5}$	$8.6 \times 10^{-18} P^{6.6}$
Counterface Mullite (3Al ₂ O ₃ ·2SiO ₂)			
6061Al	---	$1.3 \times 10^{-3} P^{0.4}$	$2.4 \times 10^{-9} P^{4.3}$
6061Al-20%Al ₂ O ₃	$4.8 \times 10^{-5} P^{1.2}$	$1.4 \times 10^{-3} P^{0.6}$	$1.3 \times 10^{-12} P^{5.4}$

*Units of \dot{W} and P are mm³m⁻¹ and N, respectively.

4.1.3. WEAR DEBRIS

(1) In regime I, the debris particles had a distinct reddish brown colour and were in the form of very fine powder to the naked eye. The results of X-ray diffraction analyses (Figure 29) revealed that this debris mainly consisted of a mixture of elemental iron and iron oxides (mainly α -Fe₂O₃).

(2) X-ray diffraction results of the debris generated in regime I are given in Figure 35 and 36 respectively for A356Al and A356Al-20%SiC. Both figures indicate the presence of Al and Si in the debris. There is no evidence for material transfer from the counterface. Scanning electron microscopy (SEM) of the wear debris collected from regime II revealed that in fact two type of debris were formed from the surface of the unreinforced A356Al and the A356Al-20%SiC. These were: (i) the "black debris" which had a dark colour to the naked eye, and readily charged by the electrons under the electron beam in the SEM. This type of debris had an irregular shape and a size of about 1 μ m. (ii) The other debris type observed was the "white debris". The particles making up this type of debris were shiny, bright metallic, and did not charge when examined by the SEM. The debris comprised of large platelike flakes and chips-about 10 to 200 μ m in thickness. The percentage of plate-like particles in the loose debris increased with the applied load.

(3) Debris particles produced in the severe wear regime (regime III) were in the form of thick plates (200-500 μ m) and usually flakes of metallic appearance. These particles appeared to have been generated by the breaking off of the extruded material at the exit side of the wear surface and consisted of specimen materials (Al, Si, and

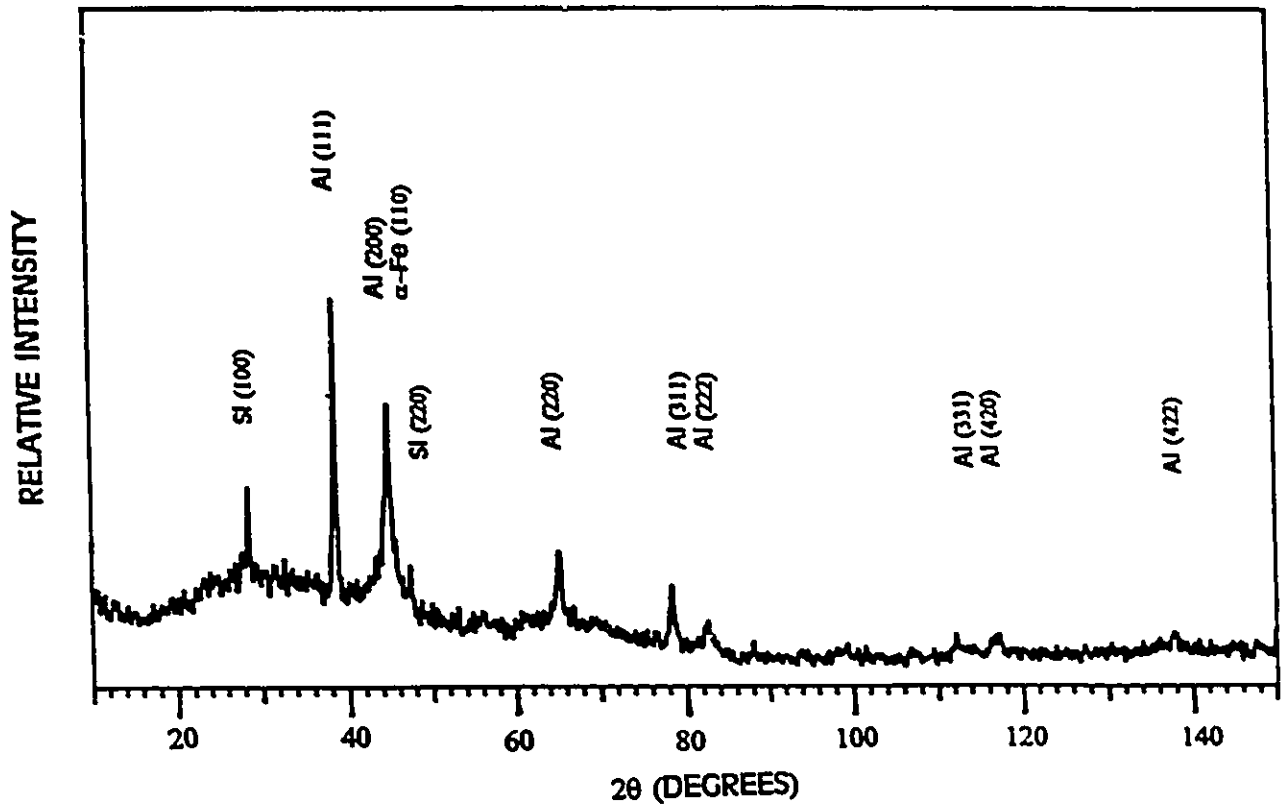


Figure 35. X-ray diffraction analysis of the loose debris of A356Al worn against SAE 52100 bearing steel in regime II. (using Cu-K α).

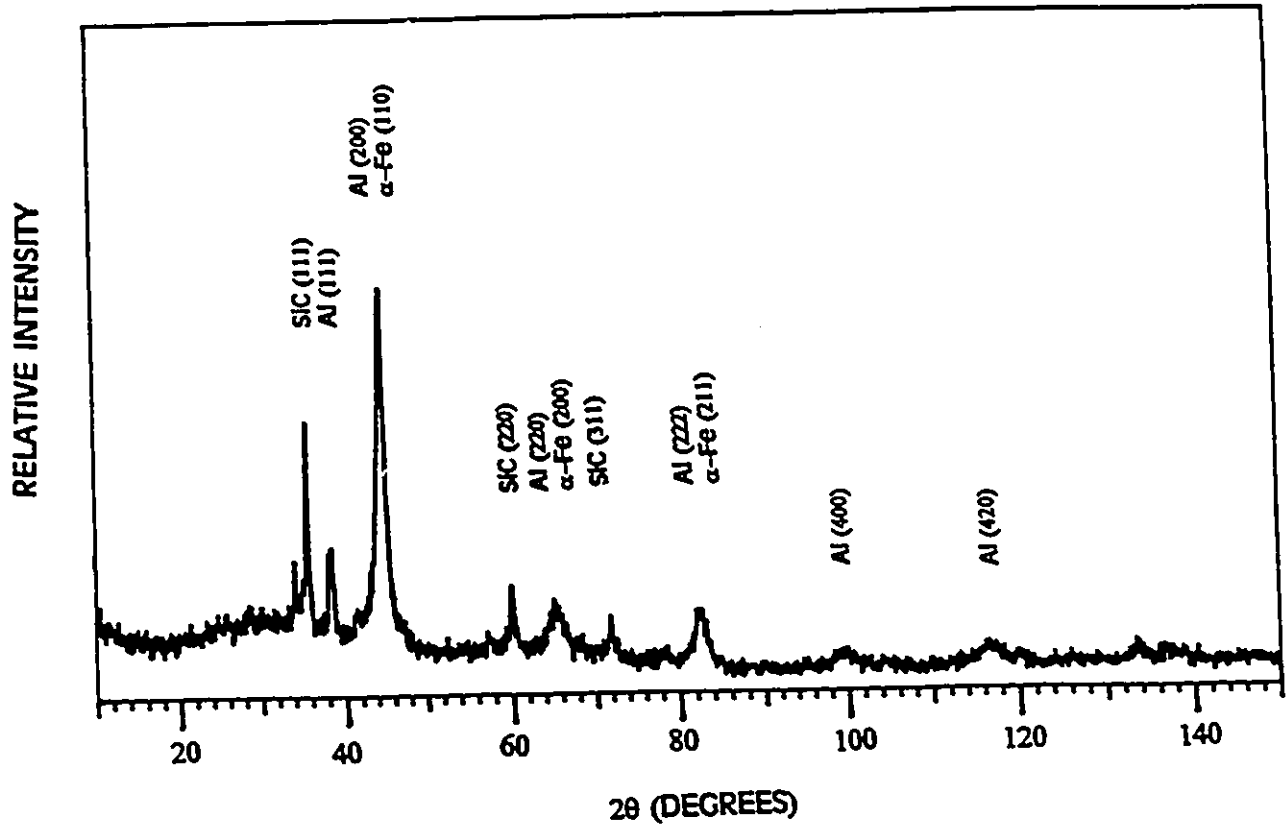


Figure 36. X-ray diffraction analysis of the loose debris of A356Al-20%SiC worn against SAE 52100 bearing steel in regime II. (using Cu-K α).

SiC).

4.1.4. BULK TEMPERATURE-SLIDING DISTANCE DIAGRAMS

When two surfaces slide together, most of the work done against friction is transformed into heat. The frictional heat generated at the mating interface may modify the mechanical and metallurgical properties of the sliding surfaces, and may cause events such as oxidization, plastic deformation or even melting of the surfaces. Thermal effects relating to the sliding surfaces are either due to changes in the bulk temperature (or average contact surface temperature), or the flash temperature at contacting asperities. The bulk temperature can be measured directly during the wear test by inserting a thermocouple to a subsurface region near to the contact surface.

The average contact (bulk) surface temperature distribution curves in the material close to the contact surfaces, *i.e.*, within 0-100 μm depth, for the unreinforced A356Al alloy and the A356Al-20%SiC at different loads are given in Figures 37(a) and 37(b) respectively. The results reveal that at a constant applied load and sliding velocity, the surface bulk temperature initially increases with the sliding distance (*i.e.* sliding time) and then stabilizes at a constant value unless a transition to another wear regime takes place at this particular load. For the unreinforced A356Al alloy, it is observed that the transition from regime II to III occurred whenever the surface temperature reached 418 K (145 °C). The transition temperature was reproducible within ± 10 K and corresponded to $T/T_m=0.45$ (where $T_m=888$ K is the melting temperature of the A356 Al ^[136]). The transition temperature in the A356Al-20%SiC was higher than that of

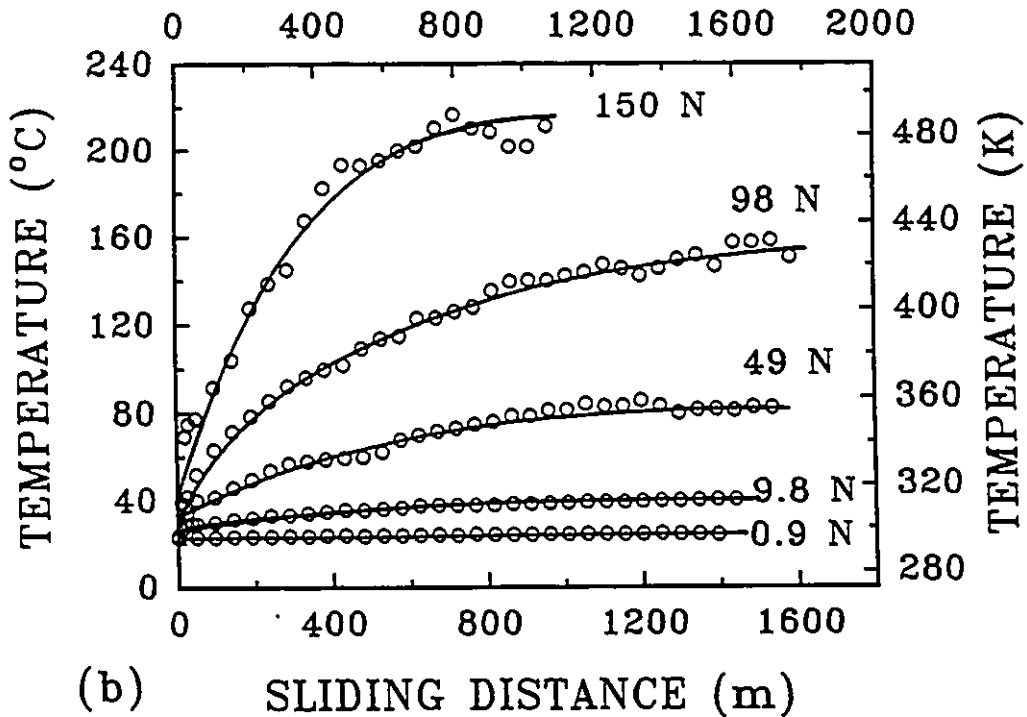
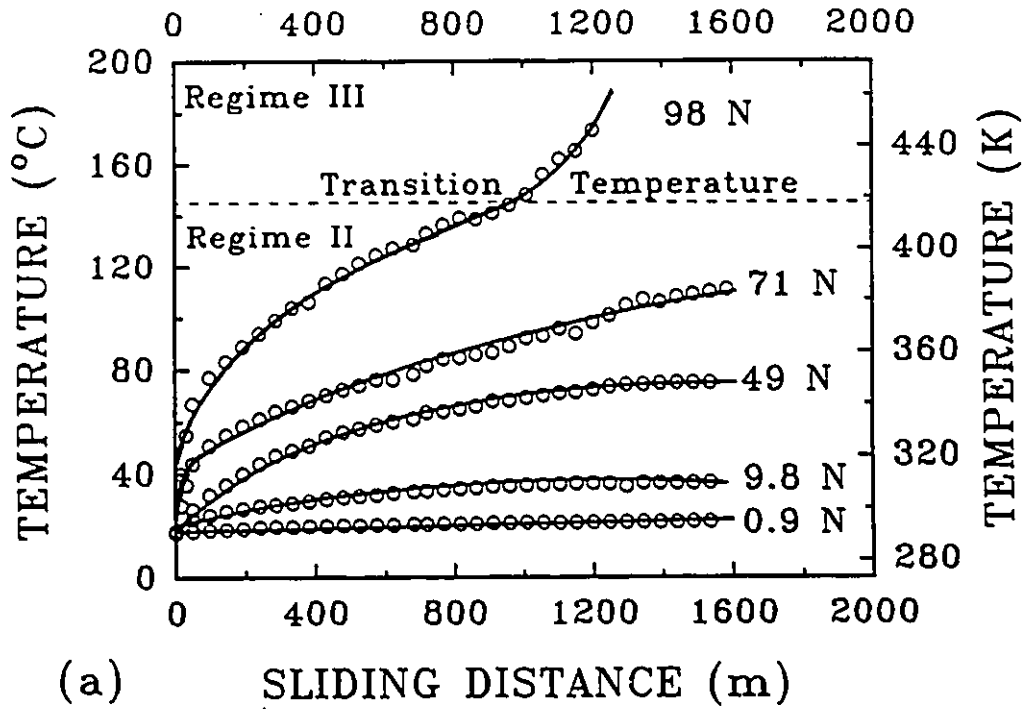


Figure 37. The temperature distribution at the contact surface of (a) A356Al and (b) A356Al-20%SiC as a function of sliding distance.

unreinforced alloy (no transition has been found below 480 K for this material).

4.2. EXPERIMENTAL RESULTS ON Al-Mg-Si (6061) ALUMINUM ALLOY REINFORCED WITH Al_2O_3 PARTICLES

4.2.1. VOLUMETRIC WEAR-SLIDING DISTANCE DIAGRAMS

At several different loads between 1-450 N, the weight losses from the surfaces of the unreinforced 6061Al alloy and the Al_2O_3 particle reinforced composites were determined as a function of sliding distance. The measured weight losses were then converted to volume losses by dividing them by their densities. Figures 38(a)-(d) show the relationship between the volumetric wear and sliding distance for the unreinforced 6061Al and the 6061Al-20% Al_2O_3 composites tested under a load of 1, 17, 52 and 98 N respectively (sliding speed: 0.8 m/s). As shown in these figures, similar to A356Al based composites, a linear relationship was observed between the volume loss and the sliding distance. Several aspects of the volumetric wear-sliding distance curves deserve attention: As shown in Figure 38(a), at the lowest load (1 N), the wear rate of the 6061Al-20% Al_2O_3 ($9.7 \times 10^{-6} \text{ mm}^3\text{m}^{-1}$) is two orders of magnitude lower than that of the unreinforced 6061Al ($9.8 \times 10^{-4} \text{ mm}^3\text{m}^{-1}$). At 98 N (Figure 38(d)), there exists more than one order of magnitude difference between the wear rates of the unreinforced 6061Al ($9.5 \times 10^{-2} \text{ mm}^3\text{m}^{-1}$) and that of the 6061Al-20% Al_2O_3 ($5.9 \times 10^{-3} \text{ mm}^3\text{m}^{-1}$). However, at the intermediate load levels, such as 52 N (Figure 38(c)) no significant difference between the wear resistance of the unreinforced 6061Al ($4.8 \times 10^{-3} \text{ mm}^3\text{m}^{-1}$) and the Al_2O_3 -reinforced alloy ($3.6 \times 10^{-3} \text{ mm}^3\text{m}^{-1}$) could be observed. Between the different wear

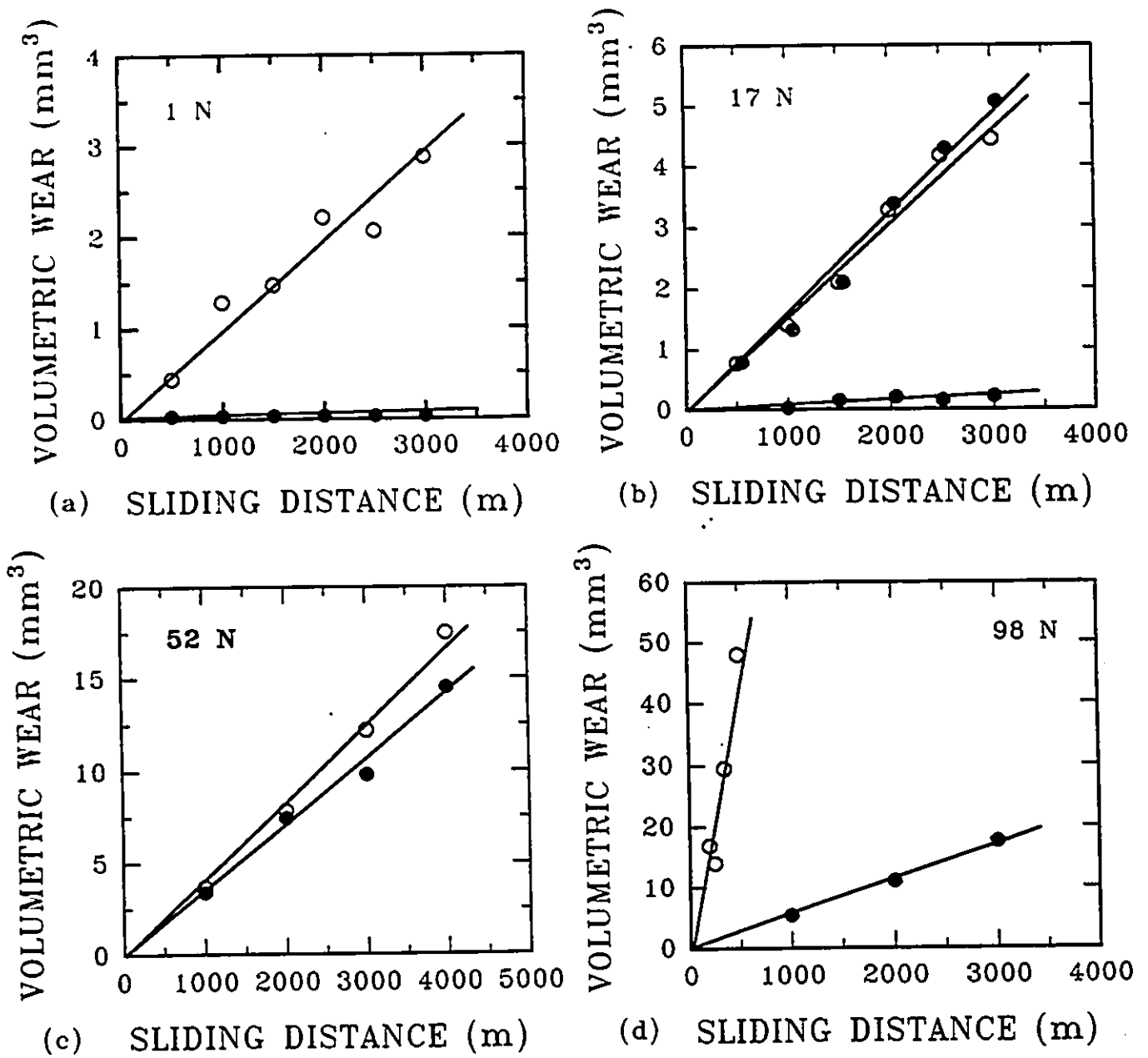


Figure 38. Graphs of volume loss vs. sliding distance curves for (\circ) 6061Al and (\bullet) 6061Al-20%Al₂O₃ at different load levels.

behaviours exemplified in Figure 38 there is also a load range where the composite shows a “dual” wear resistance behaviour. For example, at 17 N (Figure 38(b)) about 50% of the 6061Al-20%Al₂O₃ specimens exhibited wear rates comparable to that of the unreinforced alloy ($1.6 \times 10^{-3} \text{ mm}^3\text{m}^{-1}$). However, the other half of the composite specimens indicated low wear rates ($9.7 \times 10^{-5} \text{ mm}^3\text{m}^{-1}$) as depicted by the lower curve in Figure 38(b). When compared to the results in section 4.1, it becomes clear that wear rates of Al₂O₃ reinforced 6061Al and SiC reinforced A356Al show a very similar load dependence.

4.2.2. WEAR RATE REGIMES AND TRANSITIONS

The wear rates of the 6061Al-20%Al₂O₃ composites and the unreinforced 6061Al are plotted against the applied load on a double logarithmic scale in Figure 39. The figure again reveals the presence of three distinct wear rate regimes for the particulate reinforced materials.

In regime I, which covers the lower end of the applied load range, the wear rates of the composite are lower than $2 \times 10^{-5} \text{ mm}^3\text{m}^{-1}$, which is about two orders of magnitude lower than those of the unreinforced alloys (e.g. $3.6 \times 10^{-6} \text{ mm}^3\text{m}^{-1}$ at 1 N, $1.7 \times 10^{-5} \text{ mm}^3\text{m}^{-1}$ at 10 N). In regime II which extends from approximately 10 N to 230 N the wear rates increase steadily (from about $10^{-3} \text{ mm}^3\text{m}^{-1}$ at 20 N, $6.8 \times 10^{-3} \text{ mm}^3\text{m}^{-1}$ at 185 N). This regime ends with an abrupt increase in the wear rates at loads above 230 N which marks the onset of regime III. In this severe wear regime the wear rates can reach to values as high as $10^{-1} \text{ mm}^3\text{m}^{-1}$. The wear in this regime can be described as

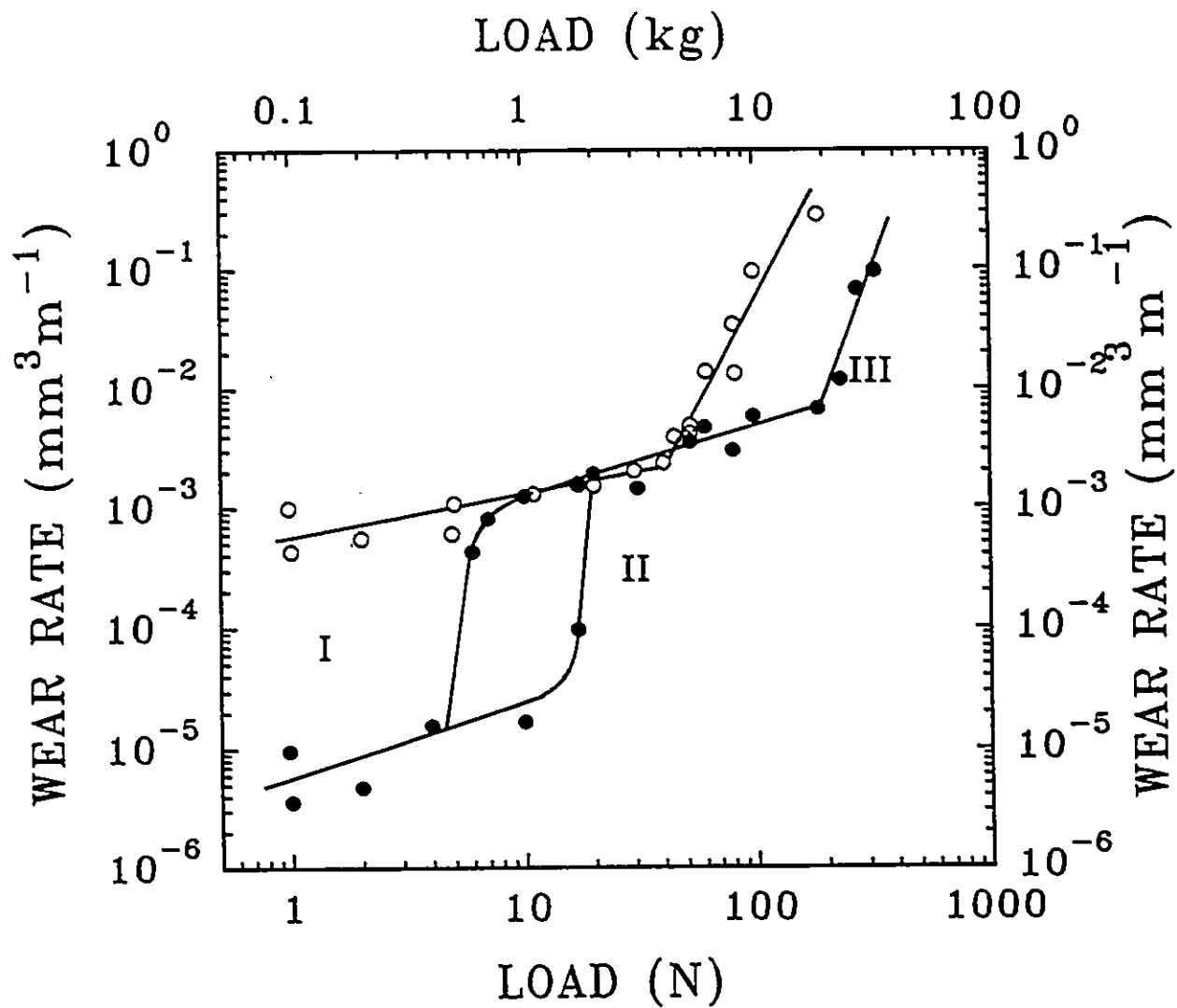


Figure 39. Wear rate vs. applied load diagram for (○) 6061Al and (●) 6061Al-20%Al₂O₃.

catastrophic since the whole test piece can be consumed within the first few minutes of wear (at 322 N which is the highest test load used, $\dot{W}=9.6 \times 10^{-2} \text{ mm}^3\text{m}^{-1}$).

Regression analyses performed using equation 4.1 in each of the regimes identified in figure 39 again showed that the wear rates \dot{W} obey a power law expression. The numerical values of the constants K and n are given in Table III.

The transition from regime II to severe wear appears to have happened at a well-defined load. It is however important to emphasize that towards the high load end of regime II, some specimens showed a sliding distance dependent wear transition. An example of the transition to severe wear in the 6061Al-20%Al₂O₃ is shown in Figure 40. In this case (150 N) the wear transition to regime III occurred at 1300 m. These sliding distance-dependent transitions took place whenever the temperature at the contact surfaces reached a critical value. This will be considered in detail in section 5.2.1.

4.2.3. COMPARISON OF THE WEAR RATE OF 6061Al-20%Al₂O₃ WITH THE UNREINFORCED 6061Al

Figure 39 shows the wear rate against load plot for the unreinforced 6061Al. This curve is different from the wear rate-load curve for the Al₂O₃-reinforced 6061Al in two main respects: (i) the wear rate-load curve of the unreinforced 6061Al is marked by the absence of the low wear rate regime I, so that regime II extends down to the smallest test load used ($\dot{w}=4.2 \times 10^{-4} \text{ mm}^3\text{m}^{-1}$ at 1 N); (ii) the transition from mild wear regime II to severe wear (regime III) occurs at 60 N, *i.e.* at a load level considerably lower than that observed for the 6061Al-20%Al₂O₃ (230 N).

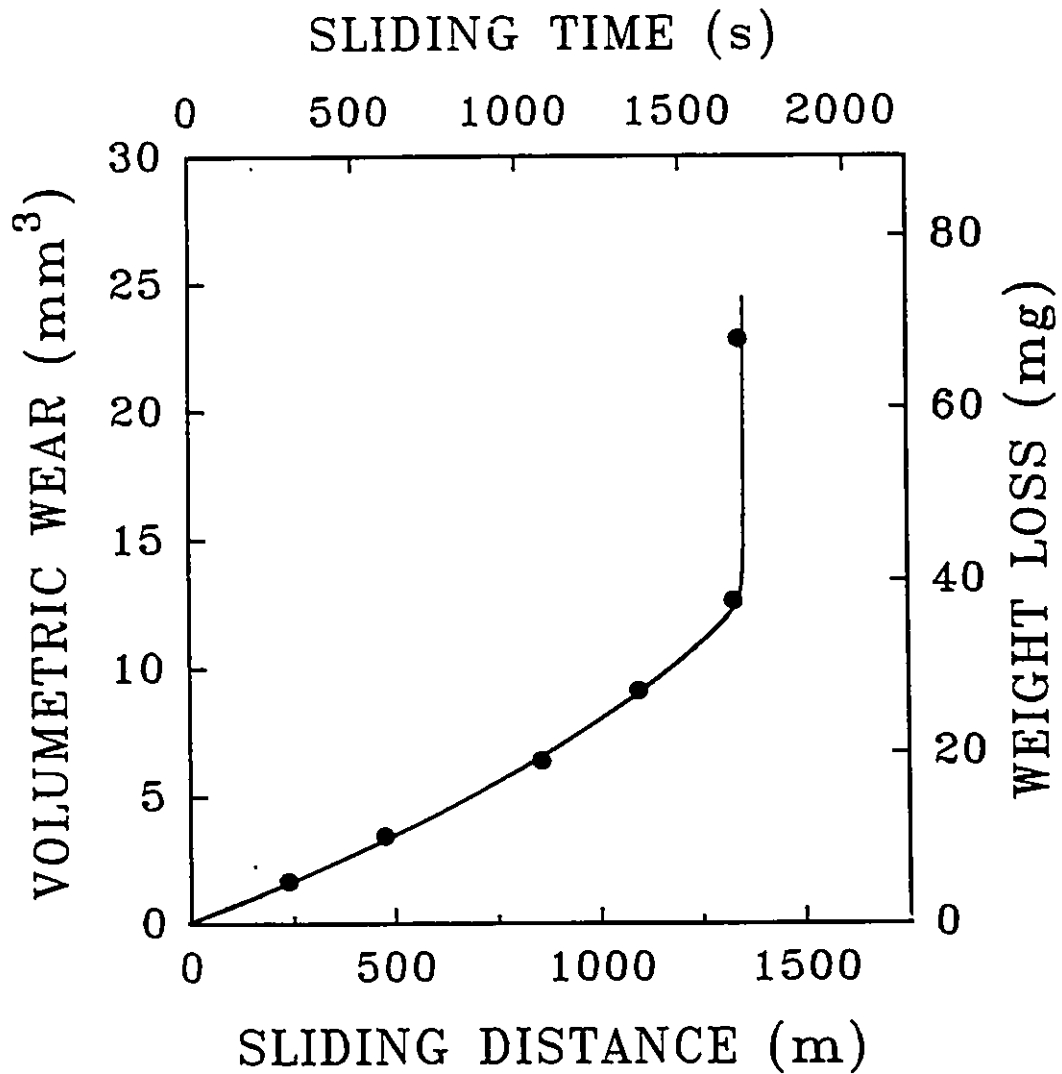


Figure 40. Wear-sliding distance curve of 6061Al-20%Al₂O₃ at 150 N which shows sliding distance dependent transition from mild wear (region II) to severe wear (region III).

Therefore, it can be concluded that the Al_2O_3 reinforcement serves to delay the transition to severe wear rate regime and also improves the wear resistance of the aluminum alloy at low loads by almost two orders of magnitude. However, at the intermediate load levels (where the regime II of the 6061Al and that of the composite coincide) it is not beneficial to incorporate Al_2O_3 particles in the base alloy since there is not any significant difference between the wear rates of the unreinforced and Al_2O_3 -reinforced 6061Al alloy (Figure 39).

4.2.4. WEAR OF STEEL COUNTERFACE AGAINST 6061Al-20% Al_2O_3

The wear of the SAE 52100 bearing steel counterface is shown in Figure 41. The wear rate of the bearing steel increases first with the applied load. At a given load, the wear rate of the counterface is higher when it is rubbed against Al_2O_3 reinforced alloy than when rubbed against the unreinforced 6061Al. In the case of rubbing against the composite, the steady increase in the wear rates of the counterface arrests at about 230 N and this is eventually followed by a net weight gain at the loads corresponding to the regime III for the composite. This is the result of aluminum transfer from the surface of specimens to the steel slider in the severe wear rate regime. Similarly, in the case of rubbing against the unreinforced 6061Al, the counterface starts to gain weight at loads above 60 N which is the transition load to regime III for the unreinforced alloy.

4.2.5. METALLOGRAPHY OF WORN SURFACES AND WEAR DEBRIS

Typical, low magnification micrographs of the worn 6061Al-20% Al_2O_3 ,

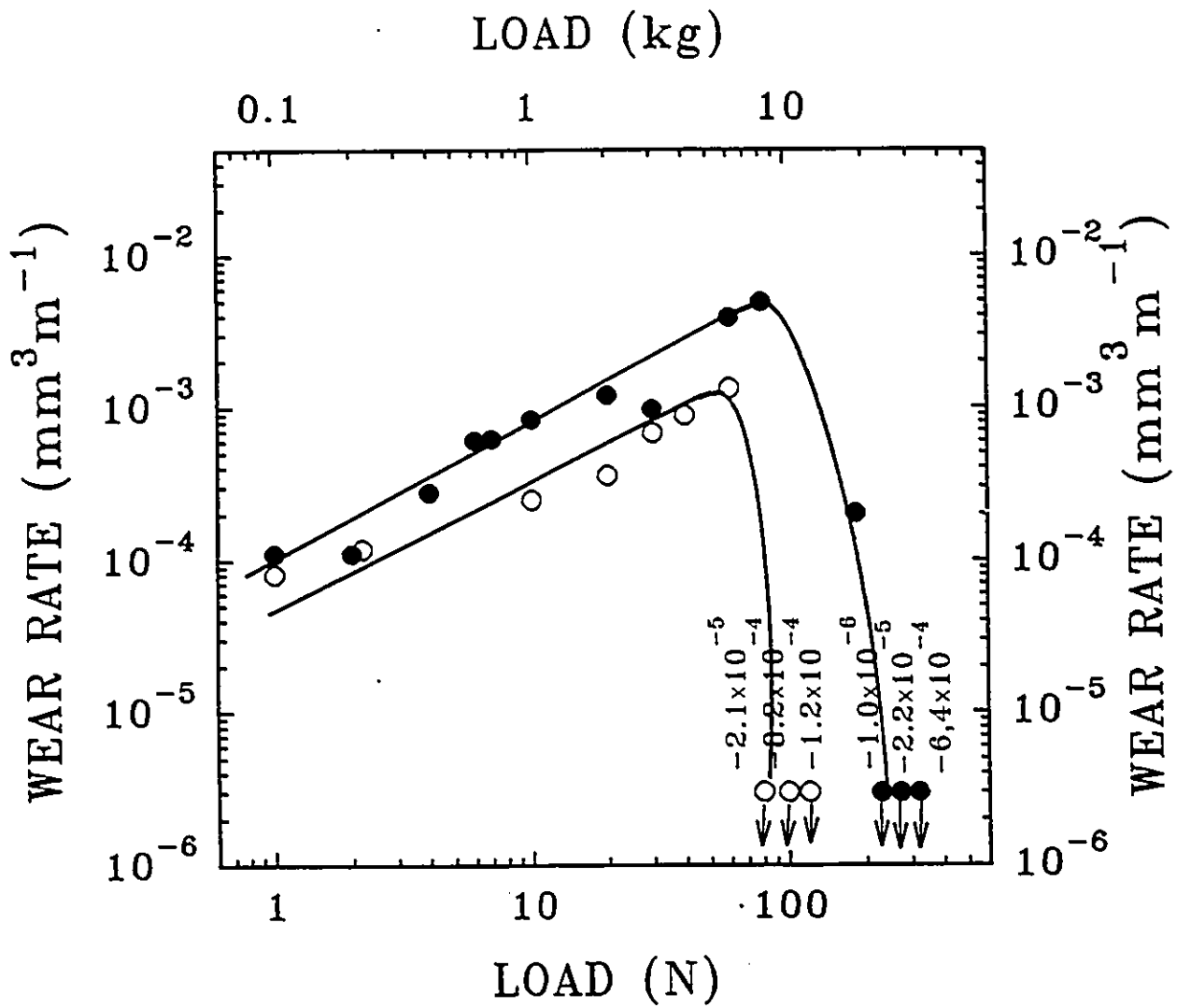


Figure 41. Wear rate vs. applied load diagram for the SAE52100 bearing steel counterface. (○) rubbed against 6061Al; (●) rubbed against 6061Al-20%Al₂O₃.

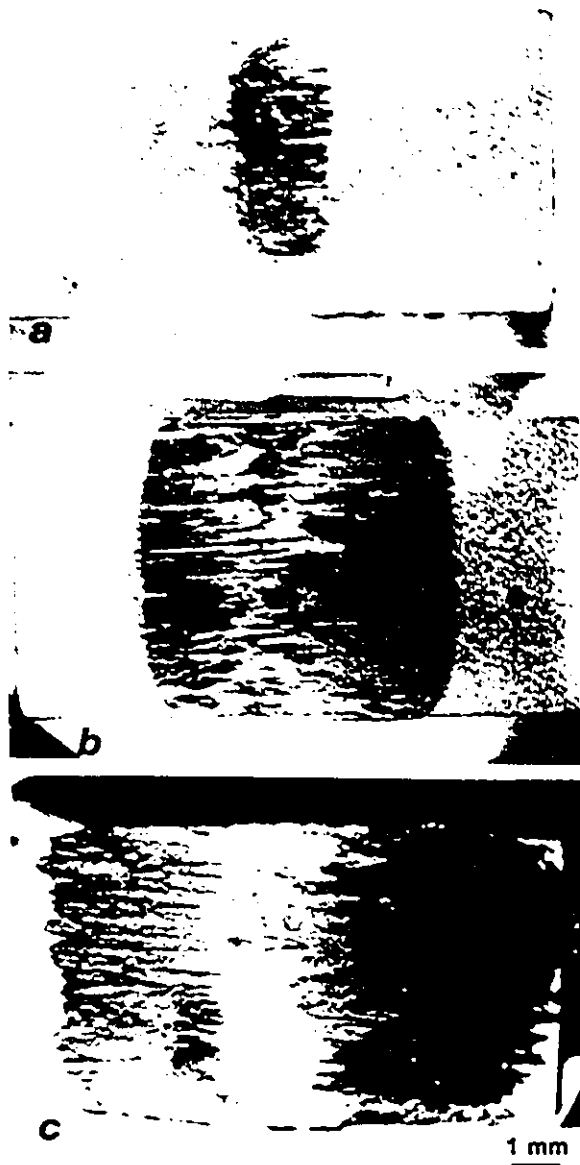


Figure 42. Surface morphologies of 6061Al-20%Al₂O₃ specimens worn at different rates representing: (a) Regime I: load=1 N, sliding distance=1000 m; (b) Regime II: load=20 N, sliding distance=1000 m; (c) Regime III: load=210 N, sliding distance=110 m.

specimens representing each of the three wear rate regimes (Figure 39) are shown in Figure 42. The scale of wear damage was the least severe in regime I as expected (Figure 42(a)). A two-order of magnitude increase in wear rates was accompanied by a higher degree of damage in regime II (Figure 42(b)). The specimen representative of regime III (Figure 42(c)) exhibited extensive plastic deformation and damage that covered the whole test surface within a very short sliding distance. These figures also reveal some other features of wear in each of these regimes. For instance, in the regime I the worn surfaces were mostly dull in appearance which is an indication of the formation of transfer layers on the contact surfaces. The severe wear in regime III produced shiny and metallic looking wear surfaces.

The wear debris produced during the wear tests was examined visually, and also by the SEM and the X-ray diffraction analyses, and found to be different in colour, size and composition depending on the wear mechanism which is responsible for its formation. In the 6061Al-Al₂O₃ (as in the A356Al-SiC composites), three types of wear debris are observed. These are described below:

(1) In the regime I, a mixture of reddish-brown, fine-powdery debris was collected. EDS analysis (Figure 43) indicated that the contact surfaces of the composite specimens in this regime were characterized by the formation of iron-rich layers. The typical morphology of the layers deposited on the contact surfaces of composites is shown in Figure 44. X-ray diffractometry (Figure 45) revealed that the iron-detached from the surface of the SAE 52100 steel slider was oxidized mainly to α -Fe₂O₃ during the transfer process. The debris also contained elemental Fe particles but no obvious

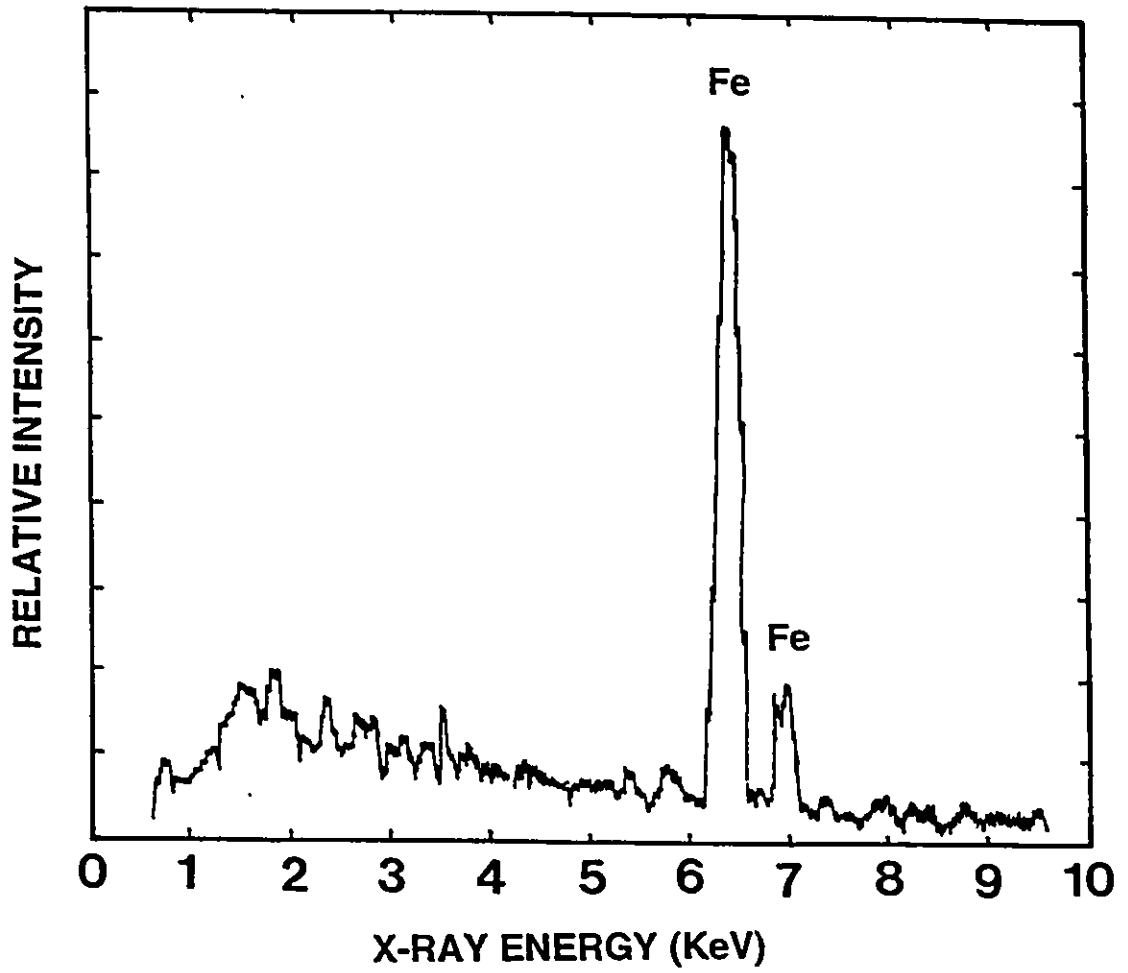


Figure 43. EDS analysis of the 6061Al-20%Al₂O₃ worn surface revealing that the transfer layers on the contact surface are iron-rich. (Counterbody: SAE52100 steel).



Figure 44. Scanning electron micrograph of the contact surface of the composite (load=3 N). The contact surface is covered by iron-rich transfer layers. The Al_2O_3 particles ahead of the wear front form protrusions on the unworn surface (regime I).

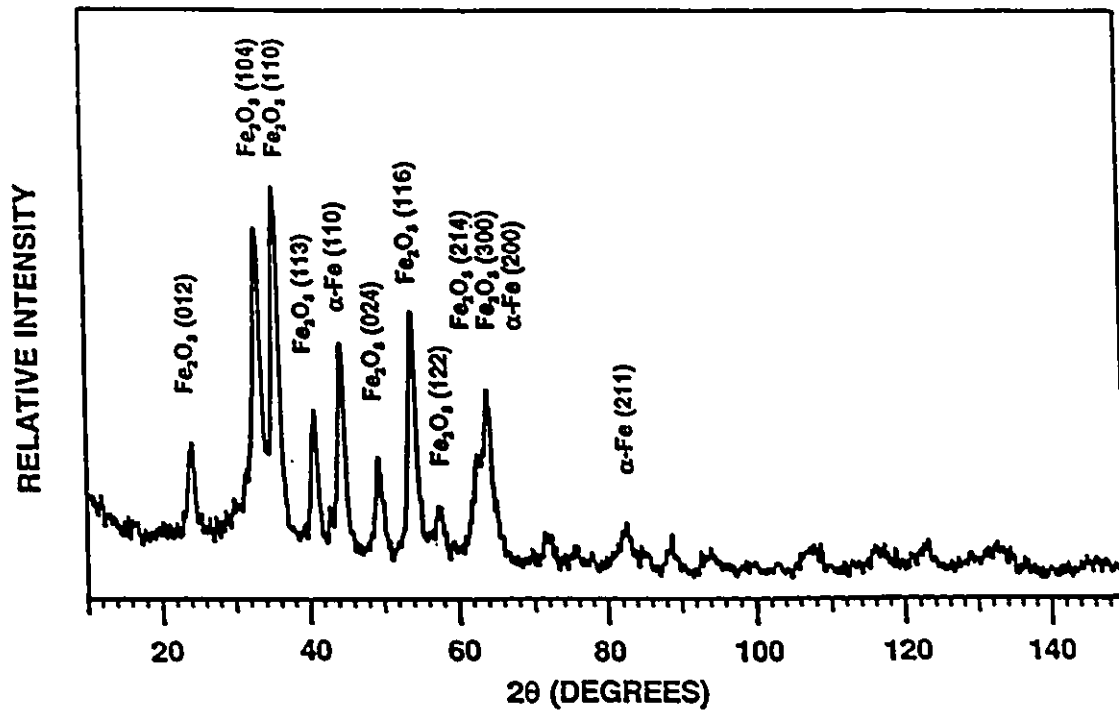


Figure 45. X-ray diffraction analysis of the loose debris of 6061Al-20%Al₂O₃ worn against SAE 52100 bearing steel in regime I. (using Cu-Kα).



Figure 46. Debris of 6061Al-20%Al₂O₃ (regime II); (a) platelike debris particles; (b) equiaxed particles.

aluminium peak could be identified.

(2) A mixture of black, fine-powdery particles (usually less than 2 μm) and relatively-large, plate-like, shiny and bright metallic particles (Figure 46(a) & (b)), were generated during wear in regime II. It was observed that the percentage of plate-like particles in the loose debris increased with the applied load. About 10% of the debris in 6061Al-20%Al₂O₃ consisted of platelike particles at 20 N. However this ratio increased to 90% for the composites tested at 100 N. X-ray diffraction results given in Figure 47 indicate that the debris consisted of a mixture of materials detached from both the composites and the steel counterbody, *i.e.* Al, Fe and α -Al₂O₃. However in this regime no clear evidence for iron oxide could be found contrary to regime I. It is also difficult to distinguish between the aluminum and iron peaks.

(3) In the severe wear regime III, very large (200-500 μm), flakes of shiny metallic appearance were generated.

For the unreinforced 6061Al alloy, since the regime I does not exist, the wear debris have only characteristics of the last two types. X-ray diffraction results of the debris are given in Figures 48 and 49 for regimes II and III respectively.

4.2.6. EFFECT OF SLIDING VELOCITY ON THE WEAR RATES

In a similar way to the load dependence of the wear rates, the variation of wear rates with the sliding velocity can be grouped into three wear regimes as shown in Figure 50. Two reference lines have been drawn to delineate wear rate transition between regimes I, II and III. These lines correspond to wear rates where slope changes from one

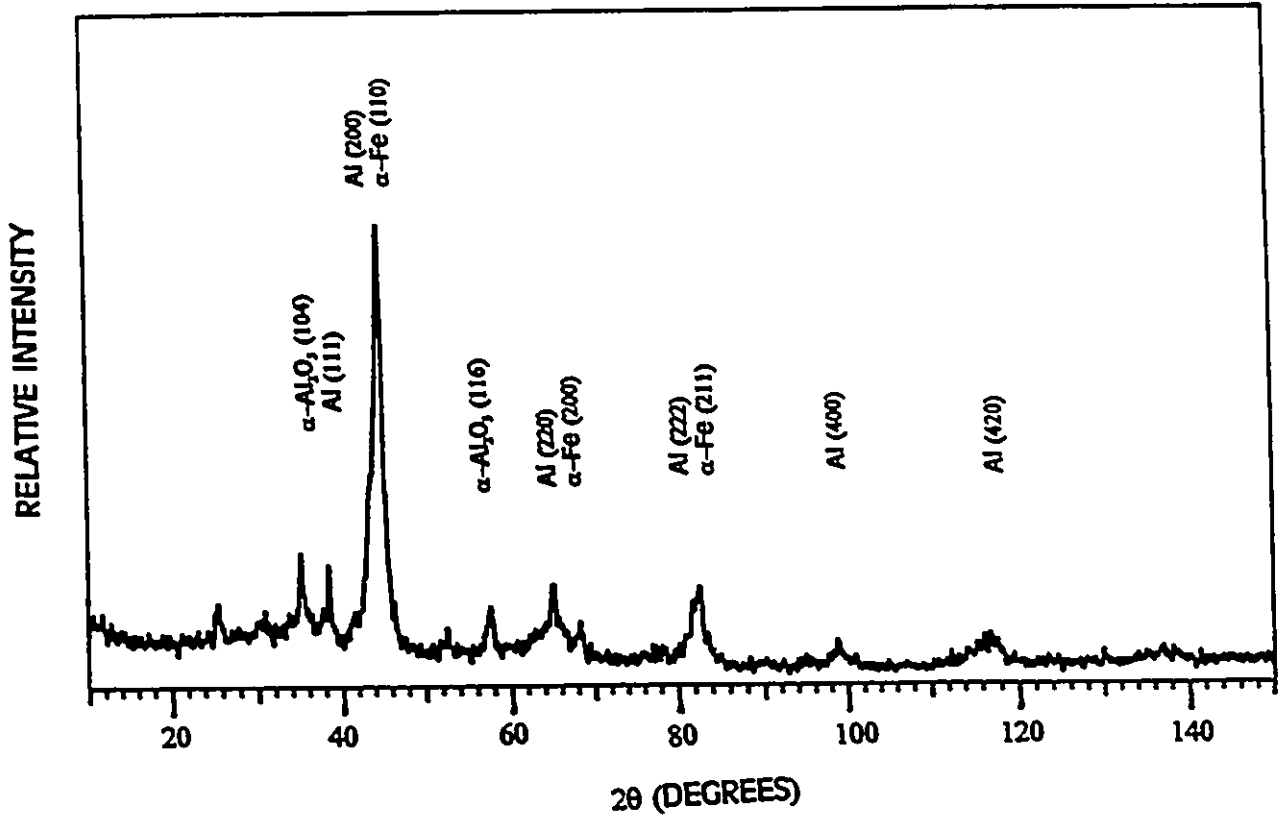


Figure 47. X-ray diffraction analysis of the loose debris of 6061Al-20%Al₂O₃ worn against SAE 52100 bearing steel in regime II. (using Cu-Kα).

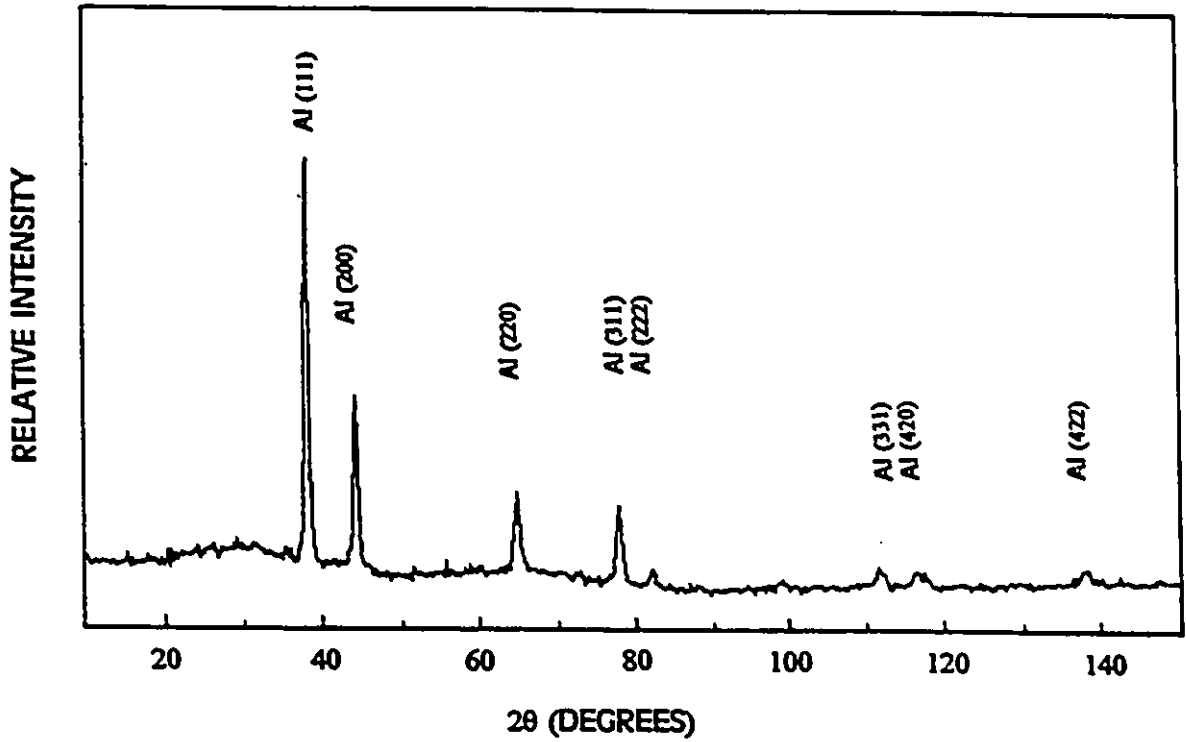


Figure 48. X-ray diffraction analysis of the loose debris of 6061Al worn against SAE 52100 bearing steel in regime II. (using Cu-K α).

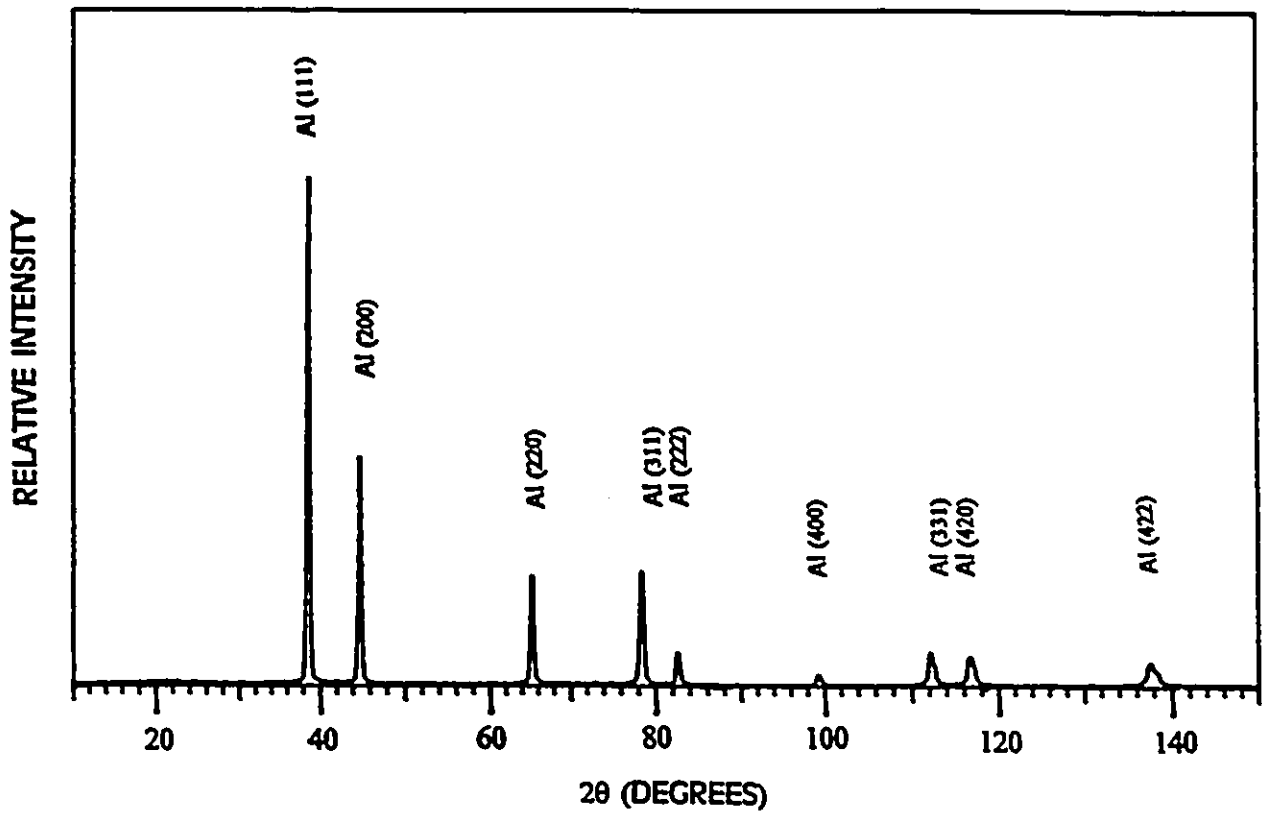


Figure 49. X-ray diffraction analysis of the loose debris of 6061Al worn against SAE 52100 bearing steel in regime III. (using Cu-K α).

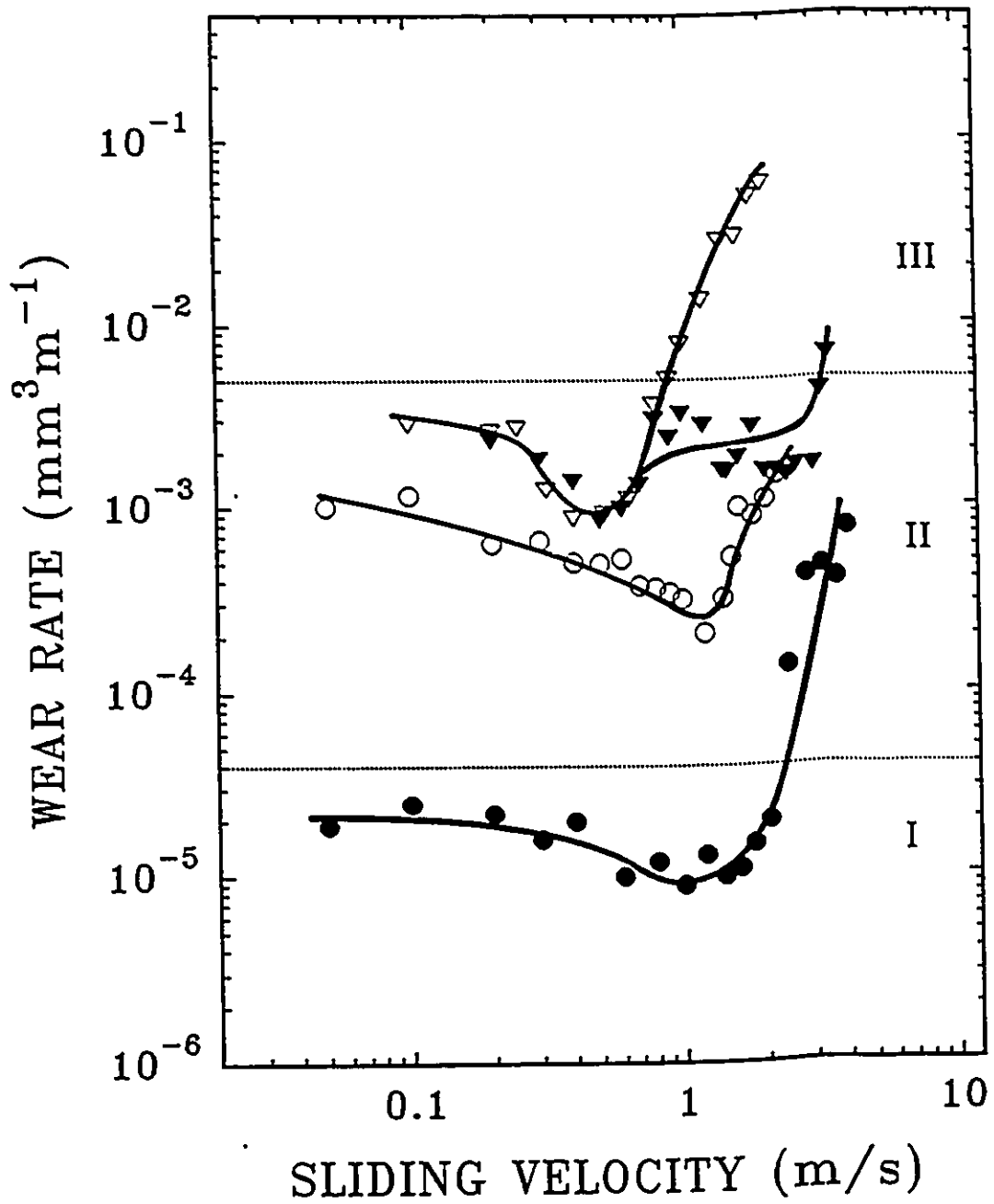


Figure 50. Wear rate vs sliding velocity for 6061Al under (\circ) 4.9 N, (∇) 49 N; and for 6061Al-20%Al₂O₃ under (\bullet) 4.9 N, (\blacktriangledown) 49 N.

regime to another occurred in figure 39. This is however a simplification because the transition wear rates of a given material varies with the applied load and the sliding velocity as will be discussed in section 5.5. The regime I has only been observed for the 6061Al-20%Al₂O₃ at the low applied load levels (*i.e.* at 4.9 N) and between the sliding velocities 0.1 to 2.2 m/s. In regime II, the wear rates generally show a decrease with increasing sliding velocity but then increase again above a certain velocity. The transition from regime II to III takes place at a higher sliding velocity in the composite compared to the unreinforced 6061Al. For example at 49 N, the transition velocity is about 0.8 m/s for the unreinforced 6061Al but this is shifted to about 3.2 m/s in the composite.

To study the effect of velocity on the transition from regime II to regime III in detail, wear rate versus load diagrams have been constructed. As shown in Figure 51, the transition load for 6061Al decreases by an order of magnitude (from 230 N to 9 N) when the sliding velocity is increased from 0.4 m/s to 5 m/s. A similar behaviour is observed for the 6061Al-20%Al₂O₃ (Figure 52). The transition loads as a function of sliding velocity are summarized in Tables IV and V.

4.2.7. BULK TEMPERATURE DIAGRAMS

The temperature distribution curves for the composite and the unreinforced 6061Al alloy are given in Figure 53 for a constant velocity ($V=0.8$ m/s). The changes of surface temperature with sliding distance show similar trends in the unreinforced 6061Al and the composite, *i.e.*: the surface temperature increases rapidly initially with the sliding distance and then reaches a steady state. The magnitude of the steady state

Table IV. Variation of Transition Load P_t of 6061Al-20%Al₂O₃,
between Regime I and II as a function of velocity V

V (m/s)	P_t (N)
0.2	25
0.4	15
0.8	10
2	7
3	4

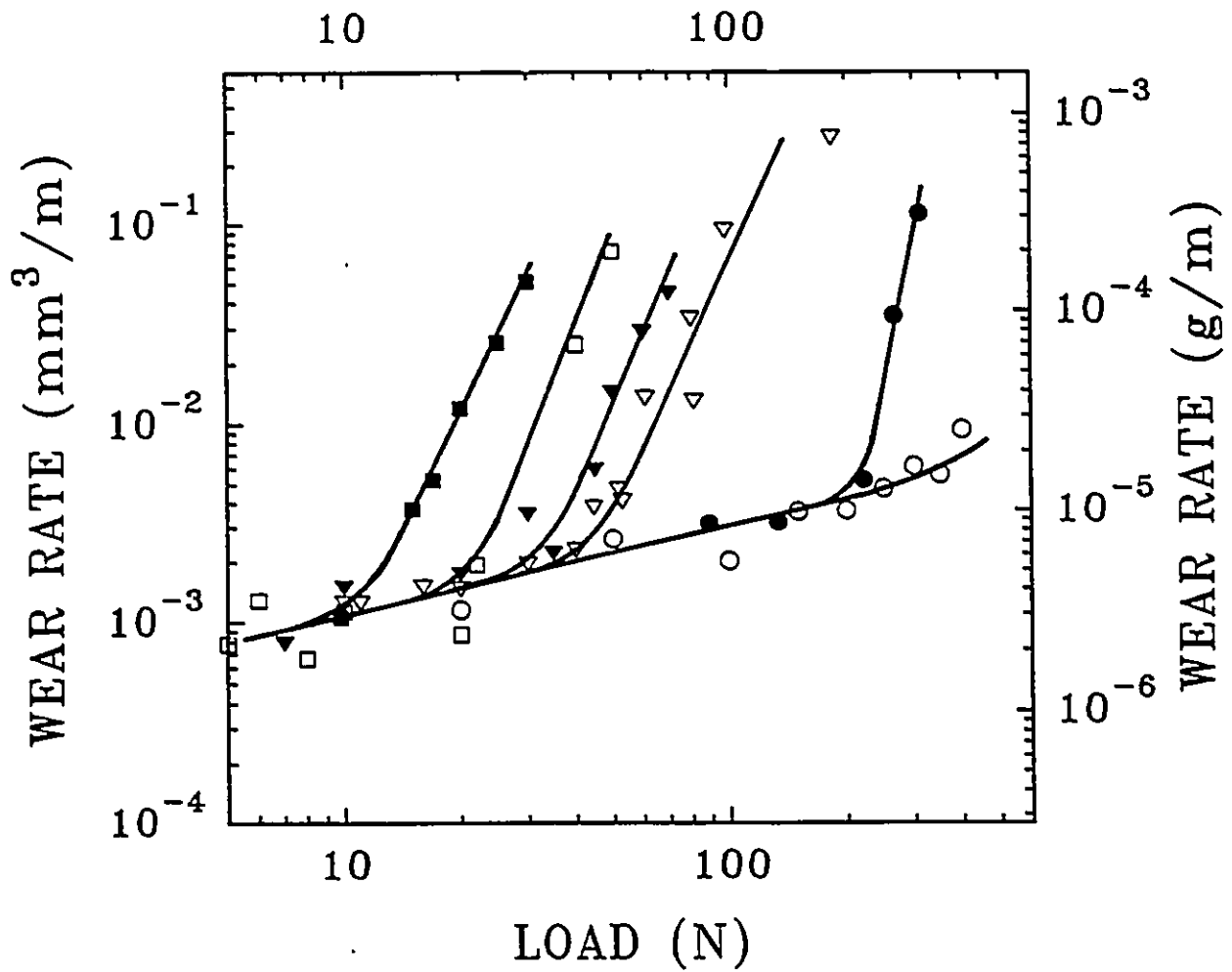


Figure 51. Wear rate vs applied load diagram for 6061Al with sliding velocity (\circ) 0.2 m/s; (\bullet) 0.4 m/s; (∇) 0.8 m/s; (\blacktriangledown) 1.2 m/s; (\square) 2.0 m/s and (\blacksquare) 5.0 m/s.

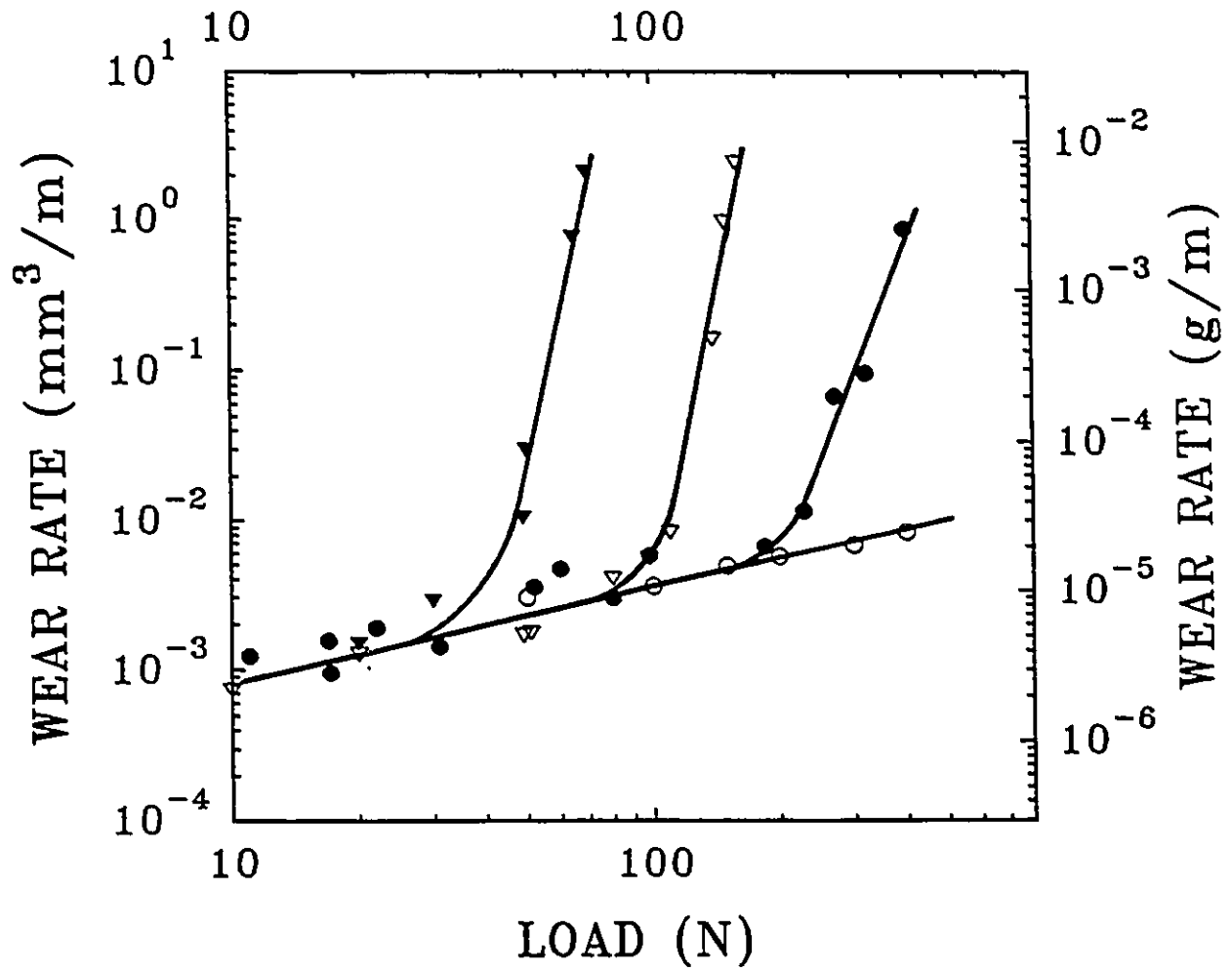


Figure 52. Wear rate vs applied load diagram for 6061Al-20%Al₂O₃ with sliding velocity (○) 0.2 m/s; (●) 0.8 m/s; (▽) 2.0 m/s and (▼) 4.0 m/s.

Table V. Variation of Transition load P_t between Regime II and III as a function of velocity V

6061Al		6061Al-20%Al ₂ O ₃	
V (m/s)	P_t (N)	V (m/s)	P_t (N)
0.2	>420	0.2	>420
0.4	230	0.4	350
0.8	50	0.8	230
1.2	35	2.0	100
2.0	20	3.2	49
5.0	9	4.0	40

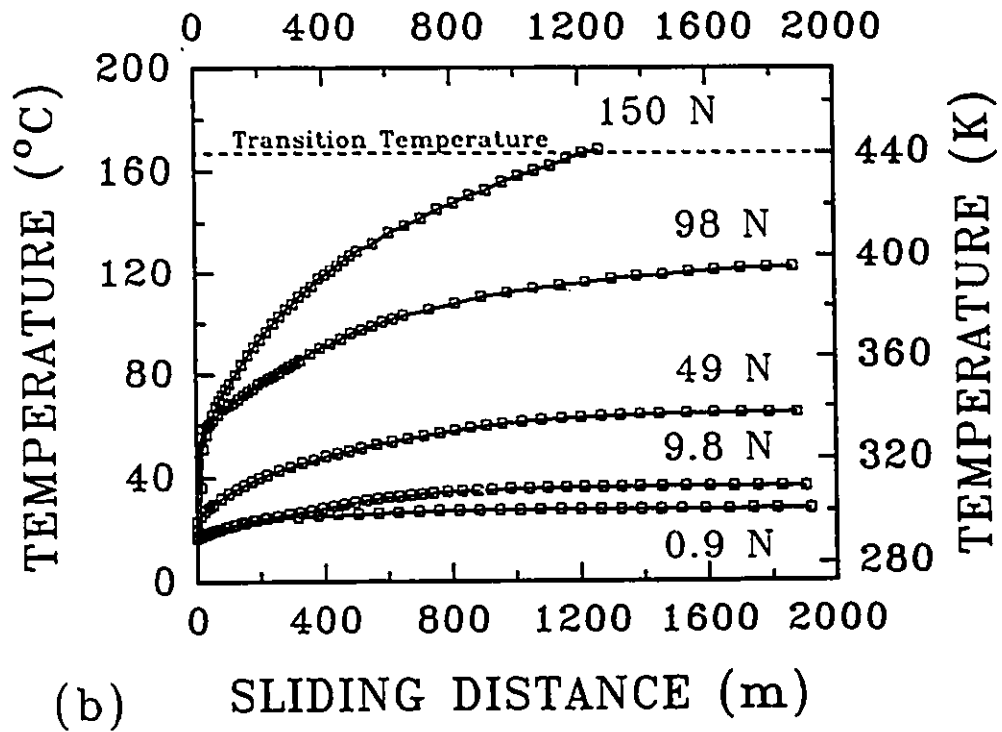
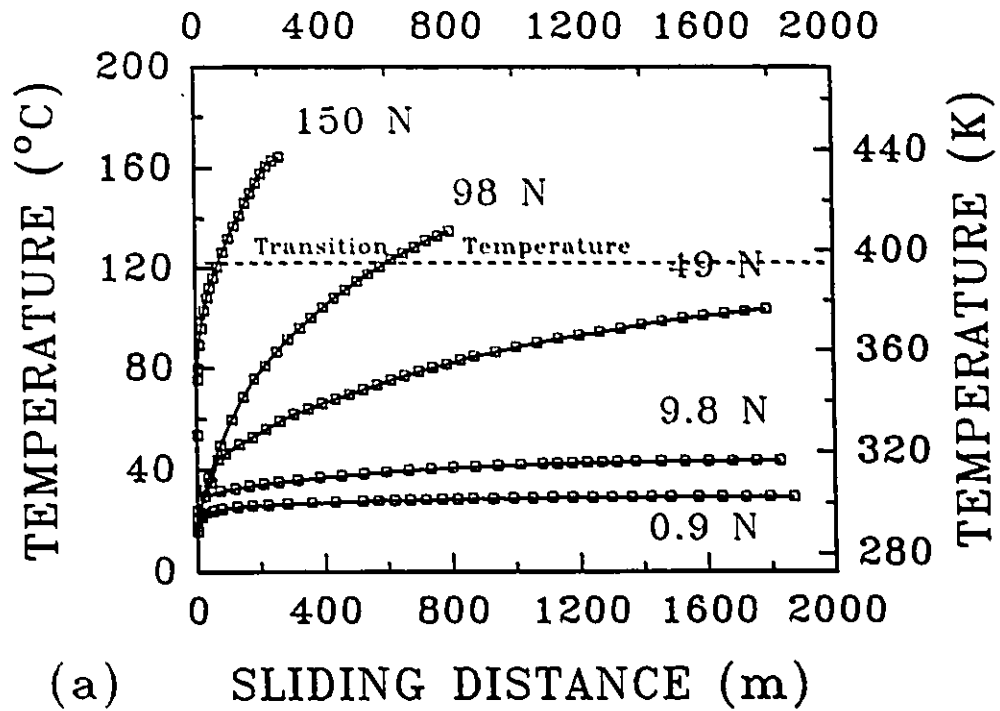


Figure 53. Temperature distribution at the contact surface of (a) 6061Al; (b) 6061Al-20%Al₂O₃ as a function of sliding distance. sliding velocity: 0.8 m/s.

contact temperature increases with the applied load. For the unreinforced alloy, it was observed that the transition from regime II to III occurred whenever the surface temperature reached 395 ± 10 K (or 122 ± 10 °C). The transition temperature was reproducible within ± 10 K and corresponded to $T/T_m = 0.4$ (where $T_m = 925$ K^[136] is the melting temperature of the 6061Al). In the 6061Al-20%Al₂O₃ composite the transition temperature was higher (440 ± 10 K or 167 ± 10 °C). Experiments showed that when the block-on-ring tester was cooled by circulating cold water around the specimen holder assembly, the transition was reversed (*i.e.*, no aluminum accumulation on the slider was observed and the regime II wear rates prevailed). The bulk contact temperature of the composite was lower than that of the unreinforced aluminium at any given load and sliding distance (Figure 53). The variation of surface temperature with sliding velocity in the 6061Al is shown in figures 54 and 55. In figure 55, the contact temperature increases with sliding time and at the transition from regime II to III the temperature is 395 ± 10 K (49 N, 1.2 m/s).

4.2.8. EFFECT OF COUNTERFACE MATERIAL

The variation of the wear rates of the 6061Al-20%Al₂O₃ and the 6061Al worn against a mullite slider is shown in Figure 56. The overall shape of the wear rate curves in Figure 56 is similar to that obtained when the materials are rubbed against a steel slider (Figure 39). The effect of using a mullite slider is to increase the wear rates in each regime to higher levels. It is seen that at any given load level, the wear rates of the composite accelerated by a factor of about 10. Also, as shown in Table III, both the wear

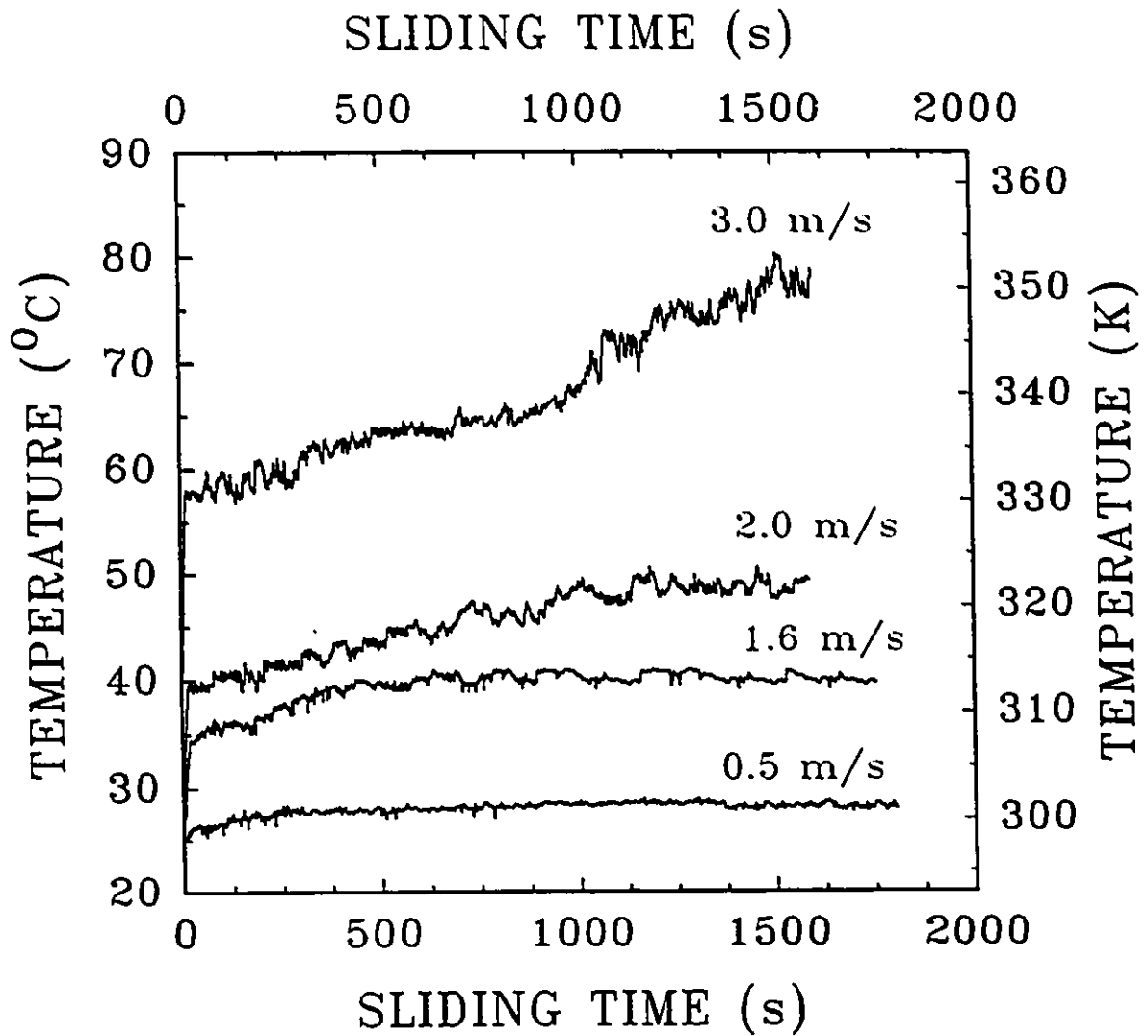


Figure 54. Temperature distribution at the contact surface of 6061Al as a function of sliding time and sliding velocity. Load=4.9 N.

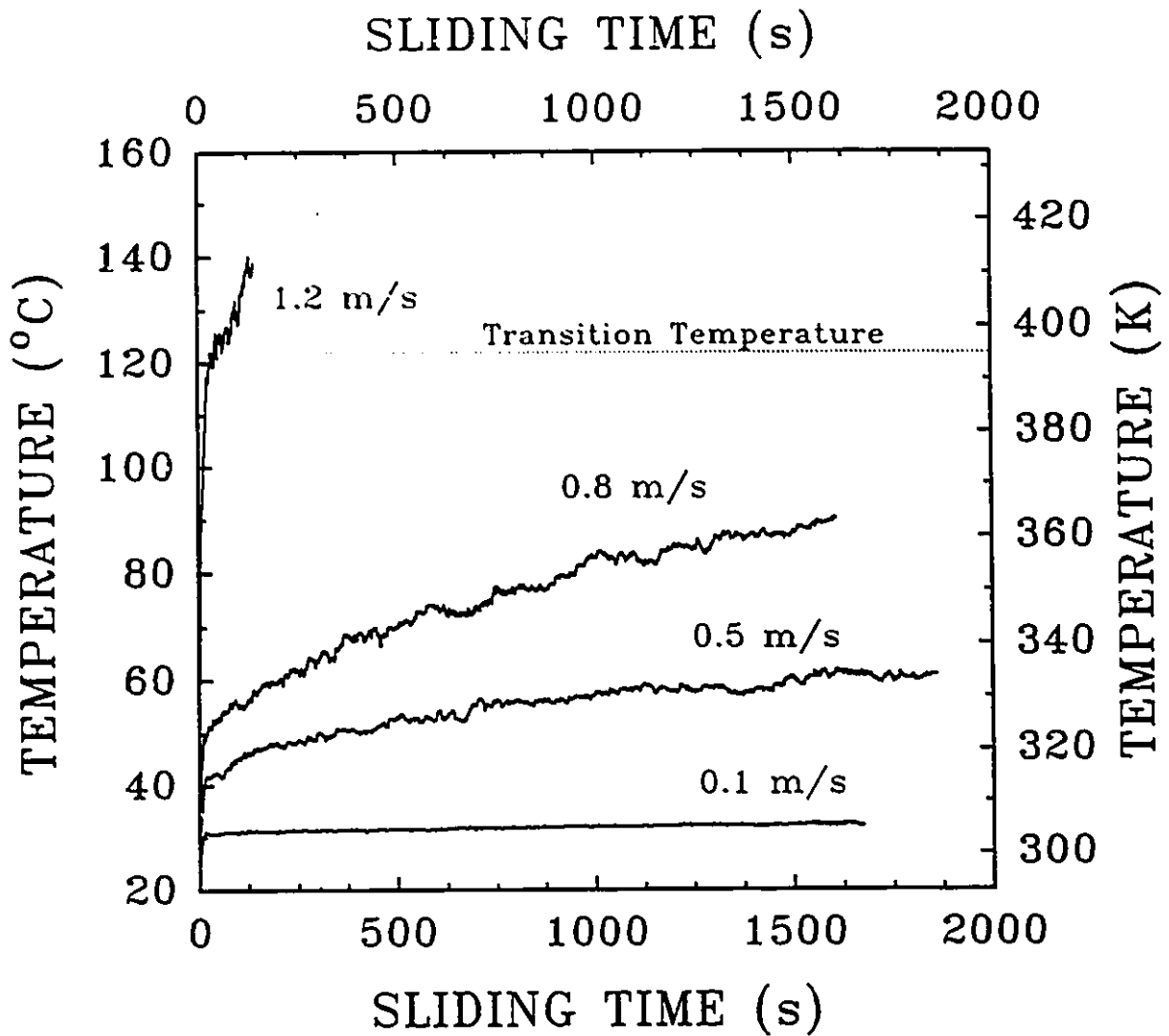


Figure 55. Temperature distribution of 6061Al at the contact surface as a function of sliding time and sliding velocity. Load=49 N.

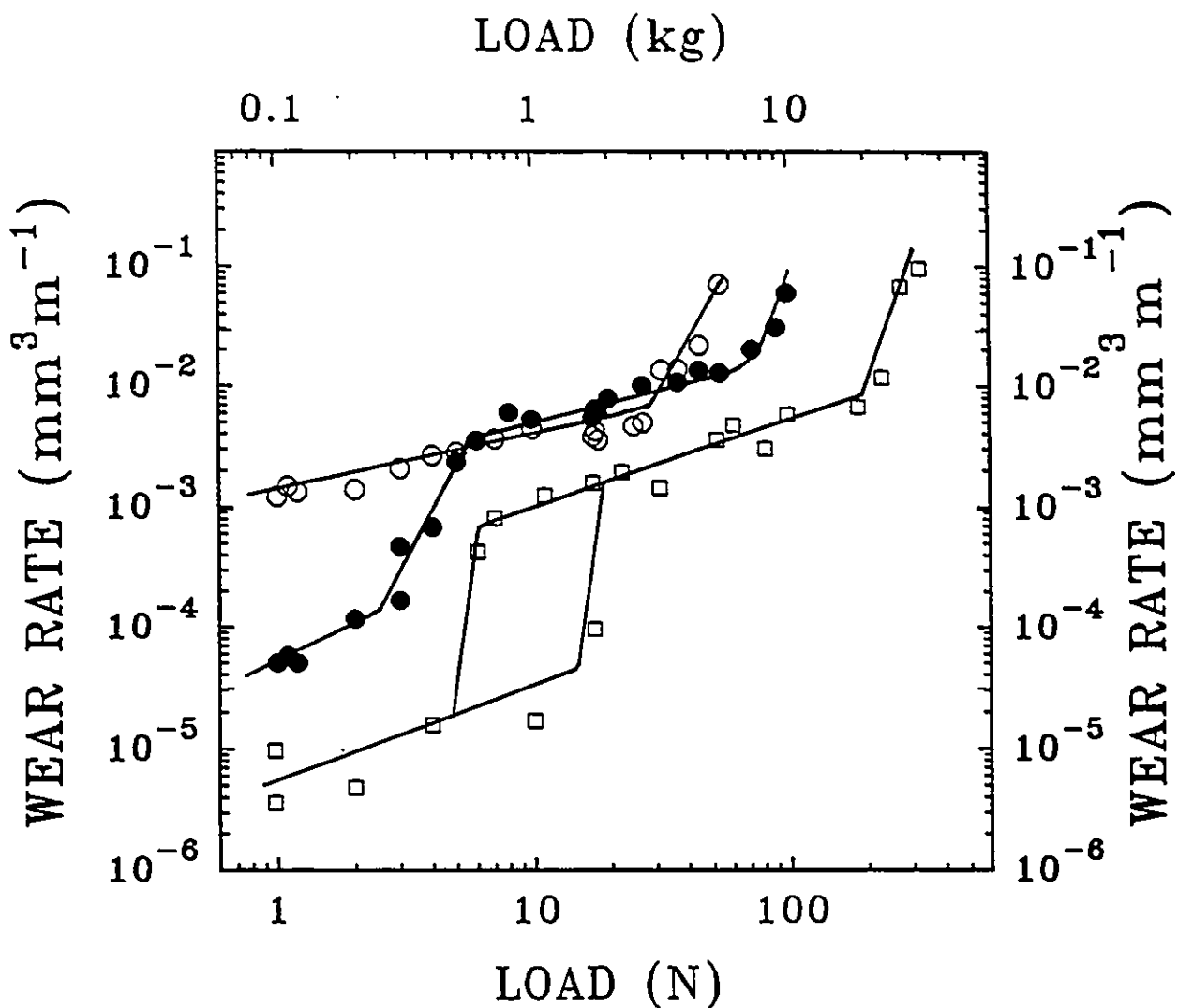


Figure 56. Wear rate vs applied load diagrams for (\circ) 6061Al and (\bullet) 6061Al-20%Al₂O₃ worn on mullite. Wear rates of 6061Al-20%Al₂O₃ (\square) worn on ASE52100 are shown for comparison. Sliding velocity: 0.8 m/s.

constant (k) and the exponent (n) in all the regimes are higher in the case of sliding on a mullite slider. In addition, the transition loads between the wear regimes are shifted to lower load levels. For example, the transition from regime I to II occurs within a 2 to 5 N load range when 6061Al-20%Al₂O₃ is worn against mullite compared to the 5 to 20 N range observed when a steel slider is used. However, the magnitude of increase of the wear rates during the transition remains unchanged ($10^2 \text{ mm}^3\text{m}^{-1}$) regardless of the type of slider material. The second transition, between regimes II and III, in 6061Al-20%Al₂O₃ occurs at 110 N. For the unreinforced 6061Al, the transition load to severe wear is only 25 N. Thus, in summary, subjecting these materials to wear against a mullite slider shortens the range of regime II and facilitates the transition to the severe wear regime (III).

4.3 EFFECT OF MICROSTRUCTURAL FACTORS ON THE WEAR RATES OF MMCs

4.3.1. EFFECT OF VOLUME FRACTION OF PARTICLES ON THE WEAR RATES

Figure 57 illustrates the effect of varying the volume fraction of the reinforcing particles on the wear rates. The wear rates of three 6061Al alloys containing 0, 10, 20 pct Al₂O₃ particles with comparable particle size (*e.g.* 14 μm for 6061Al-10%Al₂O₃ and 19 μm for 6061Al-20%Al₂O₃) are compared in this figure. Increasing the volume fraction of the particles leads to a delay in the transition load ranges between the wear regimes to higher levels. The transition between regime I and II occurs within a load range of 3

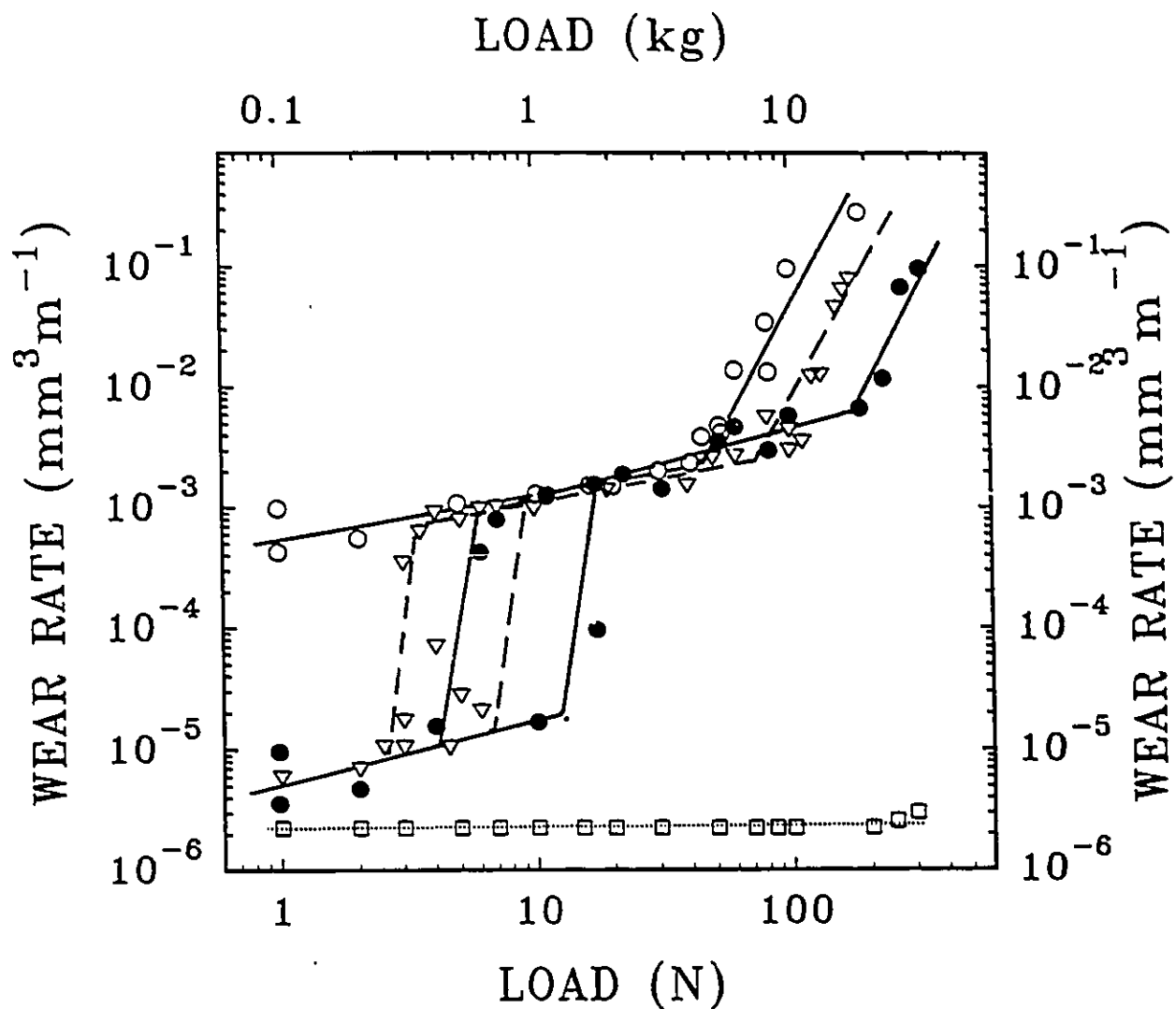


Figure 57. Wear rate vs applied load diagrams for (\circ) 6061Al; (∇) 6061Al-10%Al₂O₃, (\bullet) 6061Al-20%Al₂O₃, and (\square) Al₂O₃-SiC. Counterface: SAE52100 steel.

to 7 N in the 6061Al-10%Al₂O₃. This range is delayed to 5 to 20 N for the 6061Al-20%Al₂O₃. Similarly, the transition to severe wear is moved to higher loads as the percentage of particles increased so that the transition loads correspond to 50, 90, and 230 N for the unreinforced alloy and alloys with 10% and 20% reinforcement, respectively. In view of the scatter in the data, the wear rates within regimes I and II can be considered to remain relatively unaffected by the changes in the particle volume fraction. But overall, increasing the particle volume fraction has a positive effect on the wear resistance of the aluminum alloys by delaying transitions to higher loads. The values of the transition loads as a function of particle volume fraction have been shown in Table VI.

4.3.2. EFFECT OF PARTICLE SIZE ON THE WEAR RATES

Experiments to determine the effect of the particle size were performed on SiC-reinforced Al-Cu-Mg matrix alloys. The wear rates of the alloys reinforced with an average SiC particle sizes of 2.4 ± 1.7 and 15.8 ± 5.0 μm (both with 20% SiC) are compared in Figure 58. These experiments were performed using a steel slider. At low loads, where regime I prevails, the composite with coarse SiC particles clearly has a better wear resistance than that of the composite reinforced with fine SiC particles. For example, at 1 N, the composite with 2.4 μm particle size has a wear rate of 9×10^{-5} mm^3m^{-1} , which is an order of magnitude higher than that of the composite with coarse particles (8×10^{-6} mm^3m^{-1}). (The wear rate of the unreinforced 2014Al at 1 N is 2×10^{-4} mm^3m^{-1} .) It appears that the size of reinforcing particles does not have a prominent effect

Table VI. Effect of Al₂O₃ Particle Volume Fraction V_f in 6061Al-Al₂O₃ composites on Transition Load P_t

V _f (%)	P _t ^(I-II) (N)	P _t ^(II-III) (N)
0	0	50
10	3-7	90
20	5-20	230

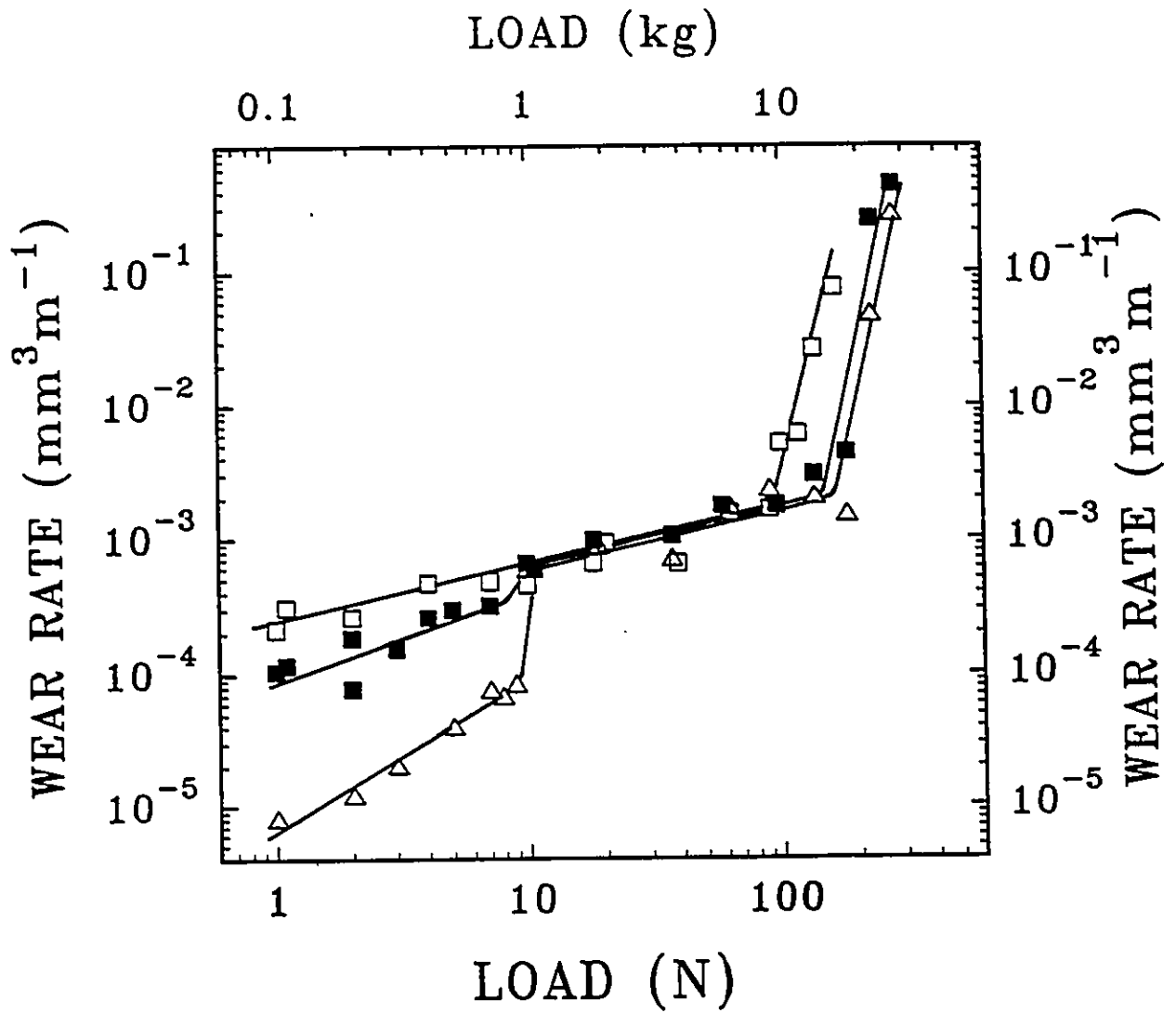


Figure 58.. Wear rate vs applied load diagrams for (□) 2014Al; (■) 2124Al-20%SiC (2.4 μm), and (△) 2014Al-20%SiC (15.8, μm). Counterface SAE52100; Sliding Velocity: 0.8 m/s.

on the wear rates in regimes II and III, since the wear rate curves of the composites with fine and coarse particles coincide at above 20 N. But the transition to severe wear in the SiC-reinforced composites occurs at higher loads (140 N) than that for the unreinforced 2014Al (90 N).

4.4. SUBSURFACE STRAINS AND STRESSES

4.4.1. STRAIN ACCUMULATION BELOW THE WORN SURFACES

Sliding contact between the surfaces of ductile materials (even a small nominal contact stresses) is often accompanied by severe plastic deformation localized within a small volume of material adjacent to contact surfaces. The process of debris formation, especially in the unlubricated systems, is closely related to the magnitude and distribution of local strains and strain gradients as well as to the variation of stress state within the deformed subsurface zones. Therefore, characterization of subsurface strain and stress distributions in dry sliding wear is important in order to rationalize the events involved in the production of wear debris of the aluminum alloys and the composites.

The material selected for the investigation subsurface stress-strain states was the unreinforced A356Al. Details for specimen preparation and test methods are given in section 3.3. The plastic strain distribution beneath the contact surface was obtained from the measurements of the displacement of a reference marker perpendicular to the contact surface. The morphology of the interface between the marker and the rest of the specimen before and after a wear test is shown in Figure 59. It is seen that the boundary between the marker and the rest of the sample which was initially straight becomes

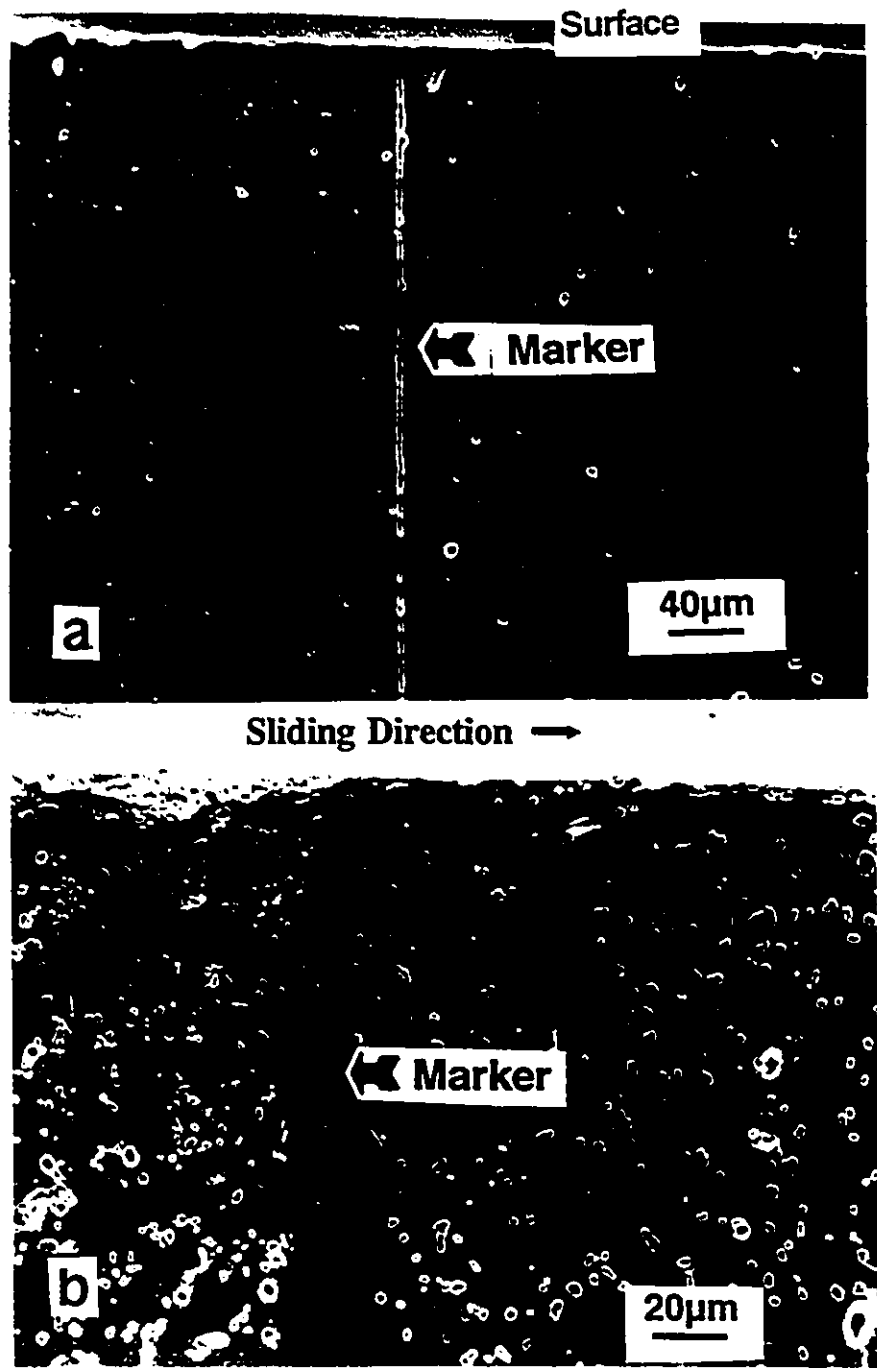


Figure 59. (a) Polished cross-section of an unworn specimen showing the interface between the marker and the specimen. (b) Displacement of the interface in a specimen worn at load=45 N, sliding distance=100 m.

curved towards the sliding direction after a certain sliding distance. Figure 60 shows the measured values of the sliding displacements in specimens tested at 10 N. To construct this figure a different specimen was tested for each sliding distance and each curve represents the average of the two measurements made at front and rear (with respect to the sliding direction) interfaces of the marker plate. The accuracy of the measurements were rather poor very near the contact surfaces (depth less than 5 μm) particularly when material loss in the form of debris occurred in this region. At greater depths the displacement values were reproducible with a standard error of less than 0.15 of the reported mean values.

Considering that the displacement field arises as a result of shear deformation, the equivalent plastic strain, ϵ , at any given depth can be calculated from the shear angle of the interface ϕ [52, 137].

$$\epsilon = \frac{\sqrt{3}}{3} \tan \phi \quad (4.2)$$

The subsurface strain distribution curves at 10 N are shown in Figure 61. The figure indicates that a severe strain gradient was developed even after a short sliding distance of 30 m. Both the magnitude of subsurface strains and the depth of plastic zone increased with the sliding distance and with the applied load (Figure 62). For instance, as shown in Figure 60, the nominal depth of the plastic zone (defined as the thickness of material subjected to strains larger than 0.1) was 40 μm at 30 m and this became 80 μm after 10^3 m indicating continuous and progressive nature of the strain accumulation process.

Using a non-linear regression analysis the experimentally determined strain

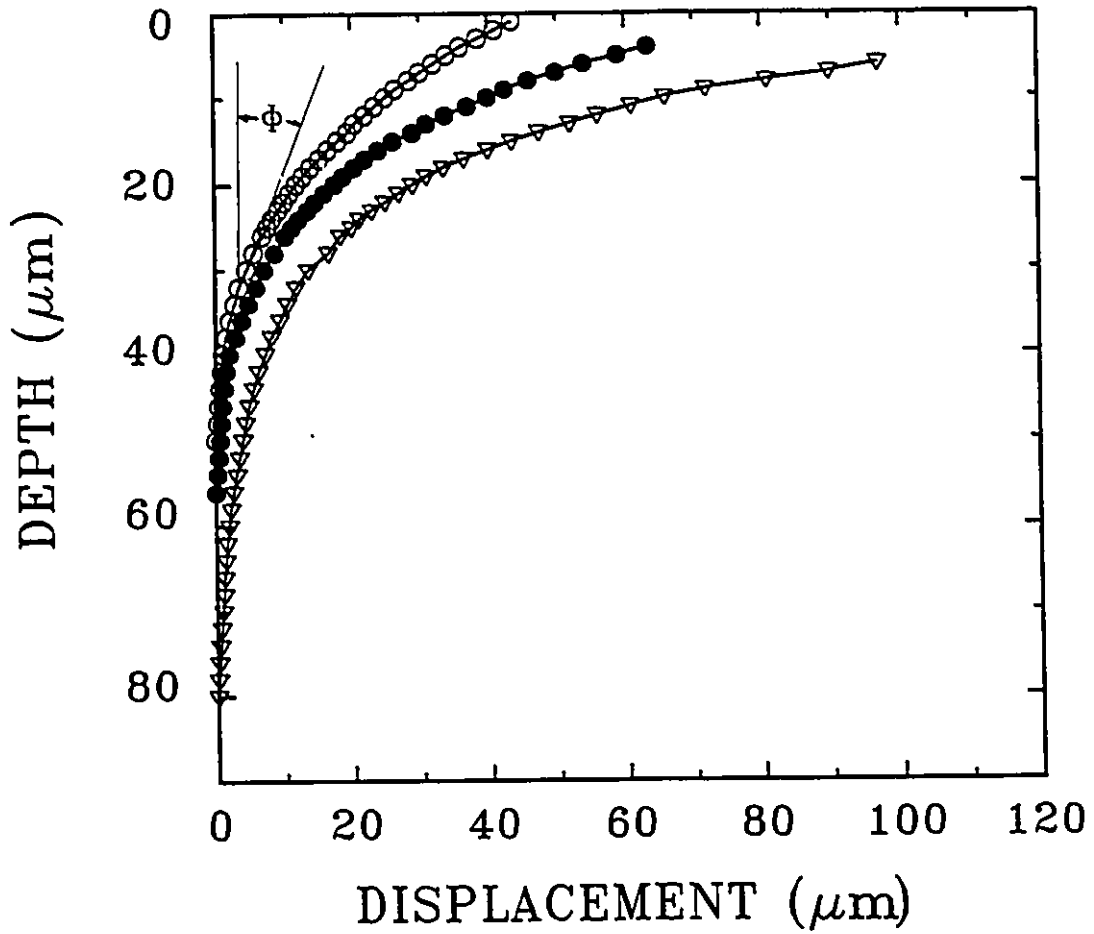


Figure 60. Subsurface displacement gradient as a function of sliding distance, Load: 10 N; Sliding Distance: (\circ) 30 m, (\bullet) 100 m and (∇) 1000 m.

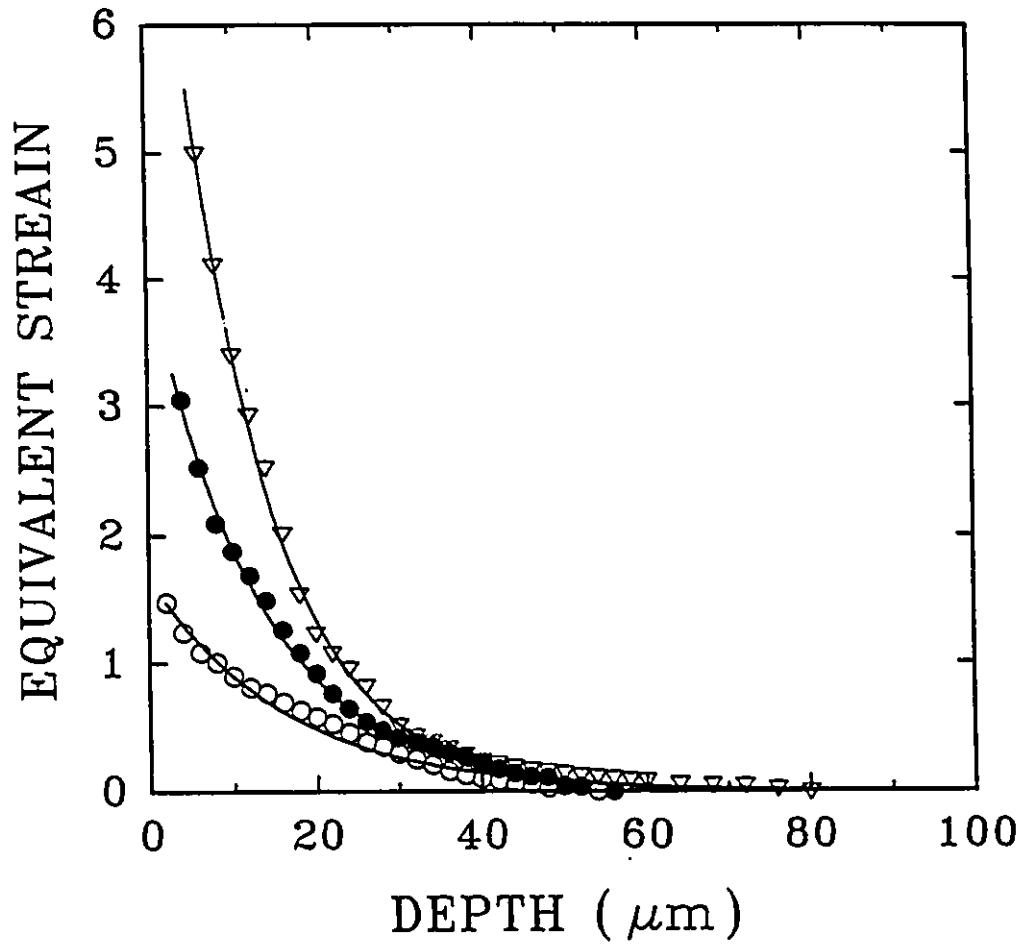


Figure 61. Equivalent plastic strain gradient as a function of sliding distance: (\circ) 30 m; (\bullet) 100 m and (∇) 1000 m. Load: 10 N.

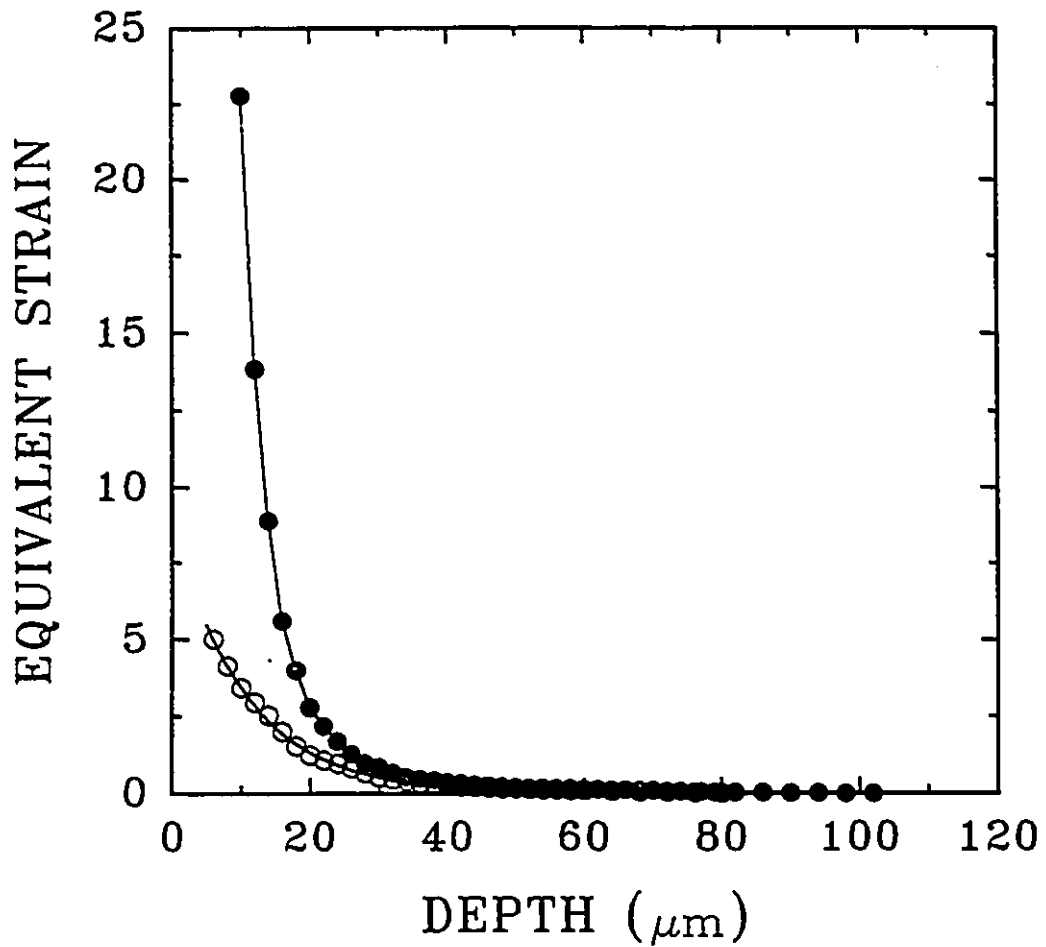


Figure 62. Plastic strain vs. depth below the worn surfaces at different loads: (O) 10 N and (●) 45 N. Sliding Distance: 1000 m.

profiles can be described as:

$$\varepsilon = A \cdot \exp(-B \cdot Z) \quad (4.3)$$

where Z is the subsurface depth (in microns). A is the extrapolated strain at the surface. The values of parameters A and B are given in Table VII for 10 and 45 N. The results demonstrate again that the surface strains can be very high and increase with sliding distance and load.

4.4.2. FLOW STRESS OF THE SUBSURFACES

In order to estimate the flow strength of the deformed layers, Vickers microhardness measurements were performed at different sliding distances and loads. Figure 63 shows hardness gradients in specimens worn at 10 and 45 N for 10^3 m. Each point represents an average of at least three measurements made at the same depth with standard deviation less than 20% of the mean. The near surface zones were considerably hardened with respect to the bulk. For example, for the tests performed at 10 N, the hardness at 5 μm below the surface (1050 MPa) was 50% higher than the bulk hardness (700 MPa). The hardness of each point in the deformed zone as well as the depth of this zone is increased with the applied load.

As a first approximation, it can be assumed that the flow strength, σ_f , of the deformed layers is related to the hardness by ^[138,139]:

$$\sigma = \frac{H}{3} \quad (4.4)$$

Table VII. Coefficients A and B in eqn.(4.2): $\epsilon=A \cdot \exp(-BZ)$

Load (N)	Sliding Distance (m)	A	B (1/micron)
10	30	1.67	6.2×10^{-2}
	100	4.10	7.7×10^{-2}
	1000	8.80	9.4×10^{-2}
45	10	31	2.5×10^{-1}
	30	34	2.7×10^{-1}
	1000	41	2.8×10^{-1}

* Sliding Velocity = 0.8 m/s

where H is the Vickers hardness so that the flow strength of the subsurface region can be estimated from data in Figure 63. As shown in Figure 63, the flow strength increased towards the contact surface.

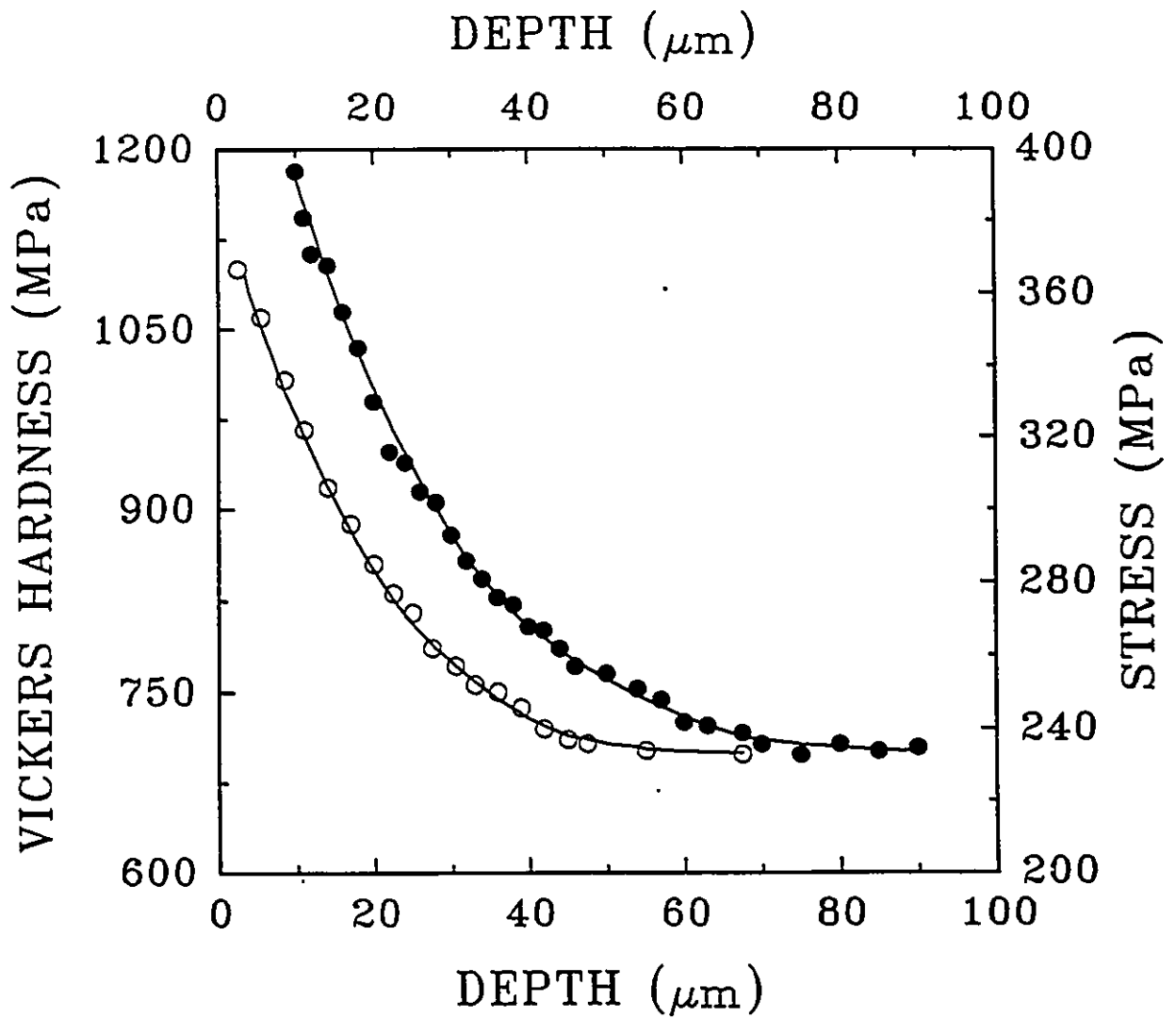


Figure 63. Vickers hardness (and flow strength) vs. depth below the worn surfaces at two different loads; Applied load: (○) 10 N and (●) 45 N; Sliding Distance: 1000 m.

CHAPTER V DISCUSSION

5.1 WEAR MECHANISMS IN PARTICLE REINFORCED Al ALLOYS

The wear resistances of aluminum alloys reinforced by SiC or Al₂O₃ particles show a similar load dependence. All three composites, namely 6061Al-Al₂O₃, 2014Al-SiC and A356Al-SiC exhibit three wear regimes. Metallographic observations and X-ray analyses revealed that the basic mechanisms that control the wear rates are different in each of these regimes. At the transition regions between the regimes, rate-controlling mechanisms change from one to another. In this section, the effects of the microstructural factors, the surface temperatures, as well as the type of counterface material on the wear rates and transition loads will be discussed in relation to the wear mechanisms.

5.1.1. WEAR MECHANISMS IN REGIME I (ULTRA MILD WEAR)

The high wear resistance of composite materials in the wear regime I can be attributed to the presence of SiC and Al₂O₃ particles that act as load-supporting elements. In order to be as effective as load-bearing elements, the particles should maintain their structural integrity during wear. Therefore, regime I is limited to the low applied loads where the local stresses generated beneath the slider are lower than the fracture strength of the particles. The initial surface topographies of the composites prior to the wear tests are suitable to facilitate the transfer of the applied load directly onto the particles. This is because the SiC and Al₂O₃ particles stand proud of the polished contact surfaces and particle protrusions as high as 5 μm could be formed on the surfaces of the composites

incorporating large particles (Figure 64). This topography is considered to be useful to prevent the softer aluminum matrix becoming directly involved in the wear process. It should, however, be noted that this type of initial surface finish is not essential for the occurrence of the regime I since wear rates of the order of $10^{-5} \text{ mm}^3\text{m}^{-1}$ were also measured in some of 6061Al-20%Al₂O₃, A356Al-20%SiC and 2014Al-20%SiC samples tested at 1 N (on steel) after giving them a rough polish with a 320-grit SiC paper.

Another process associated with wear in regime I is the formation of the "transfer layers" on the contact surfaces of the composites (Figures 28 and 44). These layers, which were mainly composed of a mixture of iron and iron oxides, were present on the contact surfaces of all the composites reinforced either by SiC or Al₂O₃ when these composites were worn against a steel slider at low loads, but not on the surfaces of unreinforced aluminum samples. Therefore, the origin of the transfer layers can be attributed to the abrasive action of the hard SiC or Al₂O₃ particles on the steel counterface. The debris fragments detached from the steel slider as a result of abrasion by hard particles were oxidized and deposited on the contact surfaces of the composites. The layers were generally thin (3 to 10 μm) and, as revealed by the EDS spectrum shown in Figure 27 and Figure 43, mainly consisted of ferrous elements. X-ray diffraction experiments performed on the loose wear debris generated during the wear of 6061Al-20%Al₂O₃ composites against the steel slider indicated the presence of α -Fe and Fe₂O₃ (Figure 45). A similar result has also been found for the A356Al-20%SiC composite (Figure 29). These observations imply that once the transfer layers were established on the composite samples, the steel counterface can be considered to be mainly in contact with a mixture



Figure 64. Morphology of SiC particles ($15.8 \mu\text{m}$) on the polished surface of 2014Al-20%SiC before the wear test.

of iron and iron oxides. The iron oxides are known to have a low coefficient of friction [140, 141], and thus, the layers can be expected to provide an *in situ* lubrication effect. The mechanism by which the transfer layers are formed is schematically illustrated in Figure 65.

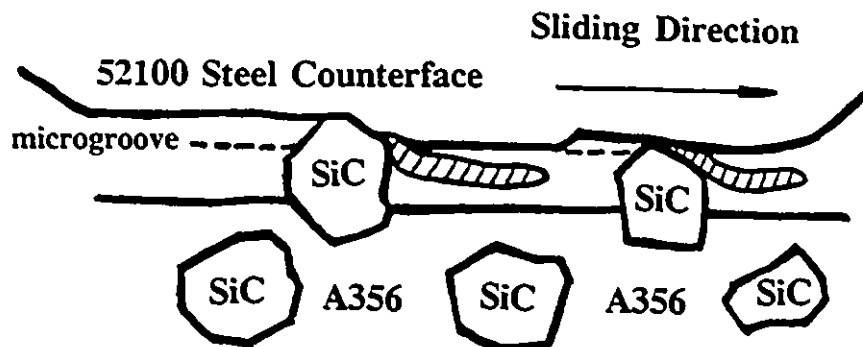
In summary, the improved wear resistance of the particle reinforced composites under small contact stresses is due to the load supporting effect of reinforced ceramic particles and the formation of iron oxide layers on the contact surfaces.

5.1.2. WEAR MECHANISMS IN REGIME II (MILD WEAR)

The SiC and Al₂O₃ particles fracture above a certain load, and the fragmented particles lose their ability to support the applied load. Consequently, the aluminum matrix comes into direct contact with the counterface. Once this happens, the wear rates of the composites increase by a factor of 10 to 100 and become almost equal to the wear rates of the unreinforced aluminum alloys. Examples of broken particles at the contact surfaces of the 6061Al-20%Al₂O₃ are shown in Figures 66(a) and 66(b). It is occasionally observed that the particles are also removed from the surface by a pull-out process as illustrated in Figure 66(c) and 52(d). Only a small amount of iron has been detected on the worn surfaces of the composites (Figure 27 and 67) revealing the absence of iron-rich layers in wear regime II.

Metallographic observations made on the longitudinal sections (on a plane normal to the wear surface and parallel to the sliding direction) often showed evidence for extensive plastic deformation of the material adjacent to the contact surfaces. A typical

STEP 1: Abrasive Action of SiC Particles on the Counterbody



STEP 2: Formation of Iron Oxide Layer

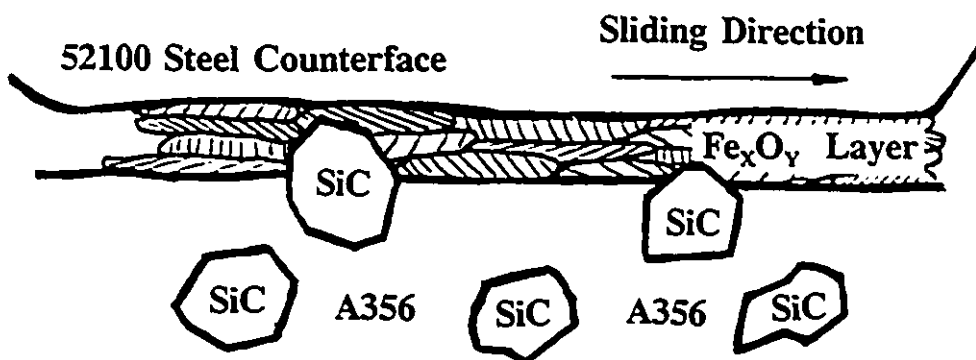


Figure 65. Schematic description of sliding wear mechanisms in particulate composites at low loads.

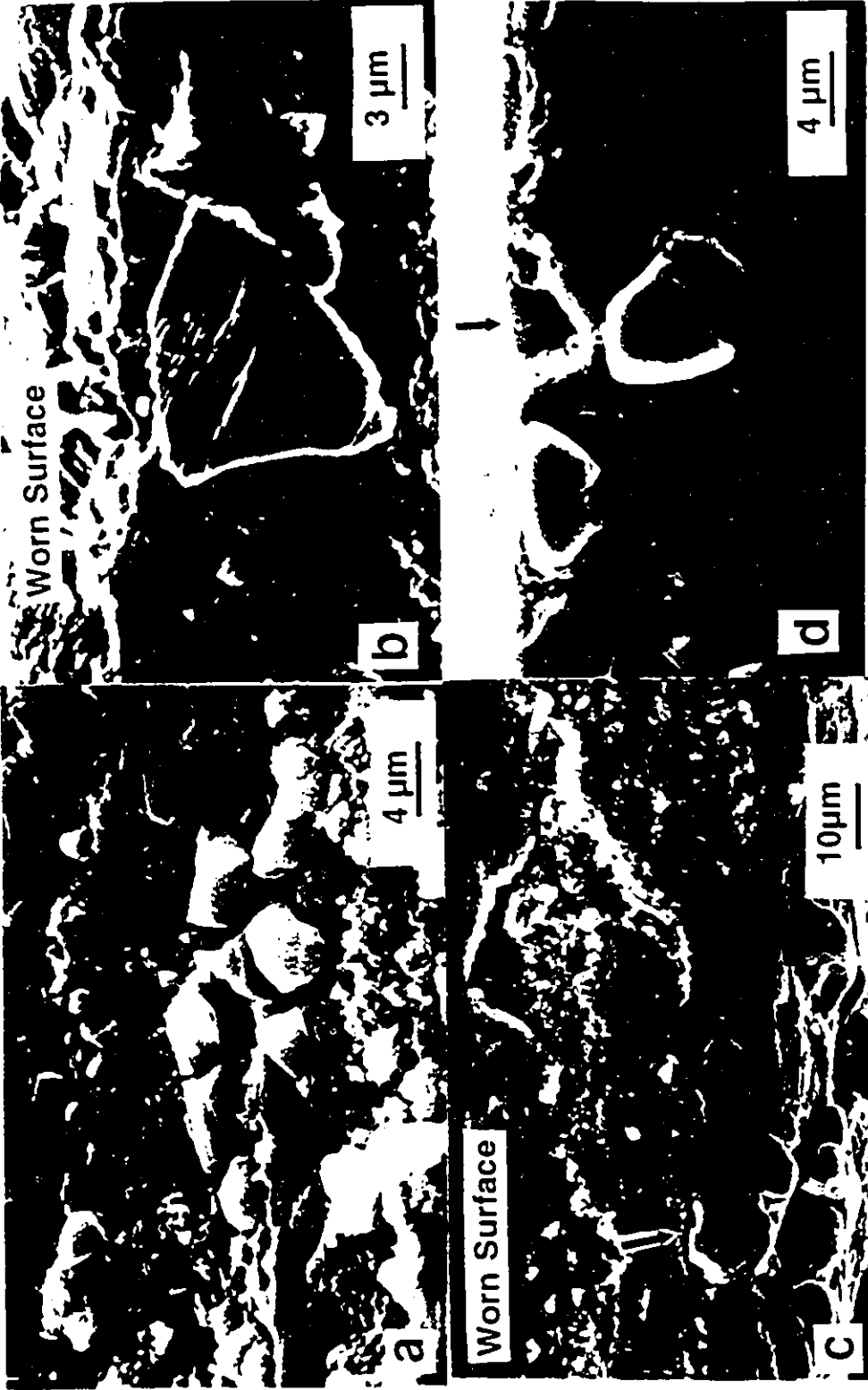


Figure 66. (a) Examples of broken Al_2O_3 particles on the worn surface of the composite; (b) cross-section through the worn surface revealing the cleavage fracture of a particle; (c) particle loss from the surface by a pull-out process; the arrow shows a particle which is about to detach; (d) a cavity left behind possibly by a decohered particle (regime II).

micrograph of the subsurface region of A356Al (Figure 30) indicates that this region is characterized by a deformation pattern in which the grain boundaries are increasingly bent towards an orientation nearly parallel to the contact surface. Very near the contact surface the microstructure exhibits a series of overlapping grain boundaries with grain thickness of less than one micron which is indicative of the large strains accumulated in this region.

The SEM investigation for A356Al reveals two other important aspects of near surface microstructure: (i) void and microcrack nucleation; (ii) subsurface crack growth. Voids are found to nucleate around the silicon particles located inside the deformation zone. As shown in Figure 31 the particle/aluminum interfaces appear to be the preferential void nucleation sites. A typical subsurface crack propagating parallel to the main plane of the contact surface is illustrated in Figure 32. A portion of the material at the tail of the crack is previously detached to form loose wear debris. Notice the presence of the secondary cracks parallel to the surface but have not yet reached the surface. Part of the loose debris particles in regime II (Figure 68) are in the form of thin plates (5-20 μm thick) revealing that they were produced by subsurface fracture. Similar results have also been found in other unreinforced Al alloy and composites. examples of subsurface cracks in 6061Al-10%Al₂O₃ is shown in Figure 69.

Thus incorporation of ceramic particles into aluminum alloys can increase the rate of the subsurface crack initiation and propagation hence promote subsurface delamination by creating additional void nucleation sites and preferential crack growth paths at the particle-matrix interfaces. Consequently, once the particles are fractured, the advantage of the increased material hardness is lost and the relatively low fracture toughness of the

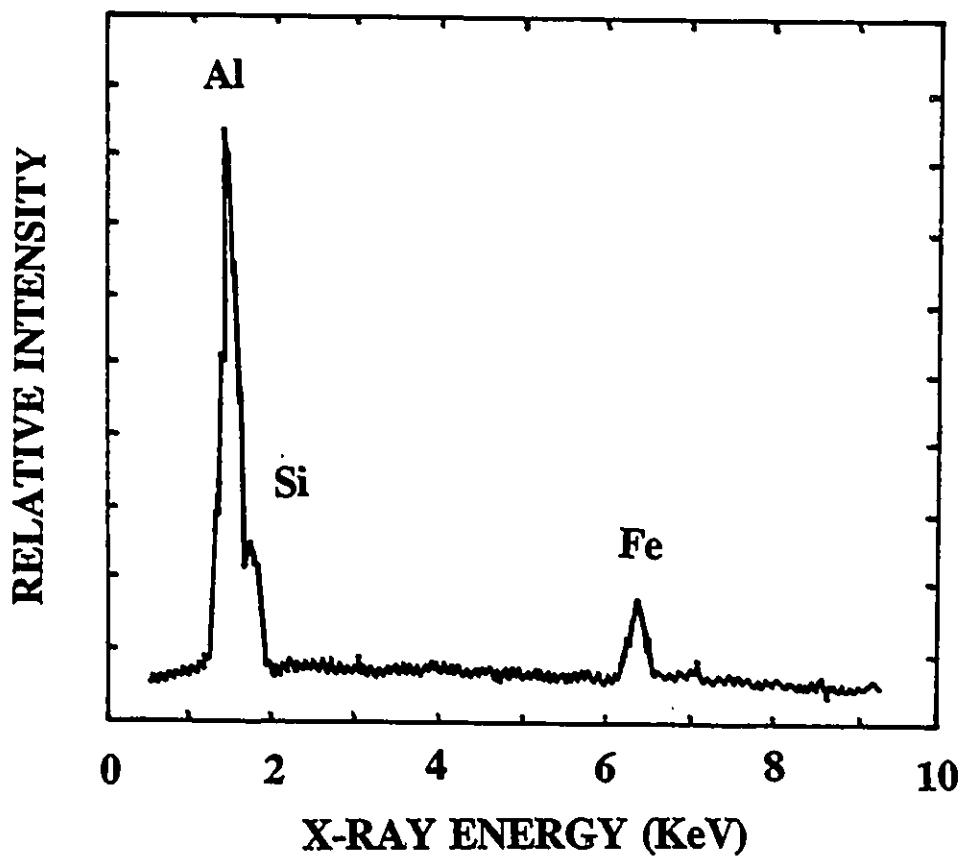


Figure 67. EDS analysis of the worn surface of A356Al-20%SiC in region II.

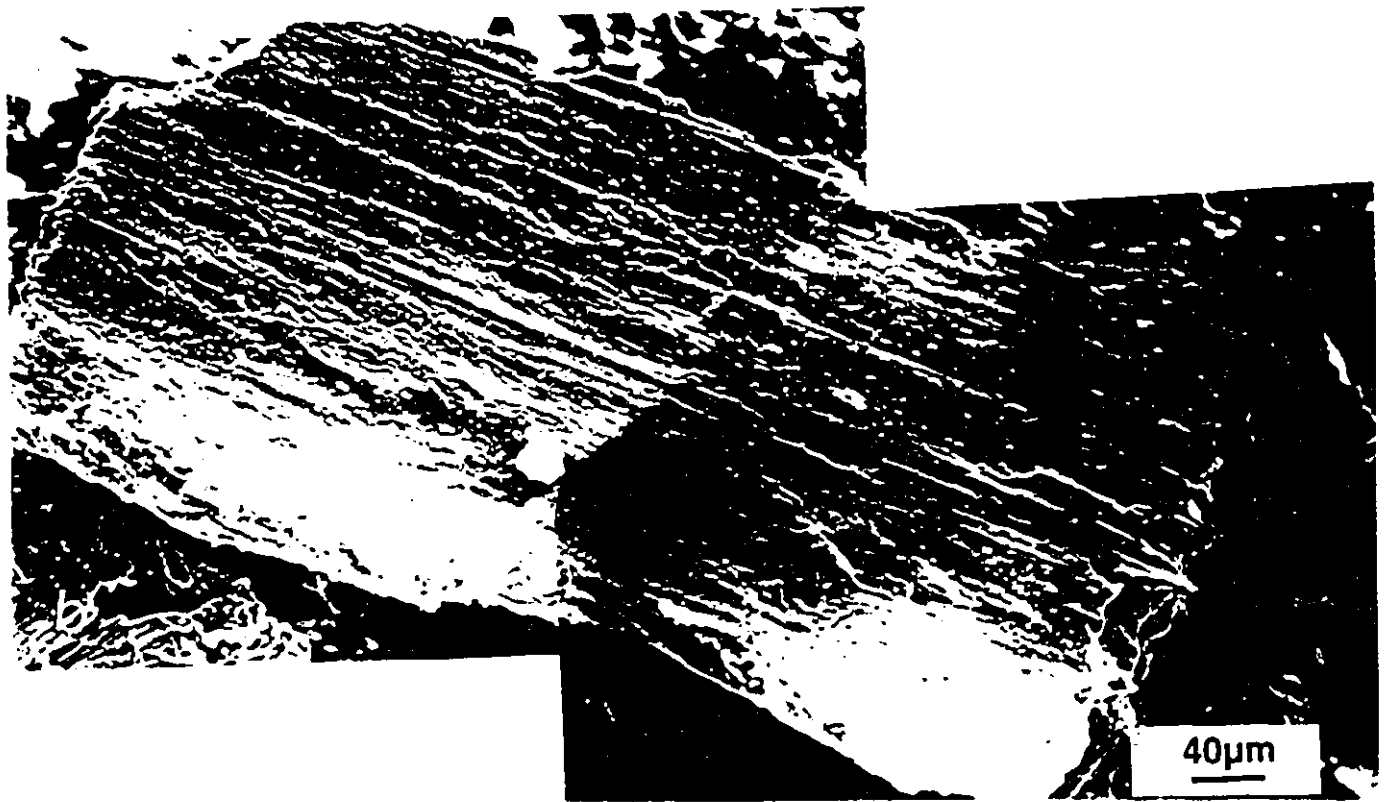
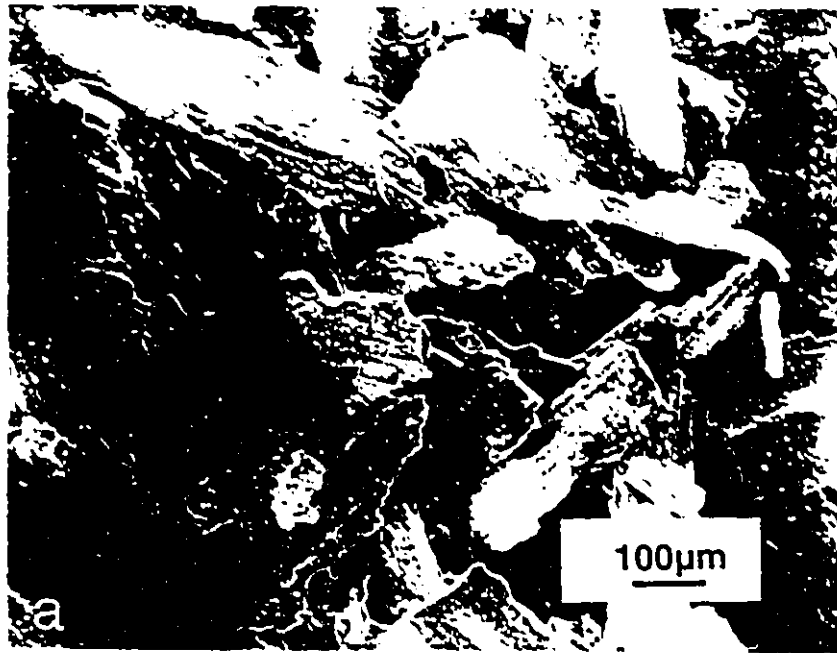


Figure 68. Loose debris particles generated from the 6061Al-20%Al₂O₃ at 40 N; (a) overall view of the plate-like debris; (b) top view of a debris particle (regime II).

composite adversely affects their wear resistance.

In addition to the plate-like debris particles which appear to be generated by delamination of subsurface layers as described above, another type of debris, namely fine-powdery particles (which are black in colour) have also been formed during the wear of monolithic alloys and the composites in the regime II. This type debris has also been observed by Antoniou *et al.* ¹¹⁴²¹ as an agglomerate of very fine particles (5-50 nm) of Al, Si and α -Fe in the case of Al-Si alloys wearing on steel. X-ray diffraction analysis of the debris particles collected directly from the wear tests did not reveal any clear evidence for aluminum oxide formation (Figure 35 and Figure 48). But when the black and powdery debris was separated from the rest (by filtering out larger platelike debris particles) and an X-ray analysis was performed on the black debris alone the presence of an amorphous phase was detected (Figure 70). Since the natural and thermally formed oxide films on aluminum alloy contain an amorphous layer ^[136, 143-145], the existence of amorphous phase on the contact surfaces may indicate formation of an aluminum oxide layer in regime II.

The importance of the formation of this black debris on the wear resistance is illustrated in Figure 71 by referring to the test performed on the 6061Al worn against the SAE 52100 steel counterface. Figure 71 shows that when a stepwise increase in sliding velocity with an initial low sliding velocity (0.2 m/s) was applied to the rubbing pair, the transition to severe wear is delayed to 473 K (200 °C), which is about 80 degree higher than the samples directly tested at a sliding velocity of 0.8 m/s under the same applied load (Figure 53(a)).

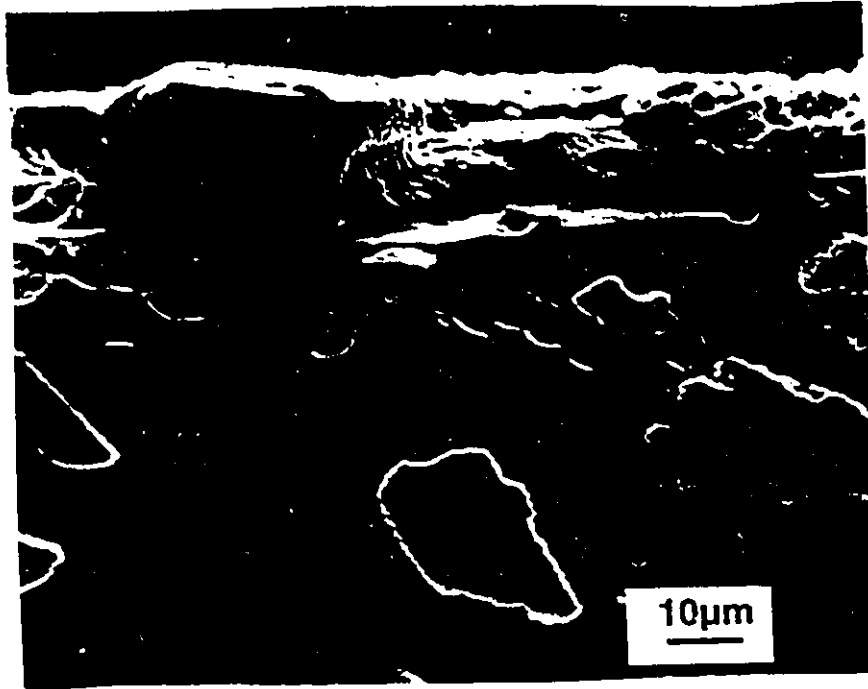


Figure 69. Subsurface crack in 6061Al-10%Al₂O₃.

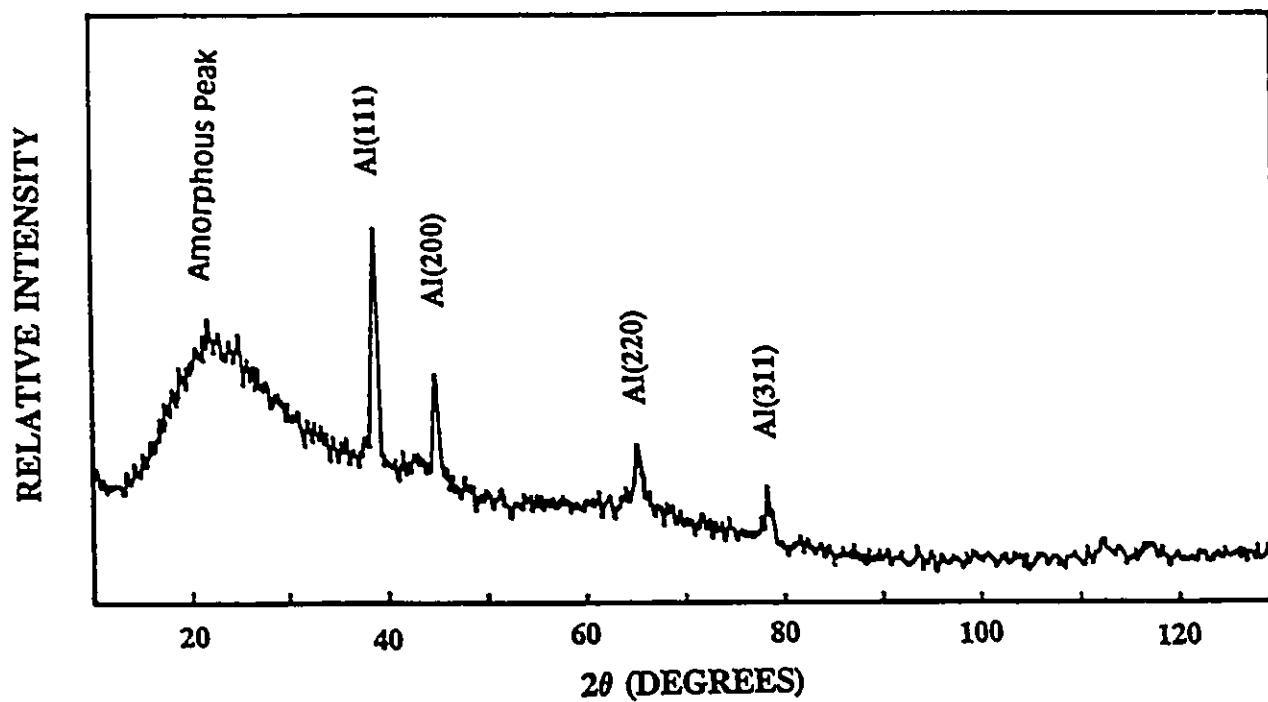


Figure 70. X-ray diffraction analysis of the black debris of 6061Al worn against 6061Al in regime II. (after filtering and using $\text{Cu-K}\alpha$).

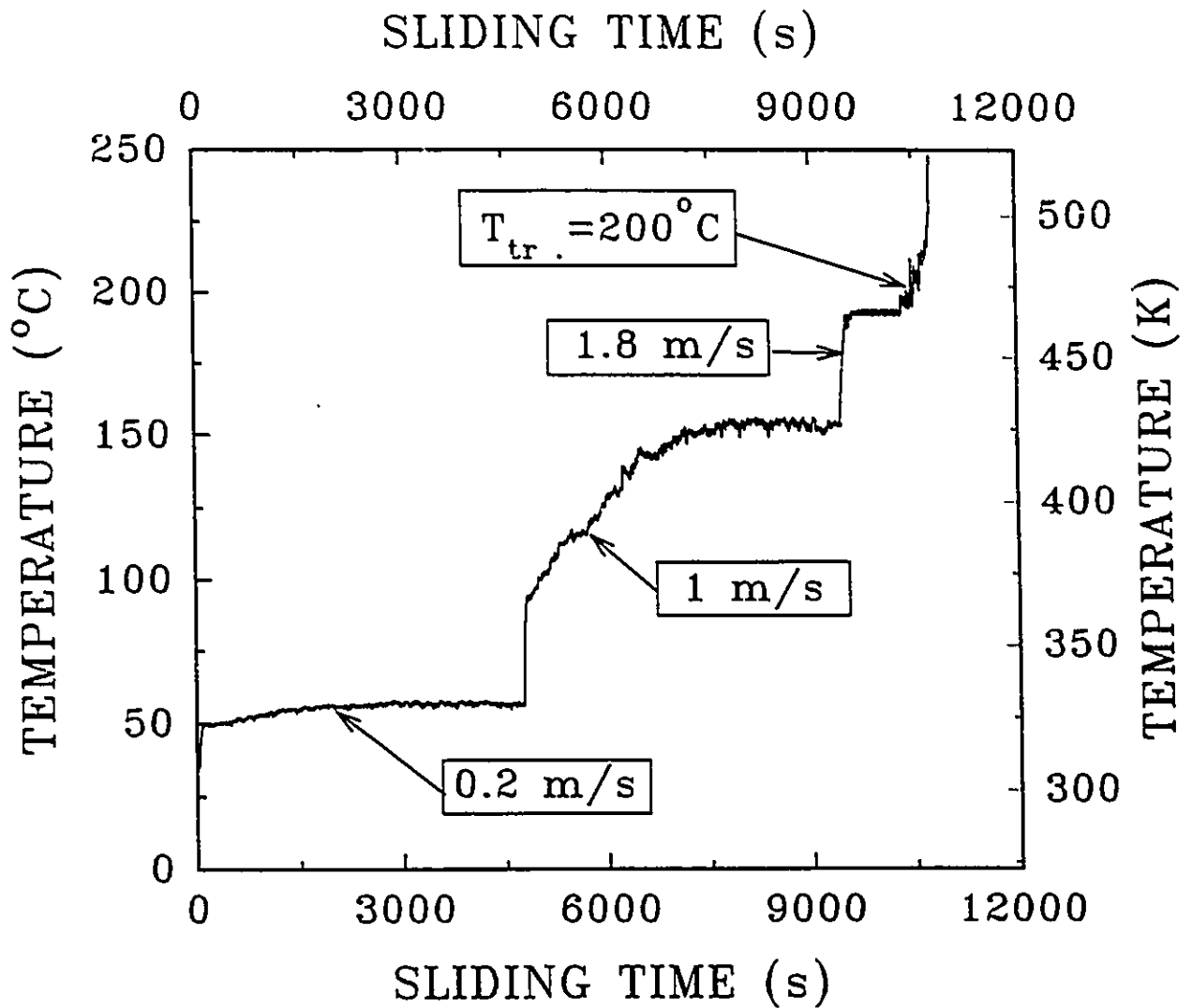


Figure 71. The temperature distribution at the contact surface of 6061Al as functions of sliding time and sliding velocity. Applied Load: 98 N; Counterface: ASE52100 bearing steel. Note: A mixture of black and white debris was formed between the contact surfaces when sliding velocity is 0.2 m/s.

Another important wear mechanism that operates in regime II is microgrooving due to the abrasive action of harder counterface asperities (two-body abrasion) and fractured (and pulled-out) SiC or Al₂O₃ particles (three-body abrasion). Both the fractured particles and the pulled-out particles are likely to act as the third-body abrasive constituents and could be responsible for the higher wear rate of the counterface (Figure 41). The additional abrasive wear (microploughing) component of the sliding wear caused by the presence of the Al₂O₃ or SiC particles can be regarded as another reason for not observing an improvement in the wear resistance of the composites in regime II.

In the light of the above discussion, it becomes clear that three possible wear mechanisms, namely abrasive wear (microploughing), oxidative wear and delamination wear, may operate in regime II. A schematic representation of the wear mechanisms in regime II is given in Figure 72. Since the proportion of platelike particles in the debris increases with the applied load, and in the meanwhile the proportion of small equiaxed particles (oxidized particles) decreases, it can be proposed that initially at low loads the abrasive and oxidative wear could be the dominant rate-controlling mechanisms, but with increasing load, the subsurface delamination becomes predominant.

5.1.3. WEAR MECHANISMS IN REGIME III (SEVERE WEAR)

The transition from mild to severe wear at a critical load is a well-documented phenomenon in cast aluminum alloys ^[48, 128, 146]. Present results indicate that, above a certain characteristic load at the end of the regime II, the slopes of wear rate vs load curves increase drastically. The transition to severe wear occurs at higher loads in the

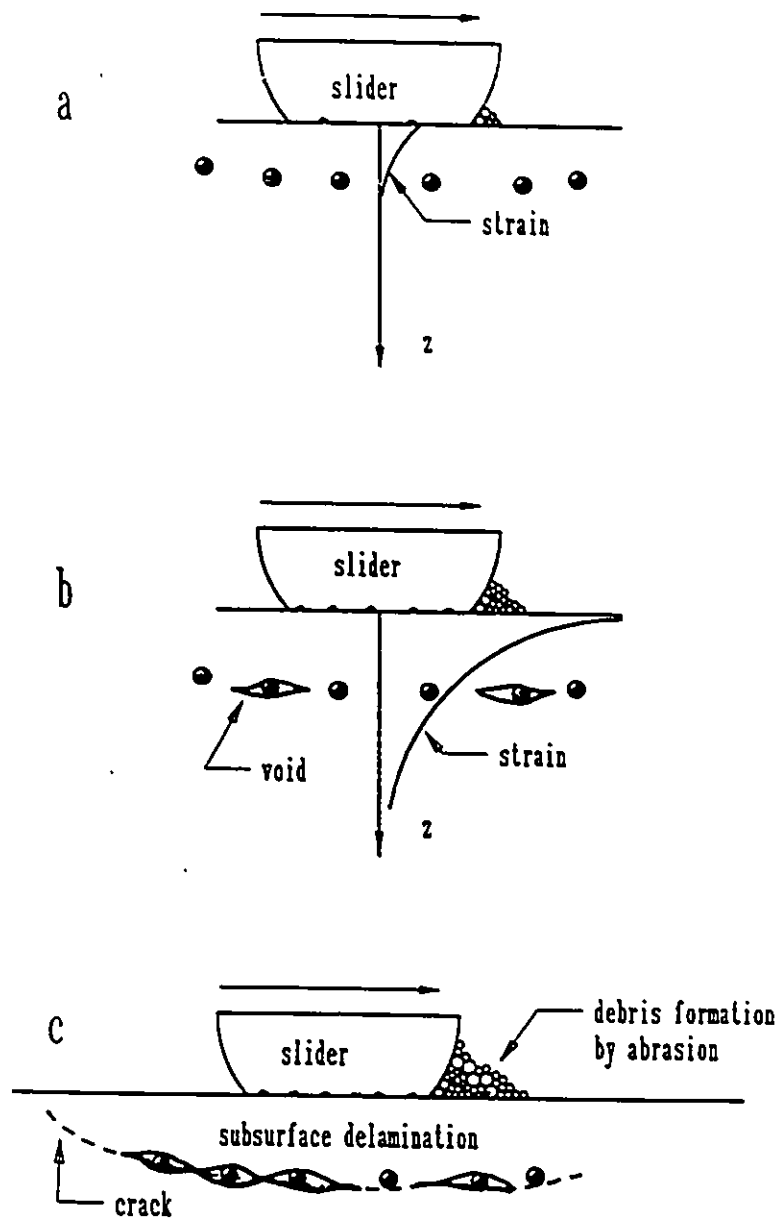


Figure 72. Schematic representation of the wear mechanisms in regime II; (a) in the incubation period both abrasive and cumulative damage processes are in progress. Plastic strains accumulate with each succeeding contact cycle; (b) the plastic strain has reached a critical level such that nucleation of voids has taken place in some critical depth away from the surface; (c) platelike debris formation occurs when the subsurface damage has reached the contact surface. Equiaxed particles are formed by partial disintegration at the contact surface.

composites compared to the unreinforced Al alloys (Table VIII). For example, in the 6061Al, the transition occurs at 50 N and the 20%Al₂O₃ reinforcement impedes the transition until 230 N.

The wear in regime III proceeds by severe surface damage and involves large scale material transfer to the counterface (Figure 73(a)). This is the type of wear also referred to as galling, scuffing or seizure. However, the wear process in regime III is essentially a large scale deformation and damage accumulation process. But the surface damage and the rate of material loss in regime III is so extensive that from a practical point of view the transition to severe wear can be considered as the upper limit of the useful wear life of aluminum alloys in actual service conditions. Understanding wear mechanisms in regime III is however important for controlling the extent of regime II and is also relevant to MMC processing technology because this type of wear is likely to occur between the material and the die in hot extrusion and between two composites being joined by solid state diffusion bonding. The loose debris particles generated during severe wear are often in the form of thick plates (50-200 μm) as shown in Figure 74. Irregular and larger particles are also found especially at higher loads in this region. The plate-like debris produced during severe wear is different from the delamination debris of region II (Figure 68) because the former possess a lamellar structure, i.e. as seen in Figure 74(b) the debris is typically a composite aggregate formed by several severely deformed layers (in this case, three) stuck together. The depths of the deformed aluminum layers below the worn surfaces are of the order of 300-400 μm, i.e., about 10 times deeper than the typical thickness of the deformed zones in regime II. Also, because of the extremely high surface

Table VIII. The Transition Load P_t and Transition Temperature T_t ,
for the Materials Tested ($V=0.8$ m/s)

Materials	Regime I to II		Regime II to III	
	P_t (N)	P_t (N)	T_t (K)	
A356Al	---	95	418	
A356Al-20%SiC	15	250	>500	
6061Al	---	50	395	
6061Al-10%Al ₂ O ₃	5	90	---	
6061Al-20%Al ₂ O ₃	10	230	440	
2014Al	---	90	---	
2014Al-20%SiC	9	150	---	
2124Al-20%SiC	8	140	---	

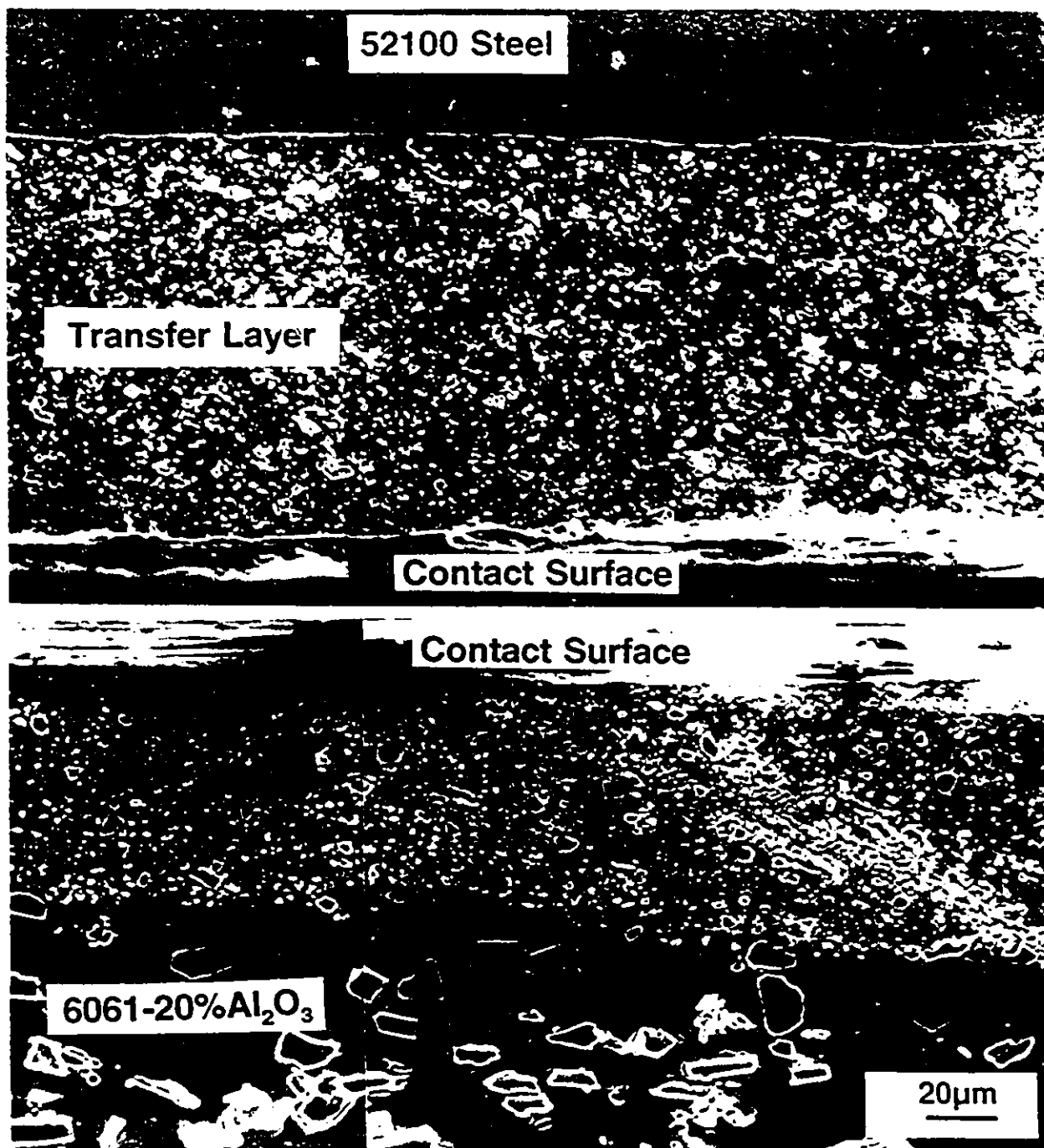


Figure 73. Cross-section of 6061Al-20%Al₂O₃ showing (a) the layers consisting of broken Al₂O₃ particles on the test piece and (b) same layers transferred on to the SAE52100 counterface (regime III).

strains, particles became fragmented and comminuted to a mean particle size which is roughly one-fifth of the original. The morphology of the surface layers consisting of fractured ceramic particles is shown in Figure 73(b). These layers have a thickness of approximately 100 μm and were found to spread continuously on the contact surfaces. During the wear tests the layer with broken particles transferred and adhered on to the counterface material leading to a weight gain of the counterface (figure 73(a)). Examination of the worn surfaces of the composites revealed that as a result of severe surface deformation these layers formed a pattern of "shear wedges". During the wear process some parts of the wedges broke away by a tensile fracture mechanism as revealed by the dimple morphology left behind (Figure 75). The average dimple diameter is of the order of 1 to 5 μm which correlates well with the size of comminuted particles. The origin of the tensile failure can be attributed to the development of adhesive forces between the surface layers and the material transferred to the counterface. During the wear tests in regime III, the worn material was often welded to the counterface. Shear wedges (and tensile dimples) were also apparent on the material adhered to the counterface. This implies that transfer and back transfer events occurred during wear. Debris particles in the form of multilayered (about 3-5 layers) fragments consisting of severely deformed materials layers are believed to have formed during the transfer and back transfer processes between both contact surfaces. Another type of material removal mechanism observed in regime III was associated with the formation of a "prow" ahead of worn surfaces (Figure 76). Detachment of the fragments of material by tearing away from the prow appears to be an important debris formation mechanism, especially at high

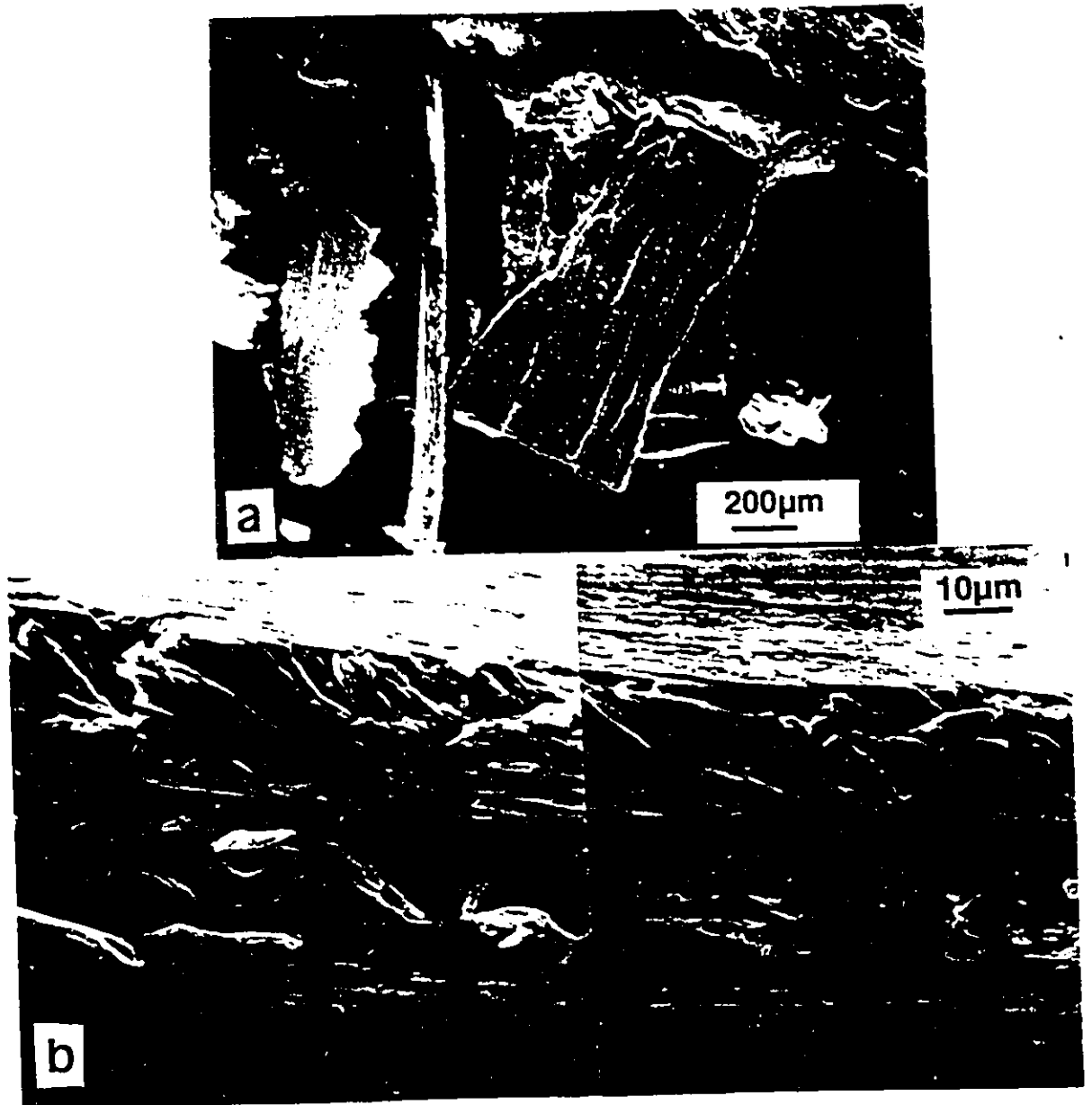


Figure 74. Debris particles produced from the surface of 6061Al-20%Al₂O₃ at 300 N; (a) overall view of debris particles; (b) high magnification cross-sectional view of a debris particle showing its lamellar structure (regime III).

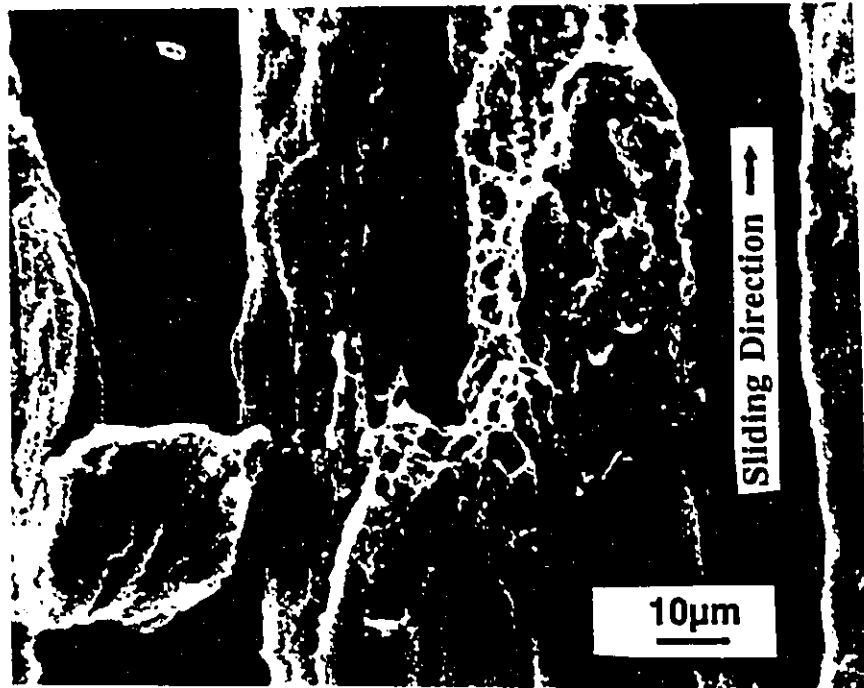


Figure 75. Worn surface morphology in regime III (6061Al-20%Al₂O₃, 230 N); tensile dimples formed during fracturing of the "shear wedges".

loads where most of the debris particles were coarse and irregular in shape.

5.2. FACTORS INFLUENCING THE WEAR TRANSITIONS

5.2.1. EFFECT OF SLIDING VELOCITY

In addition to the applied load, the dry sliding wear behaviour is also affected by the sliding velocity. When the steady state wear rates obtained from the sliding distance vs volume loss curves are plotted against the sliding velocity (under a constant applied load), such as the ones shown in Figure 50, they exhibit the following features: the wear rate first decreases with increasing sliding velocity and then starts to increase again. The decrease in the wear rates with velocity could be attributed to the competition between strain hardening and thermal softening that occurs concomitantly in the material. The hardness of a material increases with the strain rate and decreases with the temperature. According to Archard's equation of wear^[42]: $W=kPS/H$ (Eqn. 2.1), the volume of material lost would decrease with increasing hardness. During the dry sliding tests, with increasing sliding velocity, the strain rate at the surface increases but at the same time the contact surface temperatures increase simultaneously. In the lower sliding velocity region, the temperature increase is not significant and the strain hardening of the material appears to play a more important role than the thermal softening. But in the higher sliding velocity region, the softening of the material because of frictional heating may become the controlling factor. Therefore, as a result of the competition between these two opposing effects, the wear rate decreases to a minimum with sliding velocity and then increases again.



Figure 76. Material squeezed out of the front edge of the worn surface (prow). Large debris particles are formed as a result of tearing away from the prow. (6061Al-20%Al₂O₃, 270 N, regime III).

Figure 50 indicates that under lower applied load (4.9 N, for example), the wear resistance of 6061Al-20%Al₂O₃ is more than ten times higher compared to that of the unreinforced 6061Al throughout the sliding velocity range studied (0.01-4 m/s). This improvement, as discussed before, can be attributed to the load bearing effect of ceramic particles and to the formation of oxides on the contact surfaces. At higher applied loads, such as 49 N, the wear resistance of the composite is similar to the unreinforced 6061Al in the low sliding velocity region. But the transition to severe wear in the composite material is delayed to 3.2 m/s as compared to 0.8 m/s for the unreinforced 6061Al. Also as shown in Figures 51 and 52 which illustrate the effect of sliding velocity on the transition load in both 6061Al and 6061Al-20%Al₂O₃, the transition load is delayed to higher load with decreasing sliding velocity. Since attainment of a critical temperature is needed for this transition (see section 5.2.3. for detailed discussion), it follows that when the sliding velocity decreases, a higher applied load is required to produce the same contact temperature. However, when the sliding velocity is low (*e.g.* 0.2 m/s), no severe wear has been observed for the unreinforced 6061Al alloy throughout the load range studied (1 -420 N). In this situation even the maximum load applied was not enough to increase the surface temperature to the critical temperature for the transition (figure 51).

5.2.2. EFFECT OF TEMPERATURE

A better understanding of the severe wear behaviour can be obtained by studying the thermal conditions under which the surfaces are rubbed together. Kragelskii ^[51], Hirst and Lancaster ^[147], and Welsh ^[38] proposed that a transition from mild to severe wear in

ferrous materials would occur when the temperature at the contact surfaces exceeded a critical temperature. It has been observed that for various metals, adhesion increased rapidly as temperature reaches about $0.4 T_m$ ^[148]. The contact temperatures reached after a sliding distance of 10^3 m are plotted against the applied load (Figure 77 and 78) and the sliding velocity (Figure 79). The measured temperature represents an average temperature of subsurface material 5 to 50 μm below the contact surfaces. In the unreinforced 6061Al, the severe wear (which is easily detected by the unaided eye during the tests) initiates whenever the temperature reaches 395 ± 10 K. This corresponds to about 0.4 of the absolute melting temperature of aluminum. At this temperature range, thermally activated deformation processes are expected to become active and lead to the softening of the layers adjacent to the contact surfaces. Recently Singh and Alpas ^[149] gave metallographic evidence for dynamic recrystallization during severe wear in 6061Al alloy. The transition temperature can thus be regarded as a characteristic temperature where thermally activated processes become a rate controlling parameter. However, as indicated in Figure 53, the transition temperature in the 6061Al-20%Al₂O₃ is 440 ± 10 K which is 45 K higher than that in the unreinforced 6061Al.

The temperature rise due to the frictional heating depends upon the combined effects of the load and speed. Thus one way of avoiding the transition to seizure is to properly select applied load and sliding velocity in order to keep the temperature below the critical transition temperature under the operating conditions. It can be proposed that in general the rate of heat dissipation from the wear system will determine the magnitude of the transition temperature. This depends, in addition to the effect of load and velocity

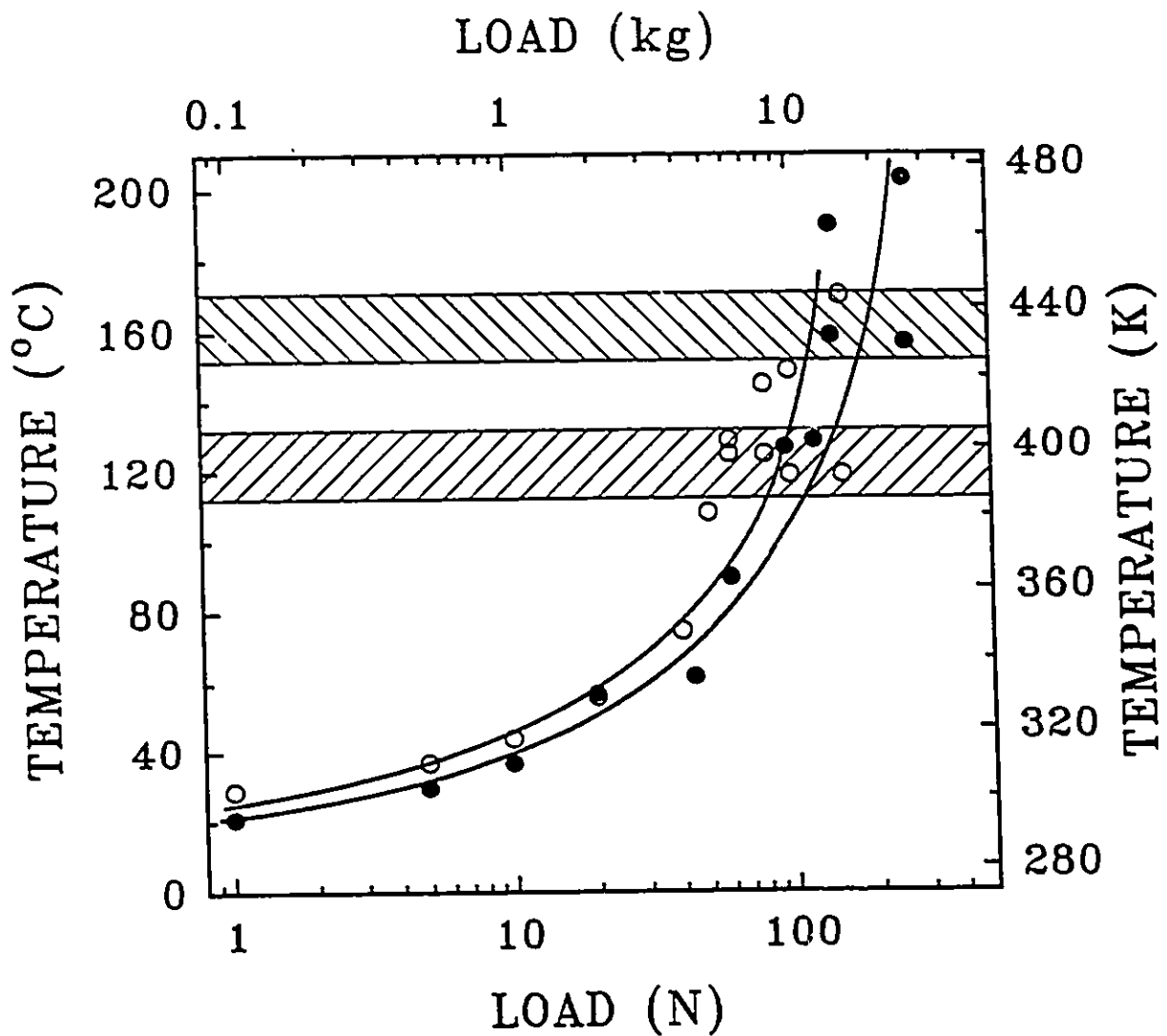


Figure 77. Temperature of the worn surfaces after sliding to 1000 m vs. applied load on: (○) 6061Al, and (●) 6061Al-20%Al₂O₃. Transition occurred when the temperature reached 395 ± 10 K in 6061Al and 435 ± 10 K in 6061Al-20%Al₂O₃. Data in the shadow area indicate temperatures at which transition to severe wear is first observed during sliding at a given applied load. Sliding velocity=0.8 m/s.

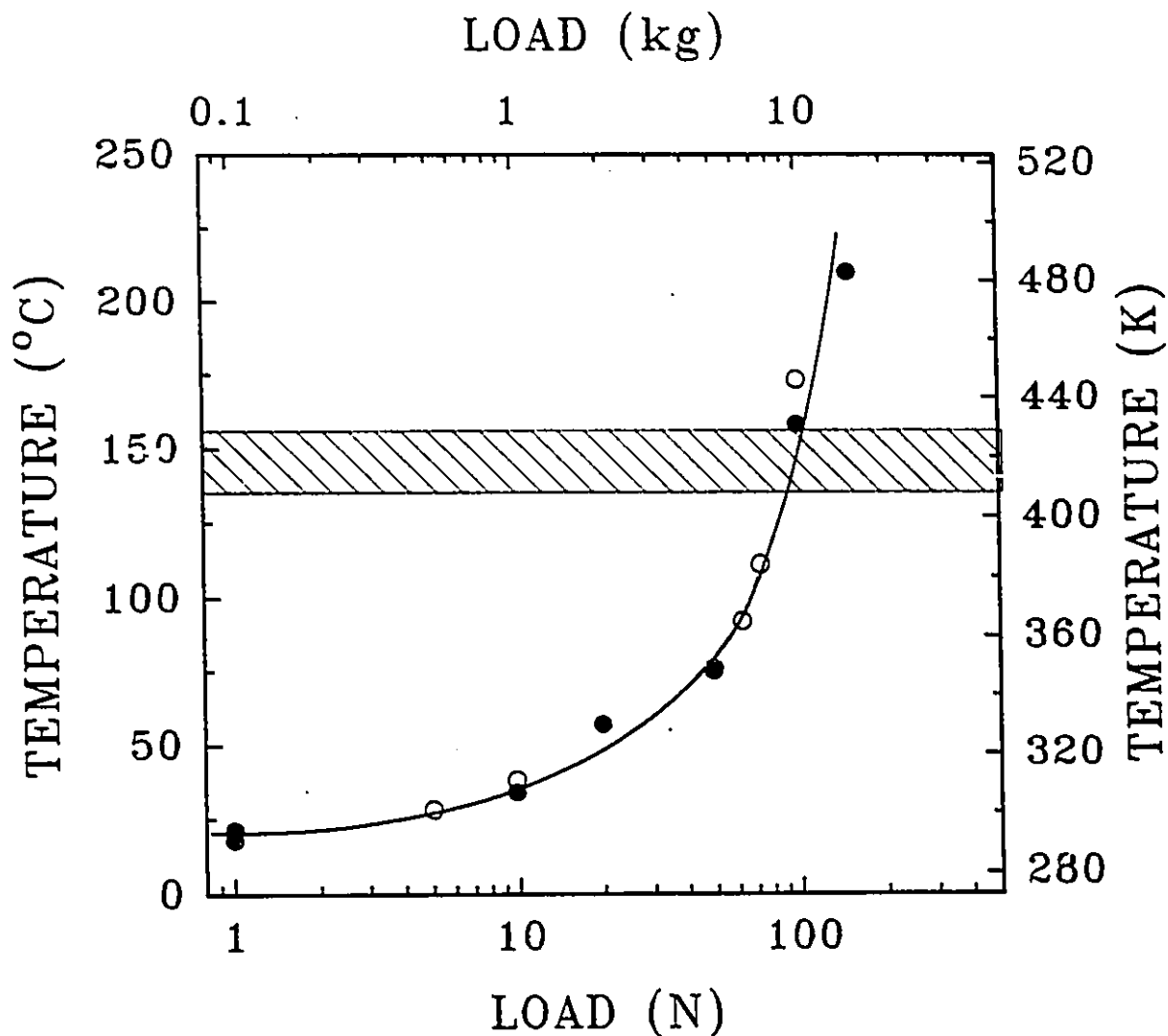


Figure 78. Temperature of the worn surfaces after sliding to 1000 m vs. applied load: (\circ) A356Al, and (\bullet) A356Al-20%SiC. Transition occurred when the temperature reached 418 ± 10 K in A356Al. No transition has been found in A356Al-20%SiC below 480 K. Sliding Velocity: 0.8 m/s.

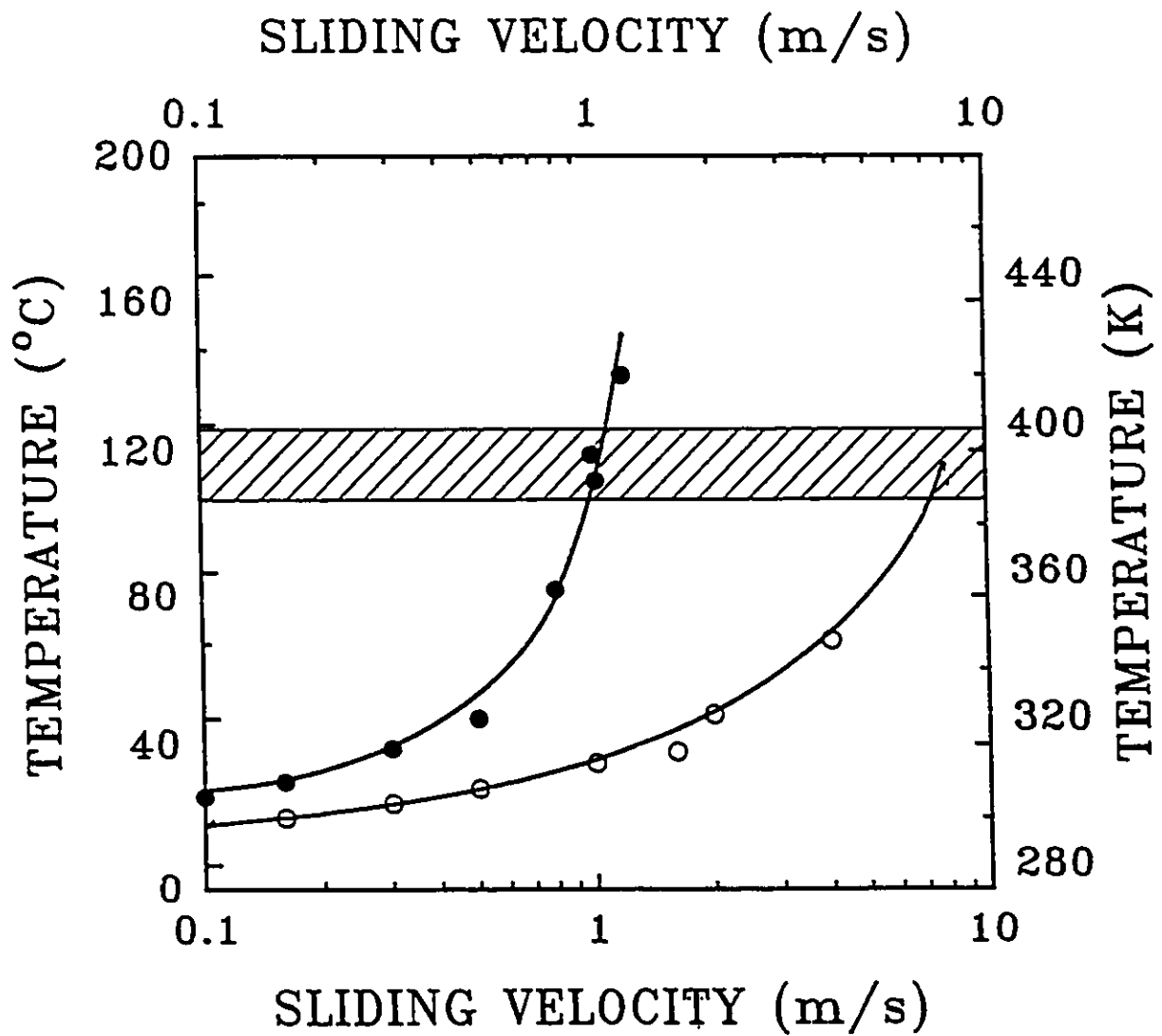


Figure 79. Temperature of the worn surfaces after sliding to 1000 m vs. sliding velocity on 6061Al: (○) 4.9 N and (●) 49 N. Transition occurred when the temperature reached 395 ± 10 K. Data in the shadow area indicate temperatures at which transition to severe wear is first observed during sliding at a given sliding velocity.

which have been already discussed, on the geometry of the system and on the thermal properties of the materials involved in the tribological system. By increasing the heat dissipation rate from the tribological system, the mild wear regime can be extended to higher loads and sliding velocities. This view is experimentally proven as shown in Figure 80, in which two groups of unreinforced 6061Al alloy specimens were tested under 98 N and a constant sliding speed 0.8 m/s. One set of specimens was cooled by circulating cold water around the specimen holder during the tests. The results indicate that surface bulk temperatures of the water cooled specimens remained lower than the transition temperature, 395 K, obtained during the "regular tests", and therefore no transition from regime II to regime III was observed. But when the test was repeated under the same applied load and sliding velocity conditions without cooling the system, a transition to severe wear occurred as soon as the surface temperature reached the critical transition temperature (395 K). The effect of the thermal properties on the transition will be discussed in conjunction with the role of counterface material in Section 5.4.

It should be noted that transition temperature may also vary with the contact surface conditions. Formation of oxide layers and surface lubrication will delay the transition to higher temperature. One example to illustrate the effect of surface conditions is given in Figure 71. When the speed is increased step-wise under a constant applied load, the transition of 6061Al has been found to occur at about 473 K which is about 80 K higher than the one obtained under constant velocity. This is possibly due to solid lubrication effect of the oxides formed at low speeds.

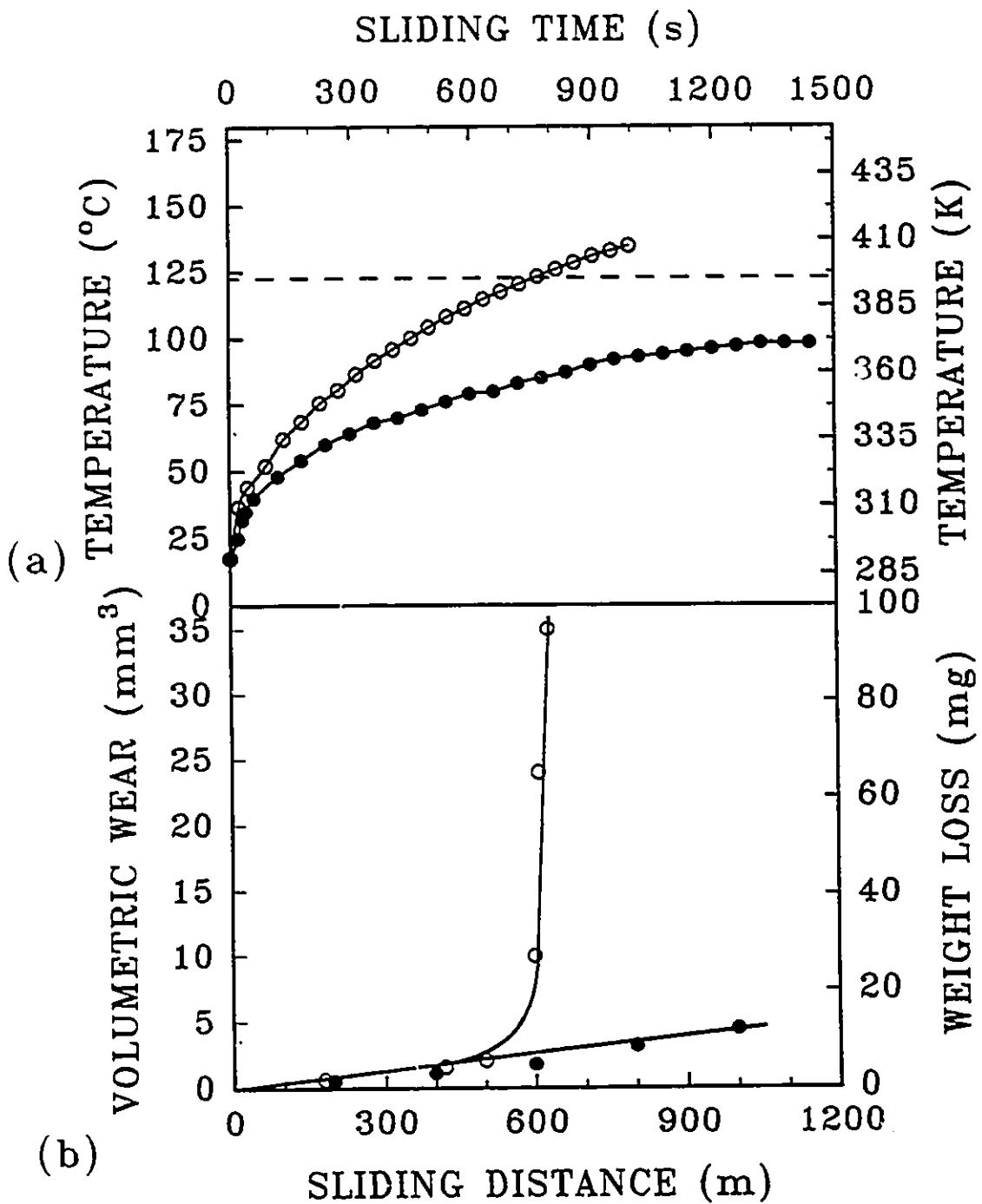


Figure 80. Effect of heat dissipation rate of the test system
 (a) Temperature distribution at the contact surface;
 (b) Volume loss vs. sliding distance under same test condition.
 (o) Without cooling; (●) With cooling. Applied Load: 98 N.
 (6061Al sliding on SAE52100 steel)

5.3. EFFECT OF MICROSTRUCTURE ON WEAR RATES

5.3.1. EFFECT OF PARTICULATE SIZE

The wear resistance of the aluminium-matrix composites in the ultra mild wear regime (regime I) is sensitive to the size of the reinforcing particles (Figure 58). The relationship between the particulate size and the wear damage is schematically illustrated in Figure 81. When the particulate size is of the order of surface roughness (e.g., 1 to 2 μm), particles can only provide a limited protection to the matrix (Figure 81(a)). When the mean particulate size is increased by a factor of 6 as in Figure 81(b), particles can carry the applied load and protect the aluminum matrix efficiently. In the case of wear against a steel counterface, it was observed that the transfer layers were thicker and entirely covered the contact surfaces of the composites reinforced with 15.8 μm SiC. This implies that coarser particles are more effective either in leading to the abrasion of the steel or holding the transfer layers on the contact surfaces than the composites with 2.4 μm SiC. In fact, SEM investigations revealed that the matrices of the composites reinforced with fine particles received more extensive damage. Wear in regime I involves processes such as particle fracture, decohesion, and pull-out processes that occurred at higher loads (in regime II) in the alloys with coarse particles. In this respect, it can be suggested that composites with fine SiC particles show a mixed wear behaviour at low loads and their wear resistances are only slightly higher than those of the unreinforced alloys.

The wear resistances of the unreinforced and the reinforced materials in regime II are similar under a sliding velocity of 0.8 m/s (figure 58). The reasons for this

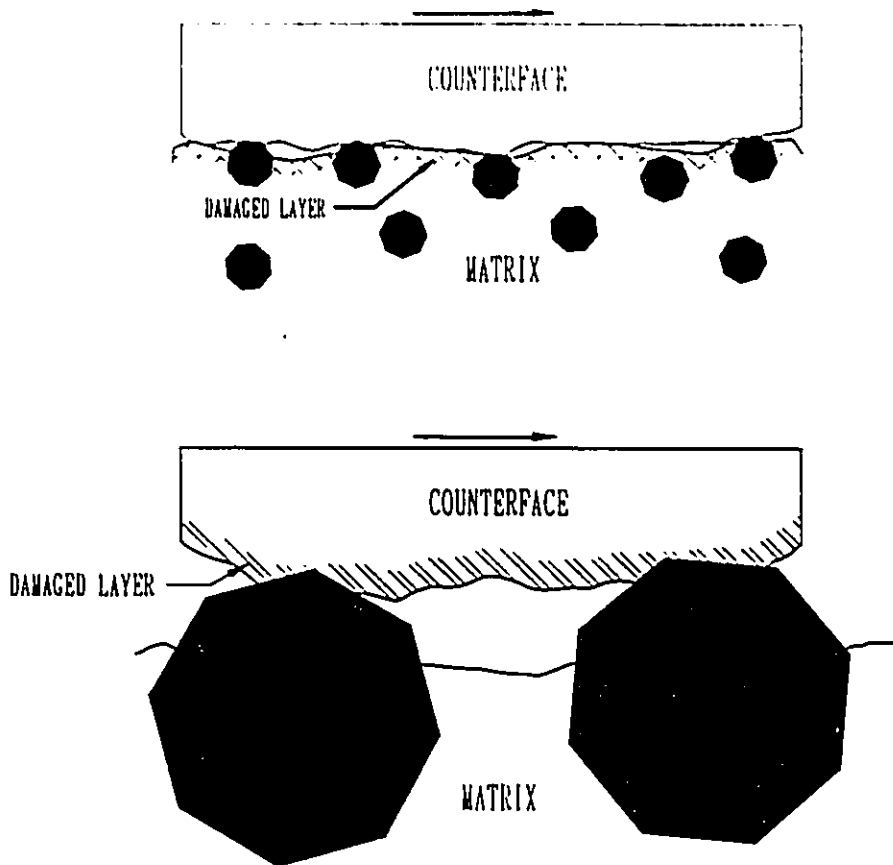


Figure 81. Schematic illustration of the effect of the particle size on the wear of the matrix in regime I: (a) when the mean particle size is of the order of the surface roughness, particles are not effective restricting the damage of the matrix; (b) coarse particles (mean particle size is six times larger than that of (a)) provide better protection to the matrix and may induce damage to the counterface.

behaviour have already been discussed and can be summarized as follows: (i) The reinforced particles are fractured and lose their ability to support the applied load, and thus the aluminium matrices become in direct contact with the counterfaces. (ii) The fractured particles provide preferential propagation paths for subsurface cracks which increase the propensity for material loss by subsurface delamination. (iii) The fractured and pulled-out particles are entrapped between the counterface and the composites and may cause abrasive wear. Consequently the benefits of the reinforcement are balanced by these disadvantages.

In regime III, there is also no significant difference between the wear resistances of the composites with different particle sizes. This could be because when the applied load is higher than the transition load almost all of the ceramic particles in the deformed zones adjacent to the worn surfaces would be fractured and eventually become fragmented into small particles (figure 73).

5.3.2. EFFECT OF VOLUME FRACTION

Increasing the volume percent of particles has a positive effect of delaying the transitions (both from regime I to regime II and regime II to regime III) as shown in Figure 57. In regime I, since there is no significant difference in the wear rates of 6061Al-10%Al₂O₃ and 6061Al-20%Al₂O₃, it follows that 10 percent reinforcement is as effective as 20 percent reinforcement in supporting the applied load at the low loads of regime I.

It is interesting to note that the wear resistances of the 6061Al-Al₂O₃ composites

which contain relatively coarse particles ($\approx 14 \mu\text{m}$) are comparable to those of the 2014 alloy reinforced with coarse SiC particles ($\approx 16 \mu\text{m}$) (Figure 58) despite the differences in the compositions of the matrices and the particles. The probability of particle fracture increases with the applied load until the fraction of the unfragmented particles on the contact surfaces is no longer adequate to carry the load. The total area fraction of the unbroken particles in the material with 10 percent reinforcement decreases faster than that with 20 percent reinforcement. Consequently, the transition to regime II occurs earlier in the composites with lesser amount of reinforcement. An extreme example is given in Figure 57 in which results of a Al_2O_3 -SiC ceramic specimen rubbing against a SAE 52100 bearing steel are shown by a dashed line. This material can be considered to be equivalent to a 100% reinforcement and no transition has been found in this material (sliding velocity: 0.8 m/s) up to an applied load of 200 N.

The transition load to severe wear is moved to higher loads as the percentage of particles increased so that the transition loads correspond to 60, 90 and 230 N for the unreinforced alloy and alloys with 10% and 20% reinforcement, respectively. The wear resistance of the alloy with 20% Al_2O_3 is the highest in the severe wear regime. As discussed in the previous section, the transition to severe wear takes place when the temperature at the contact surface exceeds a critical temperature and the transition temperature increases with ceramic particle additions.

5.4. EFFECT OF COUNTERFACE MATERIAL

The overall shape of wear rate curves for the 6061Al and the 6061Al-20% Al_2O_3

sliding against the mullite is similar to those for sliding against the SAE 52100 steel (Figure 56). The effect of using a mullite slider is to increase the wear rates in each regime to higher levels (by a factor of about 10), and the transition loads between the wear regimes are shifted to lower load levels.

In order to rationalize the effect of the counterface material on the wear resistances of the aluminum and the composites, attention should be given to the following properties: (i) hardness difference between the counterface and the specimens; (ii) thermal conductivity and surface temperature. Since the mullite is much harder (VHN=1700 kg/mm²) than SAE 52100 steel (VHN=950 kg/mm²), the increase in the wear rate of composites sliding against the mullite ring could be at least partly attributed to the enhanced abrasive wear.

As the thermal conductivity of the mullite is nearly an order of magnitude less than that of steel (4.1 and 45 W/mK, respectively), the heat input into the sample is larger when compared to tests involving steel rings because the frictional heat has to be removed mainly through the 6061Al alloy (or its composites). The role of the counterface material on the transition to severe wear can be rationalized on the basis of the critical transition temperature concept. The results show that the transition load is reduced (e.g., from 200 to 90 N for 6061Al-20%Al₂O₃ (Figure 56) when the materials are worn against the mullite instead of the steel. Consequently, the transition temperature is reached at lower loads. This is demonstrated in Figure 82 for an unreinforced 6061Al. At a load of 49 N when the alloy is worn on mullite, the transition temperature (395 °K) is reached shortly after the test has started. The wear rate of the material is high at ($\dot{W}=3 \times 10^{-1}$ mm³/m (Figure

56)). When the same material is worn on an SAE 52100 counterface at the same load, the surface temperature remains below the transition temperature ($T_{\text{tr}}=395$ K) and the wear rate is 1.5×10^{-3} mm³/m. Consequently, rubbing the reinforced or monolithic alloys on a counterface with low heat conductivity reduces the transition load and promotes severe wear.

5.5. WEAR MAPS

It has been shown that the aluminum matrix composites exhibit a transitional wear behaviour and show three wear rate regimes namely Regime I (ultra mild wear), Regime II (mild wear) and Regime III (severe wear). Figures 83 and 84 show wear regime maps, *i.e.* boundaries between the wear regimes on log load-log velocity axes, for the 6061Al alloy and the 6061Al-20%Al₂O₃ composite respectively. As discussed previously, only two wear regimes are identified for the unreinforced 6061Al alloy. The solid line in Figure 83 shows the boundary separating the mild and severe wear regimes. If the combination of the applied load and the sliding velocity falls above the solid line, severe wear will occur. For any combination below it, mild wear will occur. Thus Figure 83 provides a convenient way of predicting the wear behaviour of this material in terms of applied mechanical factors. On the other hand, three wear regimes are identified for 6061Al-20%Al₂O₃ (Figure 84). Two solid lines have been drawn to separate the three wear regimes. The lower line, which gives the average value of the transition load zone, delineates the transition from ultramild (regime I) wear to mild wear (regime II). Any combination of load and sliding velocity lying below this line would give ultra mild wear.

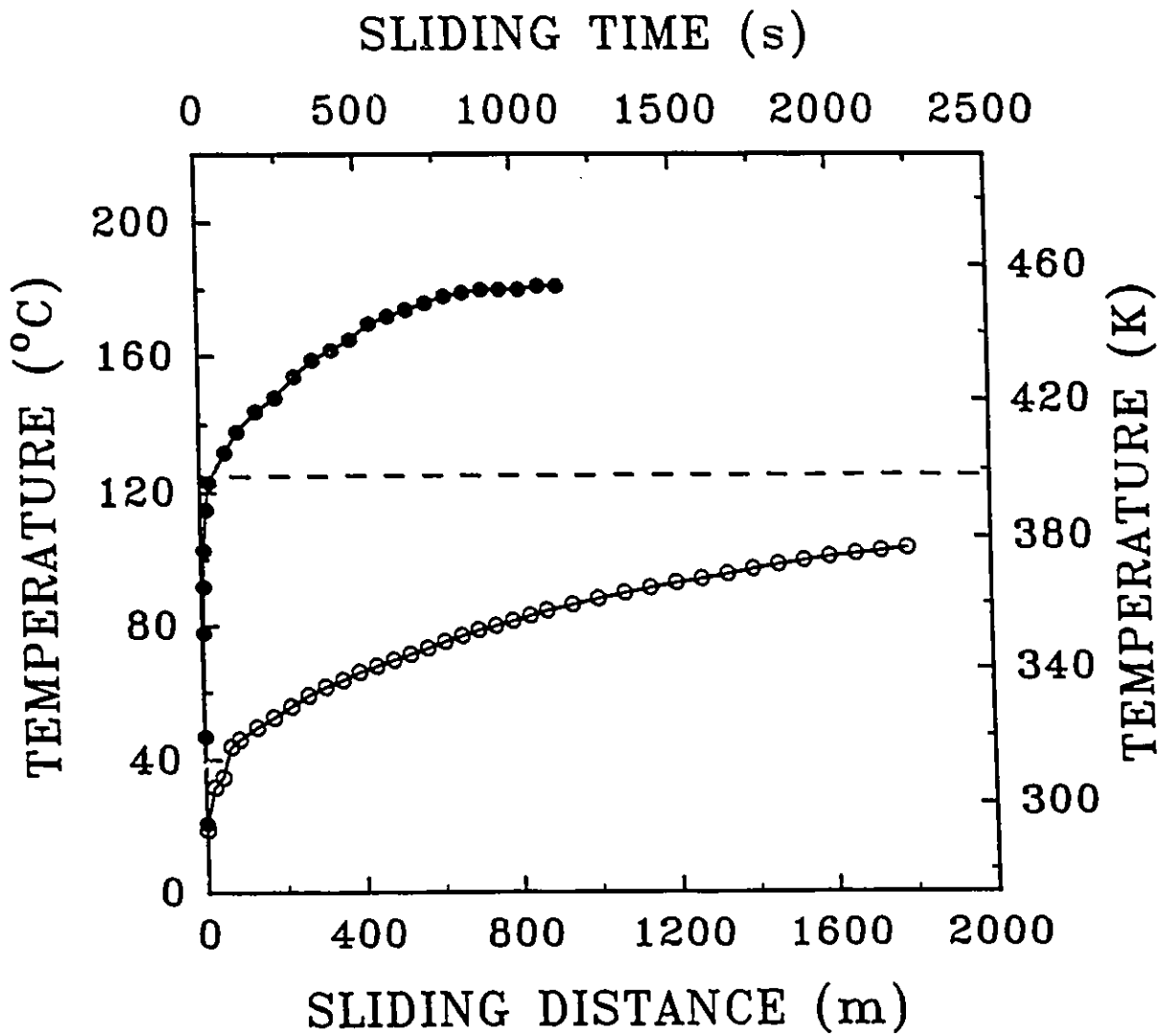


Figure 82. Temperature vs sliding distance diagram for 6061Al (○) against SAE 52100 steel slider and (●) against a mullite slider. The transition temperature (to severe wear) is indicated by the dashed line. Load: 49 N; Sliding Velocity: 0.8 m/s.

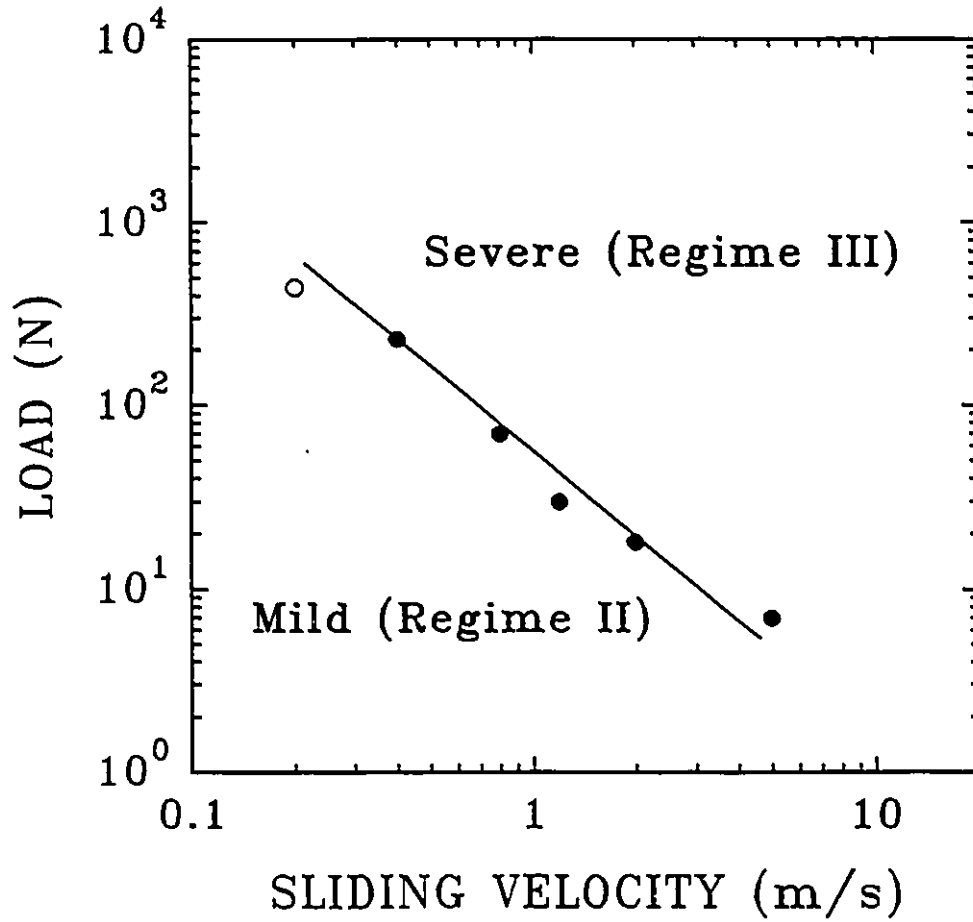


Figure 83. Wear regime map of 6061Al alloy against SAE52100 steel. The open circle indicates that no transition was observed at that combination of load and sliding velocity.

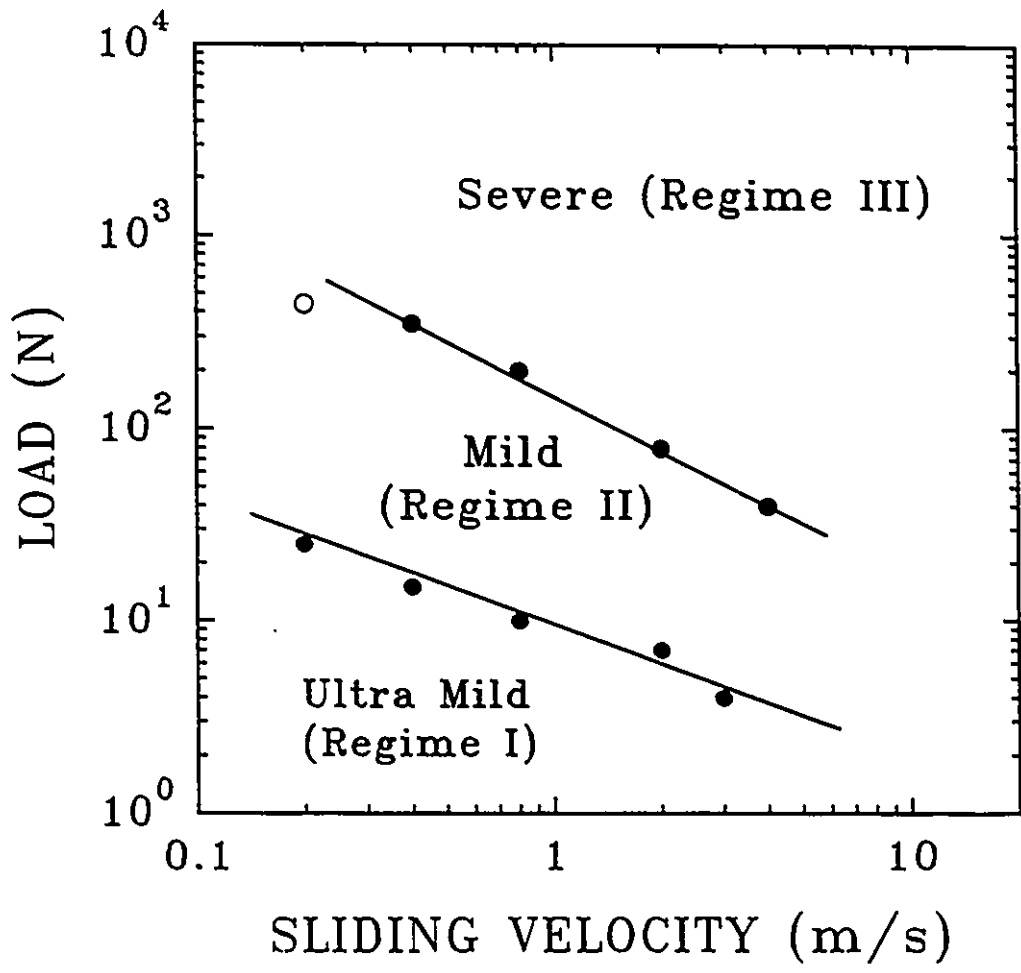


Figure 84. Wear regime map of 6061Al-20%Al₂O₃ alloy against SAE52100 bearing steel. The open circle means that no transition was observed at that combination of load and sliding velocity.

When the combination of load and the sliding velocity falls within the two solid lines, the mild wear regime prevails. The higher line marks the transition between mild wear (regime II) and severe wear (regime III). This line represents the upper limit of the useful service life of the composite.

The wear regime maps can be made more informative by plotting the measured wear rates with load-velocity axes. This is done in Figure 85 for the 6061Al and Figure 86 for 6061Al-20%Al₂O₃, where contours of constant wear rates are plotted. It should be pointed out that at a given isorate contour, both mild and severe wear mechanisms may exist together. This is because the transition load or velocity was identified as the critical load or velocity where the slopes of wear rate vs load or wear rate vs sliding velocity curves change. As seen in Figure 85, a wear rate of $6 \times 10^{-3} \text{ mm}^3\text{m}^{-1}$ corresponds to the severe wear rate regime when the sliding velocity is 0.8 m/s or higher. The same wear rate corresponds to the mild wear rate regime if the tests were performed at 0.2 m/s.

Another piece of information that can be included into the wear maps is achieved by plotting isotherm lines on the load-velocity axes. An example of a Load-Velocity-Temperature diagram is shown in Figures 87 for 6061Al. The temperature increase shown here is a result of frictional heating of the contact surfaces. A load-velocity-temperature map can be a useful material design tool because in actual service conditions tribological materials (such as in pistons and brakes) are often subjected to frictional heating and thus required to operate at elevated temperatures. Under the steady state wear conditions, once any two of these three variables are fixed the third is automatically determined.

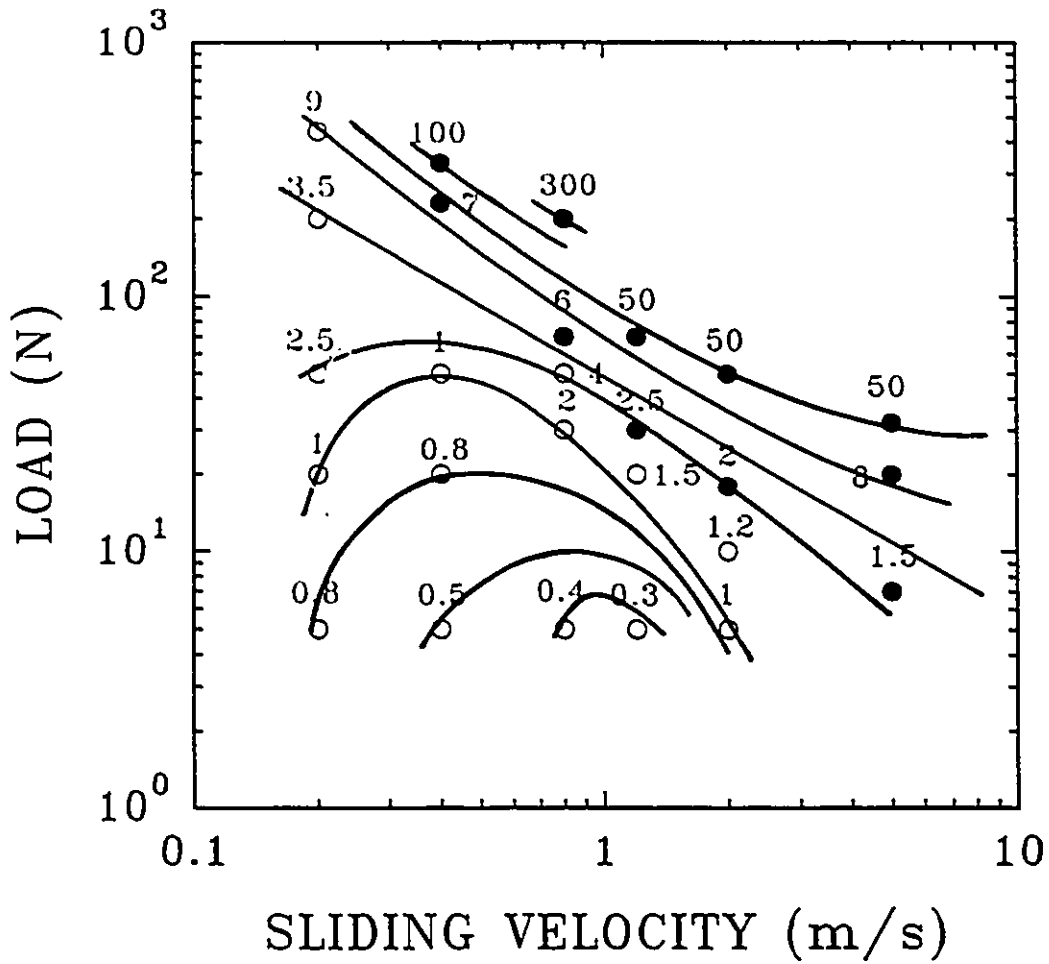


Figure 85. Wear rate map of 6061Al alloy against SAE52100 bearing steel. (\circ) mild wear (regime II); (\bullet) severe wear (regime III). The wear rate data have also been shown in this figure ($\times 10^{-3} \text{ mm m}^{-1}$)

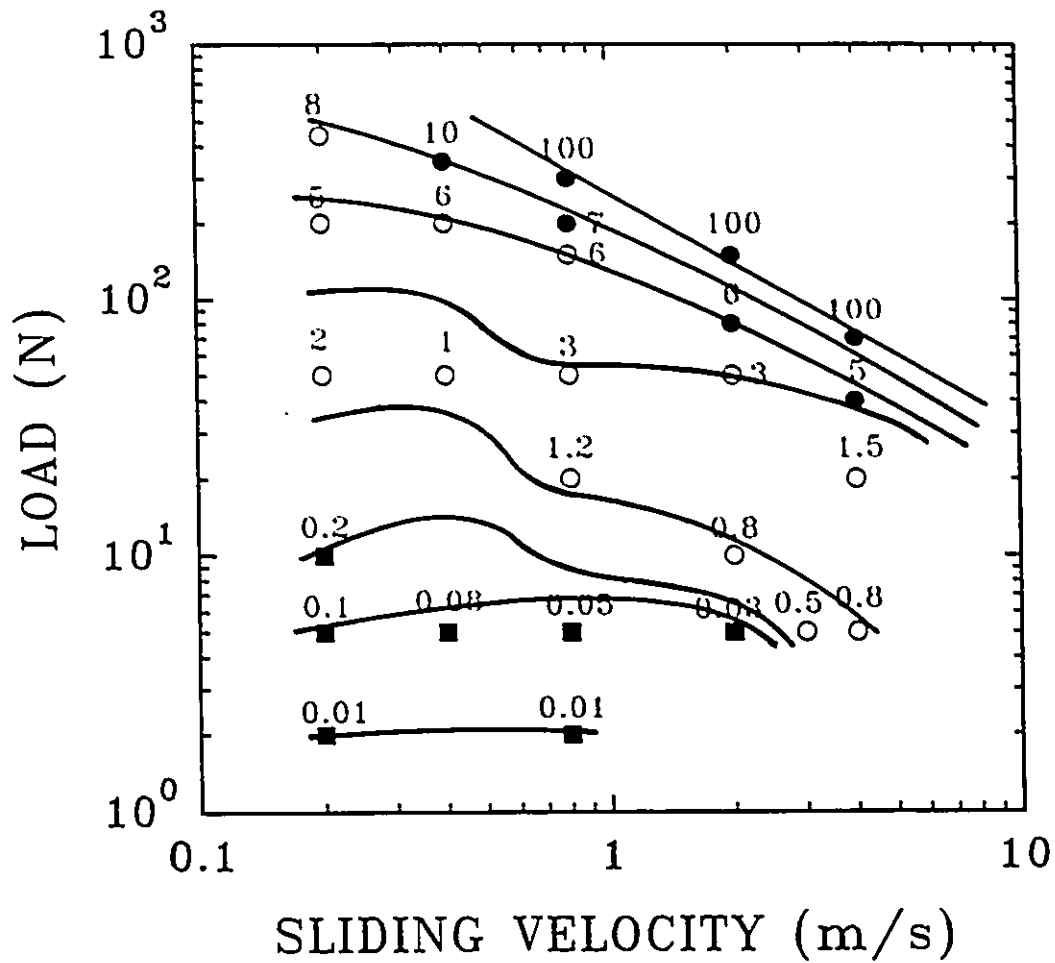


Figure 86. Wear rate map of 6061Al-20%Al₂O₃ alloy against SAE52100 bearing steel. (■) extra mild wear (regime I); (○) mild wear (regime II); (●) severe wear (regime III). The wear rate data have been in this figure ($\times 10^{-3}$ mm m⁻¹).

Table IX summarizes the main characteristics of wear for 6061Al and 6061Al-20%Al₂O₃. Since this system is well characterized the data shown in this table is used for constructing an experimental wear mechanism map shown in Figure 88 which indicates wear processes and mechanisms operating in each of the wear regimes. The wear regime map Figure 89 shows the effect of the volume fraction of reinforcement on the transition boundary. With increasing volume fraction, the transition boundaries move to lower loads and velocities. The figure illustrates how the volume fraction of reinforcement can increase the critical transition limit. The use of mechanism maps together with wear rate maps (Figure 85 & 86) and a temperature map (Figure 87) gives the most complete description of the wear behavior of these materials.

5.6. MODELLING OF WEAR MECHANISMS: A MODEL FOR DELAMINATION WEAR (REGIME II)

Sliding contact between the surfaces of ductile materials is often accompanied by severe plastic deformation localized within a small volume of material adjacent to the contact surfaces ^[52, 147]. The process of debris formation, especially in unlubricated systems, is closely related to the magnitude and distribution of local strains and strain gradients as well as to the variation of stress state within the deformed subsurface zones ^[137, 150, 151]. Rigney and coworkers ^[152, 153] emphasized the importance of the energy expended during the near-surface deformation associated with friction and wear. Metallographic observations of the subsurface layers have shown that the deformation results in the formation of a well-defined cell structure elongated in the sliding direction

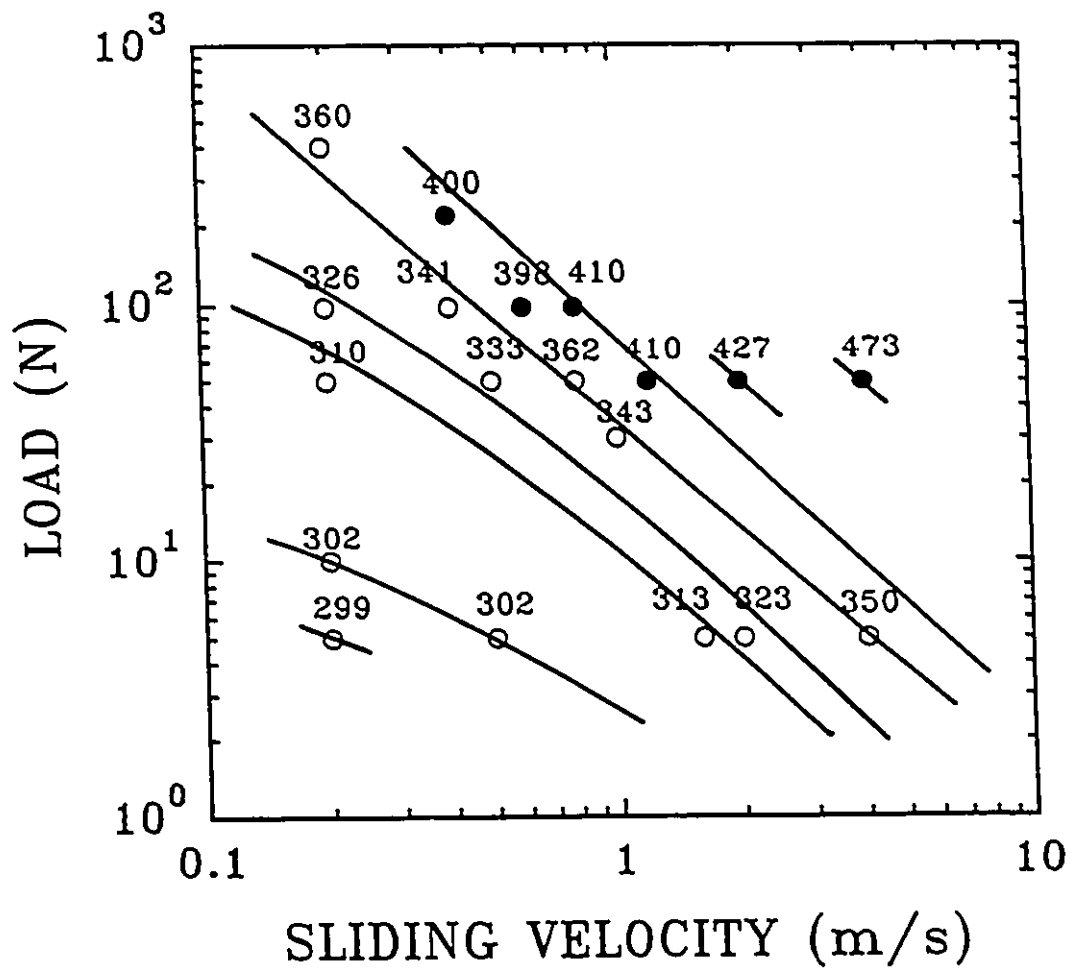


Figure 87 Wear temperature map of 6061Al alloy against SAE 52100 bearing steel. (○) mild wear (regime II); (●) severe wear (regime III). The temperatures (degree K) given in this Figure are (1) the temperature at steady state (in regime II); (2) the reading when the wear machine was stopped (in regime III).

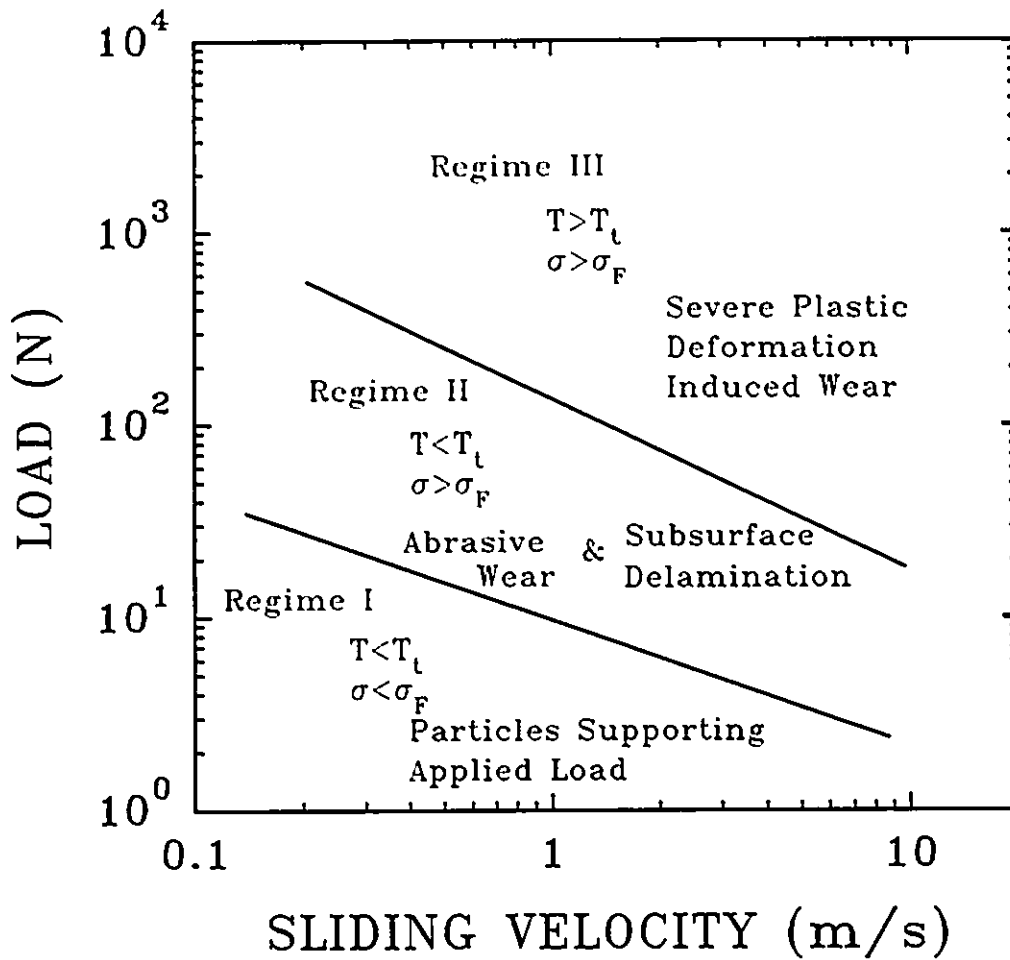


Figure 88. Wear mechanism map of 6061Al-20%Al₂O₃. σ_F -fracture strength of the particles; T_t -critical temperature for transition to severe wear. The boundary between regime I and II is the average of "dual" load range.

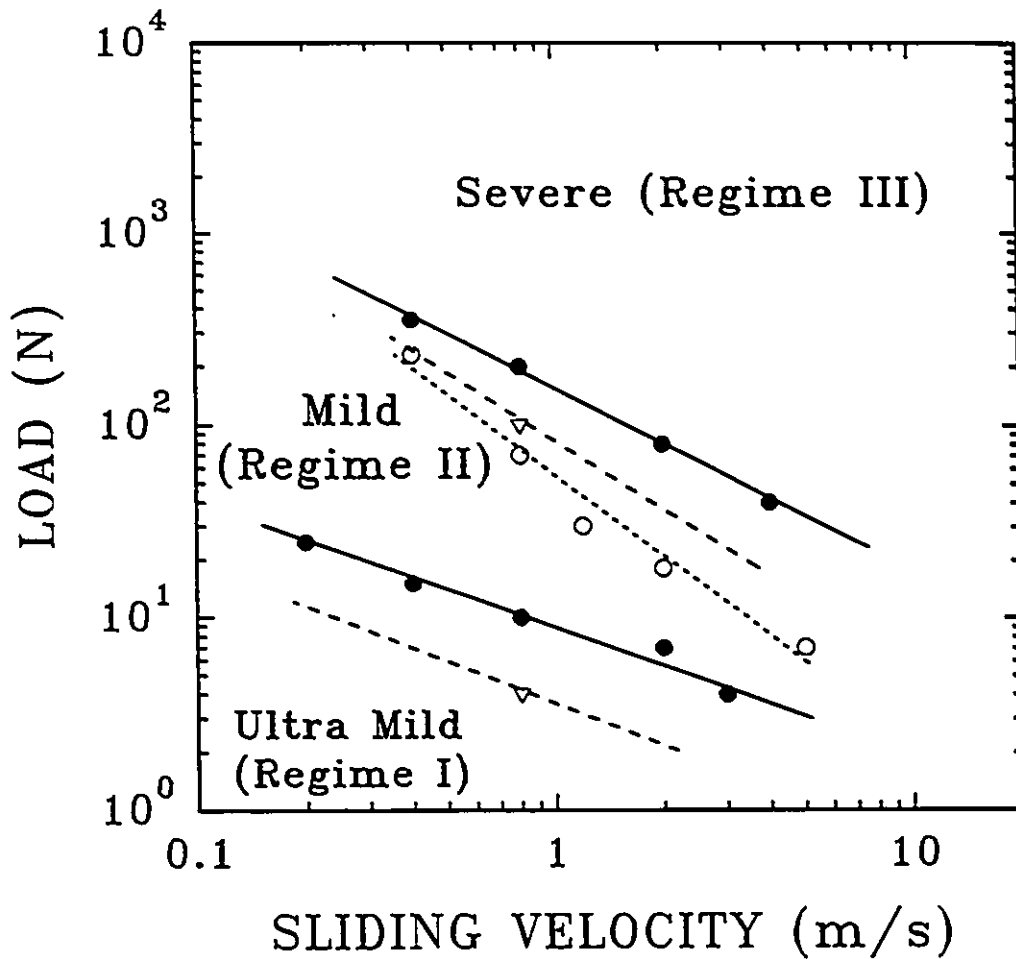


Fig. 89 Wear regime map of 6061Al alloy reinforced with 0, 10% and 20% Al₂O₃ particles against SAE 52100 bearing steel. The boundaries between wear regimes have been presented by (○) 6061Al, (▽) 6061Al-10%Al₂O₃ and (●) 6061Al-20%Al₂O₃.

Table IX. Summary of Wear Characteristics for 6061Al and 6061Al-20%Al₂O₃ Sliding on SAE52100 Steel

Wear Characteristics	Materials & it's counterbody	Regime I	Regime II	Regime III
Wear Rates mm ³ m ⁻¹	Block: 6061Al Ring: Steel	----	4x10 ⁻⁴ ~6x10 ⁻³ 4x10 ⁻⁵ ~7x10 ⁻⁴	>1x10 ⁻² < 0
	Block: 6061Al - 20%Al ₂ O ₃ Ring: Steel	3x10 ⁻⁶ ~8x10 ⁻⁵ 8x10 ⁻⁵ ~6x10 ⁻⁴	4x10 ⁻⁴ ~1x10 ⁻² 3x10 ⁻⁴ ~4x10 ⁻³	>1x10 ⁻² < 0
Worn Surface	Block: 6061Al	-----	<ul style="list-style-type: none"> • shallow grooves • black (oxide) layer (low load) • plastic deformation • hardened layer 	<ul style="list-style-type: none"> • rough • heavy plastic deformation • formation of hardened fingers
	Block: 6061Al - 20%Al ₂ O ₃ Ring: steel	<ul style="list-style-type: none"> • smooth • reddish brown layer (Fe₂O₃) • small or no plastic deformation • smooth & shiny • partly reddish brown layer (Fe₂O₃) 	<ul style="list-style-type: none"> • similar to 6061Al • with broken Al₂O₃ particles • fine grooves • partly black (amorphous Al oxide) layer 	<ul style="list-style-type: none"> • similar to 6061Al • with deep broken Al₂O₃ particles layers • no plastic deformation • transfer layer from counterbody
Wear Debris		<ul style="list-style-type: none"> • fine reddish brown powder (Fe₂O₃) 	<ul style="list-style-type: none"> • mixture of black powder (Al oxide) & white plates (metallic Al) 	<ul style="list-style-type: none"> • large metallic Al flakes
Wear Mechanisms		<ul style="list-style-type: none"> • load supporting particles; formation of transfer films 	<ul style="list-style-type: none"> • delamination & abrasion; (oxidation of Al plausible) 	<ul style="list-style-type: none"> • severe plastic deformation wear
Surface Bulk Temperature	6061Al 6061Al-20%Al ₂ O ₃	----- ~305 (K)	290~395 (K) 290~440 (K)	>395 (K) >440 (K)

^[154, 155]. On the other hand, the delamination theory developed by Suh and co-workers ^[71, 156] describes the debris formation process as a result of damage initiation at the second phase particles and considers that the damage initiation is governed by a stress criterion ^[157].

There exist various models that describe subsurface crack growth. Models based on fracture mechanics ^[34, 158-160] consider the effect of stress intensity factors either in mode I (opening) or II (shear) at the tip of the crack as a driving force for its propagation. These models also have been extended to take into account the cyclic nature of asperity loading ^[35, 161]. Fatigue models of wear seek a correlation between wear rates with either low cycle fatigue strength ^[162] or threshold cyclic stress intensity factor, ΔK_{th} ^[163] of the materials. However, these are not readily applicable to the wear of ductile materials. A second group of ideas uses the concept of damage accumulation, i.e. void nucleation and coalescence ^[164] to model the wear debris formation in ductile materials. Some of these ideas were reviewed by Lim and Ashby ^[8]. These models consider that subsurface cracking is controlled by plastic strain rather than stress intensity at the crack tip. A critical shear strain criteria for subsurface crack propagation was proposed by Kuhlmann-Wilsdorf ^[138] and possible locations of subsurface cracks were computed by Rosenfield ^[165] and Johnson ^[166] from a mechanistic viewpoint. But so far, there is little definitive metallographic evidence on the microstructural changes that occur during sliding wear.

In this section, dry sliding wear behaviour of an aluminum alloy containing a dispersion of silicon particles has been investigated. The stress and strain distributions in the subsurface regions were determined as a function of sliding distance and applied

normal load. The role of second phase particles in delamination wear has been assessed. Observations indicated the importance of damage accumulation events in delamination wear. It will be shown that delamination wear can be modeled by applying void growth theories of ductile fracture.

5.6.1. SUBSURFACE STRESS-STRAIN BEHAVIOUR

As described in Chapter IV, the plastic strain distribution beneath the contact surface was obtained from the measurements of the displacement of the marker plate. The equivalent plastic strains $\hat{\epsilon}$, shown in Figure 62, have been evaluated from the shear angle of the interface, ϕ , by the relationship

$$\epsilon = \frac{\sqrt{3}}{3} \tan \phi \quad (5.1)$$

As a first approximation, the flow strength, σ_f (Figure 63), of the near surface layers has been estimated from the Vickers hardness, H, using a simple expression

$$\sigma_f = \frac{1}{3} H \quad (5.2)$$

Having determined plastic strain and flow strength of the material layers below the contact surfaces, a relationship between these can then be established. The stress σ_f corresponding to plastic strain ϵ at a given depth has been computed from data in Figures 62 and 63. A cumulative stress-strain curve determined in this way is presented in Figure 90. The figure shows that the layers strain harden very steeply towards the contact surface but at strains larger than five the curve flattens out indicating exhaustion of the strain

hardening capacity of the material at high strains. A regression analysis showed that the stress-strain relation can be represented according to the basic form of the Voce equation [167].

$$\sigma_f = \sigma_s - (\sigma_s - \sigma_0) \exp\left(-\frac{\epsilon}{\epsilon_c}\right) \quad (5.3)$$

where σ_f is the flow stress at strain ϵ , σ_0 (=240 MPa) is the bulk flow strength, σ_s (=400 MPa) is the saturation stress, i.e. the stress at which the work hardening rate becomes zero. ϵ_c (=4.79) is a constant. The Voce-type logarithmic work hardening relation is a common description of the stress-strain characteristics of heavily deformed aluminum alloys by torsion, wire drawing, etc. [168]. An alternative way of expressing the Voce equation is to use the differential form of Eqn.5.3 as follows:

$$\frac{d\sigma_f}{d\epsilon} = \frac{\sigma_s}{\epsilon_c} \left(1 - \frac{\sigma_f}{\sigma_s}\right) \quad (5.4)$$

where $(d\sigma_f/d\epsilon)$ is the work hardening rate which is plotted against σ_f in Figure 91. The figure shows that the Voce equation is an appropriate representation of the flow stress-strain state below the worn surfaces.

5.6.2. DELAMINATION WEAR IN DUCTILE MATERIALS CONTAINING SECOND PHASE PARTICLES

The metallographic observations underline the importance of strains and strain gradients localized within a region of 30-80 μm depth below the worn surfaces. Both the depth of the plastically deformed zone and the magnitude of surface strains increase with

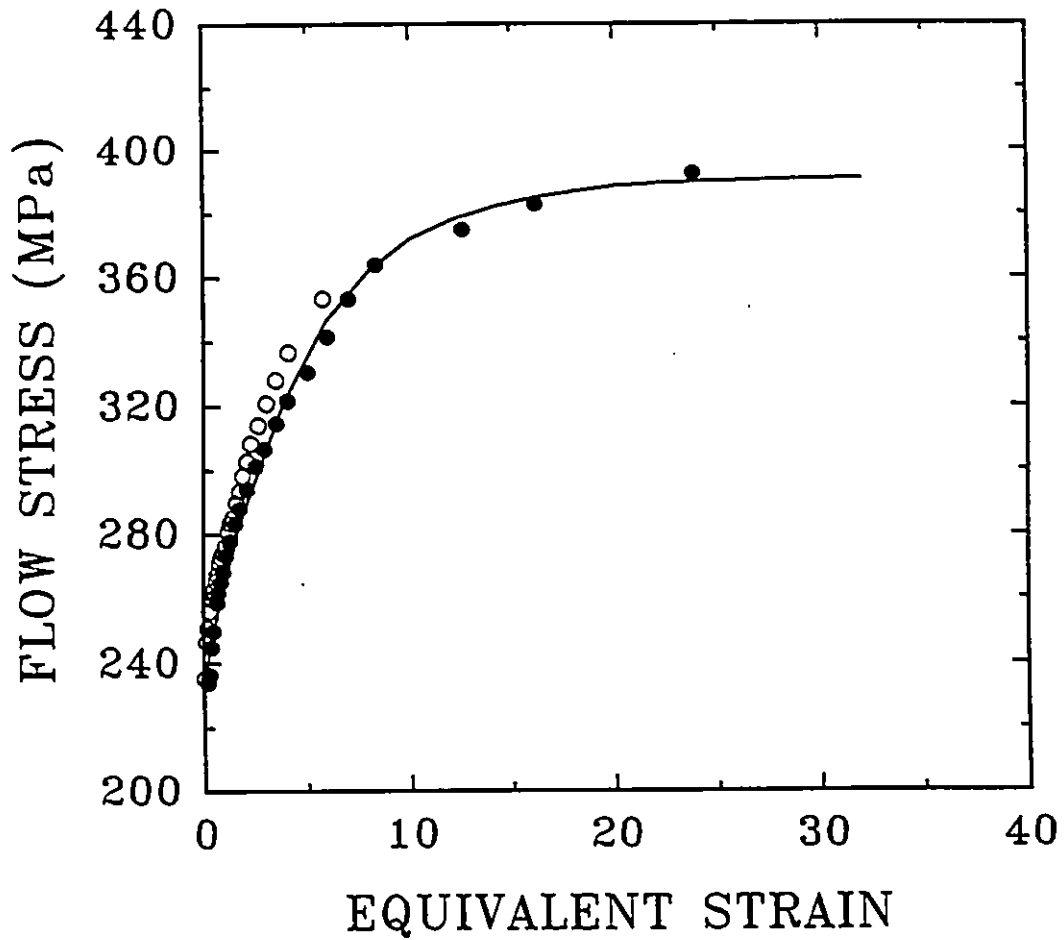


Figure 90. Cumulative flow stress vs. plastic strain curve for the material below the contact surfaces. The solid line represents the Voce function computed from the experimental data. Load: (○) 10 N and (●) 45 N.

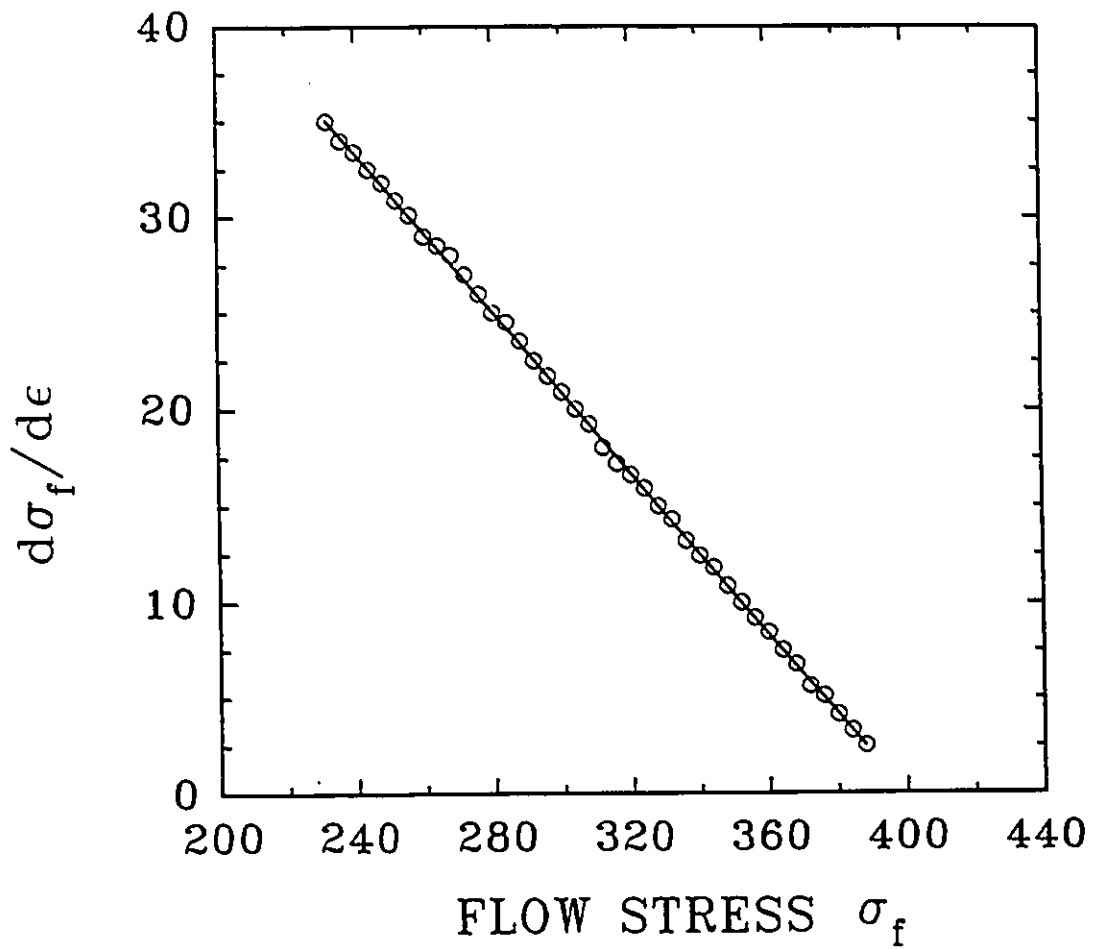


Figure 91. Variation of the work hardening rate with flow stress.

sliding distance and applied load. The stress within this zone is complex but a simplified analysis indicated that a cumulative stress/strain curve of Voce type can be constructed. The experiments also revealed the importance of second phase particles in debris formation. It appears that the initial stage of subsurface crack formation involves void initiation at the silicon-aluminum interfaces within the deformed zone and wear proceeds by the linking of these voids at a certain critical depth (10-20 μm). The following discussion is focused on the conditions that determine the critical depth at which the damage accumulation rate is maximum.

It is well established that a hydrostatic pressure gradient exists below the contact areas under normal loading ^[169, 150]. Bridgeman ^[170] demonstrated that a large superimposed hydrostatic pressure, σ_{11} , should improve ductility by retarding the growth rate of the damage. Plastic strains in the deformed subsurface layers have the opposing effect of promoting failure. In the immediate vicinity of the contact surface, damage initiation is made difficult by the large hydrostatic pressure; therefore a large local tensile stress is required for void nucleation to occur ^[164]. The growth rate of the damage is also suppressed by the large hydrostatic pressure. At large depths the strain (and the strain rate) is small; consequently, the damage rate is drastically reduced. Thus, the competition between the hydrostatic pressure and large plastic strain can result in a damage gradient in the highly deformed layer giving rise to a critical depth for the maximum rate of damage accumulation. Accordingly, a simple model can be developed to estimate the critical depth for maximum rate of damage accumulation.

Consider a void of radius (R) which has nucleated at a particle-matrix interface.

Then, the rate of the void growth (R) can be estimated by applying Rice and Tracy void growth analysis ^[171]. The void will be growing to an ellipsoidal shape and the rate of increase in the radius of void is given by:

$$R = \left[\gamma + 0.558 \sinh \left(\frac{3\sigma_H}{2\sigma_f} \right) \right] \dot{\epsilon} R \quad (5.5)$$

where σ_f is the flow stress of the worn layers, $\dot{\epsilon}$ is the strain rate and γ is an amplification factor (of 1-2) which relates the growth rate of the void to the strain in the matrix. Here it is assumed that $\gamma=1.5$. It is also assumed that $\dot{\epsilon}$ is linearly proportional to the strain ϵ , i.e. from Eqn.(4.2):

$$\dot{\epsilon} = G\epsilon = GA \exp(-BZ) \quad (5.6)$$

It is also assumed that in the highly work hardened material, the variation of the hydrostatic pressure beneath the contact area can be considered equivalent to the Boussinesq solution for point loading (see Appendix). The analysis indicates that the hydrostatic stress under the loading point is always compressive with its maximum located at the surface and falls with increasing depth as a function of $1/Z^2$. However, the magnitudes of the stresses predicted by the Boussinesq equation are too high because of the unrealistic assumption that the load is concentrated over a single asperity of infinitely small size. Thus, Eqn.(A5) (see Page 202) was modified to a more general form:

$$\sigma_H = -\frac{C}{Z^2} \quad (5.7)$$

where the coefficient C is a factor that takes into account the effect of distributed load

on the contact area. Since the geometry of the contact area is not accurately known, we do not have a theoretical value for C. Different values for this coefficient can be substituted in Eqn.(5.7) in order to estimate the magnitude of hydrostatic pressure σ_{II} . The change of σ_{II} with depth Z (at 10 N applied load) is shown in figure 92. This figure also shows the measured flow stress gradient σ_f for comparison.

Based upon the above assumptions, the Rice and Tracey equation (Eqn.(5.5)) can be numerically evaluated to find the variation of the damage rate, R, with respect to depth. By inserting Eqns.(5.3), (5.6) and (5.7) in Eqn.(5.5) this equation becomes:

$$\frac{R}{GR} = \left[\gamma + 0.558 \sinh \left(-\frac{3}{2} \frac{c}{Z^2 [\sigma_s - (\sigma_s - \sigma_0) \exp(-\frac{\epsilon}{\epsilon_c})]} \right) \right] \quad (5.8)$$

$$\times [A \exp(-BZ)]$$

For a given load and sliding distance, Eqn.(5.8) can be solved using data in Table (VII). As an example, the variation of the normalized damage rate (R/GR) with respect to depth, Z, at a load of 10 N and a sliding distance of 10^3 m is shown in Figure 93. The rate of damage is at its maximum when:

$$\frac{d\left(\frac{R}{GR}\right)}{dZ} = 0 \quad (5.9)$$

Thus Eqn.(5.8) can be differentiated with respect to Z to give

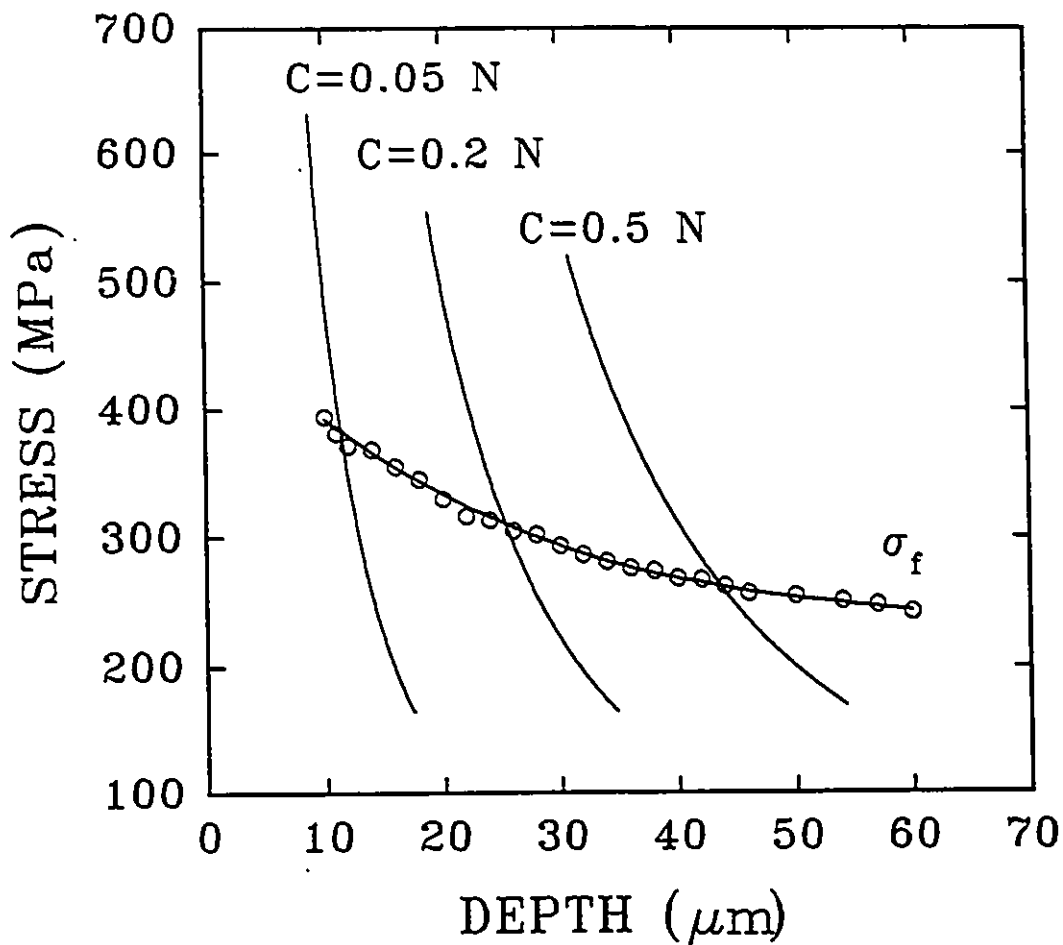


Figure 92. Hydrostatic pressure, σ_H , gradients at different C levels compared with flow stress, σ_f gradient. Load: 10 N, Sliding Distance: 1000 m.

$$\begin{aligned} \frac{d(\frac{R}{Z})}{dZ} = & [\gamma + 0.558 \sinh(\frac{3\sigma_H}{2\sigma_f})] \frac{d\epsilon}{dZ} \\ & + [0.837 \epsilon \cosh(\frac{3\sigma_H}{2\sigma_f}) (\frac{\sigma_f(\frac{d\sigma_H}{dZ}) - \sigma_H(\frac{d\sigma_f}{dZ})}{\sigma_f^2})] = 0 \end{aligned} \quad (5.10)$$

where

$$\begin{aligned} \frac{d\epsilon}{dZ} &= -BGA \exp(-BZ) = -BG\epsilon \\ \frac{d\sigma_H}{dZ} &= \frac{2C}{Z^3} \\ \frac{d\sigma_f}{dZ} &= -\frac{\sigma_s - \sigma_0}{\epsilon_c} B \epsilon \exp(-\frac{\epsilon}{\epsilon_c}) \end{aligned} \quad (5.11)$$

The solution of Eqn.(5.9) gives the critical depth Z_c where the damage rate is maximum. Results obtained for an applied load of 10 N are shown in Figure 94.

The salient points that arise from this analysis are:

(i) The critical depth Z_c at which the damage rate is maximum increases with the hydrostatic pressure, σ_H .

(ii) A large hydrostatic stress σ_H suppresses the rate of damage \dot{R} .

According to Figure 94 there is a slight decrease in Z_c with increasing sliding distance (under constant hydrostatic stress). This effect can be attributed to the increase of the strain hardening rate of the subsurface layers with the sliding distance (as evidenced by higher B values in Eqn.(4.2) at longer sliding distances (see Table VII).

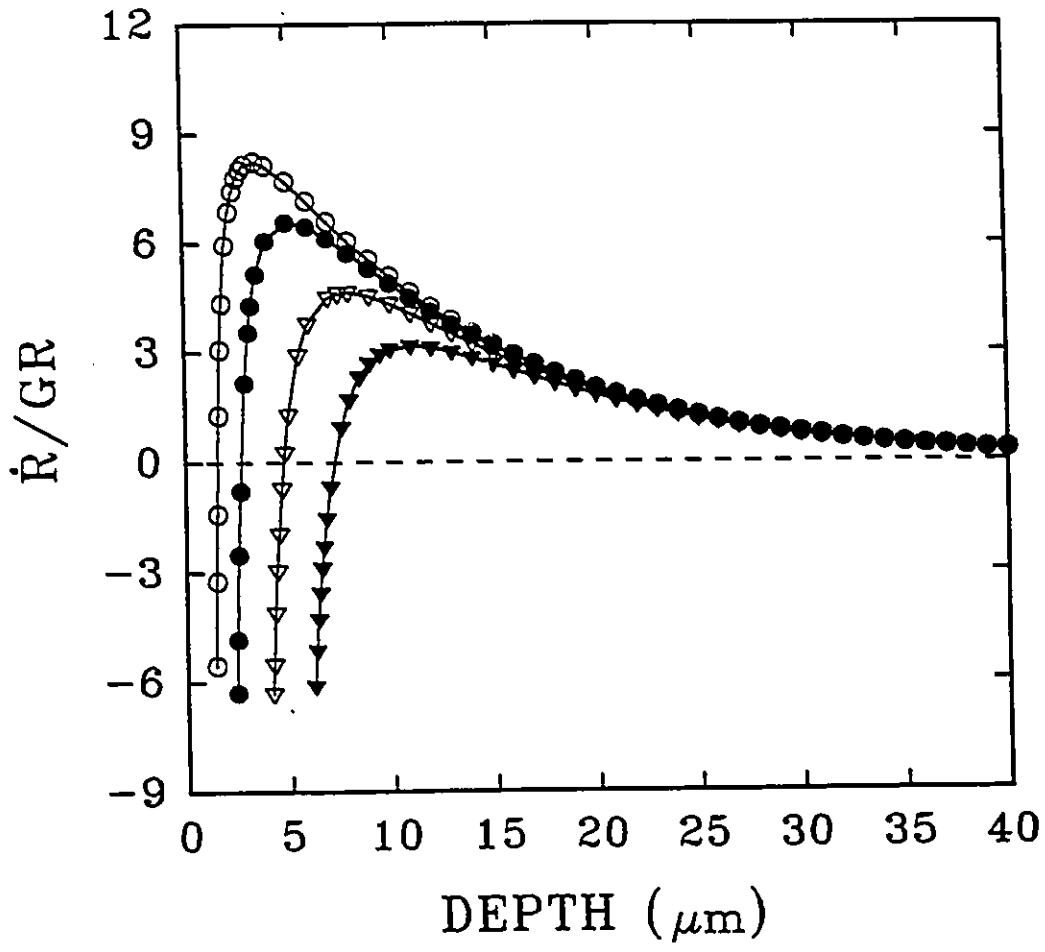


Figure 93. Change in the damage rate with the depth below the contact surfaces. Load: 10 N; Sliding Distance: 1000 m; (\circ) $C=1 \times 10^{-3}$ N; (\bullet) $C=3 \times 10^{-3}$ N; (∇) $C=9 \times 10^{-3}$ N and (\blacktriangledown) $C=2 \times 10^{-2}$ N.

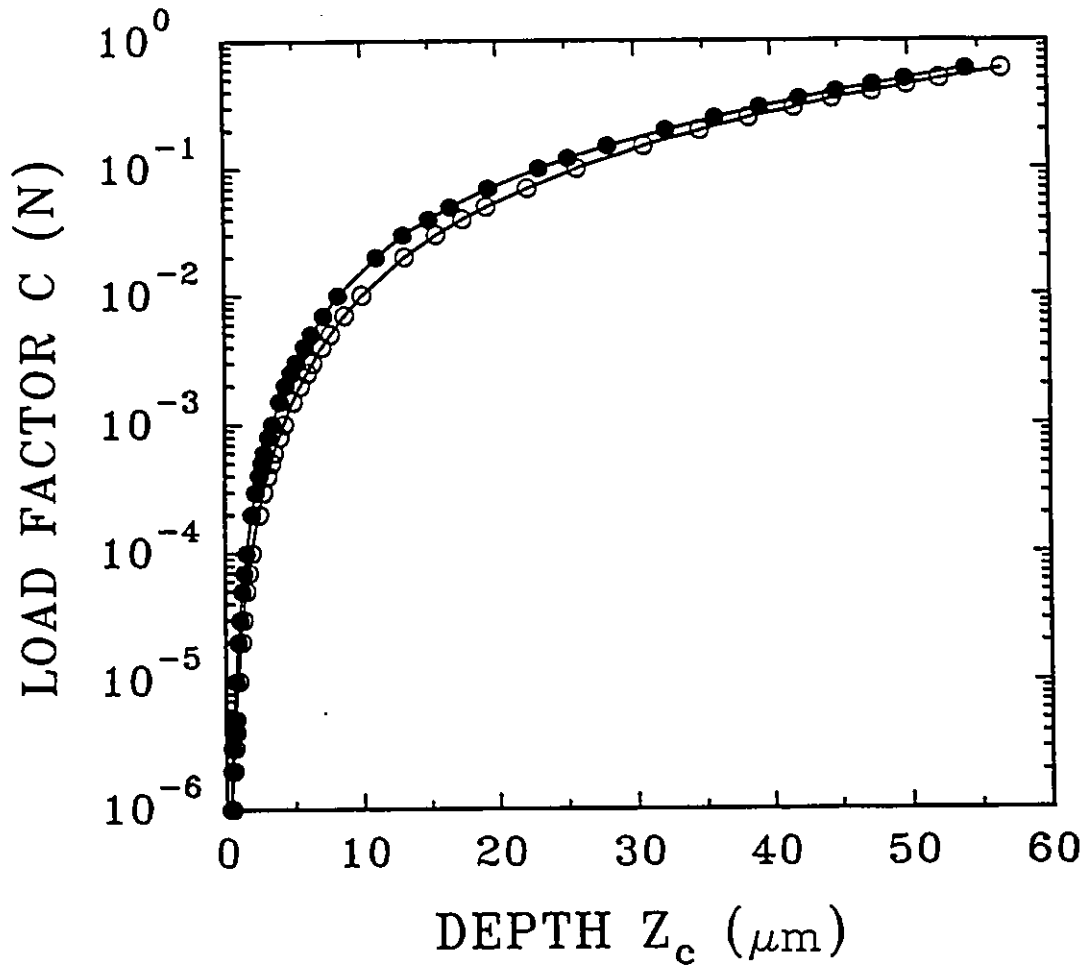


Figure 94. Variation of the critical depth Z_c at which the subsurface damage rate is maximum with the load factor C. Load: 10 N; Sliding Distance: (O) 30 m and (●) 1000 m.

Figure 95 shows the effect of normal load on Z_c . To compare the magnitude of Z_c at a constant hydrostatic pressure level the load factor C was normalized with respect to the applied load (i.e. $C' = C/P$ where P is the applied load). Figure 95 reveals that an increase in the value of Z_c should be expected at higher applied loads. This is in agreement with the current experimental observations that the thickness of the debris particles increased with the applied load.

In summary, although its accuracy is limited by the assumptions made on the Rice and Tracey analysis, the model can be used to predict the location of the maximum damage rate. Hence it sets a guideline to quantify the thickness of the debris particles generated during dry sliding wear. The model is not readily applicable to service conditions but it does present a way to quantify sliding wear of materials for which the crack growth is the rate controlling process by recognizing that this type of wear can be described as a cumulative damage process sensitive to microstructural elements like second phase particles.

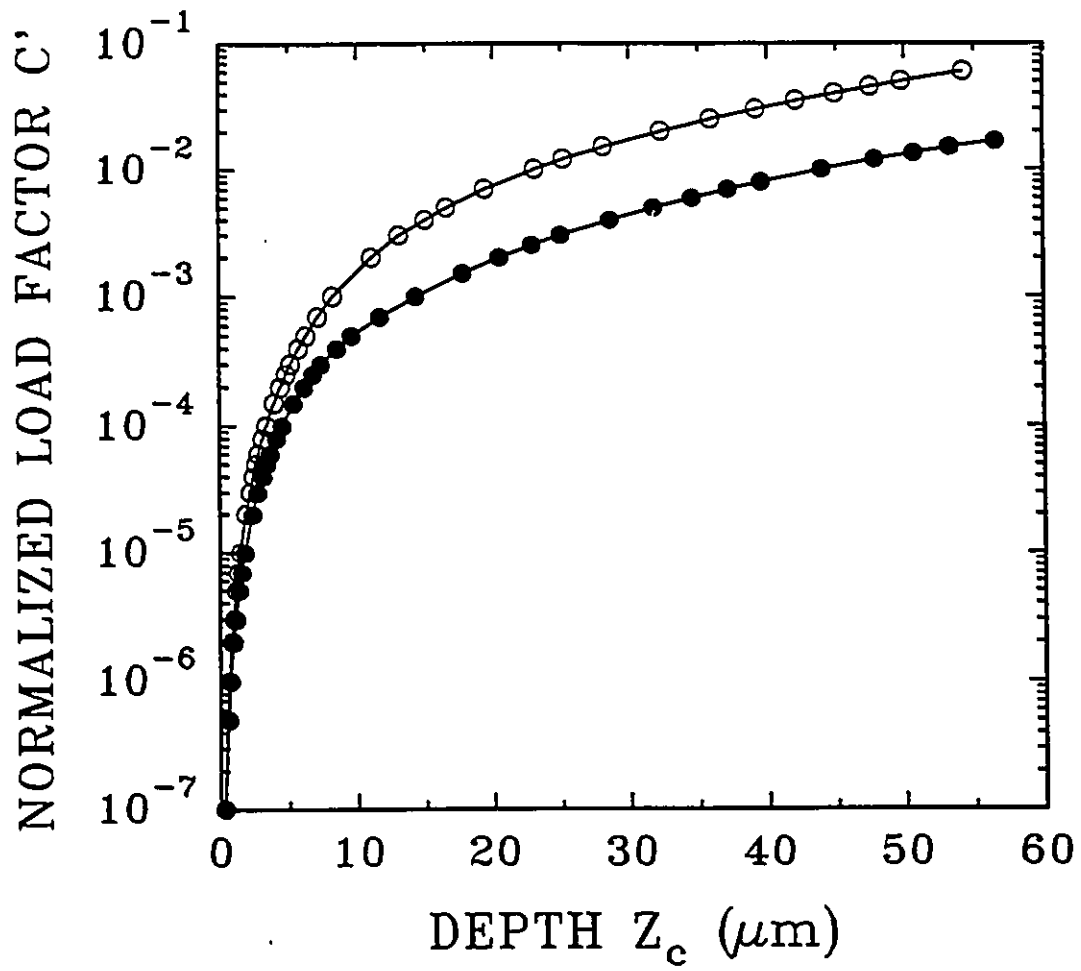


Figure 95. Normalized (with respect to the applied load) C' vs. Z_c at two applied load levels (O) 10 N and (●) 45 N. Sliding distance: 1000 m.

CHAPTER VI CONCLUSIONS AND RECOMMENDATIONS

6.1. NEW INFORMATION REVEALED BY THIS WORK

Some of the previously unknown aspects of the wear of MMC's which are revealed for the first time can be summarized as follows:

1. Delineation of three wear rate regimes common to the sliding wear of all MMC's,
2. Characterization of the load induced, velocity induced and sliding distance induced transitions;
3. Metallographic and spectroscopic evidence for the wear mechanisms that operate in each wear regime;
4. Experimental proof that the transition between mild and severe wear occurs upon contact surface temperature exceeding a critical value and demonstration that severe wear is controlled by thermally activated softening processes;
5. Experimental evidence that in the mild wear regime, the wear resistances of MMC's are not superior to those of unreinforced materials;
6. Experimental proof for load supporting effect of particulates in the ultramild regime;
7. Representation of wear data in the form of wear transition and wear mechanism maps;
8. Determination of the effect of microstructure factors such as particulate size and reinforcement volume fraction on wear resist of MMC's

9. Assessment of the role of the counterface materials and forced cooling process on wear transitions;
10. Observation of the effect of surface films on the transitions;
11. Rationalization of subsurface delamination process on the basis of a damage accumulation model.

6.2. GENERAL SUMMARY AND CONCLUSIONS

6.2.1. WEAR REGIMES AND MECHANISMS

The wear resistance of metal matrix composites (A356Al-SiC, 6061Al-Al₂O₃, and 2014Al-SiC) can be summarized into three wear regimes:

(1). Regime I (Ultra-mild Wear): At low loads and low sliding velocity, the reinforced ceramic particles (SiC and Al₂O₃) serve as load-carrying particles to support the applied load; exposed portions of these particles machine the counterface such that the debris removed from the counterface is transferred onto the surface of the composites. Iron-rich oxide layers formed as a result of the machining of the steel counterface by the particles increase the wear resistance of composites. In this regime, the wear resistances of the ceramic particulate (SiC and Al₂O₃) reinforced alloys are at least an order of magnitude better than that of monolithic aluminum alloys.

(2). Regime II (Mild Wear): At higher loads and/or higher sliding velocities, the reinforced ceramic particles are fractured and contact strains are transmitted to soft aluminum matrices. A subsurface damage accumulation process leading to the formation of subsurface cracks is responsible for material loss in the form of platelike debris. Reinforcement particles promote the subsurface damage and also act as third-body abrasives; thus, the particulate-reinforced composites wear at rates comparable to those of monolithic alloys.

(3). Regime III (Severe Wear): At high loads and/or high sliding velocities, the transition from mild wear (regime II) to severe wear (regime III) takes place when the surface temperatures exceed a critical value. The severe wear involves massive surface

damage and material transfer to the counterface. The reinforced ceramic particles improve the thermal stability of the alloy and delay this transition to higher temperatures and loads.

6.2.2. FACTORS INFLUENCING WEAR RATES AND WEAR TRANSITIONS

The dry-sliding wear resistances of the aluminum alloys reinforced by ceramic particles are strongly influenced by the applied mechanical factors such as the applied load and the sliding velocity which lead to an increase in the surface temperature. Microstructural factors such as reinforced particle size and reinforced particle volume fraction also have an important effects on the wear resistance. The role of mechanical and microstructural factors on the wear resistance can be summarized as follows:

(1). Applied Load: Contact stresses and surface temperatures vary with the applied load. When the applied stress σ is lower than the fracture strength of the reinforced ceramic particles σ_f and the bulk surface temperature T_b is smaller than the transition temperature T_c , the wear rates are low, e.g. ultra-mild wear (regime I). When conditions are such that $\sigma \geq \sigma_f$ and $T_b < T_c$, mild wear dominates the wear behavior (regime II). When $\sigma > \sigma_f$ and $T_b \geq T_c$, a severe wear regime prevails.

(2). Sliding Velocity: The wear rates of both MMCs and monolithic alloys first decrease with the sliding velocity and then increase possibly due to the competition between strain hardening and the thermal softening of the subsurface layers.

(3). Surface Temperature: Critical transition temperatures from regime II to regime III, T_c , correspond to about 0.4-0.45 of the absolute melting temperature of aluminum

alloys. Particulate reinforcement increases the transition temperature.

(4). Particulate Size: Increasing particle size improves the wear resistance in regime I and delays the transition to regime II. However no significant difference in the wear resistances of the composites reinforced with different particle sizes in regime II and regime III could be detected in this work.

(5). Particle Volume Fraction: Increasing the volume percent of particles causes a delay in the transitions between the regimes I and II as well as between regimes II and III.

(6). Counterface Material: Sliding the alloys against a mullite slider instead of steel ring increases the wear rates of the unreinforced Al alloys and composites by an order of magnitude. This is possibly due to the enhanced abrasive effect of harder counterface and/or the low-heat conductivity of mullite which causes localized heating of the surfaces of the materials during friction and hence promotes severe wear.

6.2.3. WEAR MECHANISM MAPS

A group of wear maps, *i.e.* wear regime maps, wear rate maps, wear temperature maps and wear mechanism maps, have been constructed in terms of the applied mechanical parameters such as the load and the sliding velocity. These maps provide a convenient way of summarizing wear rate controlling mechanisms and give the most complete description of the experimental data pertaining to the sliding wear behavior of the composites.

6.2.4. MODELING OF DELAMINATION WEAR

(1). It was observed that the strains and stresses accumulate with sliding distance at regions under the contact surfaces. The flow stress-strain behavior of the subsurface regions obey a Voce type exponential work hardening equation.

(2). Subsurface crack propagation contributes to the material removal in the form of platelike debris. Below the contact surfaces, there exists a damage gradient determined by opposing effects of plastic strain which enhance damage accumulation rate and hydrostatic pressure which suppresses it.

(3). A model based on the Rice and Tracey analysis of ductile fracture is proposed to predict the location where the damage rate is the highest. It is shown that the critical depth corresponding to the maximum damage rate increases with the hydrostatic pressure but a high hydrostatic pressure on the contact surface also reduces the rate of damage.

6.3. RECOMMENDATIONS FOR FUTURE WORK

The new results presented in this dissertation suggest a number of ways in which the research could be extended. The following are those which the author believes to be promising.

(1). A mixture of black, fine-powdery particles has been found in the mild wear regime for the Al alloys and the composite materials especially under low applied load and sliding velocity conditions. The importance of this type of debris to the wear transition has been discussed in the section 5.1.2. Conflicting reports exist in the literature regarding the composition of this debris. Shivanath, Sengupta and Eyre ^[48] pointed out that this black debris was oxidised but did not give further evidence. Antoniou, Brown and Cashion ^[42] reported that no Al oxide existed in this type of debris. But using the X-ray diffraction analysis in the present study, evidence for a very strong amorphous peak has been found. This could be evidence for Al oxide. Detailed analysis is still needed to clarify this amorphous phase.

(2). The effect of the particulate size and the volume fraction of the ceramic particles on the damage accumulating under the contact surfaces is important. Further studies of the modeling of delamination wear should include these microstructural parameters.

APPENDIX

For an isotropic Hookean material under a point load P, Boussinesq's and Cerruti's solution for stress components are^[67]:

$$\begin{aligned}
 \sigma_{rr} &= \frac{P}{\pi R^2} \left[\left(\frac{1-2\nu}{4} \right) \sec^2 \frac{\phi}{2} - \frac{3}{2} \cos\phi \sin^2\phi \right] \\
 \sigma_{\theta\theta} &= \frac{P}{\pi R^2} \left[\left(\frac{1-2\nu}{2} \right) \left(\cos\phi - \frac{1}{2} \sec^2 \frac{\phi}{2} \right) \right] \\
 \sigma_{zz} &= \frac{P}{\pi R^2} \left[-\frac{3}{2} \cos^3\phi \right] \\
 \sigma_{rz} &= \frac{P}{\pi R^2} \left[-\frac{3}{2} \cos^2\phi \sin\phi \right] \\
 \sigma_{r\theta} &= \sigma_{\theta z} = 0
 \end{aligned} \tag{A1}$$

ν =Poisson's ratio.

The principal normal stresses are as follows:

$$\begin{aligned}
 \sigma_{11} &= \sigma_{rr} \sin^2\alpha + \sigma_{zz} \cos^2\alpha - 2\sigma_{rz} \sin\alpha \cos\alpha \\
 \sigma_{22} &= \sigma_{\theta\theta} \\
 \sigma_{33} &= \sigma_{rr} \cos^2\alpha + \sigma_{zz} \sin^2\alpha + 2\sigma_{rz} \sin\alpha \cos\alpha
 \end{aligned} \tag{A2}$$

where

$$\alpha = \frac{1}{2} \arctan \frac{2\sigma_{rz}}{\sigma_{zz} - \sigma_{rr}}$$

On the area directly below the point load P, *i.e.* along the Z-axis where $\phi=0$, $R=Z$,

the stress components are:

$$\begin{aligned}\sigma_{rr} = \sigma_{\theta\theta} &= \frac{P}{\pi Z^2} \left[\frac{1-2\nu}{4} \right] \\ \sigma_{zz} &= -\frac{3P}{2\pi Z^2} \\ \sigma_{r\theta} = \sigma_{\theta z} = \sigma_{rz} &= 0\end{aligned}\tag{A3}$$

Based on the analysis as above, the principal normal stresses should be:

$$\begin{aligned}\sigma_{11} &= -\frac{3P}{2\pi Z^2} \\ \sigma_{22} = \sigma_{33} &= \frac{1-2\nu}{4} \frac{P}{\pi Z^2}\end{aligned}\tag{A4}$$

Thus, the hydrostatic stress σ_H ($=(\sigma_{11}+\sigma_{22}+\sigma_{33})/3$) is:

$$\sigma_H = -\frac{(1+\nu)P}{3\pi Z^2}\tag{A5}$$

REFERENCES

- [1] I.A. Ibrahim, F.A. Mohamed and E.J. Lavernia, Particulate Reinforced Metal Matrix Composites, *J. Materials Science*, 26(1991) 1137-1156.
- [2] A.L. Geiger and J.A. Walker, The Processing and Properties of Discontinuously Reinforced Aluminum Composites, *JOM*, August (1991) 8-15.
- [3] J.E. Allison and G.S. Cole, Metal-matrix composites in the Automotive Industry: Opportunities and Challenges, *JOM* 45(1993) No.1, 19-25.
- [4] M.G. McKimpson, E.L. Pohlenz and S.R. Thompson, Evaluating the Mechanical Properties of Commercial DRA, *JOM* 45(1993) No.1, 26-29.
- [5] Y. Wu and E.J. Lavernia, Spray-atomized and Codeposited 6061 Al/SiC_p Composites, *JOM*, August (1991) 16-23.
- [6] M.B. House, K.C. Meinert and R.B. Bhagat, The Aging Response and Creep of DRA Composites, *JOM*, August (1991) 24-28.
- [7] T.S. Eyre, Wear Characteristics of Metals, *Tribology International*, Oct. (1976).
- [8] S.C. Lim and M.F. Ashby, Wear Mechanism Maps, *Acta Metal.*, 35(1987) 1-24.
- [9] Glossary of Terms and Definitions in the Field of Friction, Lubrication and Wear (Tribology), Research Group on Wear of Engineering Materials, Organization for Economic Cooperation and Development (OECD), Paris, 1968.
- [10] J.T. Burwell and C.D. Strang, On the Empirical Law of Adhesive Wear, *J. Appl. Phys.*, 23(1952) 18-28.
- [11] J.T. Burwell, Survey of Possible Wear Mechanisms, *Wear*, Vol.1, 1957-58, 119-141.
- [12] T.S. Eyre, Wear Resistance of Metals, in *Treatise on Materials Science and Technology*, D. Scott ed., 13(1979) 363-441.
- [13] J.F. Archard, Wear Theory and Mechanisms, in *Wear Control Handbook*, M.B. Peterson and W.O. Winer ed., ASME (1980) 35-80.
- [14] M.B. Peterson, Classification of Wear Processes, in *Wear Control Handbook*, M.B. Peterson and W.O. Winer ed., ASME (1980) 9-16.

- [15] S.L. Rice, A Review of Wear Mechanisms and Related Topics, in Fundamentals of Tribology, N.P. Suh and N. Saka ed., MIT Press, (1980), 469-476.
- [16] N.P. Suh, Wear Mechanisms: An Assessment of the State of Knowledge, in Fundamentals of Tribology, N.P. Suh and N. Saka ed., MIT Press, (1980), 443-453.
- [17] S. Jahanmir, On the Wear Mechanisms and the Wear Equations, in Fundamentals of Tribology, N.P. Suh and N. Saka ed., MIT Press, (1980), 455-467.
- [18] T.F.J. Quinn, The Classifications, Laws, Mechanisms and Theories of Wear, in Fundamentals of Tribology, N.P. Suh and N. Saka ed., MIT Press, (1980), 477-492.
- [19] D. Godfrey, Diagnosis of Wear Mechanisms, in Wear Control Handbook, M.B. Peterson and W.O. Winer ed., ASME (1980) 283-312.
- [20] C.S. Yust, Tribology and Wear, Inter. Met. Rev., 30(1985) 141-154.
- [21] K. Zum Gahr, Microstructure and Wear of Materials, Tribology Series, 10, Elsevier, 1987.
- [22] M.A. Moore, A Review of Two-body Abrasive Wear, Wear, 27(1974) 1-17.
- [23] E. Rabinowicz, Friction and Wear of Materials, John Wiley & Sons, Inc., New York, (1965).
- [24] J.F. Archard and W. Hirst, The Wear of Metals Under Unlubricated Conditions, Proc. Roy. Soc., A236(1956) 397-410.
- [25] E.F. Finkin, Adhesive Wear: A General Review of the State of Experimental Knowledge and Theory, Materials in Engineering Applications, 1(1979) 154-161.
- [26] I.M. Hutchings, Tribology-Friction and Wear of Engineering Materials, (1992).
- [27] R.F.J. Quinn, The origins of oxidational wear, Tribology International, 16(1983) 257-271.
- [28] R.F.J. Quinn, Recent Developments and Future Trends in Oxidational Wear Research, Tribology International, 16(1983) 305-315.
- [29] F.P. Bowden and D. Tabor, The Friction and Lubrication of Solids, Clarendon, Oxford, (1958).
- [30] T.S. Eyre, An Introduction to Wear-Wear Characteristics of Metals, in Source Book on Wear Control Technology, D.A. Rigney and W.A. Glaeser ed., ASM, Metals Park, Ohio, (1978) 1-10.

- [31] K. Kato, Tribology of Ceramics, *Wear*, 136(1990) 117-128.
- [32] T. Yamamoto, M. Olsson and S. Hogmark, Three-body Abrasive Wear of Ceramic Materials, *Wear*, 174(1994) 21-31.
- [33] N.P. Suh, Tribophysics, Prentice-Hall Inc., (1986).
- [34] A.D. Hearle and K.L. Johnson, Mode II Stress Intensity Factors for a Crack Parallel to the Surface of an Elastic Half-space Subjected to a Moving Point Load, *J. Mech. Phys. Solids*, 33(1985) 61-81.
- [35] Y. Kimura, The role of Fatigue in Sliding Wear, in *Fundamentals of Tribology*, N.P. Suh and N. Saka ed., MIT Press, (1980), 187-221.
- [36] R.A. Smith, Interfaces of Wear and Fatigue, in *Fundamentals of Tribology*, N.P. Suh and N. Saka ed., MIT Press, (1980), 477-492.
- [37] G.T. Hahn and Q. Huang, Rolling Contact Deformation of 1100 Aluminum Disks, *Metallurgical Transaction*, 17A(1986) 1561-1572.
- [38] N.C. Welsh, The Dry Wear of Steels, *Philos. Trans. R. Soc. London Ser. A*257(1965) 31-50.
- [39] C. Lipson, *Wear Considerations in Design*, Prentice-Hall, Inc., (1967).
- [40] M.B. Peterson, Design Consideration for Effective Wear Control, in *Wear Control Handbook*, M.B. Peterson and W.O. Winer ed., ASME (1980) 413-474.
- [41] P.J. Blau, Competition Between Wear Processes During the Dry Sliding of Two Copper Alloys on 52100 Steel, in *Wear of Materials*, K.C. Ludema ed., ASME (1983) 526-533.
- [42] J.F. Archard, Contact and Rubbing of Flat Surfaces, *J. of Applied Physics*, Vol.24, No.8 August, (1953), 981-988.
- [43] H.S. Meng and K.C. Ludema, Wear Life Equations for Mechanical Designers: State of the Art, WOM-93 9th International Conference on Wear of Materials, San Francisco, April 13-16, (1993).
- [44] D.A. Rigney, Sliding Wear of Metals, *Ann. Rev. Mater. Sci.* 18(1988) 141-163.
- [45] K.C. Ludema, Sliding and Adhesive Wear, in *ASM Handbook*, Vol.18, Friction, Lubrication, and Wear Technology, ASM International, (1992), 236-241.

- [46] J.K. Lancaster, The Formation of Surface Films at the Transition Between Mild and Severe Metallic Wear, Proc. Roy. Soc. A, 273(1963) 466-478.
- [47] F.H. Scott and G.C. Wood, The Influence of Oxides on the Friction and Wear of Alloys, Tribology International, 11(1978) 211-218.
- [48] R. Shivanath, P.K. Sengupta and T.S. Eyre, Wear of Aluminium Silicon Alloys, The British Foundryman, 70(1977) 349-356.
- [49] L.K. Ives, M.B. Peterson and E.P. Whintont, Galling: Mechanism and Measurement, in Engineered Materials for Advanced Friction and Wear Applications, (1988) 33-40.
- [50] M.B. Peterson, L.K. Ives and K.J. Bhansali, A Literature Review of the Galling Process, in Metal Transfer and Galling in Metallic System, (1986).
- [51] I.V. Kragelsky, Friction and Wear, Butterworths, London, (1965).
- [52] J.H. Dautzenberg and J.H. Zaat, Quantitative Determination of Deformation by Sliding Wear, Wear, 23(1973) 9-19.
- [53] A.W. Ruff, L.K. Ives and W.A. Glaeser, Characterization of Wear Surfaces and Wear Debris, in Fundamentals of friction and wear of materials, D.A. Rigney ed., ASM, (1981), 235-289.
- [54] F.E. Kennedy, Single Pass Rub Phenomena-analysis and Experiment, Trans. of the ASME, 104(1982) 582-588.
- [55] F.E. Kennedy, Jr., Determination of Near-surface Plastic Deformation in Sliding Contacts, Journal of Applied Mechanics, 51(1984) 687-689.
- [56] F.E. Kennedy, L.A. Hartman, K.E. Hauck and V.A. Surprenant, The role of Near-surface Plastic Deformation in the Wear of Lamellar Solids, Wear of Materials, K.C. Ludema ed., ASME (1985) 273-279.
- [57] K. Kato, T. Kayaba and Y. Ono, Dislocation Density and Cell Structure Produced in the Subsurface Layer of Aluminum During Sliding Wear, Wear of Materials, (1985) 463-470.
- [58] W.A. Glaeser, High Strain Wear Mechanisms in Ferrous Alloys, Wear of Materials, (1985) 155-162.
- [59] T. Kjer, A Lamination Wear Mechanism Based on Plastic Waves, Wear of Materials, (1987) 191-198.

- [60] S.L. Rice, H. Nowotny and S.F. Wayne, A Survey of the Development of Subsurface Zones in the Wear of Materials, *Key Engineering Materials*, 33(1989) 77-100.
- [61] S.L. Rice, H. Nowotny and S.F. Wayne, Characteristics of Metallic Subsurface Zones in Sliding and Impact Wear, *Wear of Materials*, (1981) 47-52.
- [62] P. Heilmann, J. Don, T.C. Sun, W.A. Glaeser and D.A. Rigney, Sliding Wear and Transfer, *Wear of Materials*, K.C. Ludema ed., ASME (1983) 414-425.
- [63] D.A. Rigney, L.H. Chen, M.G.S. Naylor, and A.R. Rosenfield, Wear Processes in Sliding Systems, *Wear*, 100(1984) 195-219.
- [64] L.H. Chen and D.A. Rigney, Transfer During Unlubricated Sliding Wear of Selected Metal Systems, *Wear of Materials*, K.C. Ludema ed., ASME (1985) 437-446.
- [65] M. Cocks, Interaction of Sliding Metal Surfaces, *J. Appl. Phys.*, 33(1962) 2152-2161.
- [66] M. Antler, Processes of metal transfer and wear, *Wear*, 7(1964) 181-203.
- [67] B.R. Lawn and M.V. Swain, Microfracture Beneath Point Indentations in Brittle Solids, *J. Mater. Sci.*, 10 (1975) 113-122.
- [68] K.L. Johnson, *Contact Mechanics*, Cambridge Univ. Press., (1985).
- [69] D.H. Buckley, *Surface Effects in Adhesion, Friction, Wear and Lubrication*, Elsevier Scientific Publishing Company, (1981).
- [70] J. Zhang, Y. Liu, D. Venugopalan and P.K. Rohatgi, The Stress Field Induced by Contact with Asperities, *J. Mater. Eng.* (1990) 12, 271-278.
- [71] S. Jahanmir and N.P. Suh, Mechanics of Subsurface Void Nucleation in Delamination Wear, *Wear*, 44(1977) 17-38.
- [72] J.E. Merwin and K.L. Johnson, An Analysis of Plastic Deformation in Rolling Contact, *Proceedings of the Institution of Mechanical Engineers*, 177(1963) 676-690.
- [73] H.C. Sin and N.P. Suh, Subsurface Crack Propagation due to Surface Traction in Sliding Wear, *J. Applied Mechanics*, 51(1984) 317-323.
- [74] H. Blok, Theoretical Study of Temperature Rise at Surface of Actual Contact Under Oiliness Lubricating Conditions, *Proc. Instn. Mech. Engrs*, General Discussion on Lubrication and Lubricants, 2(1937) 222-235.
- [75] H. Blok, The Flash Temperature Concept, *Wear*, 6(1963) 483-494.

- [76] J.C. Jaeger, Moving Sources of Heat and the Temperature at Sliding Contacts, Proc. Roy. Soc., 56(1942) 203-224.
- [77] F.F. Ling and E. Saibel, Thermal Aspects of Galling of Dry Metallic Surfaces in Sliding Contact, Wear, 1(1957) 80-91.
- [78] J.F. Archard, Moving Sources of Heat and the Temperature at Sliding Contacts, Wear, (1959), 438-455.
- [79] J.F. Archard and R.A. Rowntree, The Temperature of Rubbing Bodies; Part 2, The Distribution of Temperatures, Wear, 128(1988) 1-17.
- [80] J.R. Barber, Distribution of Heat Between Sliding Surfaces, J. Mech. Engg. Sci., 9(1967) 351-354.
- [81] D.G. Powell and S.W.E. Earles, An Assessment of Surface Temperature Predictions in the high Speed Sliding of Unlubricated SAE 1113 Steel Surfaces, ASLE Trans., 15(1972) 103-112.
- [82] S. Malkin and A. Marmur, Temperatures in Sliding and Machining Processes with Distributed Heat Sources in the Subsurface, Wear, 42(1977) 333-340.
- [83] H. Uetz and K. Sommer, Investigations of the Effect of Surface Temperatures in Sliding Contact, Wear, 43(1977) 375-388.
- [84] T.F.J. Quinn, The Division of Heat and Surface Temperatures at Sliding Steel Interfaces and Their Relation to Oxidational Wear, ASLE trans., 21(1978) 78-86.
- [85] R.T. Spurr, Temperatures reached during sliding, Wear, 55(1979) 289-293.
- [86] F.E. Kennedy, Surface Temperatures in Sliding Systems: A Finite Element Analysis, Trans. of the ASME, 103(1981) 90-96.
- [87] X. Tian and F.E. Kennedy, Contact Surface Temperature Models for Finite Bodies in dry and Boundary Lubricated Sliding, J. Tribology, 115(1993) 411-418.
- [88] C.M.McC. Ettles, The Thermal Control of Friction at High Sliding Speeds, Trans. of the ASME, 108(1986) 98-104.
- [89] C.M.McC. Ettles, Heat Generation and Friction in Rotating Bands, ASLE Trans., 29(1986) 312-320.
- [90] M. Akkok, C.M.McC. Ettles and S.J. Calabrese, Parameters Affecting the Kinetic Friction of ice, Trans. of the ASME, 109(1987) 552-561.

- [91] B. Bhushan, Magnetic Head-media Interface Temperatures, *J. tribology*, 109(1987) 243-256.
- [92] H.S. Kong and M.F. Ashby, Friction-heating Maps and Their Applications, *MRS RUU FT1N*, Oct. (1991).
- [93] M.F. Ashby, J. Abulawi and H.S. Kong, Temperature Maps for Frictional Heating in dry Sliding, *STLE Tribology Tran.*, 34(1991) 577-587.
- [94] P.K. Rohatgi, Y. Liu and R. Asthana, Some Issues in the Construction of Wear Mechanism Maps for Metal Matrix Composites, in *Tribology of Composite Materials*, (1990) 69-79.
- [95] B.K. Prasad, S.V. Prasad and A.A. Das, Mechanisms of Material Removal and Subsurface Work Hardening During Low-stress Abrasion of a Squeeze-cast Aluminium Alloy- Al_2O_3 Fibre Composite, *Mater. Sci. Eng.*, A156(1992) 205-209.
- [96] M. Noguchi and K. Fukizawa, Alternate Materials Reduce Weight in Auto Mobiles, *Advanced Materials and Processes*, 143(1993) 20-26.
- [97] P.K. Rohatgi, Y. Liu and S. Ray, Friction and Wear of Metal-matrix Composites, Vol.18, *Friction, Lubrication, and Wear Technology*, ASM Handbook, (1992), 801-811.
- [98] R.J. Sample, R.B. Bhagat, and M.F. Amateau, *Proceedings on Cast Reinforced Metal Composites*, ASM International (1988), 179.
- [99] Y. Pan, M.E. Fine and H.S. Cheng, Wear Mechanisms of Aluminum-based Metal Matrix Composites Under Rolling and Sliding Contact, in *Tribology of Composite Materials*, P.K. Rohatgi, P.J. Blau and C.S. Yust ed., ASM Materials Park, (1990) 93-101.
- [100] S. Turenne, C. LeDeore and J. Masounave, Slurry Erosion of Al_2O_3 - SiO_2 /Al-4Mg Metal Matrix Composites, *Wear Resistance of Metals and Alloys*, G.R. Kingsbury ed., ASM (1988) 39-45.
- [101] J. Yang and D.D.L. Chung, Wear of Bauxite-particle-reinforced Aluminum Alloys, *Wear* 135(1989) 53-65.
- [102] P.K. Rohatgi, S. Ray and Y. Liu, Friction and Wear Behavior of Metal Matrix-graphite Particle Composites, *Int. Mater. Rev.*, (1990).
- [103] L. Cao, Y. Wang, and C.K. Yao, The Wear Properties of a SiC-whisker Reinforced Aluminium Composite, *Wear*, 140(1990) 273-277.

- [104] A. Wang and H.J. Rack, Transition Wear Behaviour of SiC-particulate-and Sic-whisker-reinforced 7092 Al Metal Matrix Composites, *Materials Science and Engineering*, A147(1991).
- [105] C.S. Lee, Y. H. Kim, K.S. Han and T. Lim, Wear Behaviour of Aluminium Matrix Composite Materials, *J. Mater. Sci.*, 27(1992) 793-800.
- [106] M.D. Aghajanian, R.A. Langensiepen, M.A. Rocazella, J.T. Leighton and C.A. Andersson, The Effect of Particulate Loading on the Mechanical Behaviour of Al₂O₃/Al Metal-Matrix Composites, *J. Mater. Sci.*, 28(1993) 6683-6690.
- [107] N. Axen, A. Alahelisten and S. Jacobson, Abrasive Wear of Alumina Fibre-reinforced Aluminium Wear, *Wear* 173(1994) 95-104.
- [108] N. Saka and D.P. Karalekas, Friction and Wear of Particle-reinforced Metal-ceramic Composites, *Wear of Materials*, K.C. Ludema ed., ASME (1985) 784-793.
- [109] I.M. Hutchings, Abrasive and Erosive Wear of Metal-matrix Composites, *Advanced Structural Materials*, T.W. Clyne and P.J. Withers ed., (1992) 56-64.
- [110] K.J. Bhansali and R. Mehrabian, Abrasive Wear of Aluminum-matrix Composites, *J. of Metals.*, 34(1982) 30-34.
- [111] A. Banerji and P.K. Rohatgi, Cast Aluminium Alloy Containing Dispersions of TiO₂ and ZrO₂ Particles, *J. Mater. Sci.*, 17(1982) 335-342.
- [112] S.V. Prasad, P.K. Rohatgi and T.H. Kosel, Mechanisms of Material Removal During Low Stress and High Stress Abrasion of Aluminum Alloy-zircon Particle Composites, *Mat. Sci. Eng.*, 80(1986) 213-220.
- [113] S. Wilson and A. Ball, Wear Resistance of an Aluminum Matrix Composite, *Tribology of Composite Materials*, P.K. Rohatgi, P.J. Blau and C.S. Yust ed., ASM Materials Park, (1990) 103-112.
- [114] A.G. Wang and I.M. Hutchings, Wear of Alumina Fibre-aluminium Metal Matrix Composites by Two-body Abrasion, *Mater. Sci. Tech.*, 5(1989) 71-76.
- [115] S. Turenne, S. Caron, O. Weiss and J. Masounave, Abrasion Behaviour of Particulate Reinforced Composites, *Fabrication of Particulate Reinforced Metal Composites*, J. Masounave and F.G. Hamel ed., ASM (1990) 271-276.
- [116] K.C. Goretta, W. Wu, J.L. Routbort and P.K. Rohatgi, Solid-particle Erosion of Al/particulate Ceramic Composites, *Tribology of Composite Materials*, P.K. Rohatgi, P.J. Blau and C.S. Yust ed., ASM (1990) 147-155.

- [117] A. Wang and I.M. Hutchings, Erosion of Short Delta-alumina Fiber Aluminum Metal Matrix Composites by Solid Particles, *Metal and Ceramic Matrix Composites: Processing, Modelling and Mechanical Behaviour*, R.B. Bhagat, A.H. Clauer, P. Kumar and A.M. Ritter, ed., (1990) 499-508.
- [118] S. Turenne, Y. Chatigny, D. Simard, S. Caron and J. Masounave, The Effect of Abrasive Particle Size of the Slurry Erosion Resistance of Particulate-reinforced Aluminium Alloy, *Wear* 141(1990) 147-158.
- [119] F.M. Hosking, F. Folgarportillo, R. Wunderlin and R. Mehrabian, Composites of Aluminum Alloys: Fabrication and Wear Behaviour, *J. Mater. Sci.*, 17(1982) 477-498.
- [120] P.K. Rohatgi, B.C. Pai and S.C. Panda, Preparation of Cast Aluminium-silica Particulate Composites, *J. Mater. Sci.*, 14(1979) 2277-2283.
- [121] A. Banerji, M.K. Surappa and P.K. Rohatgi, Cast Aluminum Alloys Containing Dispersions of Zircon Particles, *Metall. Trans.*, 14B(1983) 273-283.
- [122] B.P. Krishnan, N. Raman, K. Narayanaswamy and P.K. Rohatgi, Performance of an Al-Si-graphite Particle Composite Piston in a Diesel Engine, *Wear* 60(1980) 205-215.
- [123] P.K. Rohatgi, S. Ray and Y. Liu, Tribological Properties of Metal Matrix-graphite Particle Composites, *International Materials Reviews*, 37(1992) No.3, 128-150.
- [124] D. Nath, S.K. Biswas and P.K. Rohatgi, Wear Characteristics and Bearing Performance of Aluminium-mica Particulate Composite Material, *Wear* 60(1980) 61-73.
- [125] R.T.B. Deonath and P.K. Rohatgi, Preparation of Cast Aluminium Alloy-mica Particle Composites, *J. Mater. Sci.*, 15(1980) 1241-1251.
- [126] S.V. Prasad and K.P. Mecklenburg, Friction Behaviour of Ceramic Fiber-reinforced Aluminum Metal-matrix Composites, *Wear* 162-164(1993) 47-56.
- [127] R.A. Antoniou, Wear Behaviour of Aluminium-based MMCs Containing SiC Particulate, *Materials Processing and Performance*, (1991) 51-54.
- [128] O.P. Modi, B.K. Prasad, A.H. Yegneswaran and M.L. Vaidya, Dry Sliding Wear Behaviour of Squeeze Cast Aluminum Alloy-silicon Carbide Composites, *Mater. Sci. Eng.* A151(1992) 235-245.
- [129] A.R. Nesarikar, S.N. Tewari and E.E. Graham, Room Temperature Wear Characteristics of Al₂O₃-particle-reinforced Aluminum Alloy Composite, *Mater. Sci. Eng.*, A147(1991) 191-199.

- [130] P.R. Gibson, A.J. Clegg and A.A. Das, Wear of Cast Aluminium-silicon Alloys Containing Graphite, *Wear* 95(1984) 193-198.
- [131] S. Das, S.V. Prasad and T.R. Ramachandran, Microstructure and Wear of Cast (Al-Si alloy)-graphite Composites, *Wear* 133(1989) 173-187.
- [132] A.K. Jha, S.V. Prasad and G.S. Upadhyaya, Dry Sliding Wear of Sintered 6061 Aluminium Alloy-graphite Particle Composites, *Tribol. Int.*, 22(1989) No.5 321-327.
- [133] S.K. Biswas and B.N. Pramila Bai, Dry Wear of Aluminium-graphite Particle Composites, *Wear* 68(1981) 347-358.
- [134] A.K. Jha, S.V. Prasad and G.S. Upadhyaya, Sintered 6061 Aluminium Alloy-solid Lubricant Particle Composites: Sliding Wear and Mechanisms of Lubrication, *Wear* 133(1989) 163-172.
- [135] F.A. Badia and P.K. Rohatgi, Gall Resistance of Cast Graphitic Aluminium Alloys, *SAE Trans.*, 78(1969) 1200-1206.
- [136] Properties and Selection: Nonferrous Alloys and Pure Metals, *Metals Handbook*, 9th ed., ASM, Metals Park, OH, (1979).
- [137] M.A. Moore and R.M. Douthwaite, Plastic Deformation Below Worn Surface, *Metall. Trans.*, 7A(1976) 1833-1839.
- [138] D. Kuhlmann-Wilsdorf, Dislocation Concepts in Friction and Wear, *Fundamentals of Friction and Wear of Materials*, D.A. Rigney ed., ASM (1981), 119-186.
- [139] D.M. Marsh, Plastic Flow in Glass, *Proc. R. Society (London)*, Ser. A, 279(1964) 420-435.
- [140] E. Rabinowicz, Compatibility Criteria for Sliding Metals in Friction and Lubrication in Metal Processing, F.F. Ling, R.L. Whitely, P.M. Ku, and M.B. Peterson, eds., ASME, New York, (1966) 90-102.
- [141] F.P. Bowden and D. Tabor, *The Influence of Surface Films on the Friction and Deformation of Surfaces in Properties of Metallic Surfaces*, Institute of Metals, London, (1953) 197-212.
- [142] R.A. Antoniou, L.J. Brown and J.D. Cashion, The Unlubricated Sliding of Al-Si Alloys Against Steel: Mossbauer Spectroscopy and X-ray Diffraction of Wear Debris, *Acta Metall. Mater.* 42(1994) 3545-3553.

- [143] M.S. Hunter and P. Fowle, Natural and Thermally Formed Oxide Films on Aluminum, *J. of the Electrochemical Society*, 103(1956) 482-485.
- [144] P.H. Doherty and R.S. Davis, Direct Observation of the Oxidation of Aluminum Single-crystal Surfaces, *J. of Applied Physics*, 34(1963) 619-628.
- [145] Corrosion, *Metals Handbook*, 9th ed., ASM, Metals Park, OH. (1987) 581-609.
- [146] A.D. Sarkar, Wear of Aluminium-silicon alloys, *Wear*, 31(1975) 331-343.
- [147] W. Hirst and J.K. Lancaster, The Influence of Speed on Metallic Wear, *Proc. R. Soc.*, 259A(1960) 228-241.
- [148] J.A. Schey, *Tribology in Metalworking*, ASM, Metals Park, Ohio, (1983).
- [149] J. Singh and A.T. Alpas, Elevated Temperature Wear of Al6061 and Al6061-20%Al₂O₃, *Scripta Metallurgica et Materialia*, 32(1995) 1099-1105.
- [150] G.M. Hamilton and L.E. Goodman, The Stress Fields Created by a Circular Sliding Contact, *J. Applied Mechanics*, 33(1966) 371-376.
- [151] A.V. Olver, H.A. Spikes, A.F. Bower and K.L. Johnson, The Residual Stress Distribution in a Plastically Deformed Model Asperity, *Wear*, 107(1986) 151-174.
- [152] D.A. Rigney and J.P. Hirth, Plastic Deformation and Sliding Friction of Metals, *Wear*, 53(1979) 345-370.
- [153] P. Heilmann and D.A. Rigney, An Energy-based Model of Friction and its Application to Coated Systems, *Wear*, 72(1981) 195-217.
- [154] P. Heilmann, W.A. Clark and D.A. Rigney, Orientation Determination of Subsurface cells Generated by Sliding, *Acta Metall.*, 31(1983) 1293-1305.
- [155] D.A. Rigney, L.H. Chen, M.G.S. Naylor and A.R. Rosenfield, Wear Processes in Sliding Systems, *Wear*, 100(1984) 194-219.
- [156] N.P. Suh, An Overview of the Deamination Theory of Wear, 44(1977) 1-16.
- [157] A.S. Argon, J. Im and R. Safoglu, Cavity Formation from Inclusion in Ductile Fracture, *Metall. Trans.*, 6A(1973) 825-837.
- [158] D.A. Hills and D.W. Ashelby, On the Determination of Stress Intensification Factors for a Wearing half Surface, *Eng. Fract. Mech.*, 13(1980) 69-78.

- [159] D.A. Hills and D.W. Ashelby, On the Application of Fracture Mechanics to Wear, *Wear*, 54(1979) 321-330.
- [160] A.R. Rosenfield, A Fracture Mechanics Approach to Wear, *Wear*, 61(1980) 125-132.
- [161] J.R. Fleming and N.P. Suh, The Relationship Between Crack Propagation Rates and Wear Rates, *Wear*, 44(1977) 57-64.
- [162] E.F. Finkin, An Explanation of the Wear of Metals, *Wear*, 47(1978) 107-117.
- [163] R.O. Ritchie, On the Relationship Between Delamination Wear and the Initiation and Growth of Fatigue Cracks in Ultrahigh Strength Steels, *Fundamentals of Tribology*, N.P. Suh and N. Saka ed., MIT Press, (1980), 127-134.
- [164] G. LeRoy, J.D. Embury, G. Edwards and M.F. Ashby, A Model of Ductile Fracture Based on the Nucleation and Growth of Voids, *Acta Metall.*, 29(1981) 1509-1522.
- [165] A.R. Rosenfield, A Shear Instability Model of Sliding Wear, *Wear*, 116(1987) 319-328.
- [166] K.L. Johnson, The Mechanics of Plastic Deformation of Surface and Subsurface Layers in Rolling and Sliding Contact, *Key Engineering Materials*, 33(1989) 17-34.
- [167] E. Voce, The Relationship Between Stress and Strain for Homogeneous Deformation, *J. Inst. Metals*, 74(1948) 537-562.
- [168] D.J. Lloyd and D. Kenny, The Structure and Properties of some Heavily Cold-worked Aluminum Alloys, *Acta Metall.*, 28(1980) 639-649.
- [169] M.A. Moore, R.C.D. Richardson and D.G. Attwood, The Limiting Strength of Worn Metal Surfaces, *Metall. Trans.*, 3(1972) 2485-2491.
- [170] P.W. Bridgeman, *Studies in Large Plastic Flow and Fracture*, McGraw-Hill, (1952).
- [171] J.R. Rice and D.M. Tracey, On the Ductile Enlargement of Voids in Triaxial Stress Fields, *J. Mech. Phys. Solids*, 17(1969) 201-217.
- [172] *Properties and Selection: Irons and Steels*, *Metals Handbook*, 9th ed., ASM, Metals Park, OH. 1978.
- [173] A.T. Alpas and J.D. Embury, The Role of Subsurface Deformation and Strain Localization on the sliding wear behaviour of laminated composites, *Wear*, 146(1991) 285-300.

LIST OF PUBLICATIONS RESULTING FROM THIS WORK

- 1 A.T. Alpas and J. Zhang, Effect of Microstructure (Particulate Size, Volume Fraction) and Counterface Material on the Sliding Wear Resistance of Particulate Reinforced Aluminum Matrix Composites, Metallurgical and Materials Transactions, 25A(1994) 969-983.
- 2 J. Zhang and A.T. Alpas, Wear Rate Regimes in Ceramic Particulate Reinforced Aluminum Alloy, Friction and Wear of Technology for Advanced Composite Materials, P.K. Rohatgi ed., ASM Int., (1994) 65-77.
- 3 J. Zhang and A.T. Alpas, Wear Regimes and Transitions in Al₂O₃ Particulate Reinforced Aluminum Alloys, Materials Science and Engineering, A161(1993) 273-284.
- 4 J. Zhang and A.T. Alpas, Delamination Wear in Ductile Materials Containing Second Phase Particles, Materials Science and Engineering, A160(1993) 25-35.
- 5 A.T. Alpas, H. Hu and J. Zhang, Plastic Deformation and Damage Accumulation Below the Worn Surfaces, Wear, 162-164(1993) 188-195.
- 6 J. Zhang and A.T. Alpas, Tribological Behaviour of Al₂O₃ Particulate Reinforced 6061 Al Matrix Composites, Advances in Production and Fabrication of light Metals and Metal Matrix Composites, M.M. Avedesian etc. ed., (1992) 651-663.
- 7 A.T. Alpas and J. Zhang, Effect of SiC Particulate Reinforcement on the dry Sliding Wear of Aluminium- silicon Alloys (A356), Wear, 155(1992) 83-104.
- 8 A.T. Alpas and J. Zhang, Wear Rate Transitions in Cast Aluminum-silicon Alloys Reinforced with SiC Particles, Scripta METALLURGICA et MATERIALIA, Vol.26, (1992) 505-509.

LIST OF PRESENTATIONS

(Resulting from this work)

- 1 J. Zhang and A.T. Alpas, Wear Rate Regimes in Particulate Reinforced Aluminum Alloys, 9th International Conference on Wear of Materials, San Francisco, California, U.S.A., April 13-16, 1993.
- 2 A.T. Alpas, H. Hu and J. Zhang, Plastic Deformation and Damage Accumulation Below Worn Surfaces, 9th International Conference on Wear of Materials, San Francisco, California, U.S.A., April 13-16, 1993.
- 3 J. Zhang and A.T. Alpas, The Effects of Applied Load, Sliding Speed, Particulate Size, Volume Percentage, Counterface and Heat Dissipation Rate on Dry Sliding Wear of MMC, 5th Canadian Materials Science Conference, Kingston, Ontario, Canada, June 21-25, 1993.
- 4 J. Zhang and A.T. Alpas, Tribological Behaviour of a Al_2O_3 Particulate Reinforced 6061 Al Matrix Composites, 31st Annual Conference of Metallurgists of CIM, Edmonton, Alberta, Canada, August 23-27, 1992.
- 5 J. Zhang and A.T. Alpas, Delamination Wear in Ductile Materials Containing Second Phase Particles, 4th Canadian Materials Science Conference, Kingston, Ontario, Canada, June 16-19, 1992.
- 6 J. Zhang and A.T. Alpas, Sliding Wear of Aluminum Alloys (A356) Reinforced by SiC Particles, 3rd Canadian Materials Science Conference, Kingston, Ontario, Canada, June 18-21, 1991.

VITA AUCTORIS

The author was born in P.R. of China on February 19, 1958.

EDUCATION

Bachelor of Science in Materials Engineering, Harbin Shipbuilding Engineering Institute, Harbin, Heilongjiang, P.R. of China, 1982.

Master of Science in Materials Engineering, Harbin Shipbuilding Engineering Institute, Harbin, Heilongjiang, P.R. of China, 1985.

Joined the Ph.D. Program at the University of Windsor, Ontario, Canada, in January 1991.

EMPLOYMENT

Lecturer, Mechanical Engineering Department, Harbin Shipbuilding Engineering Institute, P.R. of China, 1982-1989.

Visiting Scholar, University of Windsor, 1989-1990.

Research Assistant/Teaching Assistant, Mechanical Engineering Department, University of Windsor, Canada, 1991-1995.